University of Nottingham

School of Mathematical Sciences

Multiscale Methods for the Flow During Grinding

Zakhary Crowson

A thesis submitted to the University of Nottingham for the degree of

Doctor of Philosophy

November 2022

ABSTRACT

When the machining process known as grinding is used, a grinding fluid is applied to regulate the temperature of the workpiece and reduce the risk of expensive thermal damage. The factors which influence the transport of this fluid are not well understood. However, they are important to understand otherwise unnecessary cost can be incurred from inefficient application of the grinding fluid.

This thesis identified three length scales of the flow during surface and creep-feed grinding, and used asymptotic methods on a multiphase model to derive a multiscale system of equations governing the flow. Under the lubrication approximation, we have shown that it is possible to calculate the flux through the grinding zone without having to solve for the flow far from the grinding zone. No extra empirical boundary conditions need to be imposed. This was done using the method of matched asymptotic expansions.

Focusing on Trizact$^{\mathrm{TM}}$ abrasive profiles, we used two-scale homogenisation on the grinding zone flow to derive a model at realistic Reynolds numbers. We found that the angle of orientation of the abrasives influenced the velocity of the flow across the grinding zone. In particular, we observed that the angle affected the speed at which the grinding fluid was transported through the grinding zone, as well as which side of the grinding wheel that grinding fluid leaked out of.

We also identified potential regimes where the flow became turbulent in the grinding zone, finding that the onset of turbulence occurred at lower Reynolds number when there was a larger concentration of grinding fluid surrounding the abrasives. This finding supports an existing argument against the use of flooding the grinding zone prior to start-up and during the grinding process.

ACKNOWLEDGEMENTS

I would like to express my sincere gratitude to my supervisors Professor John Billingham, Professor Paul Houston and Professor Dragos Axinte for their remarkable support, motivation but most of all patience during my Ph.D. studies. This thesis would not have been possible without them all, and they have all given me invaluable advice and discussions throughout the process. I wish them the best for whatever the unpredictable future may bring.

I would also like to thank my family, friends and partner, Daria, for their support, encouragement and seemingly everlasting enthusiasm for asking if it is done yet throughout my Ph.D. I can now finally give them all a simple answer.

CONTENTS

1

INTRODUCTION

Tribology is the science of interacting surfaces in relative motion. Although tribological processes have been fundamental throughout the history of human civilisation, the scientific study of these processes begin as recently as the mid-20^{th} century. In fact, the term tribology was first introduced in 1966 by the Department of Education and Science in a report on the cost to industry of friction and wear in such processes [43]. Since then, the word tribology has been used to encompass many processes which involve any aspect of friction, wear or lubrication: lubrication of bearings, gear rotations and milling are just a few processes which would now be considered tribological.

A machining process which dates back far longer than the word tribology, but which is unanimously considered a tribological process, is grinding. Grinding is commonly used to rapidly remove material from and finish metallic and ceramic components, which will be referred to as the workpiece throughout this thesis. Grinding aims to produce components with a required surface profile and smoothness. To do this, the workpiece is fed into the path of a spinning, thin cylinder which consists of many small, discrete, sharp cutting points. These cutting points are referred to as the abrasives, which are bonded together to form the grinding wheel. When an abrasive impacts the workpiece, it removes a small quantity of material from the surface of the workpiece. The aim of this process is to ensure the cutting points produce a workpiece fit to the consumer's desired specifications. Familiar examples of grinding are the sharpening of metal blades against a rotating sharpening wheel, and the

Figure 1: From [1]. Image taken during the surface grinding of a workpiece. Sparks can be seen being emitted from the cutting occurring in the grinding zone. The nozzle in the bottom right is closely positioned to the wheel to deliver grinding fluid into the grinding zone.

polishing of surfaces with a sanding machine. An image of the grinding process described here is provided in figure 1.

However, due to the large number of cutting operations occurring over small timescales, there are many potential issues that may arise during grinding: the generation of discarded chips (the removed workpiece material) and high surface temperature are two that may be faced in many grinding situations [58]. High surface temperatures are a primary concern in grinding due to the increased risk of direct or indirect thermal damage to the workpiece. Thermal damage can affect the workpiece through undesirable cosmetic damage, plastic deformation or increased brittleness due to repeated extreme heating and cooling from the air.

The usual method in industry to remedy these issues is to deliver a fluid, referred to as the grinding fluid, to the grinding zone. This is the region of contact between the workpiece and grinding wheel. The fluid is delivered by placing a nozzle near the entrance of the grinding zone which ejects grinding fluid into the path of the spinning grinding wheel. This causes it to be dragged into the grinding zone by the grinding wheel. Then, depending on the rheology of the grinding fluid, the grinding fluid can work by lubricating the grinding zone to reduce heat generation or wear, or by cooling the workpiece through

heat conduction from the workpiece. Other than lubricating and cooling the workpiece, the grinding fluid is able to wash away and dislodge chips or abrasive fragments that can become stuck in the spaces between the abrasives. It is worth remarking that although it is referred to as a grinding fluid, this can not only be a single-phase fluid such as air or water, but also a mixture, a commonly used one being oil and water.

In this process, a variety of flow regimes can be identified. The simplest of these is far from the grinding wheel and nozzle, where there is quiescent air. At the nozzle head, we can expect there to be entrained bubbles which form, or are already present in, the high speed grinding fluid bulk as it travels through and out of the nozzle. This slug flow regime persists until the grinding fluid is close to the grinding wheel, where a small amount of the grinding fluid-air mixture is dragged into and through the grinding zone, but with the rest existing as pockets of liquid in air around the grinding wheel due to splashing. Additional flow regimes can arise from the formation of bubbles on the surface of the wheel due to high shearing effects, or the formation of grinding fluid vapour due to film boiling inside the grinding zone. However, such phenomena are outside the scope of this thesis.

While this method of fluid delivery has been in use for many years, there is no consensus in the current scientific research for methods of maximising cooling while minimising the applied fluid. As a result, the industry standard has been to use as much fluid that the operator deems reasonable to provide sufficient cooling. Thus, empirical experience is the knowledge that is used by operators for fluid delivery during grinding. However, an immediate consequence of this approach is that costs associated with the application of grinding fluid can account for up to 17% of the total costs incurred in grinding a workpiece [47].

Over the years, different grinding operations have been adapted and developed to accommodate the demands of industry. This thesis will be focused on up-grinding in surface and creep-feed grinding regimes, two of the most common grinding operations. Up-grinding refers to the situation where the grinding wheel cuts the workpiece in the reverse direction to the path of the workpiece,

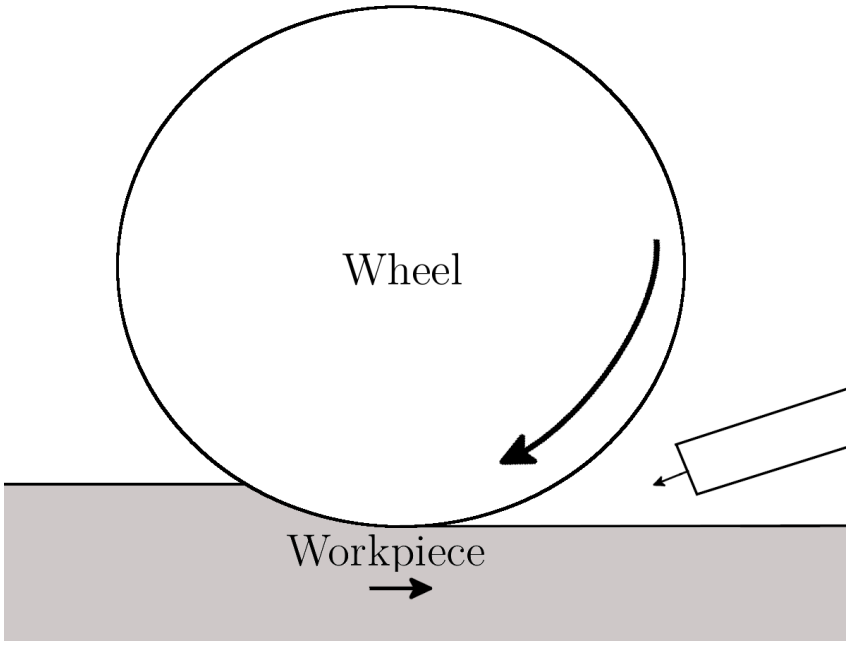

Figure 2: Illustration of the up-grinding regime with the nozzle positioned such that grinding fluid is directed towards the grinding zone. The arrows represent the direction of velocity.

see figure 2. Both surface and creep-feed grinding regimes are similar to the situation depicted in figure 2, namely, the workpiece is slowly passed under a high-speed spinning grinding wheel in order to achieve a flat, finished surface. With each pass, a thin layer of thickness d_c is removed. This is referred to as the depth of cut. The speed that the grinding fluid exits the nozzle is usually chosen to be around the speed that the grinding wheel spins.

The differences between surface and creep-feed grinding lie in their purpose. Surface grinding is used for removing material off a workpiece's surface to acquire a smooth finish. For this purpose, surface grinding uses grinding wheels with fine abrasives, low depth of cuts and multiple passes of the workpiece across the grinding wheel.

In contrast, the purpose of creep-feed grinding is the quick removal of a large quantity of material from the workpiece's surface. This is done by using grinding wheels with coarse abrasives and large depth of cuts. There is only one low speed pass of the workpiece across the grinding wheel. Illustrations of surface and creep-feed grinding regimes in the region around the grinding zone

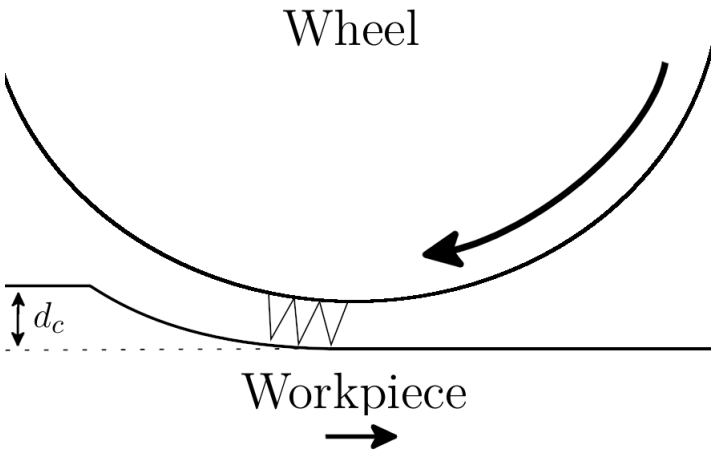

Figure 3: Illustration of a surface up-grinding regime. The arrows represent the direction of velocity. Surface grinding typically uses smaller abrasives and shallower depths of cut, d_c, than creep-feed grinding.

Grinding parameter	Surface	Creep-feed
Grinding wheel speed	2×10^{1} m s^{-1}	3.5×10^{1} m s^{-1}
Nozzle grinding fluid velocity	2×10^{1} m s^{-1}	3.5×10^{1} m s^{-1}
Workpiece speed	1×10^{-1} m	1×10^{-3} m
Abrasive size	1×10^{-5} m	5×10^{-4} m
Depth of cut	2×10^{-5} m	2.4×10^{-3} m

Table 1: Typical values for distinguishing quantities of surface and creep-feed grinding regimes.

are shown in figures 3 and 4, respectively. Typical values for these quantities can be found in table 1.

Another commonly used grinding operation in industry is centreless grinding. This is used for efficient large-scale manufacturing of cylindrical objects by using a second wheel to rotate the workpiece. Centreless grinding is outside the scope of this thesis, but an extensive review of the many grinding methods used in industry can be found in [59].

In the following section, we examine the current literature associated with the work presented in this thesis. This chapter will then end with a discussion on the aims and outline of this thesis.

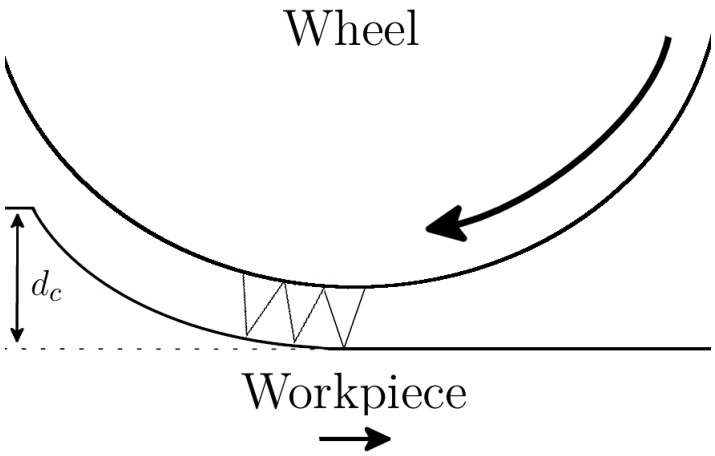

Figure 4: Illustration of a creep-feed up-grinding regime. The arrows represent the direction of velocity. Creep-feed grinding typically uses larger abrasives and deeper depths of cut, d_c, than surface grinding.

1.1 EXPERIMENTAL STUDIES

During grinding, a thin layer of air can be observed surrounding the grinding wheel and moving with it. At high speeds, this air layer can have devastating effects on the quality of the workpiece as it is capable of reducing the flow of the grinding fluid through the grinding zone to such an extent that the cooling of the workpiece is insignificant. Depending upon the fluid delivery system and grinding machine setup, it is even possible that no grinding fluid is able to penetrate the layer, thus starving the grinding zone of all grinding fluid [28]. In order to develop methods that ensure sufficient cooling of the workpiece, research has been conducted to understand the behaviour of this layer.

Alenius et al. [5] measured the tangential velocity of the air boundary layer, v_t, at various distances from the grinding wheel's surface. They found that v_t followed an exponentially decreasing behaviour with respect to normal distance from the surface. They also sought measurements along the width of the grinding wheel, observing that the maximum in v_t occurred at the midpoint of the width. It is worth noting that the measuring device was an (intrusive) pitot tube, and the data they collected is from various angles of inclination for the tube, thus leading to possible inconsistencies with the collected data.

Wu. et al. [38] used a laser Doppler anemometry[1] system to measure the velocity of the air boundary layer at points below the grinding wheel. At a fixed point in the air boundary layer, they observed that an increase in the grinding wheel's velocity corresponded to an increase in v_t. Additionally, their results agree with Alenius and Johansson's with respect to the dependence of v_t on the increasing radial distance from the grinding wheel's surface; however, their results taken along the width of the grinding wheel disagree: Wu. et al. did not observe the distinctive maximum of v_t. The authors' conjecture that the reason for such contradicting observations was due to the differing grinding wheels. Specifically, the roughness and also the experimental conditions. The uncertainty behind these different measurements and the implications this could have on the delivery of the grinding fluid highlights a necessity to gain a deeper understanding of the physics in the process.

Concerning flow field measurements in grinding, it is important to note a commonality in all of the aforementioned experiments, which is that the grinding process is only simulated. The grinding wheel spins above and makes no physical contact with the workpiece. Therefore, although a model may correlate well with these experiments, consideration of the variance between the simulated experiments and realistic grinding scenarios must be taken into account when inferring any of this model's predictions for a realistic grinding scenario.

Engineer et al. [29] used an elaborate scraper and funnel system during wet grinding to collect the grinding fluid which had been transported from the nozzle and through the grinding zone. At a depth of cut of 6×10^{-6} m, they observed that an increase in the porosity of the grinding wheel corresponded with an increase in the grinding fluid which was transported to the end of the grinding zone. This supports the intuitive belief that increasing the available space between abrasives correlates with an increase in grinding fluid transported through the grinding zone, due to the extra space available as pores in the grinding wheel. Interestingly, for certain porosities, there seemed to be an

1 Further information on this method of measurement, as well as its application to grinding, can be found in [93].

almost linear proportionality between the nozzle flow rate and flow rate through the exit of the grinding zone. This reinforces the idea that increasing the amount of grinding fluid that is delivered towards the grinding zone can lead to an increase in grinding fluid through the grinding zone.

Mandal et al. [46] used a simple guard and funnel system to capture the fluid passing through the grinding zone. They observed the existence of a critical flow rate of the grinding fluid, below which no fluid passed through the grinding zone. Furthermore, they observed that increasing the flow rate at the nozzle increased the total flow through the grinding zone. For their particular experimental set-ups, Mandal et al. found that the flow rate through the grinding zone varied from 0 to 35% of the flow rate at the nozzle. They also discuss the use of various shaped nozzles to deliver the grinding fluid and how the shape can affect the percentage of fluid passing through the grinding zone, although the variance in their experimental parameters leaves this to be a qualitative observation.

O'Donovan et al. [68] measured the velocity of air exiting a nozzle in a two dimensional plane near the grinding zone. Using Particle Imaging Velocimetry (PIV) over a sampling area of roughly 1.6×10^{-3} m^2 and 3×10^{-2} m from the grinding zone, they observed a region of recirculation approximately 45mm away from the grinding zone due to the impenetrability of the entrained air boundary layer. It was remarked that flow field measurements were only available for low velocities of the air exiting the nozzle, due to the difficulty in taking PIV measurements at high velocities.

In the following section, we will discuss the progress that has been made towards accurately predicting the dynamics of the fluid flow during grinding.

1.2 MATHEMATICAL STUDIES

1.2.1 *Previous Results*

Researchers have long been aware of the role of the space between abrasives in transporting fluid to the grinding zone [24]. Those that have attempted to

Figure 5: From [60]. Image taken of simulated grinding whereby a thin gap exists between the grinding wheel and workpiece. The grinding fluid is observed to travel through the gap in a far greater amount than it would be expected to travel through the grinding zone.

mathematically describe the grinding fluid have simplified this by supposing that the spaces between abrasives form an effective gap between the workpiece and the grinding wheel. More precisely, they consider the grinding wheel to be spinning at a non-zero distance above the workpiece such that no contact is made between the two surfaces. An image of a simulated grinding setup is shown in figure 5.

A common approach is to then model the flow in this effective gap with Reynolds equation. Originally derived by Reynolds [74], the one dimensional Reynolds equation is given by

$$\frac{\partial}{\partial x}\left(\frac{h^3}{\mu}\frac{\partial p}{\partial x}\right) = 6\left(u_1 + u_2\right)\frac{\partial h}{\partial x} + 12\frac{\partial h}{\partial t}, \tag{1}$$

which governs the pressure distribution, p, in the gap between two surfaces separated by an a-priori known distance, h. Here, u_1 and u_2 are the speeds of the two surfaces and μ is the dynamic viscosity of the fluid.

The key assumptions in the derivation of (1) are that the fluid is Newtonian and incompressible, the gap between the surfaces is thin enough that viscous forces dominate over inertial forces and that body forces (e.g. gravity) are negligible.

Although Reynolds equation was originally derived to describe the lubrication of a journal bearing using olive oil, similar derivations have been used on flows involving thin layers of fluid to formulate similar models. Some examples include the motion of a droplet near its moving contact line [25], the air flow in a hard drive [80] and the thin flow of deposited liquid films in coating processes (e.g. curtain coating) [90]. We shall review some of the work which apply the same principles behind the derivation of Reynolds equation to model the flow during grinding, as well as other approaches.

Assuming an incompressible fluid surrounded the grinding wheel, Schumack et al. [78] considered the two dimensional stream function form of the steady Navier-Stokes equations at small Reynolds numbers. They set up their flow domain as the region $L_u \leq x \leq L_d$, where L_u and L_d are points beneath the grinding wheel where they experimentally measured pressure. Instead of taking the grinding wheel to spin at high speeds, they supposed the grinding wheel was held stationary and that the infinitely long workpiece was moving at a typical grinding wheel speed. They treat the grinding fluid as incompressible and remark that "pressure is small in grinding situations and hence does not influence the viscosity". By assuming that the gap between the grinding wheel and the workpiece was thin enough that viscous forces dominate over inertial forces, they were able to derive an expression for the pressure in the gap.

In order to close their problem, empirically determined flow rates had to be prescribed at the boundaries given by $x = L_u$ and $x = L_d$. The numerical results for the pressure appeared to correlate well with the measurements taken when the flow was characterised by a small Reynolds number. However, this was not the case when the experimental parameters were such that inertial effects started to dominate in the flow, i.e. at large Reynolds numbers. Furthermore, there are drawbacks in their approach. The notable problems arise from the lack of generality due to the empirically determined flow rate, and excessive reliance on experimental data in the unsteady case. These issues highlight the necessity for models which can be solved without depending on difficult-to-obtain measurements. Additionally, after presenting their numerical results, it

was suggested that an alternative approach is necessary when considering flows with large inertial effects.

Hryniewicz et al. built upon the work of Schumack et al. in their two papers [36] and [37] by considering the effect that roughness of the grinding wheel's surface has on the pressure in the grinding zone. To incorporate the effects of roughness, they used a volume averaging technique on the leading order Reynolds equation at moderate Reynolds number and equated the distance between the bottom of the grinding wheel and the workpiece in their model as the minimum distance between the grinding wheel's abrasives and the workpiece in their experiments. Their numerical results for the pressure show a reasonable correlation with experimental results, although the predicted pressure values deviate further from the experimental ones as the grinding wheel speed increases (that is, as the Reynolds number increases). As the authors' focus was only the hydrodynamic pressure in the grinding zone, they encounter the same difficulties as Schumack et al. when attempting to solve for the velocity field, specifically the unknown velocity boundary conditions. Furthermore, their results experience a similar breakdown of accuracy when inertial effects become relevant at higher Reynolds numbers.

More recently, both commercial and open-source computational fluid dynamics software, such as Fluent [2] and OpenFoam [3], respectively, has allowed researchers to simulate the full problem: assembling models of the flow process from pre-specified sets of equations and solving them automatically. This approach has made an arduous task accessible and convenient to researchers with various backgrounds. Mihić et al. [62] used Fluent to investigate the two-phase (air and grinding fluid) flow in the presence of heat transfer. A key feature of their model is the use of the multiphase mixture model for the flow (we refer the reader to [20] for further details on this model). In this model, only one momentum equation must be solved for both phases, reducing the computational burden substantially. A second feature of the approach in [62] is the inclusion of roughness effects through a sink term in the momentum equation, applied in a region defined by the authors as being representative of the grinding zone re-

gion. Their numerical results appear to correlate well with experimental results. Namely, that there is an increase of the grinding fluid flux into the grinding zone when there is an increase in the grinding wheel speed.

Concerning general lubrication systems, Patir et al. [69] advanced the study of lubrication fluid systems by extending the standard Reynolds equation into the 'average Reynolds equation'. They began by considering a single incompressible fluid that occupied the lubrication domain between two (possibly contacting) rough boundaries, and then assumed the existence of a control volume that is 'sufficiently large to include a large number of asperities', but small relative to the dimensions of the whole lubrication domain. After separating the flow through the control volume into contributions due to pressure gradients and imposed shear forces, they introduced three flow factor functions which essentially act as functions of proportionality between the averaged fluid flux (over the control volume) and the actual fluid flux. This allows the final average Reynolds equation to be stated, which includes these flow factors. This method is similar to that used in the field of homogenisation, which takes advantage of the large scale separation between the dimensions of the control volume and, in this case, the lubrication domain. We refer the reader to [70] for further details on the field of homogenisation.

The primary advantage of using such a Reynolds equation is that the precise geometry of the domain is no longer necessary when solving for the pressure distribution, instead being replaced by quantities which represent the average (smoothed) geometries. The primary advantage of this is a large reduction in the computational cost of solving problems involving very rough boundaries. However, disadvantages lie in the rigour of the method, namely whether the flow factors as defined are capable of capturing the correct mean behaviour, or whether the dimensions that the control volume takes has an overwhelming effect on the mean pressure distributions.

Since the work of Patir et al., a great deal of research has been performed on applying homogenisation to lubrication systems. In particular, Bavada et al. [16] considered the Stokes system with different regimes of roughness. The

vanishing periodicity of the rough geometry allowed them to homogenise the system with respect to this quantity and obtain a weak formulation for the homogenised system. This allowed them to inspect different limits corresponding to each regime of roughness. Following this, various existence and weak convergence results of the homogenised system were presented.

While the aforementioned work was primarily concerned with theoretical results, there has been research into numerical results of homogenised lubrication systems. One such example is the work by Almqvist et al [12], who considered flow in a bearing with a (periodic) sinusoidal roughness profile. The results showed that in the one dimensional case, the mean pressure solution for their homogenised Reynolds equation matched very well with the solution to the Reynolds equation with deterministic roughness for a suitably small periodicity.

1.2.2 *Turbulence*

While the literature on turbulence in various fluid flows is extensive, it is still an open question how turbulent effects should be resolved in any single flow. In the following paragraphs, we will briefly recapitulate the relevant studies on turbulence and discuss the methods of resolution of turbulent effects in flow studies.

The initial key research began in the mid-20^{th} century with Kolmogorov and Richardson in the studies [48] and [75], respectively. The summary of Richardson's work is that over the macroscopic length scale, turbulent kinetic energy is produced and is transferred to eddies of characteristic lengths of the same order as that over which the flow takes place. Due to the instability of these eddies, break-up occurs and their energy is transferred into smaller eddies. This energy cascade continues until the energy is transferred to the smallest stable eddies, where it is dissipated through viscous effects.

Kolmogorov deduced that the smallest eddies are present at extremely-small length scales in any flow. Thus, solving the Navier-Stokes equations directly

while resolving all scales of a turbulent flow is infeasible. It becomes necessary to incorporate the effect of small-scale turbulent structures on the flow in such a way that the problem is not too computationally demanding. In engineering applications involving complex flow geometries, the prevailing method to perform the aforementioned incorporation is through the modelling of the Reynolds stress, $\left\langle u_i' u_j' \right\rangle$. This term arises from separating the flow variables into mean and fluctuating components, i.e. $u_k = \langle u_k \rangle + u_k'$, and using an averaging operator $\langle \cdot \rangle$ over the Navier-Stokes equations.

Typically, the Reynolds stress is modelled by applying the Boussinesq hypothesis. This introduces the eddy viscosity, a quantity which models the transport and dissipation of energy in the smallest eddies, and relates it to the Reynolds stress through the relation

$$\rho \left\langle u_i' u_j' \right\rangle = \frac{2}{3}\rho k \delta_{ij} - 2\mu^t \varepsilon_{ij} \left(\langle \boldsymbol{u} \rangle \right), \tag{2}$$

$$k = \frac{1}{2} \left\langle u_i' u_i' \right\rangle, \tag{3}$$

$$\boldsymbol{E} \left(\langle \boldsymbol{u} \rangle \right) = \frac{1}{2} \left(\nabla \langle \boldsymbol{u} \rangle + \left(\nabla \langle \boldsymbol{u} \rangle \right)^T \right), \tag{4}$$

where ρ is the fluid density, δ_{ij} are components of the Kronecker delta tensor, k represents the turbulent kinetic energy and μ^t denotes the eddy viscosity. In order to close the problem, turbulent kinetic energy and eddy viscosity must be modelled, which is generally done using an established turbulence model.

The mixing length model is the simplest turbulence model, introduced by Prandtl in [72]. The essence of the mixing length model is that an element of fluid will maintain its momentum across a characteristic distance, l_x. The turbulent kinetic energy is neglected and μ_t in (2) is taken to be

$$\mu^t = \rho l_x^2 \sqrt{2\boldsymbol{E} \left(\langle \boldsymbol{u} \rangle \right) : \boldsymbol{E} \left(\langle \boldsymbol{u} \rangle \right)}. \tag{5}$$

This simplicity comes at a cost, and in problems with boundary layer separation or adverse pressure gradients, the mixing length model fails to accurately capture physics of the turbulent structures [92]. Other turbulence models which are

popular in industrial applications include the two transport equation $k-\epsilon$ [53] and $k-\omega$ [91] models and the one equation Spalart-Allmaras (SA) turbulence model [84].

Extensions to existing turbulence models are continually being proposed which widen a model's applicability to specific flows. For example, one extension to the SA model reduces the numerical instabilities that the SA model exhibits in wall-bounded flows [9], another extension incorporates the effects of curvature on turbulent structures into the model [82]. However, there is currently no work in the literature on the validity of existing turbulence models for the flow during grinding.

1.3 THESIS AIMS AND OUTLINE

The aim of this thesis is to apply a variety of mathematical modelling methods in order to investigate and understand the behaviour of fluid transport during grinding. The main methods which form the foundation of the work in this thesis are the method of matched asymptotic expansions and asymptotic homogenisation for model reduction over distinct scales. Such model reductions are necessary to study the flow behaviour of grinding fluid, as the complexity of the flow does not lend the original model to theoretical or numerical consideration. Reduced models inevitably fail to reproduce the exact behaviour of the original models, or have a smaller scope of applicability than the original. However, the approach of model reduction is that each subsequent model builds upon the previous one. Therefore, we examine the predicted flow behaviour of the reduced models and the assumptions we used to derive them. This is done so that disadvantages of the reduced model can be detected, even for models commonly used in the literature for studying grinding fluid transport, and amendments can be made.

Concisely, our aim is to investigate whether these multiscale mathematical methods can be applied to the flow during grinding. If so, can these reduced models help us to gain valuable knowledge into the factors which influence the

flow? Will this knowledge help us to then optimise the application of grinding fluid in the process and reduce costs associated with wasted grinding fluid?

1.3.1 *Mathematical Fundamentals*

The journey towards the answer to these questions begins in Chapter 2. In this chapter, we state the mathematical tools we will need to study the flow during grinding. We begin with the multiphase model, a system of equations derived from the Navier-Stokes equations using the concept of volume averaging. We then familiarise the reader with the Navier slip boundary condition, and finally we describe the abrasive profiles for the grinding wheels that we will focus on in this thesis. Namely, a mathematically smooth profile and an engineered profile formed of repeating regular pyramids, known as Trizact$^{\text{TM}}$ abrasives.

1.3.2 *Multiscale Methods Introduction*

In Chapter 3, we introduce the asymptotic methods that are used in each chapter thereafter. The goal of this chapter is to investigate multiscale methods on a simplified problem of grinding which retains the dominant transport induced by the shearing of the grinding wheel. We see on this problem how we can exploit the distinct multiple scales inherent in grinding.

In greater detail, this simplified problem is the idealised geometry of a smooth, spinning wheel situated a small distance above the workpiece. We separate the flow domain into two domains and exploit the small length scales expected in the grinding zone to derive a reduced dimension model there, the widely familiar Reynolds equation. We find that we are able to solve for the flow in the grinding zone without needing to solve for the large scale flow associated with the grinding wheel. This allows us to calculate the flux of grinding fluid through the grinding zone, and we find that this is a negligible amount when

viewed on the large scale. Further, it motivates us to apply the same methods on a problem with a more realistic grinding geometry.

1.3.3 *Lubrication Flow*

Chapter 4 is concerned with applying the method of matched asymptotic expansions from Chapter 3 on a more realistic grinding geometry. In this chapter, we model the depth of cut in the workpiece. Building upon the work of Chapter 3, we focus on the flow around the grinding zone and find that the depth of cut changes the mathematical behaviour of the solution. We find that there are three separate cases to consider depending on the size of the depth of cut. In each case, we find that decreasing the depth of cut leads to an increase in the flux of grinding fluid through the grinding zone. Additionally, we separate the flux into two components: one due to the shearing of the grinding wheel and another due to the pressure gradient across the grinding zone. We find that the flow is primarily driven by the shearing of the wheel, with the pressure gradient responsible for only around 10% of the total flux in both the surface and creep-feed grinding regimes that we consider.

We then extend the problem to include slip at the surface of the grinding wheel and workpiece. We find that there are now five separate cases to consider depending on the size of the depth of cut and slip. In the slip regime, we find that the shearing of the wheel is still the primary driver of the flow through the grinding zone.

1.3.4 *Two-Scale Homogenisation Model*

Due to the limited applicability of the lubrication approximation to boundaries with $O(1)$ slope, we begin Chapter 5 by focusing on a Stokes flow regime. We determine that there are at least two distinct length scales in the grinding zone flow. In particular, these length scales are the size of a single abrasive and the

length of the grinding zone. We concentrate only on manufactured grinding wheels in this chapter; that is, where the abrasive profile is engineered to a certain specification. As the manufactured grinding wheels of interest have periodic abrasive profiles, the problem is appropriate for two-scale asymptotic homogenisation. This, in essence, averages the flow over a single abrasive and then upscales this flow to derive a system of equations similar to the lubrication approximation, but with coefficients which depend on information from the abrasive-scale flow.

The homogenisation of Stokes equations in similar geometries has previously been done in the literature by Fabricius et al. [31]. However, we find that when homogenising these equations in a cylindrical (or polar) coordinate system, there are additional curvature terms that arise in the upscaled equations. These terms have not been reported in the aforementioned previous work due to their use of a Cartesian coordinate system. We investigate these terms and find that, in certain regimes, these terms are not zero and can have an auxiliary influence on the transport.

We deduce that the flow in all regimes studied behaves in the large shear rate limit. With regard to the homogenisation process, this is the distinguishing factor in the study of the flow that separates grinding from flow in porous media. Hence, taking the appropriate assumptions for this high shear limit, we derive a novel model which considers inertial effects of the flow.

With this model, we present and investigate solutions for different regimes of grinding fluid flow at realistic Reynolds numbers. Particularly, we discover that there is an inverse relation between the amount of grinding fluid surrounding abrasives and the onset of turbulent flow. Additionally, an aspect in the design of the abrasive profile has been found to have an effect on the speed that grinding fluid is transported across the grinding zone. We conclude these investigations with discussions of potential optimisations in the application of grinding fluid that can be inferred from the results. Emphasis is placed on understanding the high Reynolds number flow behaviour here, primarily due to the undesirable consequences that turbulence effects could have on the flow. Inefficient

cooling, diminished lubrication and poor chip removal from the grinding zone due to regions of stagnation or recirculation are just a few of the consequences that could dramatically affect the efficiency of the grinding fluid application. Thus, with the goal of avoiding costly thermal or cosmetic damage to the workpiece, understanding the onset on these flow structures is necessary to develop methods to prevent them from occurring.

2

MATHEMATICAL FUNDAMENTALS

2.1 MODEL MOTIVATION

The continuum approximation is an averaging process over a small sampling volume element whereby discrete fields associated with individual molecules are replaced by a smooth field. Thus, instead of considering the conservation of each individual molecule's mass, for example, it is necessary to only consider the conservation of the macroscopic property density, the mass per unit volume. This simplifying approximation allows a countless number of otherwise-intractable fluid and solid mechanics problems to be solved and better understood.

The foundational equations which govern the behaviour of fluids under the continuum approximation are derived based on three conservation laws: conservation of mass, conservation of (linear and angular) momentum and conservation of energy (also known as the First Law of Thermodynamics [94]). We will treat the flow as an isothermal process. Thus, conservation of energy is automatically satisfied and it will not form part of the governing equations.

Conservation laws are able to be mathematically described in integral (global) form or differential (local) form. In differential form, the conservation of mass and momentum can be stated as

$$\frac{\partial \rho}{\partial t} + \nabla \cdot (\rho \boldsymbol{u}) = \rho Q, \tag{6}$$

$$\frac{\partial \rho \boldsymbol{u}}{\partial t} + \nabla \cdot (\rho \boldsymbol{u}\boldsymbol{u} - \boldsymbol{P}) = \rho \boldsymbol{f}, \tag{7}$$

respectively [15]. Here, ρ is fluid density, t is time, $\boldsymbol{u}$ is fluid velocity with $\boldsymbol{uu}$ a dyadic product, Q is an internal sink or source of mass,

$$\boldsymbol{P} = -p\boldsymbol{I} + 2\mu\boldsymbol{E}\left(\boldsymbol{u}\right) - \left(\frac{2}{3}\mu - \zeta\right)\left(\nabla \cdot \boldsymbol{u}\right)\boldsymbol{I}, \tag{8}$$

$$\boldsymbol{E}\left(\boldsymbol{u}\right) = \frac{1}{2}\left(\nabla\boldsymbol{u} + \left(\nabla\boldsymbol{u}\right)^{T}\right), \tag{9}$$

with $\boldsymbol{P}$ and $\boldsymbol{E}$ denoting the fluid stress tensor and rate of strain tensor, respectively, where p denotes pressure (measured relative to atmospheric pressure throughout this thesis), $\boldsymbol{I} = \boldsymbol{e}^{i} \cdot \boldsymbol{e}^{j}\boldsymbol{e}_{i}\boldsymbol{e}_{j}$ is the metric tensor of the coordinate system which the equations are described in[1], where $\boldsymbol{e}^{i}$ and $\boldsymbol{e}_{i}$ are the i^{th} contavariant and covariant basis vector, respectively, μ is the dynamic viscosity, ζ is the second coefficient of viscosity and $\boldsymbol{f}$ is the body force acting on the fluid.

While the reduction of the many-body problem for interacting particles into the simpler two equation system is a considerable leap in simplicity of the problem, this is not the final step. Typically, for the system given by equations (6) and (7), the density and velocity are the unknowns to solve for. As such, constitutive relations for the remaining quantities much be specified in order to close the system. It is the goal of the modeller to accurately determine these constitutive relations for specific flows.

The system as introduced above concerns the flow of a single fluid. The problem is made considerably more difficult when multiple fluids are involved, particularly due to the complex interactions of the fluids at their mutual interfaces. In this thesis, we will focus on the flow of two incompressible, Newtonian fluids, a gas and a liquid, with constant viscosities. The quantities belonging to a particular phase are denoted by a subscript g and l for the gas and liquid, respectively.

Although heat distribution is a vital part of both the motivation for studying the flow during grinding and of the grinding process itself, it is outside the scope of this thesis. Consequently, internal exchanges of mass due to effects such as

1 In a three dimensional Cartesian coordinate system, the metric tensor is just the 3×3 identity matrix

phase change due to boiling will be neglected. Similarly, both phases are likely to be in the compressible regime during grinding due to the large deformations and temperature gradients they experience. However, in the absence of a mathematical description for these temperature gradients, we choose to simplify the description of both phases by assuming they are incompressible, and leave the compressible description to future work.

Thus, the conservation laws that we look to study are

$$\frac{\partial \rho_k}{\partial t} + \nabla \cdot (\rho_k \boldsymbol{u}_k) = 0, \tag{10}$$

$$\frac{\partial \rho_k \boldsymbol{u}_k}{\partial t} + \nabla \cdot (\rho_k \boldsymbol{u}_k \boldsymbol{u}_k - \boldsymbol{P}_k) = \rho_k \boldsymbol{f}, \tag{11}$$

where $k = g, l$,

$$\boldsymbol{P}_k = -p_k \boldsymbol{I} + 2\mu_k \boldsymbol{E}(\boldsymbol{u}_k), \tag{12}$$

$$\boldsymbol{E}(\boldsymbol{u}_k) = \frac{1}{2}\left(\nabla \boldsymbol{u}_k + (\nabla \boldsymbol{u}_k)^T\right), \tag{13}$$

and $\boldsymbol{f}$ represents the constant body force acting on the fluid due to gravity.

In principle, equations (10) and (11) can be solved after closure of the problem with the specification of necessary quantities and boundary conditions in order to fully determine the behaviour of the flow. In reality, resolving every aspect of the flow numerically is extremely computationally expensive. For the flow during grinding where large inertial effects could cause, for example, rapid mixing with creation, destruction and distortion of interfaces, solving this problem is infeasible.

Despite this, we can look to simplify this system by recognising that resolving every structure across all scales of the flow is unnecessary. Therefore, a reasonable approach is to attempt to filter out small scale perturbations in the flow, and instead look to solve a simpler system which can capture the important aspects of the transport of grinding fluid. In this thesis, we follow the principle of volume averaging where quantities are averaged over a small representative volume element at every point in the flow domain. This is to filter out

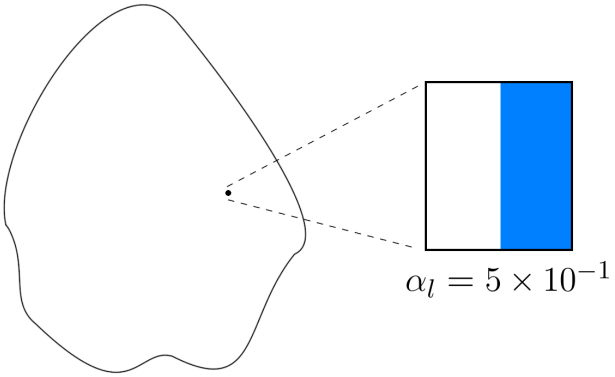

Figure 6: Illustration of the volume averaging at a point in the flow domain, shown on the left-hand image. The right-hand image shows the representative volume element at a point. This volume element is occupied by an equal amount of air and liquid phase, represented by a white and blue colour, respectively, giving that the liquid volume fraction $\alpha_l = 5 \times 10^{-1}$.

perturbations and determine the mean behaviour of each quantity inside this volume element. We will not detail the derivation of the governing multiphase equations here, but the reader is referred to the monograph of Brennen [20] for further details. Additionally, a similar derivation by Ishii et al. using time averaging can be found at [39].

2.2 MIXTURE MODEL

We consider a simple multiphase model, referred to as the mixture model. The mixture model is given by the equations

$$\nabla \cdot \boldsymbol{u}_m = 0, \tag{14}$$

$$\rho_m \left(\frac{\partial \boldsymbol{u}_m}{\partial t} + \boldsymbol{u}_m \cdot \nabla \boldsymbol{u}_m \right) = \nabla \cdot \left(\boldsymbol{P}_m + \boldsymbol{P}_m^t \right) + \rho_m \boldsymbol{g}, \tag{15}$$

$$\frac{\partial \alpha_l}{\partial t} + \nabla \cdot (\alpha_l \boldsymbol{u}_m) = 0, \tag{16}$$

with the additional relations

$$1 = \sum_{k=g,l} \alpha_k, \tag{17}$$

$$\rho_m = \sum_{k=g,l} \alpha_k \rho_k, \tag{18}$$

$$\mu_m = \sum_{k=g,l} \alpha_k \mu_k, \tag{19}$$

$$\boldsymbol{P} = -p_m \boldsymbol{I} + 2\left(\sum_{k=g,l} \alpha_k \mu_k\right) \boldsymbol{E}\left(\boldsymbol{u}_m\right), \tag{20}$$

$$\boldsymbol{E}\left(\boldsymbol{u}_m\right) = \frac{1}{2}\left(\nabla \boldsymbol{u}_m + \left(\nabla \boldsymbol{u}_m\right)^T\right). \tag{21}$$

Equations (14)-(16) are the continuity equation governing conservation of mixture mass, the multiphase Navier-Stokes equations governing conservation of momentum and the advection equation governing conservation of phase mass, respectively. Quantities denoted with subscript m are referred to as mixture quantities. The additional variable α_l denotes the volume fraction. This is a variable in space and time which represents the concentration of liquid inside an arbitrary volume element around a point. It takes values between 0 and 1, with 0 corresponding to a purely gas phase, and 1 corresponding to a purely liquid phase, see figure 6 for an illustration of the volume fraction. The tensor $\boldsymbol{P}_m^t$ is the multiphase turbulent stress tensor (also known as the Reynolds stress tensor in single-phase flows) which models the effect of the turbulence in each phase on the mixture's momentum.

In order to close the mixture model given by (14)-(21), we must provide an expression for $\boldsymbol{P}_m^t$. For the flow during grinding, the geometry of the flow gives an inherently wall-bounded turbulent flow. While various turbulence models for such flows have been proposed in the literature, their extension to multiphase mixture models is flow-specific and largely empirical. Thus, it is a futile effort to complicate the mixture model with the inclusion of a turbulence model when

neither its applicability to the mixture model or the flow during grinding has been studied. Therefore, we assume in this thesis that

$$\boldsymbol{P}_m^t = \boldsymbol{0} \tag{22}$$

and leave the study of modelling this term to future work. We refer the Subsection 1.2.2 for a brief overview of turbulence modelling with references to some of the many proposed turbulence models, as well as [39] for examples of proposed extensions to turbulence models in particular multiphase flows.

With further specification of initial and boundary conditions, the problem is fully specified and we have a closed system of equations.

2.3 NAVIER SLIP

The typical boundary condition for the fluid at an impermeable solid surface is the no-slip condition. This requires that the velocity of fluid particles at the surface are equal to the velocity of the surface, i.e. for a wall moving with velocity $\boldsymbol{V}$, the no-slip condition states that

$$\boldsymbol{u} = \boldsymbol{V}. \tag{23}$$

However, this condition is not always appropriate and it becomes necessary to allow for the possibility that fluid particles can slip and travel at a different velocity to the surface. A common condition that is used to model slip is the Navier slip condition which states that

$$\boldsymbol{u} - \boldsymbol{V} = \beta \boldsymbol{n} \cdot \boldsymbol{P}\left(\boldsymbol{u}\right) \cdot \left(\boldsymbol{I} - \boldsymbol{n}\boldsymbol{n}\right), \tag{24}$$

where $\boldsymbol{P}$ is the stress tensor given by (8), $\boldsymbol{n}$ is the inward-pointing unit normal to the surface, $\boldsymbol{I}$ is the metric tensor and β is the slip coefficient. This condition states that the velocity difference at a surface is proportional to the tangential stress of the fluid at the surface, with proportionality factor β.

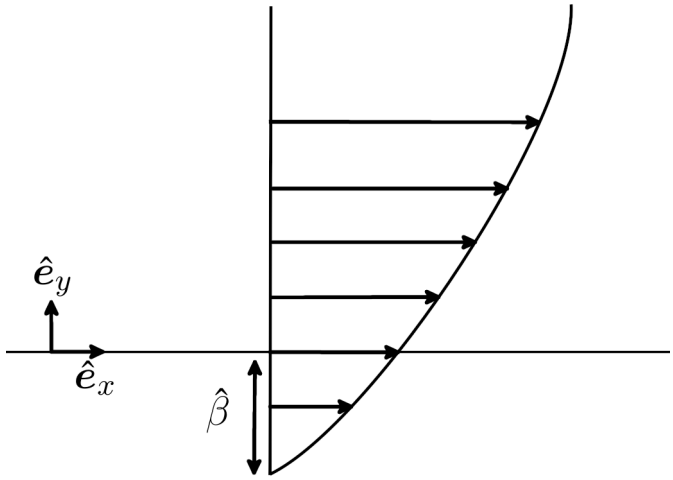

Figure 7: Illustration of the Navier slip condition for flow over a planar surface. The slip length, $\hat{\beta}$, represents a length scale over which the velocity solution with the no-slip boundary condition is offset by.

We remark that (24) can be written in an alternative form in terms of the rate of strain tensor, $\boldsymbol{E}(\boldsymbol{u})$, as

$$\boldsymbol{u} - \boldsymbol{V} = 2\hat{\beta}\boldsymbol{n} \cdot \boldsymbol{E}(\boldsymbol{u}) \cdot (\boldsymbol{I} - \boldsymbol{n}\boldsymbol{n}), \tag{25}$$

where $\boldsymbol{E}(\boldsymbol{u})$ is given by (9) and $\hat{\beta} = \beta\mu$ is referred to as the slip length. Additionally, we observe that the impermeability condition follows from both (24) and (25) as the normal projection gives that

$$\boldsymbol{u} \cdot \boldsymbol{n} = \boldsymbol{V} \cdot \boldsymbol{n}. \tag{26}$$

As this thesis is only concerned with impermeable surfaces, we will refer to (25) as the slip condition and use this form throughout.

For the simple case of an axis-aligned, two dimensional planar surface whose position is described in a Cartesian coordinate system, we have that $\boldsymbol{n} = \boldsymbol{e}_y$. The tangential component of the Navier slip condition (25) then reduces to the more well-known form given by

$$u - V_x = \hat{\beta}\frac{\partial u}{\partial y}, \tag{27}$$

with the impermeability condition given by the normal projection as

$$v = V_y. \tag{28}$$

Here, $\boldsymbol{u} = u\hat{\boldsymbol{e}}_x + v\hat{\boldsymbol{e}}_y$ and $\boldsymbol{V} = V_x\hat{\boldsymbol{e}}_x + V_y\hat{\boldsymbol{e}}_y$. This example is illustrated in figure 7, where the slip length is shown as a length scale over which the velocity solution with the no-slip boundary condition is offset by.

The slip condition has previously been used to model slip in rarefied gas flow in tight channels [14], liquid wetting [51] and liquid flow over a solid surface coated by bubbles [52] or a gas film [57]. The variability of the slip condition in these problems comes from the choice of the slip length. Typically, for gas flows, the slip length is taken from values found from theoretical studies using kinetic theory. In liquid flows, the slip coefficient is inferred from experimental studies, though depending on the flow and measurement techniques used, the slip coefficient has been found to vary considerably. In spite of this, an estimate for the slip coefficient at the interface between the liquid bulk and solid surface is

$$\hat{\beta} = 1 \times 10^{-8} \text{ m}. \tag{29}$$

This is approximately the width of a typical liquid-solid interface.

We introduce the slip condition in this thesis for two reasons. It is a simple condition that is able to alleviate nonphysical singularities which appear in flows involving contact discontinuities. It is also able to model physical effects which manifest as slip at the wall due to, for example, small-scale roughness, potential film boiling and molecular collisions, to name a few.

However, while the slip condition has been extensively studied for flows involving a moving bulk liquid phase (see, for example, [76] for a comprehensive review of the literature concerned with slip in bulk liquid flows over superhydrophobic surfaces), its applicability in mixture models is an extensive challenge to investigate, and as such has not been comprehensively studied in the liter-

ature. Therefore, we will consider the simple mixture model extension of the Navier slip condition as

$$\boldsymbol{u}_m - \boldsymbol{V} = \beta \boldsymbol{n} \cdot \boldsymbol{P}_m \cdot (\boldsymbol{I} - \boldsymbol{n}\boldsymbol{n}) \,, \tag{30}$$

where β is now a representative multiphase slip coefficient for both phases. We can express (30) in the alternative form

$$\boldsymbol{u}_m - \boldsymbol{V} = 2\hat{\beta} \left(\sum_{k=g,l} \alpha_k \frac{\mu_k}{\mu_l} \right) \boldsymbol{n} \cdot \boldsymbol{E}\left(\boldsymbol{u}_m\right) \cdot (\boldsymbol{I} - \boldsymbol{n}\boldsymbol{n}) \,, \tag{31}$$

where $\hat{\beta} = \beta \mu_l$ is a representative multiphase slip length for both phases, and $\boldsymbol{E}\left(\boldsymbol{u}_m\right)$ is given by (21). For simplicity, we will assume that the multiphase slip length $\hat{\beta}$ can be approximated by the slip length in single-phase liquid flows, i.e. we assume the estimate given by (29) in the multiphase slip condition. In a multiphase context, we will refer to the multiphase Navier slip condition (31) also as the slip condition, and the multiphase slip length as the slip length.

2.4 ABRASIVE PROFILE

In this thesis, we will focus on two types of abrasive profiles. The first is a mathematically smooth, idealised geometry where the grinding wheel is modelled as a cylinder. The second is a specialised profile used in grinding where the abrasives are periodically placed pyramid structures. These are known as Trizact$^{\text{TM}}$ abrasives. This profile will be specified in a cylindrical coordinate system (r, θ, z). Although this coordinate system will be formally introduced later, we mention here that in an up-grinding regime, the grinding wheel spins in the $-\hat{\boldsymbol{e}}_\theta$ direction where $\hat{\boldsymbol{e}}_\theta$ is the basis vector for the θ coordinate.

In figure 8, we present pictures of a Trizact$^{\text{TM}}$ belt which is wrapped around a grinding wheel and a close-up picture of a single Trizact$^{\text{TM}}$ abrasive. In grinding, such abrasives are referred to as microreplication abrasives due to their small-scale, repeating structure on the surface of the grinding wheel. Trizact$^{\text{TM}}$

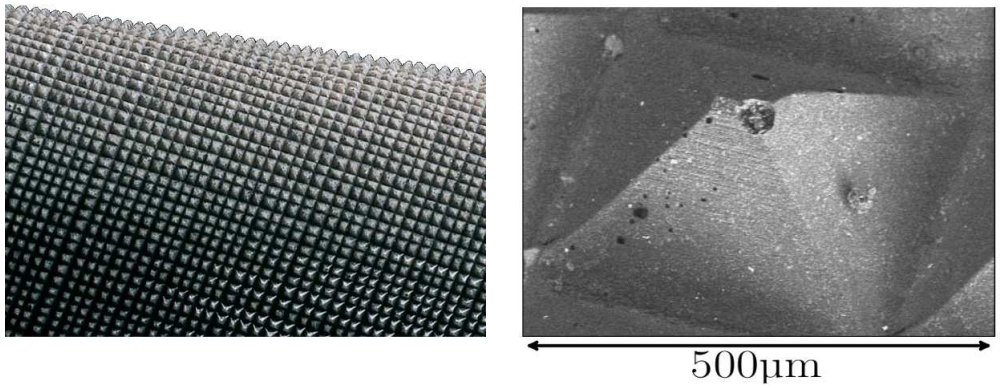

Figure 8: The left image shows a partially worn Trizact^{TM} belt with pyramid abrasives. The right image is a close-up view of a single pyramid abrasive, taken from [23].

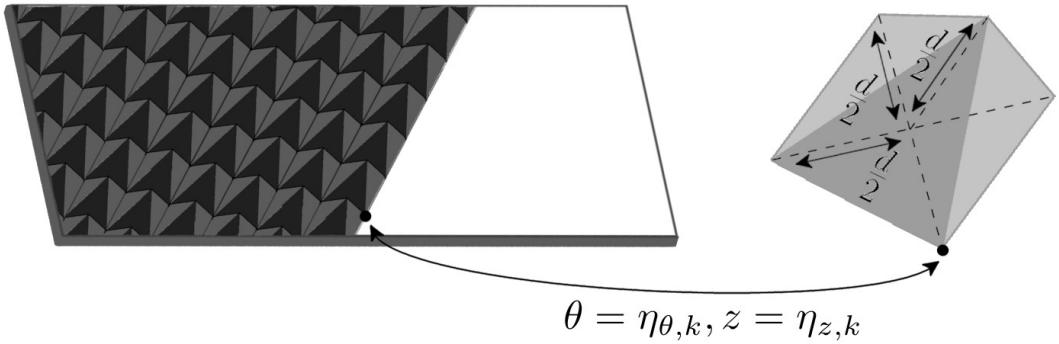

Figure 9: Illustration of the Trizact^{TM} belt showing abrasives with size d, where abrasive k's position is characterised by the coordinates $\theta = \eta_{\theta,k}, z = \eta_{z,k}$. This pattern of abrasives extends across the whole belt.

abrasive profiles are an example of a structured surface with engineered abrasives, where the abrasives and the belt are created to suit particular characteristic profiles. Pioneering work on the science of manufactured surfaces can be found in [30].

A typical fine abrasive size for these abrasives is 4×10^{-5} m, while the coarsest size is 7.5×10^{-4} m. The size is denoted d and refers to both twice the distance between the apex of the pyramid and the base, and twice the distance between maxima points of the sides and the centre point of the base. This is illustrated in figure 9.

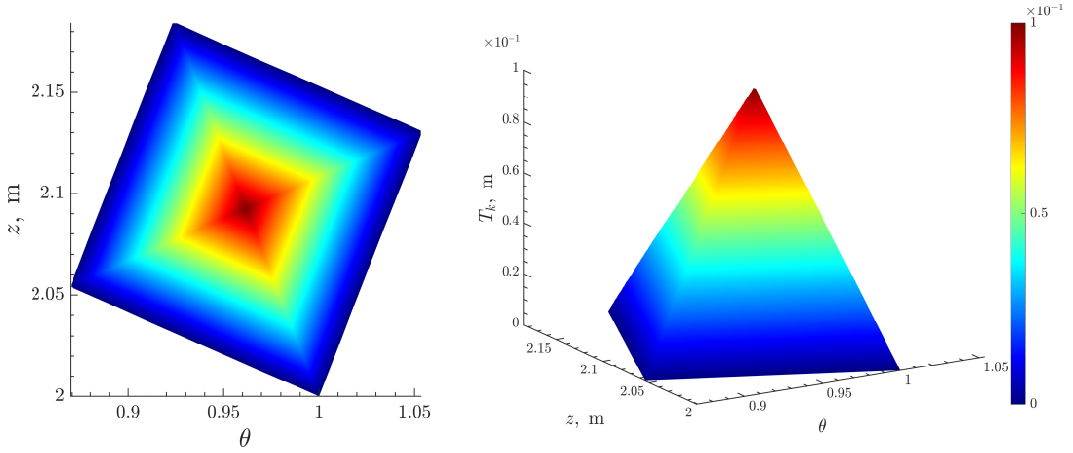

(a) Top-down perspective (b) Three dimensional perspective

Figure 10: Figures (a) and (b) above show an example of a flattened pyramid structure at different views.

The equation describing each abrasive is given by

$$T_k(\theta, z) = h_p \left[\frac{d}{2} - \left(\left| R(\theta - \eta_{\theta,k}) \cos\theta_r + (z - \eta_{z,k}) \sin\theta_r \right| + \left| (z - \eta_{z,k}) \cos\theta_r - R(\theta - \eta_{\theta,k}) \sin\theta_r - \frac{d}{2} \right| \right) \right], \tag{32}$$

with the bottom apex coordinates $\theta = \eta_{\theta,k}, z = \eta_{z,k}$ characterising the position of abrasive k. The angle $\theta_r \in \left[-\frac{\pi}{4}, \frac{\pi}{4}\right)$ represents the orientation of the abrasive and R denotes the radius of the grinding wheel. In (32), h_p denotes a scale factor which reduces the peak of T_k. For $h_p = 1$, we have the regular Trizact$^{\text{TM}}$ pyramid. For $h_p \in [0, 1)$, we have a flattened pyramid structure.

In figure 9, we illustrate one particular abrasive on a Trizact$^{\text{TM}}$ belt. In figure 10, we show an example of equation (32) for a representative Trizact$^{\text{TM}}$ abrasive, where we have taken the illustrative values $R = 1$ m, $d = 2 \times 10^{-1}$ m, $\eta_{\theta,k} = 1, \eta_{z,k} = 2$ m, $\theta_r = \frac{\pi}{8}$ and $h_p = 1$.

2.5 CONCLUSION

In this chapter, we have presented the framework that we will use for the flow during grinding. For the remainder of this thesis, this framework will be used to investigate the flow during grinding and understand what influences the transport of grinding fluid.

In the next chapter, the multiscale method that completes the foundation of this thesis will be introduced. We will then be in a position to begin with the application of the tools detailed so far.

3

MULTISCALE ASYMPTOTIC METHODS

3.1 INTRODUCTION

In this chapter, we look to introduce and apply the method of matched asymptotic expansions on the flow during grinding. The aim of this chapter is to establish the foundations of the multiscale methods which will be used throughout this thesis, and gain a basic understanding of the flow in the grinding zone. As such, the problem we consider here will be an idealised one in comparison to those which we will tackle later in this thesis.

The motivation of this chapter comes from the presence of multiple length scales in the flow during grinding, over which different flow behaviour is expected to occur. The largest length scale in the flow is associated with the transport in the region surrounding the grinding wheel. Examples of flows here are the entrained air layer surrounding the wheel, responsible for the rejection of grinding fluid moving into the grinding zone, and the grinding fluid exiting the nozzle. It is over this length scale that we would expect to see the most turbulent behaviour present due to the dominant inertia of the flow.

A smaller length scale in the flow is associated with the flow across the grinding zone. In this thin region, inertial effects are much less relevant in the flow, with viscous effects driving the flow through the grinding zone.

An even smaller length scale is given by the size of each abrasive on the grinding wheel. In grinding, the size of the abrasives that is chosen generally depends on the specific job. The size is specified through the grit size which

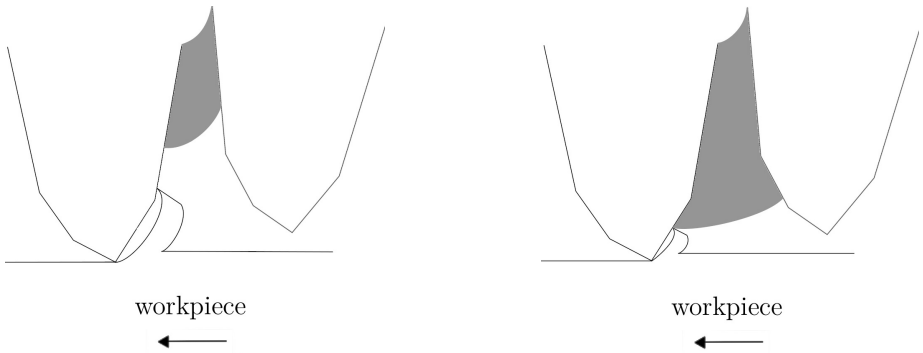

Figure 11: Illustration of how the amount of bonding material present in the grinding wheel, represented by the dark grey colour between abrasives, affects the abrasive spacing. As shown in the left image, a larger abrasive spacing increases the available volume for both grinding fluid and workpiece chips to occupy.

denotes the number of mesh openings per inch through which the abrasives are sieved before they are bonded together (though other systems also exist for specifying the size of the abrasives).

A typical finishing operation is characterised by a small depth of cut and fine abrasives for cutting. A coarser grind (for example, where greater rates of material removal are required) is characterised by relatively larger depths of cuts and abrasive sizes. Representative values for the depth of cut and abrasive size in surface and creep-feed grinding regimes are presented in table 1.

In conjunction with the abrasive size is the abrasive spacing, i.e. the space available between adjacent abrasives that is not occupied by bonding material which hold the abrasives together, see figure 11. The hardness of the grinding wheel directly correlates with the abrasive spacing, with a larger quantity of bond material improving the durability of the grinding wheel but reducing the abrasive spacing. As such, the wheel hardness has an inverse relation with the available space for grinding fluid to occupy in the grinding zone. The consequence of this is that increasing the hardness of the wheel reduces the potential lubricating and cooling effects of the grinding fluid (as well as, for example, the ability of the grinding fluid to wash away the chips generated during cutting).

Clearly, there are distinct regions over various scales where the aspects of the flow are considerably different. Given these small scale features which have an essential influence on the behaviour of the flow in their respective regions, it is unreasonable to demand that a single scaled problem is able to capture all details of the flow. It is therefore necessary to exploit the length scale disparity such that the predominant effects of the flow in each region are resolved without rendering the problem unfeasible to solve from a modelling and computational resources point of view.

In the proceeding sections, we will consider an idealised grinding geometry where the grinding wheel is separated from the workpiece by a small, non-zero distance. As we recall from the literature review in Chapter 1, this is the case that is usually studied in both experimental and theoretical works. In this simulated grinding scenario, we will separate the flow domain into two separate regions, the inner and outer domain which are characterised by a (relatively) small and large length scale, respectively. The inner region corresponds to the flow around the grinding zone and the outer region corresponds to the large scale flow around the grinding wheel. The method of matched asymptotic expansions will then be used in order to derive separate governing equations for the coupled flows in both domains.

In this chapter, we look to understand what effect the flow far from the grinding zone has on both the amount of grinding fluid reaching the grinding zone and the transport of the grinding fluid inside the grinding zone. In conjunction with this, we look to investigate whether the method of asymptotic expansions can be used in order for us to calculate what the flux through the grinding zone is. A problem of similar origin to the one studied in this chapter, concerning the movement of a circle towards a fixed boundary, can be found in [54].

3.2 PROBLEM FORMULATION

A Cartesian coordinate system (x, y) is used to specify the points in the upper half plane, $x \in \mathbb{R},\ y \in \mathbb{R}_{\geq 0}$, with corresponding unit basis vectors $\boldsymbol{e}_x, \boldsymbol{e}_y$. The

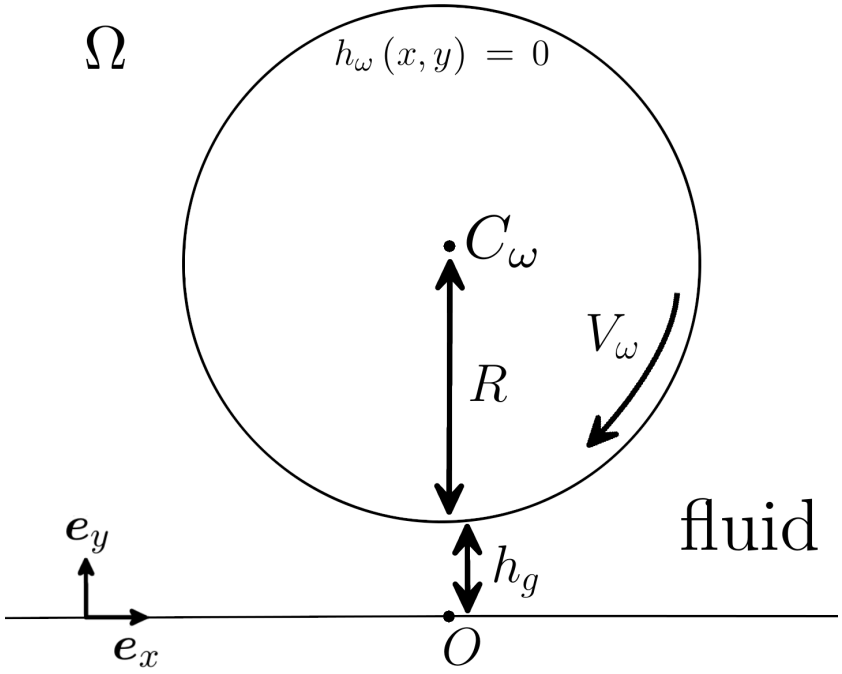

Figure 12: An illustration of the domain for the problem. The simulated grinding zone is the gap between the grinding wheel and the workpiece. The size of h_g is greatly exaggerated for illustrative purposes.

radius of the grinding wheel is R, with the grinding wheel's centre, denoted C_ω, lying on $x = 0$ and bottom-most point at a height $y = h_g > 0$. The grinding wheel rotates with a tangential speed of V_ω in a clockwise direction. The surface of the grinding wheel is taken to be a smooth circle. The workpiece surface below the grinding wheel is stationary and assumed smooth and impenetrable. We model the grinding zone as the gap around $x = 0$ between the grinding wheel and the workpiece.

The fluid surrounding the grinding wheel is assumed incompressible with constant density and viscosity, denoted by ρ and μ, respectively. The no-slip condition is imposed on the grinding wheel's surface, specified by the level set function $h_\omega(x,y) = 0$, and workpiece surface whose position is specified by $y = 0$. Here,

$$h_\omega(x,y) = x^2 + (y - R - h_g)^2 - R^2. \tag{33}$$

A constant body force due to gravity acts on the fluid. This is given by $\boldsymbol{f} = -g\boldsymbol{e}_y$, with $g = 9.81$ m s^{-2}. The flow domain is denoted by

$$\Omega = \{(x, y) \in \mathbb{R} \times \mathbb{R}_{>0} : h_\omega(x, y) > 0\}. \tag{34}$$

This problem is illustrated in figure 12.

3.3 COMPLETE PROBLEM

The governing equations of the fluid are given by the continuity equation and Navier-Stokes equations

$$\frac{\partial u}{\partial x} + \frac{\partial v}{\partial y} = 0, \tag{35}$$

$$\rho\left(\frac{\partial \boldsymbol{u}}{\partial t} + \boldsymbol{u} \cdot \nabla \boldsymbol{u}\right) = -\nabla p + \mu \nabla^2 \boldsymbol{u} - \rho g \boldsymbol{e}_y, \tag{36}$$

respectively, where $\boldsymbol{u} = u\boldsymbol{e}_x + v\boldsymbol{e}_y$ is the velocity vector of the fluid and p is the fluid pressure.

The boundary and far-field conditions are given by

$$\boldsymbol{u} = V_\omega \boldsymbol{t} \qquad \text{on } h_\omega(x, y) = 0, \tag{37}$$

$$\boldsymbol{u} = \boldsymbol{0} \qquad \text{on } y = 0, \tag{38}$$

$$\boldsymbol{u} \to \boldsymbol{0} \qquad \text{as } x \to \pm\infty,\ y \to \infty, \tag{39}$$

$$p \to 0 \qquad \text{as } x \to \pm\infty,\ y \to \infty, \tag{40}$$

where $\boldsymbol{t} = t_x\boldsymbol{e}_x + t_y\boldsymbol{e}_y$ is the unit tangent to $h_\omega(x, y) = 0$, with

$$t_x = \begin{cases} \frac{\sqrt{R^2 - x^2}}{R} & \text{for } y > R + h_g, \\ -\frac{\sqrt{R^2 - x^2}}{R} & \text{for } y \leq R + h_g, \end{cases} \tag{41}$$

$$t_y = -\frac{x}{R}. \tag{42}$$

Equations (35) and (36) subject to (37)-(40) form a closed system which can be solved to determine $\boldsymbol{u}$ and p everywhere in the domain. However, aside from computationally complexity, it will be difficult to resolve the flow in the grinding zone while simultaneously trying to solve for the flow surrounding the grinding wheel. Instead, we will exploit this large scale separation using the method of matched asymptotic expansions. In this way, we will separate the flow into two regions with distinct flow regimes: a large scale outer region where inertial effects dominant the flow, and an inner region where viscous forces are expected to have a larger role in the flow dynamics.

3.4 METHOD OF MATCHED ASYMPTOTIC EXPANSIONS

We begin by nondimensionalising the system (35)-(40). For this, we take the characteristic values to be typical values that we expect the variables to take over the largest scale. In doing so, we remove the dimensional units from the variables. This allows us to determine the relative significance of individual terms in the equations by looking at the corresponding nondimensional coefficient of each term. For the problem we are considering in this section, we introduce the nondimensional variables

$$\boldsymbol{u} = V_\omega \bar{\boldsymbol{u}}, \tag{43}$$

$$x = R\bar{x}, \tag{44}$$

$$y = R\bar{y}, \tag{45}$$

$$p = \frac{\mu V_\omega}{R}\bar{p}, \tag{46}$$

$$t = \frac{R}{V_\omega}\bar{t}, \tag{47}$$

and the corresponding nondimensional numbers

$$\mathrm{Re} = \frac{\rho V_\omega R}{\mu}, \tag{48}$$

$$\mathrm{Fr} = \frac{V_\omega}{\sqrt{gR}}, \tag{49}$$

$$\varepsilon = \frac{h_g}{R}. \tag{50}$$

The nondimensional number: Re, known as the Reynolds number, characterises the relative effect of inertial forces to viscous forces in the flow; Fr, known as the Froude number, characterises the relative effect of inertial forces to gravitational forces; ε characterises the size of the scale separation between the thin grinding zone and the remaining region surrounding the grinding wheel. A first approximation for these numbers can be found using data presented in table 1 and table 2 in Appendix A. For surface grinding, we take $h_g = 1 \times 10^{-5}$ m from the size of an abrasive and $R = 2 \times 10^{-1}$ m, which gives us that

$$\varepsilon = 5 \times 10^{-5}. \tag{51}$$

For creep-feed grinding, we instead take $h_g = 5 \times 10^{-4}$ m and $R = 2 \times 10^{-1}$ m, giving us

$$\varepsilon = 2.5 \times 10^{-3}. \tag{52}$$

Using a value of $\mathrm{Re} = 1 \times 10^5$ and $\mathrm{Fr} = 2.52 \times 10^1$, we see that for the surface grinding regime we have that

$$\mathrm{Re} = O\left(\varepsilon^{-1}\right), \tag{53}$$

$$\mathrm{Fr} = O\left(\varepsilon^{-\frac{1}{4}}\right). \tag{54}$$

For the typical values of a creep-feed grinding regime that we have presented, (53) and (54) are not true. However, there are innumerable different grinding fluids used in industry, each with their own distinct rheology. In addition, there

can be wide ranges in the radius of the grinding wheel. Thus, it can be expected that certain creep-feed grinding processes will satisfy (53) and (54), and we will assume that these hold for both surface and creep-feed grinding regimes for the remainder of the thesis.

Substituting in the nondimensional variables (43)-(47), the nondimensional form of the system (35)-(40) is then

$$\frac{\partial \bar{u}}{\partial \bar{x}} + \frac{\partial \bar{v}}{\partial \bar{y}} = 0, \tag{55}$$

$$\mathrm{Re}\left(\frac{\partial \bar{\boldsymbol{u}}}{\partial \bar{t}} + \bar{\boldsymbol{u}} \cdot \bar{\nabla}\bar{\boldsymbol{u}}\right) = -\bar{\nabla}\bar{p} + \bar{\nabla}^2\bar{\boldsymbol{u}} - \frac{\mathrm{Re}}{\mathrm{Fr}^2}\boldsymbol{e}_y, \tag{56}$$

subject to

$$\bar{\boldsymbol{u}} = \bar{\boldsymbol{t}} \qquad \text{on } \bar{h}_\omega\left(\bar{x}, \bar{y}\right) = 0, \tag{57}$$

$$\bar{\boldsymbol{u}} = \boldsymbol{0} \qquad \text{on } \bar{y} = 0, \tag{58}$$

$$\bar{\boldsymbol{u}} \to \boldsymbol{0} \qquad \text{as } \bar{x} \to \pm\infty,\ \bar{y} \to \infty, \tag{59}$$

$$\bar{p} \to 0 \qquad \text{as } \bar{x} \to \pm\infty,\ \bar{y} \to \infty, \tag{60}$$

where $\bar{\nabla}$ is the gradient operator with respect to the nondimensionalised coordinates, $\bar{\boldsymbol{t}} = \bar{t}_x\boldsymbol{e}_x + \bar{t}_y\boldsymbol{e}_y$ with

$$\bar{t}_x = \begin{cases} \sqrt{1-\bar{x}^2} & \text{for } \bar{y} > 1+\varepsilon, \\ -\sqrt{1-\bar{x}^2} & \text{for } \bar{y} \le 1+\varepsilon, \end{cases} \tag{61}$$

$$\bar{t}_y = -\bar{x}, \tag{62}$$

and

$$\bar{h}_\omega\left(\bar{x}, \bar{y}\right) = \bar{x}^2 + \left(\bar{y} - 1 - \varepsilon\right)^2 - 1. \tag{63}$$

We observe the presence of the small parameter ε in the boundary location (63). Simply setting $\varepsilon = 0$ yields a contact problem with incompatible boundary conditions (57) and (58) which cannot both be satisfied. Therefore, we must use

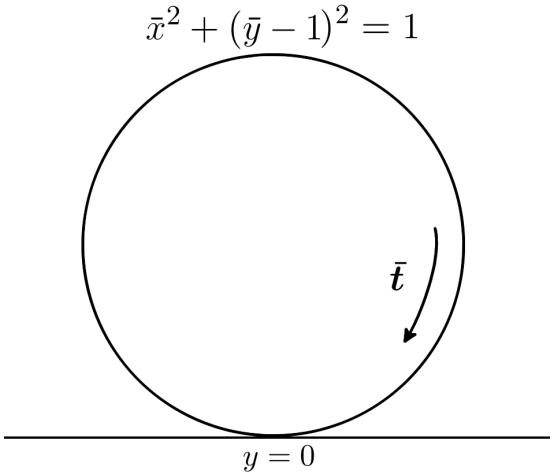

Figure 13: Illustration of the domain for the outer problem.

the method of matched asymptotic expansions to separate the problem into an outer and inner region. Typically, we must then solve each problem and match both solutions in an intermediate, overlap region for the final solution which holds in the whole domain. However, in our problem we shall see that we do not need to calculate the solution in the outer problem to be able to find the solution in the inner region.

3.4.1 *Outer Problem*

To obtain the outer problem of the system (55)-(60), we set $\varepsilon = 0$ and consider leading order terms. Recalling assumptions (53) and (54), at leading order we have the outer problem domain

$$\bar{\Omega}^o = \left\{(x, y) \in \mathbb{R} \times \mathbb{R}_{>0} : \bar{h}^o_\omega\left(\bar{x}, \bar{y}\right) > 0\right\}, \tag{64}$$

with the equations governing the flow given by the Euler equations

$$\frac{\partial \bar{u}}{\partial \bar{x}} + \frac{\partial \bar{v}}{\partial \bar{y}} = 0, \tag{65}$$

$$\frac{\partial \bar{\boldsymbol{u}}}{\partial \bar{t}} + \bar{\boldsymbol{u}} \cdot \bar{\nabla} \bar{\boldsymbol{u}} = -\bar{\nabla} \bar{p}^o, \tag{66}$$

subject to

$$\bar{\boldsymbol{u}} \cdot \bar{\boldsymbol{n}} = 0 \qquad \text{on } \bar{h}_\omega^o(\bar{x}, \bar{y}) = 0, \tag{67}$$

$$\bar{\boldsymbol{u}} \cdot \bar{\boldsymbol{n}} = 0 \qquad \text{on } \bar{y} = 0, \tag{68}$$

$$\bar{\boldsymbol{u}} \to \boldsymbol{0} \qquad \text{as } \bar{x} \to \pm\infty,\ \bar{y} \to \infty, \tag{69}$$

$$\bar{p}^o \to 0 \qquad \text{as } \bar{x} \to \pm\infty,\ \bar{y} \to \infty. \tag{70}$$

Here, we have introduced

$$\bar{p}^o = \frac{\bar{p}}{\mathrm{Re}} \tag{71}$$

in order to ensure that the leading order advection terms balance with the leading order pressure gradient and

$$\bar{h}_\omega^o(\bar{x}, \bar{y}) = \bar{x}^2 + (\bar{y} - 1)^2 - 1. \tag{72}$$

We note that boundary conditions (67) and (68) are the projections of the no-slip boundary conditions (57) and (58), respectively, with the unit normal vector to the boundary, $\bar{\boldsymbol{n}}$. These have replaced the no-slip boundary conditions due to these conditions not being applicable to the Euler equations. The outer problem's domain is illustrated in figure 13.

3.4.2 *Inner Problem*

To arrive at the inner problem, we begin by stretching the small scale region around the grinding zone. We introduce a new dimensionless coordinate $\bar{y}^\star$ which is $O(1)$ when $\bar{y}$ is $O(\varepsilon)$, i.e.

$$\bar{y} = \varepsilon \bar{y}^\star. \tag{73}$$

A rescaling argument on boundary condition (57) shows that we must also scale $\bar{x}$ such that

$$\bar{x} = \sqrt{\varepsilon}\bar{x}^{\star}. \tag{74}$$

In order to balance the terms in the continuity equation (55), the velocity component $\bar{v}$ must be scaled as

$$\bar{v} = \sqrt{\varepsilon}\bar{v}^{\star}. \tag{75}$$

Although no rescaling is necessary on $\bar{u}$, to emphasise that it is the rescaled problem we are solving we will also introduce

$$\bar{u}^{\star} = \bar{u}. \tag{76}$$

We remark that the grinding region, where the recently defined stretched variables are $O(1)$, is referred to as the inner region in the context of asymptotic methods. In contrast, the region surrounding the grinding wheel, where the unstretched variables are $O(1)$, is referred to as the outer region.

Substituting in the stretched quantities (73)-(76) to equations (55) and (56), we have that

$$\frac{\partial \bar{u}^{\star}}{\partial \bar{x}^{\star}} + \frac{\partial \bar{v}^{\star}}{\partial \bar{y}^{\star}} = 0, \tag{77}$$

$$\varepsilon\sqrt{\varepsilon}\mathrm{Re}\left(\sqrt{\varepsilon}\frac{\partial \bar{u}^{\star}}{\partial \bar{t}} + \bar{u}^{\star}\frac{\partial \bar{u}^{\star}}{\partial \bar{x}^{\star}} + \bar{v}^{\star}\frac{\partial \bar{u}^{\star}}{\partial \bar{y}^{\star}}\right) = -\frac{\partial \bar{p}^{\star}}{\partial \bar{x}^{\star}} + \varepsilon\frac{\partial^2 \bar{u}^{\star}}{\partial \bar{x}^{\star 2}} + \frac{\partial^2 \bar{u}^{\star}}{\partial \bar{y}^{\star 2}}, \tag{78}$$

$$\varepsilon\sqrt{\varepsilon}\mathrm{Re}\left(\sqrt{\varepsilon}\frac{\partial \bar{v}^{\star}}{\partial \bar{t}} + \bar{u}^{\star}\frac{\partial \bar{v}^{\star}}{\partial \bar{x}^{\star}} + \bar{v}^{\star}\frac{\partial \bar{v}^{\star}}{\partial \bar{y}^{\star}}\right) = -\frac{1}{\varepsilon}\frac{\partial \bar{p}^{\star}}{\partial \bar{y}^{\star}} + \varepsilon\frac{\partial^2 \bar{v}^{\star}}{\partial \bar{x}^{\star 2}} + \frac{\partial^2 \bar{v}^{\star}}{\partial \bar{y}^{\star 2}} - \varepsilon\sqrt{\varepsilon}\frac{\mathrm{Re}}{\mathrm{Fr}^2}, \tag{79}$$

where we have introduced

$$\bar{p} = \frac{\bar{p}^{\star}}{\varepsilon\sqrt{\varepsilon}} \tag{80}$$

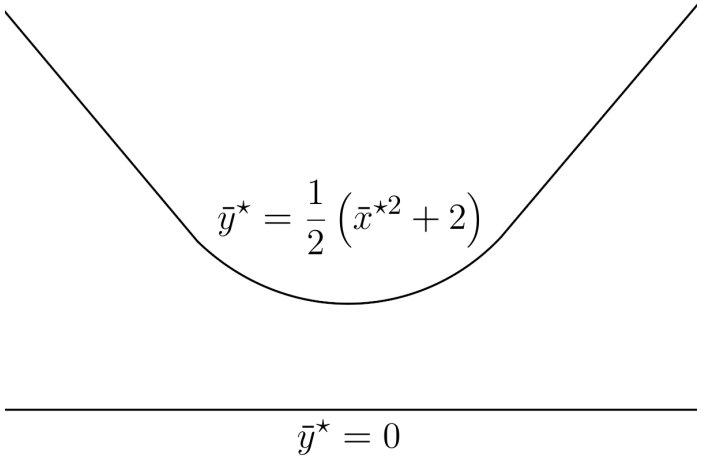

Figure 14: Illustration of the domain for the inner problem.

in order to balance the pressure gradient with leading order terms. Conditions (57) and (58) become

$$\bar{u}^\star = -\sqrt{1 - \varepsilon\bar{x}^\star} \qquad \text{on } \varepsilon\bar{x}^{\star 2} + (\varepsilon\bar{y}^\star - 1 - \varepsilon)^2 = 1, \tag{81}$$

$$\bar{v}^\star = -\bar{x}^\star \qquad \text{on } \varepsilon\bar{x}^{\star 2} + (\varepsilon\bar{y}^\star - 1 - \varepsilon)^2 = 1, \tag{82}$$

$$\bar{u}^\star = 0 \qquad \text{on } \bar{y}^\star = 0, \tag{83}$$

$$\bar{v}^\star = 0 \qquad \text{on } \bar{y}^\star = 0. \tag{84}$$

Due to the appearance of $\sqrt{\varepsilon}$ in equations (78) and (79), and assumptions (53) and (54) on the nondimensional numbers which give the consequent form of equation (66) in the outer problem, we consider the asymptotic ansatz

$$q = \sum_{n=0}^{\infty} \sqrt{\varepsilon}^n q_n, \qquad q \in \{\bar{u}^\star, \bar{v}^\star, \bar{p}^\star\}. \tag{85}$$

Substituting the asymptotic expansion (85) into the system given by (77)-(79), (81)-(84), we get the leading order problem in the inner region

$$\frac{\partial \bar{u}_0^\star}{\partial \bar{x}^\star} + \frac{\partial \bar{v}_0^\star}{\partial \bar{y}^\star} = 0, \tag{86}$$

$$\frac{\partial \bar{p}_0^\star}{\partial \bar{x}^\star} = \frac{\partial^2 \bar{u}_0^\star}{\partial \bar{y}^{\star 2}}, \tag{87}$$

$$\frac{\partial \bar{p}_0^\star}{\partial \bar{y}^\star} = 0, \tag{88}$$

subject to

$$\bar{u}_0^\star = -1 \qquad \text{on } \bar{y}^\star = \frac{1}{2}\left(\bar{x}^{\star 2} + 2\right), \tag{89}$$

$$\bar{v}_0^\star = -\bar{x}^\star \qquad \text{on } \bar{y}^\star = \frac{1}{2}\left(\bar{x}^{\star 2} + 2\right), \tag{90}$$

$$\bar{u}_0^\star = 0 \qquad \text{on } \bar{y}^\star = 0, \tag{91}$$

$$\bar{v}_0^\star = 0 \qquad \text{on } \bar{y}^\star = 0. \tag{92}$$

An illustration of the inner problem's domain is shown in figure 14.

3.4.3 *Inner Solution*

Equations (86)-(88) are the well-known lubrication equations. We are able to use system (86)-(92) to find a general solution for the pressure distribution in the inner region. Briefly, we see from (88) that

$$\bar{p}_0^\star = \bar{p}_0^\star\left(\bar{x}^\star, t\right). \tag{93}$$

Then integrating (87) twice with respect to $\bar{y}^\star$ and using boundary conditions (89) and (91), we get that

$$\bar{u}_0^\star = \bar{y}^\star\left[\frac{\bar{y}^\star}{2}\frac{\partial \bar{p}_0^\star}{\partial \bar{x}^\star} - \frac{2}{\bar{x}^{\star 2} + 2}\left(1 + \frac{\left(\bar{x}^{\star 2} + 2\right)^2}{8}\frac{\partial \bar{p}_0^\star}{\partial \bar{x}^\star}\right)\right]. \tag{94}$$

This allows us to calculate an expression for the leading order (cross-sectional) flux through the grinding zone, $\bar{Q}_0^\star$, as

$$\int_0^{\frac{1}{2}\left(\bar{x}^{\star 2}+2\right)} \bar{u}_0^\star \mathrm{d}\bar{y}^\star = \bar{Q}_0^\star, \tag{95}$$

where we have that

$$\int_0^{\frac{1}{2}\left(\bar{x}^{\star 2}+2\right)} \bar{u}_0^\star \mathrm{d}\bar{y}^\star = -\frac{\bar{x}^{\star 2}+2}{4} - \frac{\left(\bar{x}^{\star 2}+2\right)^3}{96}\frac{\partial \bar{p}_0^\star}{\partial \bar{x}^\star}, \tag{96}$$

using expression (94).

Finally, integrating (86) with respect to $\bar{y}^\star$ and using Leibniz's rule, the second fundamental theorem of calculus and boundary conditions (90) and (92), we arrive at

$$\frac{\partial}{\partial \bar{x}^\star}\int_0^{\frac{1}{2}\left(\bar{x}^{\star 2}+2\right)} \bar{u}_0^\star \mathrm{d}\bar{y}^\star = 0. \tag{97}$$

We can then substitute (96) into (97) to arrive at the well-known Reynolds equation

$$\frac{\partial}{\partial \bar{x}^\star}\left(24\bar{x}^{\star 2} + \left(\bar{x}^{\star 2}+2\right)^3 \frac{\partial \bar{p}_0^\star}{\partial \bar{x}^\star}\right) = 0. \tag{98}$$

In order to solve (98), we need additional boundary conditions on $\bar{p}_0^\star$. We acquire these from requiring that the inner solution of $\bar{p}^\star$ matches the outer solution of $\bar{p}^o$ in an intermediate region between the inner and outer regions. The matching conditions are

$$\lim_{\bar{x}^\star \to -\infty} \bar{p}^\star = \lim_{\bar{x},\bar{y}\to 0^-} \bar{p}^o, \tag{99}$$

$$\lim_{\bar{x}^\star \to \infty} \bar{p}^\star = \lim_{\bar{x},\bar{y}\to 0^+} \bar{p}^o, \tag{100}$$

which correspond to matching in the intermediate region on the left and right side of the inner region, respectively.

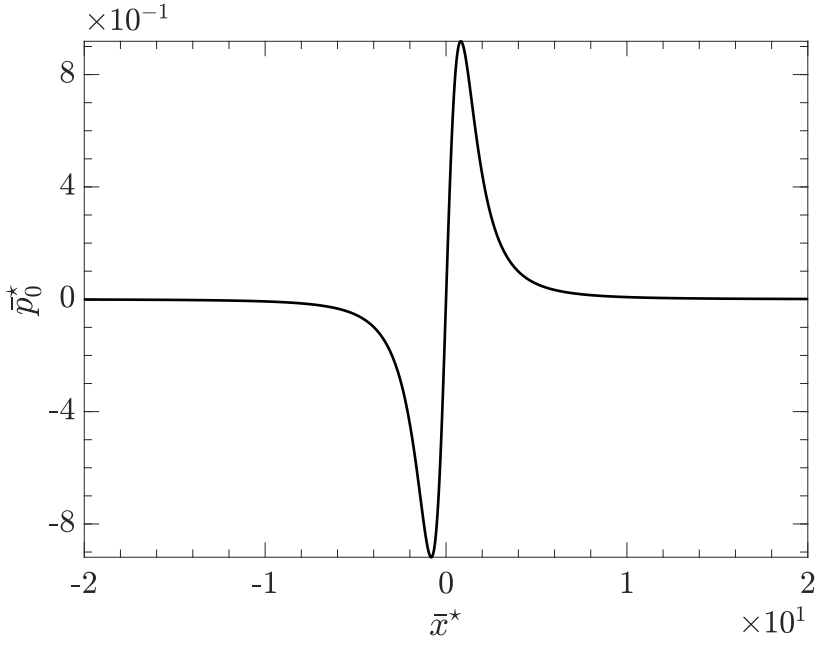

Figure 15: Plot of the leading order pressure distribution, $\bar{p}_0^\star$, across the inner region.

Typically, the general solution in both regions is required in order to use matching conditions to determine an intermediate solution and thereby particular solutions to the outer and inner regions. However, assumption (53) with the outer region pressure scaling (71) and inner region pressure scaling (80) gives us the leading order matching conditions

$$\lim_{\bar{x}^\star \to -\infty} \bar{p}_0^\star = 0, \tag{101}$$

$$\lim_{\bar{x}^\star \to \infty} \bar{p}_0^\star = 0. \tag{102}$$

Therefore, the matching conditions in the inner region essentially become homogeneous far-field conditions which close the inner problem without the need for solving an outer problem.

Thus, we can integrate (98) twice with respect to $\bar{x}^\star$ and use the matching conditions (101) and (102) to determine that the inner region's leading order pressure solution is given by

$$\bar{p}_0^\star = \frac{8\bar{x}^\star}{\left(\bar{x}^{\star 2}+2\right)^2}. \tag{103}$$

That is, the pressure distribution around the grinding zone is given by (103).

We are now in a position to determine the leading order flux through the grinding zone. Differentiating (103) with respect to $\bar{x}^\star$ and substituting the result into expression (96), we have that

$$\int_0^{\frac{1}{2}\left(\bar{x}^{\star 2}+2\right)} \bar{u}_0^\star \mathrm{d}\bar{y}^\star = -\frac{2}{3}. \tag{104}$$

Therefore, (104) tells us that the outer region only experiences a flux of $-\frac{2}{3}\varepsilon$ into the grinding zone. Hence, at leading order in the outer region, there is no flow into the grinding zone.

In figure 15, we plot the leading order pressure distribution, $\bar{p}_0^\star$, across the inner region for $\bar{x}^\star \in \left[-2\times 10^1, 2\times 10^1\right]$. We observe that the solution for $\bar{p}_0^\star$ is an odd function which has a zero at $\bar{x}^\star = 0$ with the peak given by

$$\bar{p}_0^\star\left(\sqrt{\frac{2}{3}}\right) = \frac{3\sqrt{6}}{8}. \tag{105}$$

3.5 CONCLUSION

In this chapter, we have applied the method of matched asymptotic expansions to the simple case of a spinning grinding wheel above a flat workpiece. This corresponds to the case of simulated grinding which is frequently studied in the literature. By taking the separation distance between the grinding wheel and workpiece as the typical size of an abrasive, we estimated the value of the nondimensional parameter ε, defined by (50), in surface and creep-feed grinding regimes, given by (51) and (52), respectively.

We found that at small separation distances between the grinding wheel and workpiece, the leading order flow near the grinding zone, i.e. the inner region flow, can be solved without needing to solve for the flow far from the grinding zone, i.e. the outer region flow. Additionally, no artificial or empirical boundary conditions needed to be enforced to solve for the flow near the grinding zone.

Using the inner region solution (103), we were able to calculate that the flux through the grinding zone is $-\frac{2}{3}$. This is shown in (104). Due to the stretching of the inner region, at leading order the outer problem experiences no flux into the grinding zone. Unless the grinding fluid nozzle is placed within a small $\sqrt{\varepsilon}$ distance from the grinding zone, the problem of solving for the leading order flow in the grinding zone using the method of matched asymptotic expansions is the same whether or not a nozzle is included in the problem: it suffices to only consider a fully flooded regime without a nozzle ejecting grinding fluid. We remark that placing the nozzle within a $\sqrt{\varepsilon}$ distance to the grinding zone is not physically possible, see figure 1 regarding the impracticality of this.

4

TRANSPORT OF GRINDING FLUID INTO THE GRINDING ZONE

4.1 INTRODUCTION

Throughout the physical world, multiscale problems are ubiquitous. A familiar example of this would be the multiple temporal scales during the propagation of gravity and capillary waves on deep water [42]. While some multiscale flows demand only an increase in computational cost when solving the governing equations, for example, when resolving turbulent structures at the Kolmogorov scale [71], others can require different modelling approaches. One such example of the latter is flows where the continuum limit is no longer uniformly valid. Consider, for instance, in a Couette flow where the near-wall flow is affected by micro- and nano-scale wall structures. One approach could be to describe the flow in the near-wall region by molecular dynamics, while the remaining flow is described under the continuum limit and coupling conditions link the flows over these two scales [66]. However, there are a variety of possible other techniques which can be used to deal with multiscale problems such as this.

In this chapter, we will build on the work from Chapter 3 by applying the same multiscale method to a geometry where curvature is present in the workpiece due to the depth of cut, d_c. We introduce this curvature to model the curved channel that appears in the workpiece while grinding. During our initial study of this flow, two nondimensional numbers will appear which characterise

the geometry of the flow domain. One of these numbers, ε, was discussed during Chapter 3. As we recall, for a typical surface grinding regime we have that

$$\varepsilon = 5 \times 10^{-5}, \tag{106}$$

while for a creep-feed grinding regime

$$\varepsilon = 2.5 \times 10^{-3}. \tag{107}$$

The other number is

$$\gamma = \frac{d_c}{R}, \tag{108}$$

where d_c is the depth of cut and R is the radius of the grinding wheel. This characterises the ratio between the thickness of the layer being removed from the workpiece and the size of the grinding wheel. Using table 1 with $R = 2 \times 10^{-1}$ m, we see that $\gamma = 1 \times 10^{-4}$ in surface grinding and $\gamma = 1.2 \times 10^{-2}$ in creep-feed grinding. Hence, we have that

$$\frac{\gamma}{\varepsilon} = 2, \tag{109}$$

in surface grinding,

$$\frac{\gamma}{\varepsilon} = 4.8, \tag{110}$$

in creep-feed grinding, and we will assume that

$$\frac{\gamma}{\varepsilon} = O\left(1\right) \tag{111}$$

in both the grinding regimes that we consider. We will denote the ratio of these nondimensional numbers by

$$\delta = \frac{\gamma}{\varepsilon}. \tag{112}$$

Further on in this chapter, we will consider the slip boundary condition from Section 2.3 which introduces another parameter into the flow, the slip coefficient, β, and the associated slip length, $\hat{\beta} = \beta\mu$. Here, μ is the dynamic viscosity of the fluid. We will see that the nondimensional number

$$\bar{\hat{\beta}}^{\star} = \frac{\hat{\beta}}{\varepsilon R} \tag{113}$$

is important in the flow as it characterises the effect of slip on the flow. With the approximation from (29) that $\hat{\beta} = 1 \times 10^{-8}$ m, the value of $R = 2 \times 10^{-1}$ m from table 1 and values of ε from (106) for surface grinding and (107) for creep-feed grinding, we calculate that

$$\bar{\hat{\beta}}^{\star} = 1 \times 10^{-3} \tag{114}$$

for surface grinding and

$$\bar{\hat{\beta}}^{\star} = 2 \times 10^{-5} \tag{115}$$

for creep-feed grinding. However, we remark that the value for the slip length is an estimate and there are multiple physical processes in grinding for which the modelling of could involve taking much larger slip length. Although these processes are outside the scope of this thesis, we will include slip effects on the leading order flow by assuming that

$$\bar{\hat{\beta}}^{\star} = O\left(1\right). \tag{116}$$

The aim of this chapter is to understand how the flux through the grinding zone is affected by the parameters that arise in a more realistic geometry than the planar workpiece studied in Chapter 3. The nondimensionalisation and inner region stretching will follow Chapter 3. We will primarily focus on the region near the grinding zone. As we recall, the flow there can be solved without requiring the solution to the large scale, outer region flow. To that end, we will

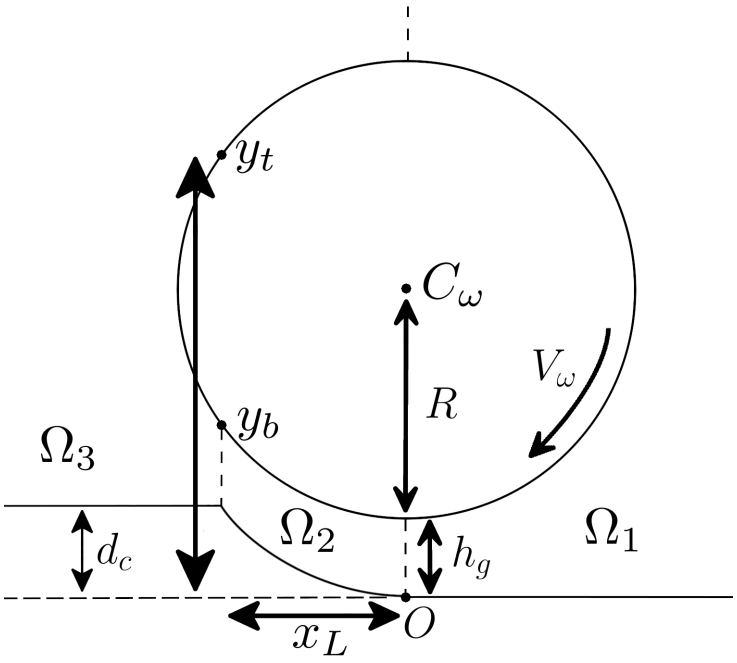

Figure 16: Illustration of introduced quantities in our problem setup.

still require the matching condition results (101) and (102). We will consider the grinding wheel to be fully submerged in a single-phase fluid. We will not consider the nozzle which ejects grinding fluid here, as we saw in the previous chapter that it has no effect on the flow inside the grinding zone.

4.2 PROBLEM FORMULATION

In this section we introduce our problem. We first set up our two dimensional coordinate system. We take the origin O to be the point on the workpiece lying directly below the centre of the grinding wheel, denoted by C_ω. Points in the domain are specified using a Cartesian coordinate system (x, y). The grinding wheel rotates in a clockwise direction with speed V_w and we assume that the workpiece has zero velocity[1]. We take the grinding wheel to be represented by a circle with radius R and lying above the workpiece by a distance $h_g > 0$. We take the workpiece surface to be a smooth curved surface along the region of contact, i.e. the grinding zone, and a planar surface lying at $y = d_c$ and $y = 0$

1 This assumption follows from the situation in most grinding applications where the magnitude of the workpiece's velocity is much less than that of the wheel.

to the left and right of the grinding zone, respectively. Here, $d_c > 0$ represents the workpiece's depth of cut with the physical assumption $d_c < R + h_g$.

We denote the surface of the workpiece by $h_1(x)$. The grinding wheel's surface is given by the level set function $h_\omega(x, y) = 0$, with the height of the bottom half of the grinding wheel denoted by $h_2(x)$. These expressions are given by

$$h_1(x) = \begin{cases} 0 & \text{for } x \geq 0, \\ R + h_g - \sqrt{(R + h_g)^2 - x^2} & \text{for } x \in (x_L, 0), \\ d_c & \text{for } x \leq x_L, \end{cases} \tag{117}$$

$$h_2(x) = R + h_g - \sqrt{R^2 - x^2}, \tag{118}$$

$$h_\omega(x, y) = x^2 + (y - R - h_g)^2 - R^2. \tag{119}$$

Here, x_L denotes the x coordinate at the grinding zone exit, given by

$$x_L = -(R + h_g)\sqrt{1 - \left(1 - \frac{d_c}{R + h_g}\right)^2}. \tag{120}$$

We suppose that there is an incompressible fluid in the domain surrounding the grinding wheel. The fluid has constant density and viscosity, denoted by ρ and μ, respectively. The flow domain is denoted Ω and is given by

$$\Omega = \bigcup_{i=1}^{3} \Omega_i, \tag{121}$$

where

$$\begin{aligned}\Omega_1 = &\left\{(x,y) : x \geq 0,\ y \in (0,y_b) \cup (y_t,\infty)\,,\ h_\omega(x,y) > 0\right\} \\ &\cup \left\{(x,y) : x \geq 0,\ y \in [y_b,y_t]\,,\ h_\omega(x,y) > 0\right\},\end{aligned} \tag{122}$$

$$\Omega_2 = \left\{(x,y) : x \in (x_L,0)\,,\ y \in \Big(h_1(x)\,, h_2(x)\Big)\right\}, \tag{123}$$

$$\begin{aligned}\Omega_3 = &\left\{(x,y) : x \leq x_L,\ y \in (d_c,y_b) \cup (y_t,\infty)\,,\ h_\omega(x,y) > 0\right\} \\ &\cup \left\{(x,y) : x \leq x_L,\ y \in [y_b,y_t]\,,\ h_\omega(x,y) > 0\right\} \\ &\cup \left\{(x,y) : x \in (x_L,0)\,,\ y > y_t,\ h_\omega(x,y) > 0\right\},\end{aligned} \tag{124}$$

represents the flow domain to the right of the grinding zone, the grinding zone and left of the grinding zone, respectively. Here,

$$y_b = R + h_g - \sqrt{R^2 - x_L^2}, \tag{125}$$

$$y_t = R + h_g + \sqrt{R^2 - x_L^2}. \tag{126}$$

Based on the work in Chapter 3, the effect of body forces on the flow is assumed negligible. An illustration of the problem setup is shown in figure 16.

4.3 COMPLETE PROBLEM AND ASYMPTOTIC REDUCTION

The governing system of the fluid is similar to Section 3.3. Specifically, we are looking to solve the equations

$$\frac{\partial u}{\partial x} + \frac{\partial v}{\partial y} = 0, \tag{127}$$

$$\rho\left(\frac{\partial \boldsymbol{u}}{\partial t} + \boldsymbol{u}\cdot\nabla\boldsymbol{u}\right) = -\nabla p + \mu\nabla^2\boldsymbol{u}, \tag{128}$$

subject to

$$\boldsymbol{u} = V_\omega \boldsymbol{t} \qquad \text{on } h_\omega(x,y) = 0, \tag{129}$$

$$\boldsymbol{u} = \boldsymbol{0} \qquad \text{on } y = h_1(x), \tag{130}$$

$$\boldsymbol{u} \to \boldsymbol{0} \qquad \text{as } x \to \pm\infty,\ y \to \infty, \tag{131}$$

$$p \to 0 \qquad \text{as } x \to \pm\infty,\ y \to \infty, \tag{132}$$

where $\boldsymbol{t} = t_x \boldsymbol{e}_x + t_y \boldsymbol{e}_y$ is the unit tangent to $h_\omega(x,y) = 0$, with

$$t_x = \begin{cases} \frac{\sqrt{R^2 - x^2}}{R} & \text{for } y > R + h_g, \\ -\frac{\sqrt{R^2 - x^2}}{R} & \text{for } y \le R + h_g, \end{cases} \tag{133}$$

$$t_y = -\frac{x}{R}. \tag{134}$$

Following Section 3.4, we introduce the nondimensional variables

$$\boldsymbol{u} = V_\omega \bar{\boldsymbol{u}}, \tag{135}$$

$$x = R\bar{x}, \tag{136}$$

$$y = R\bar{y}, \tag{137}$$

$$p = \frac{\mu V_\omega}{R}\bar{p}, \tag{138}$$

$$t = \frac{R}{V_\omega}\bar{t}. \tag{139}$$

The nondimensional system is then given as

$$\frac{\partial \bar{u}}{\partial \bar{x}} + \frac{\partial \bar{v}}{\partial \bar{y}} = 0, \tag{140}$$

$$\mathrm{Re}\left(\frac{\partial \bar{\boldsymbol{u}}}{\partial \bar{t}} + \bar{\boldsymbol{u}} \cdot \bar{\nabla}\bar{\boldsymbol{u}}\right) = -\bar{\nabla}\bar{p} + \bar{\nabla}^2 \bar{\boldsymbol{u}}, \tag{141}$$

subject to

$$\bar{\boldsymbol{u}} = \bar{\boldsymbol{t}} \qquad \text{on } \bar{h}_\omega(\bar{x}, \bar{y}) = 0, \tag{142}$$

$$\bar{\boldsymbol{u}} = \boldsymbol{0} \qquad \text{on } \bar{y} = \bar{h}_1(\bar{x}), \tag{143}$$

$$\bar{\boldsymbol{u}} \to \boldsymbol{0} \qquad \text{as } \bar{x} \to \pm\infty,\ \bar{y} \to \infty, \tag{144}$$

$$\bar{p} \to 0 \qquad \text{as } \bar{x} \to \pm\infty,\ \bar{y} \to \infty, \tag{145}$$

where $\bar{\boldsymbol{t}} = \bar{t}_x \boldsymbol{e}_x + \bar{t}_y \boldsymbol{e}_y$ with

$$\bar{t}_x = \begin{cases} \sqrt{1-\bar{x}^2} & \text{for } \bar{y} > 1+\varepsilon, \\ -\sqrt{1-\bar{x}^2} & \text{for } \bar{y} \le 1+\varepsilon, \end{cases} \tag{146}$$

$$\bar{t}_y = -\bar{x}, \tag{147}$$

and $\bar{\nabla}$ is the gradient operator with respect to the nondimensionalised coordinates.

The nondimensional forms of the boundary locations (117)-(120) are given by

$$\bar{h}_1(\bar{x}) = \begin{cases} 0 & \text{for } \bar{x} \ge 0, \\ 1+\varepsilon-\sqrt{(1+\varepsilon)^2-\bar{x}^2} & \text{for } \bar{x} \in (\bar{x}_L, 0), \\ \gamma & \text{for } \bar{x} \le \bar{x}_L, \end{cases} \tag{148}$$

$$\bar{h}_2(\bar{x}) = 1+\varepsilon-\sqrt{1-\bar{x}^2}, \tag{149}$$

$$\bar{h}_\omega(\bar{x}, \bar{y}) = \bar{x}^2 + (\bar{y}-1-\varepsilon)^2 - 1, \tag{150}$$

$$\bar{x}_L = -(1+\varepsilon)\sqrt{1-\left(1-\frac{\gamma}{1+\varepsilon}\right)^2}, \tag{151}$$

where we recall the definition of γ from (108) as

$$\gamma = \frac{d_c}{R}. \tag{152}$$

As before, the presence of the small parameter ε in the boundary locations (148)-(151) motivates us to introduce variables which stretch the small scale grinding region. A variable rescaling argument leads us to introduce the $O(1)$ stretched variables, denoted by superscript $\star$, as

$$\bar{x} = \sqrt{\varepsilon}\bar{x}^\star, \tag{153}$$

$$\bar{y} = \varepsilon\bar{y}^\star, \tag{154}$$

$$\bar{u} = \bar{u}^\star, \tag{155}$$

$$\bar{v} = \sqrt{\varepsilon}\bar{v}^\star, \tag{156}$$

$$\bar{p} = \frac{\bar{p}^\star}{\varepsilon\sqrt{\varepsilon}}. \tag{157}$$

We can then substitute (153)-(157) into (140)-(151) and consider leading order terms to arrive at the closed governing system for the flow in the inner region, i.e.

$$\frac{\partial \bar{u}^\star}{\partial \bar{x}^\star} + \frac{\partial \bar{v}^\star}{\partial \bar{y}^\star} = 0, \tag{158}$$

$$\frac{\partial \bar{p}^\star}{\partial \bar{x}^\star} = \frac{\partial^2 \bar{u}^\star}{\partial \bar{y}^{\star 2}}, \tag{159}$$

$$\frac{\partial \bar{p}^\star}{\partial \bar{y}^\star} = 0, \tag{160}$$

subject to

$$\bar{u}^\star = -1 \qquad \text{on } \bar{y}^\star = \bar{h}_2^\star(\bar{x}^\star), \tag{161}$$

$$\bar{v}^\star = -\bar{x}^\star \qquad \text{on } \bar{y}^\star = \bar{h}_2^\star(\bar{x}^\star), \tag{162}$$

$$\bar{u}^\star = 0 \qquad \text{on } \bar{y}^\star = \bar{h}_1^\star(\bar{x}^\star), \tag{163}$$

$$\bar{v}^\star = 0 \qquad \text{on } \bar{y}^\star = \bar{h}_1^\star(\bar{x}^\star), \tag{164}$$

with the matching conditions

$$\lim_{\bar{x}^\star \to -\infty} \bar{p}^\star = 0, \tag{165}$$

$$\lim_{\bar{x}^\star \to \infty} \bar{p}^\star = 0. \tag{166}$$

Here,

$$\bar{h}_1^\star\left(\bar{x}^\star\right) = \begin{cases} 0 & \text{for } \bar{x}^\star \geq 0, \\ \frac{\bar{x}^{\star 2}}{2} & \text{for } \bar{x}^\star \in \left(\bar{x}_L^\star, 0\right), \\ \delta & \text{for } \bar{x}^\star \leq \bar{x}_L^\star, \end{cases} \tag{167}$$

$$\bar{h}_2^\star\left(\bar{x}^\star\right) = \frac{1}{2}\left(\bar{x}^{\star 2} + 2\right), \tag{168}$$

$$\bar{x}_L^\star = -\sqrt{2\delta}, \tag{169}$$

where δ is defined by (112) and $\bar{x}_L^\star = O\left(1\right)$ due to assumption (111). The reader is referred back to Section 3.4 for a more detailed derivation of system (158)-(166).

4.4 LEADING ORDER ANALYTICAL SOLUTION

The procedure for solving system (158)-(166) is similar to that presented in Section 3.4. However, technicalities arise due to the varying workpiece height, $\bar{h}_1^\star$, and the solution $\bar{p}^\star$ must now be patched at $\bar{x}^\star = \bar{x}_L^\star, 0$ in order to ensure continuity of pressure between the three regions

$$\bar{\Omega}_1^\star = \left\{\left(\bar{x}^\star, \bar{y}^\star\right) : \bar{x}^\star > 0,\ \bar{y} \in \left(0, \frac{1}{2}\left(\bar{x}^{\star 2} + 2\right)\right)\right\}, \tag{170}$$

$$\bar{\Omega}_2^\star = \left\{\left(\bar{x}^\star, \bar{y}^\star\right) : \bar{x}^\star \in \left(\bar{x}_L^\star, 0\right),\ \bar{y} \in \left(\frac{\bar{x}^{\star 2}}{2}, \frac{1}{2}\left(\bar{x}^{\star 2} + 2\right)\right)\right\}, \tag{171}$$

$$\bar{\Omega}_3^\star = \left\{\left(\bar{x}^\star, \bar{y}^\star\right) : \bar{x}^\star < \bar{x}_L^\star,\ \bar{y} \in \left(\delta, \frac{1}{2}\left(\bar{x}^{\star 2} + 2\right)\right)\right\}. \tag{172}$$

To begin, we denote variables belonging to domain $\bar{\Omega}_i^\star, i = 1, 2, 3$, by subscript i, e.g. $\bar{u}_i^\star$, and we solve (158)-(166) individually in each domain. Following Section 3.4, we arrive at three separate solutions for the x velocity component

$$\bar{u}_1^\star = -\frac{8\bar{y}^\star}{4\bar{x}^{\star 2}+8} - \frac{\left(\bar{x}^{\star 2}+2\right)\left(\bar{x}^{\star 2}-2\bar{y}^\star+2\right)\bar{y}^\star}{4\bar{x}^{\star 2}+8}\frac{\mathrm{d}\bar{p}_1^\star}{\mathrm{d}\bar{x}^\star}, \tag{173}$$

$$\bar{u}_2^\star = \frac{\bar{x}^{\star 2}-2\bar{y}^\star}{2} + \frac{\left(\bar{x}^{\star 2}-2\bar{y}^\star\right)\left(\bar{x}^{\star 2}-2\bar{y}^\star+2\right)}{8}\frac{\mathrm{d}\bar{p}_2^\star}{\mathrm{d}\bar{x}^\star}, \tag{174}$$

$$\bar{u}_3^\star = -\frac{2\left(\bar{y}^\star-\delta\right)}{\bar{x}^{\star 2}+2\left(1-\delta\right)} - \frac{\left[\bar{x}^{\star 2}+2\left(1-\bar{y}^\star\right)\right]\left[\bar{x}^{\star 2}+2\left(1-\bar{y}^\star\right)\right]\left(\bar{y}^\star-\delta\right)}{4\left[\bar{x}^{\star 2}+2\left(1-\delta\right)\right]}\frac{\mathrm{d}\bar{p}_3^\star}{\mathrm{d}\bar{x}^\star}. \tag{175}$$

Integrating (158) in all three regions $\bar{\Omega}_i^\star, i = 1, 2, 3$ with respect to $\bar{y}^\star$ between $\bar{h}_1^\star$ and $\bar{h}_2^\star$ and using Leibniz's rule, we find that

$$\frac{\mathrm{d}}{\mathrm{d}\bar{x}^\star}\int_{\bar{h}_1^\star(\bar{x}^\star)}^{\bar{h}_2^\star(\bar{x}^\star)} \bar{u}_i^\star \mathrm{d}\bar{y}^\star = 0. \tag{176}$$

We can immediately integrate (176) and use conservation of mass to get that

$$\int_{\bar{h}_1^\star(\bar{x}^\star)}^{\bar{h}_2^\star(\bar{x}^\star)} \bar{u}_i^\star \mathrm{d}\bar{y}^\star = \bar{Q}^\star, \tag{177}$$

where $\bar{Q}^\star$ is a constant representing the flux.

The cross-sectional flux appearing in (177) for each domain can be found from expressions (173)-(175) and is given by

$$\int_{\bar{h}_1^\star(\bar{x}^\star)}^{\bar{h}_2^\star(\bar{x}^\star)} \bar{u}_1^\star \mathrm{d}\bar{y}^\star = -\frac{\bar{x}^{\star 2}+2}{4} - \frac{\left(\bar{x}^{\star 2}+2\right)^3}{96}\frac{\mathrm{d}\bar{p}_1^\star}{\mathrm{d}\bar{x}^\star}, \tag{178}$$

$$\int_{\bar{h}_1^\star(\bar{x}^\star)}^{\bar{h}_2^\star(\bar{x}^\star)} \bar{u}_2^\star \mathrm{d}\bar{y}^\star = -\frac{1}{2} - \frac{1}{12}\frac{\mathrm{d}\bar{p}_2^\star}{\mathrm{d}\bar{x}^\star}, \tag{179}$$

$$\int_{\bar{h}_1^\star(\bar{x}^\star)}^{\bar{h}_2^\star(\bar{x}^\star)} \bar{u}_3^\star \mathrm{d}\bar{y}^\star = -\frac{\bar{x}^{\star 2}+2\left(1-\delta\right)}{4} - \frac{\left[\bar{x}^{\star 2}+2\left(1-\delta\right)\right]^3}{96}\frac{\mathrm{d}\bar{p}_3^\star}{\mathrm{d}\bar{x}^\star}. \tag{180}$$

We observe that expressions (178)-(180) indicate that the flux, $\bar{Q}^\star$, can be decomposed into two components: one due to flow driven by the shearing of

the grinding wheel, denoted $\bar{Q}_s^\star$, and another due to flow driven by the pressure gradient, denoted $\bar{Q}_p^\star$. Thus, we have that

$$\int_{\bar{h}_1^\star}^{\bar{h}_2^\star} \bar{u}_i^\star \mathrm{d}\bar{y}^\star = \bar{Q}_{s,i}^\star + \bar{Q}_{p,i}^\star = \bar{Q}^\star \tag{181}$$

for each region $\bar{\Omega}_i^\star, i = 1, 2, 3$, where

$$\bar{Q}_{s,1}^\star = -\frac{\bar{x}^{\star 2} + 2}{4}, \tag{182}$$

$$\bar{Q}_{p,1}^\star = -\frac{\left(\bar{x}^{\star 2} + 2\right)^3}{96} \frac{\mathrm{d}\bar{p}_1^\star}{\mathrm{d}\bar{x}^\star}, \tag{183}$$

$$\bar{Q}_{s,2}^\star = -\frac{1}{2}, \tag{184}$$

$$\bar{Q}_{p,2}^\star = -\frac{1}{12} \frac{\mathrm{d}\bar{p}_2^\star}{\mathrm{d}\bar{x}^\star}, \tag{185}$$

$$\bar{Q}_{s,3}^\star = -\frac{\bar{x}^{\star 2} + 2\left(1 - \delta\right)}{4}, \tag{186}$$

$$\bar{Q}_{p,3}^\star = -\frac{\left[\bar{x}^{\star 2} + 2\left(1 - \delta\right)\right]^3}{96} \frac{\mathrm{d}\bar{p}_3^\star}{\mathrm{d}\bar{x}^\star}. \tag{187}$$

We note that (181) can be rearranged as

$$\frac{\bar{Q}_{s,i}^\star}{\bar{Q}^\star} = \frac{1}{\frac{\bar{Q}_{p,i}^\star}{\bar{Q}_{s,i}^\star} + 1}, \tag{188}$$

which we will use later on to determine the contribution of each flux component to the flux.

Due to the $\bar{x}^{\star 2} + 2\left(1 - \delta\right)$ factor in (180), there are three cases we must consider before solving for $\bar{p}_3^\star$. The three cases are

$$0 < \delta < 1, \tag{189}$$

$$\delta = 1, \tag{190}$$

$$\delta > 1. \tag{191}$$

4.4.1 *Solution for* $0 < \delta < 1$

Using expressions (178)-(180), we can determine that $\bar{p}^\star$ in each region is given by

$$\begin{aligned}\bar{p}_1^\star = -\frac{1}{2\left(\bar{x}^{\star 2}+2\right)^2}\Bigg(&3\sqrt{2}\left(3\bar{Q}^\star+2\right)\left(\bar{x}^{\star 2}+2\right)^2\tan^{-1}\left(\frac{\bar{x}^\star}{\sqrt{2}}\right)+\\ &6\bar{x}^\star\left[\left(3\bar{Q}^\star+2\right)\bar{x}^{\star 2}+\left(10\bar{Q}^\star+4\right)\right]\Bigg)+\bar{C}_1^\star,\end{aligned} \tag{192}$$

$$\bar{p}_2^\star = -6\left(2\bar{Q}^\star+1\right)\bar{x}^\star+\bar{C}_2^\star, \tag{193}$$

$$\begin{aligned}\bar{p}_3^\star = -\frac{3}{(1-\delta)^2}\Bigg(&\frac{\bar{x}^\star}{\left[\bar{x}^{\star 2}+2\left(1-\delta\right)\right]^2}\Big[\\ &\left[3\bar{Q}^\star+2\left(1-\delta\right)\right]\bar{x}^{\star 2}+2\left[5\bar{Q}^\star+2\left(1-\delta\right)\right]\left(1-\delta\right)\Big]+\\ &+\frac{\tan^{-1}\left(\frac{\bar{x}^\star}{\sqrt{2(1-\delta)}}\right)}{\sqrt{2\left(1-\delta\right)}}\left[3\bar{Q}^\star+2\left(1-\delta\right)\right]\Bigg)+\bar{C}_3^\star.\end{aligned} \tag{194}$$

In order to solve for the constants $\bar{C}_i^\star, i = 1, 2, 3$, and $\bar{Q}^\star$ we must use the matching conditions (165) and (166) along with a continuity requirement of $\bar{p}^\star$ at $\bar{x}^\star = \bar{x}_L^\star, 0$. Doing so, we find that

$$\bar{C}_1^\star = \bar{C}_2^\star = -\frac{3\sqrt{2}\pi\delta\left(6\tan^{-1}\left(\sqrt{\frac{\delta}{1-\delta}}\right)+\sqrt{4\delta(1-\delta)}(5-2\delta)-3\pi\right)}{6\pi+\sqrt{4(1-\delta)}\left(3\pi[1-\delta(2-\delta)]+16\sqrt{\delta^5}-28\sqrt{\delta^3}+6\sqrt{\delta}\right)-12\tan^{-1}\left(\sqrt{\frac{\delta}{1-\delta}}\right)}, \tag{195}$$

$$\bar{C}_3^\star = -\frac{3\sqrt{2}\pi\delta\left(3\pi+16\sqrt{\delta}\right)}{6\pi+\sqrt{4(1-\delta)}\left(3\pi[1-\delta(2-\delta)]+16\sqrt{\delta^5}-28\sqrt{\delta^3}+6\sqrt{\delta}\right)-12\tan^{-1}\left(\sqrt{\frac{\delta}{1-\delta}}\right)}, \tag{196}$$

$$\bar{Q}^\star = \frac{8(1-\delta)\tan^{-1}\left(\sqrt{\frac{\delta}{1-\delta}}\right)-4\pi(1-\delta)-2\sqrt{4(1-\delta)}\left(\pi[1-\delta(2-\delta)]+4\sqrt{\delta^5}-6\sqrt{\delta^3}+2\sqrt{\delta}\right)}{6\pi+\sqrt{4(1-\delta)}\left(3\pi[1-\delta(2-\delta)]+16\sqrt{\delta^5}-28\sqrt{\delta^3}+6\sqrt{\delta}\right)-12\tan^{-1}\left(\sqrt{\frac{\delta}{1-\delta}}\right)}. \tag{197}$$

4.4.2 *Solution for $\delta = 1$*

In the case of $\delta = 1$, $\bar{p}_3^\star$ takes the simpler form

$$\bar{p}_3^\star = \frac{40\bar{x}^{\star 2} + 96\bar{Q}^\star}{5\bar{x}^{\star 5}} + \bar{C}_3^\star, \tag{198}$$

with $\bar{p}_1^\star$ and $\bar{p}_2^\star$ given by (192) and (193), respectively. In this case, the constants are now given by

$$\bar{C}_1^\star = \bar{C}_2^\star = \frac{8\sqrt{2}\pi}{5\pi + 32}, \tag{199}$$

$$\bar{C}_3^\star = 0, \tag{200}$$

$$\bar{Q}^\star = -\frac{30\pi + 160}{45\pi + 288}. \tag{201}$$

4.4.3 *Solution for $\delta > 1$*

For $\delta > 1$, we note that

$$\left| \frac{\bar{x}^\star}{\sqrt{2\left(\delta-1\right)}} \right| > 1 \tag{202}$$

for $\bar{x}^\star < \bar{x}_L^\star$. We can find the expression for $\bar{p}_3^\star$ to be

$$\begin{aligned} \bar{p}_3^\star = -\frac{3}{\left(\delta-1\right)^2}\Bigg(& \frac{\bar{x}^\star}{\left[\bar{x}^{\star 2}-2\left(\delta-1\right)\right]^2}\Big[\\ & \left[3\bar{Q}^\star-2\left(\delta-1\right)\right]\bar{x}^{\star 2}-2\left[5\bar{Q}^\star-2\left(\delta-1\right)\right]\left(\delta-1\right)\Big]+ \\ & -\frac{\coth^{-1}\left(\frac{\bar{x}^\star}{\sqrt{2(\delta-1)}}\right)}{\sqrt{2\left(\delta-1\right)}}\left[3\bar{Q}^\star-2\left(\delta-1\right)\right]\Bigg)+\bar{C}_3^\star, \end{aligned} \tag{203}$$

with $\bar{p}_1^\star$ and $\bar{p}_2^\star$ given by (192) and (193), respectively. The constants are now given by

$$\bar{C}_1^\star = \bar{C}_2^\star = -\frac{3\sqrt{2}\pi\delta\left(\sqrt{4\delta(1-\delta)}(5-2\delta)-6\coth^{-1}\left(\sqrt{\frac{\delta}{\delta-1}}\right)\right)}{6\pi+\sqrt{4(1-\delta)}\left(3\pi[1-\delta(2-\delta)]+16\sqrt{\delta^5}-28\sqrt{\delta^3}+6\sqrt{\delta}\right)+12\coth^{-1}\left(\sqrt{\frac{\delta}{\delta-1}}\right)}, \tag{204}$$

$$\bar{C}_3^\star = 0, \tag{205}$$

$$\bar{Q}^\star = \frac{8(\delta-1)\coth^{-1}\left(\sqrt{\frac{\delta}{\delta-1}}\right)-2\sqrt{4(\delta-1)}\left(\pi[1-\delta(2-\delta)]+4\sqrt{\delta^5}-6\sqrt{\delta^3}+2\sqrt{\delta}\right)}{\sqrt{4(\delta-1)}\left(3\pi[1-\delta(2-\delta)]+16\sqrt{\delta^5}-28\sqrt{\delta^3}+6\sqrt{\delta}\right)+12\coth^{-1}\left(\sqrt{\frac{\delta}{\delta-1}}\right)}. \tag{206}$$

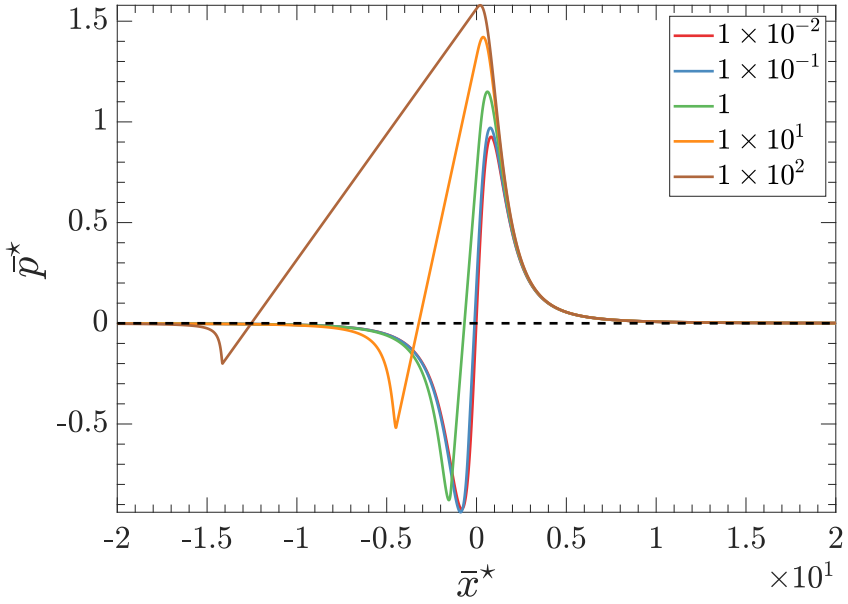

Figure 17: Plot of the pressure distribution, $\bar{p}^\star$, along the inner region. The legend corresponds to the value of δ in the no-slip regime.

4.4.4 *Solution Discussion*

Focusing on the pressure solutions (192)-(194), (198) and (203), we observe that for all three cases of δ, the forms of $\bar{p}_1^\star$ and $\bar{p}_2^\star$ are the same. In particular, $\bar{p}_1^\star$ is given by the sum of a rational polynomial and an inverse trigonometric term. In the grinding zone, $\bar{\Omega}_2^\star$, $\bar{p}_2^\star$ is given by a linear polynomial. However, the form of $\bar{p}_3^\star$ varies depending on which δ regime we are in and is given by: the sum of a rational polynomial and an inverse trigonometric term for $0 < \delta < 1$; a rational polynomial for $\delta = 1$; the sum of a rational polynomial and an inverse hyperbolic function for $\delta > 1$.

In figure 17, we plot the value of the pressure solution $\bar{p}^\star$ for five different representative values of δ. We observe that near $\delta = 0$, i.e. a smaller depth of cut than spacing between the grinding wheel and the workpiece, $\bar{p}^\star$ is almost symmetrical around $\bar{x}^\star = 0$. The problem studied in Chapter 3 corresponds to

$\delta = 0$, so it is unsurprising that for small δ, $\bar{p}^\star$ looks similar to solution (103) from that chapter. In fact, it is possible to calculate that

$$\lim_{\delta \to 0} \bar{p}^\star \left(\bar{x}^\star = 0\right) = 0, \tag{207}$$

as we would expect.

As δ increases, i.e. increasing the depth of cut with respect to the spacing between the grinding wheel and the workpiece, $\bar{p}^\star$ becomes increasing asymmetrical, with a larger peak appearing near $\bar{x}^\star = 0$ and a shallower trough at $\bar{x}^\star = \bar{x}_L^\star$. Additionally, the point of zero pressure is shifted away from the entrance of the grinding zone, $\bar{x}^\star = 0$, and towards the exit of the grinding zone, $\bar{x}^\star = \bar{x}_L^\star$. Going further, we can show that

$$\lim_{\delta \to \infty} \bar{p}^\star \left(\bar{x}^\star = 0\right) = \frac{3\sqrt{2}\pi}{8} \tag{208}$$

gives the maximum pressure in the inner region across all regimes, and that

$$\lim_{\delta \to \infty} \bar{p}^\star \left(\bar{x}^\star = \bar{x}_L^\star\right) = 0, \tag{209}$$

supporting the observations from the solution plots.

In figure 18, we plot the pressure derivative $\frac{\mathrm{d}\bar{p}^\star}{\mathrm{d}\bar{x}^\star}$ across the inner region for various values of δ. We recall from expression (181) that the pressure derivative along with the shearing of the grinding wheel drives fluid through the grinding zone. As we would expect based on the pressure plots in figure 17, an increase in δ results in a larger region of constant pressure derivative due to the corresponding increase in the length of the grinding zone. However, despite the pressure peak increasing with δ, there is a decrease in the constant pressure derivative value across the grinding zone.

In figure 19, we plot the flux $\bar{Q}^\star$ as a function of δ. We see limiting behaviours as $\delta \to 0$ and $\delta \to \infty$, with the maximum flux (in magnitude) given by

$$\lim_{\delta \to 0} \bar{Q}^\star = -\frac{2}{3}, \tag{210}$$

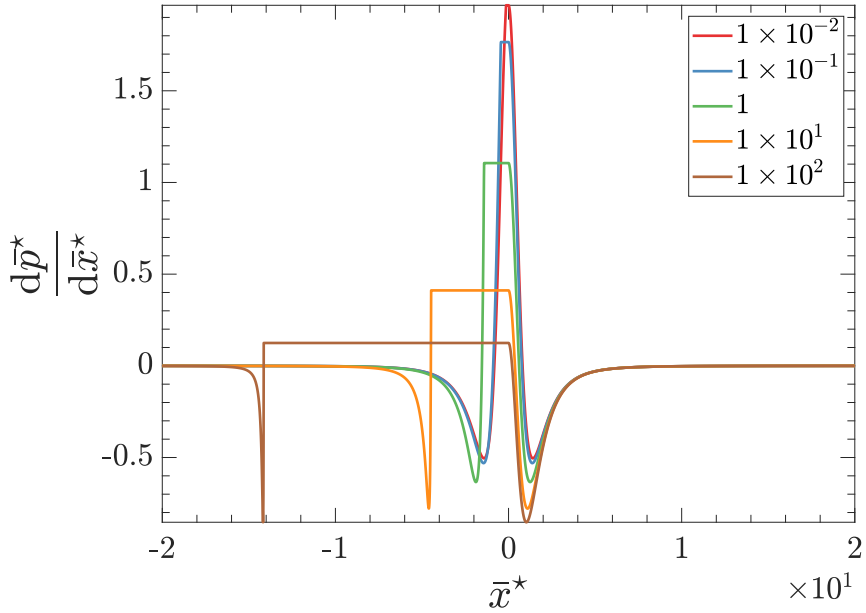

Figure 18: Plot of the pressure derivative, $\frac{d\bar{p}^\star}{d\bar{x}^\star}$, along the inner region. The legend corresponds to the value of δ in the no-slip regime.

as we had in from (104) in Chapter 3, and the minimum flux (in magnitude) given by

$$\lim_{\delta \to \infty} \bar{Q}^\star = -\frac{1}{2}. \tag{211}$$

Furthermore, in figures 20 and 21 we plot the flux components due to pressure gradient, $\bar{Q}_p^\star$, and shear effects, $\bar{Q}_s^\star$, and the flux component fraction, $\frac{\bar{Q}_p^\star}{\bar{Q}_s^\star}$, respectively. We recall that $\bar{Q}_s^\star + \bar{Q}_p^\star = \bar{Q}^\star$.

Far from the grinding zone, i.e. regions $\bar{\Omega}_1^\star$ and $\bar{\Omega}_3^\star$, on the scale of the flux components there appears to be an equal but opposite contribution to the flux from components due to the pressure gradient and shear effects. However, recalling figure 19, there is an $O(1)$ difference in the flux components present throughout the flow domain.

As the grinding zone is approached, shear effects begin to have a larger contribution to the flow. In the grinding zone, i.e. region $\bar{\Omega}_2^\star$, we can observe that there is a greater influence of the pressure gradient on the flux for smaller values of δ. As $\delta \to \infty$, this influence seems to be become negligible, with shear

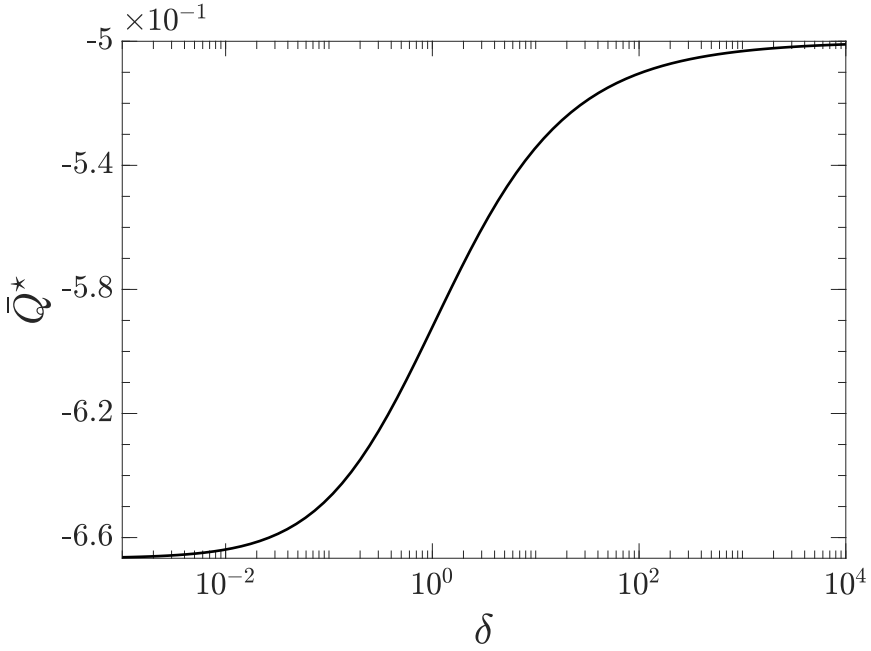

Figure 19: Plot of the flow rate, $\bar{Q}^\star$, as a function of δ.

effects dominating the transport of the grinding fluid in the grinding zone. This can be shown directly from the pressure solution via the limit

$$\lim_{\delta\to\infty}\frac{\bar{Q}^\star_{p,2}}{\bar{Q}^\star_{s,2}}=\lim_{\delta\to\infty}\frac{1}{6}\frac{\mathrm{d}\bar{p}^\star_2}{\mathrm{d}\bar{x}^\star}=0. \tag{212}$$

We can also show that the maximum flux component fraction in the grinding zone across all values of δ is given by

$$\lim_{\delta\to 0}\frac{\bar{Q}^\star_{p,2}}{\bar{Q}^\star_{s,2}}=\frac{1}{3}. \tag{213}$$

Using (188) and (213), we can deduce that across all regimes the flow due to the pressure gradient across the grinding zone only accounts for at most 25% of the flux, with the flow due to the shearing of the grinding wheel causing the remaining majority of the flux.

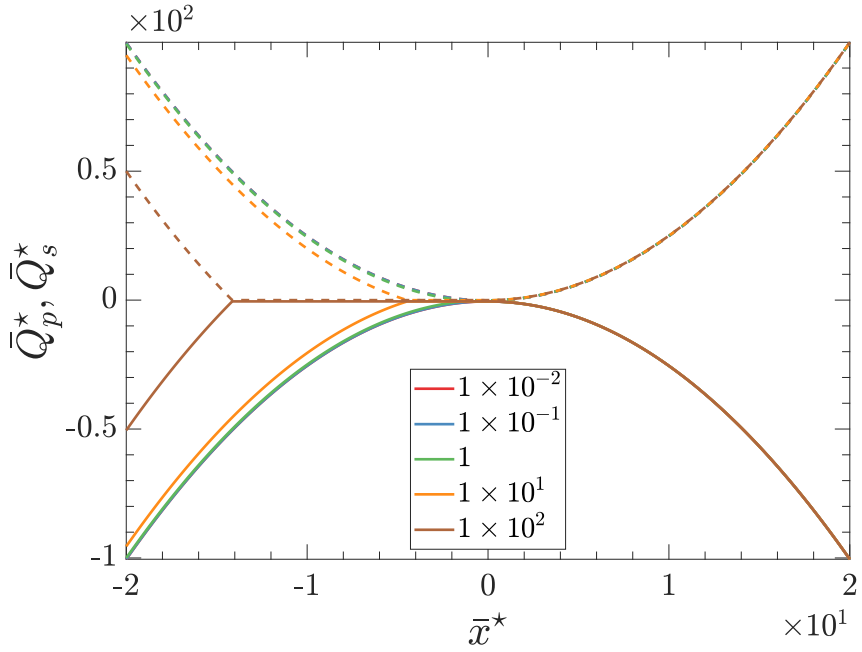

Figure 20: Plot of the flux components, $\bar{Q}_p^\star$ and $\bar{Q}_s^\star$, along the inner region. The dashed line represents the value of $\bar{Q}_p^\star$ while the solid line represents the value of $\bar{Q}_s^\star$. The legend corresponds to the value of δ in the no-slip regime. There is significant overlap of the lines corresponding to $\delta = 1 \times 10^{-2}, 1 \times 10^{-1}, 1$.

Recalling the estimations (109) and (110) of δ for surface and creep-feed grinding, respectively, we can calculate that in the grinding zone for $\delta = 2$,

$$\frac{\bar{Q}_{p,2}^\star}{\bar{Q}_{s,2}^\star} \approx 1.43 \times 10^{-1}, \tag{214}$$

and for $\delta = 4.8$,

$$\frac{\bar{Q}_{p,2}^\star}{\bar{Q}_{s,2}^\star} \approx 9.79 \times 10^{-2}. \tag{215}$$

This gives us that for $\delta = 2$

$$\begin{aligned} \frac{\bar{Q}_{p,2}^\star}{\bar{Q}^\star} \times 10^2 &\approx 1.3 \times 10^1, \\ \frac{\bar{Q}_{s,2}^\star}{\bar{Q}^\star} \times 10^2 &\approx 8.7 \times 10^1, \end{aligned} \tag{216}$$

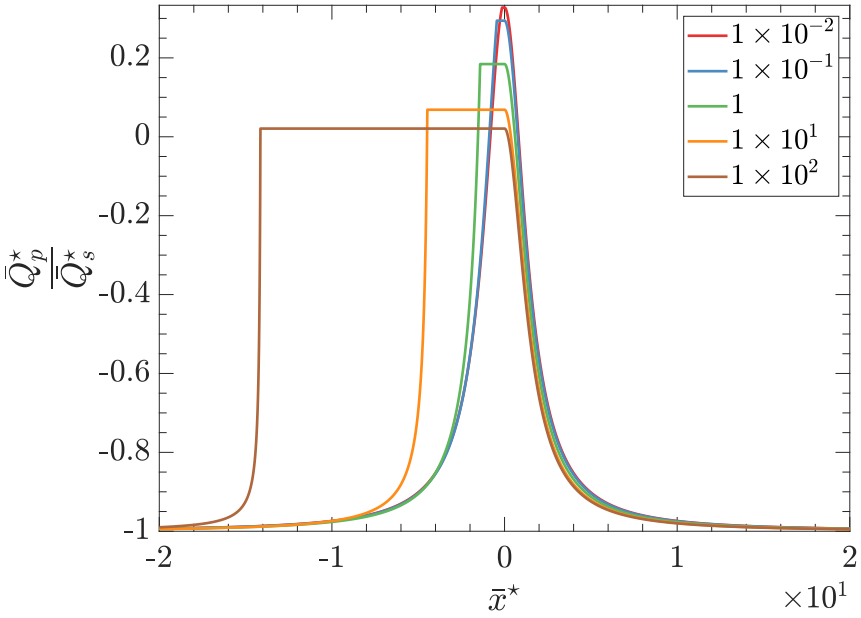

Figure 21: Plot of the flux component fraction, $\frac{\bar{Q}_p^\star}{\bar{Q}_s^\star}$, along the inner region. The legend corresponds to the value of δ in the no-slip regime.

and for $\delta = 4.8$

$$\begin{aligned} \frac{\bar{Q}_{p,2}^\star}{\bar{Q}^\star} \times 10^2 &\approx 9, \\ \frac{\bar{Q}_{s,2}^\star}{\bar{Q}^\star} \times 10^2 &\approx 9.1 \times 10^1, \end{aligned} \tag{217}$$

Therefore, from (216) we have that for surface grinding regimes, around 13% of the flux is caused by the pressure gradient and the remaining majority of 87% is caused by the shearing of the grinding wheel. Meanwhile, from (217) we have that for creep-feeding grinding regimes there is an even larger influence of the shearing of the grinding wheel on the flux, with 9% of the flux caused by the pressure gradient and the remaining majority of 91% caused by the shearing of the grinding wheel. We note that this argument does not hold outside the grinding zone, as $\left|\bar{Q}_{p,i}^\star\right| \geq \left|\bar{Q}^\star\right|$ and $\left|\bar{Q}_{s,i}^\star\right| \geq \left|\bar{Q}^\star\right|$ for $i = 1, 3$. Thus, (188) does not represent the fraction of the flux attributable to shear effects for $i = 1, 3$.

4.5 PROBLEM FORMULATION WITH SLIP

In this section, we extend the problem in Section 4.2 to include slip at the surface of the grinding wheel and the workpiece. Recalling Section 2.3 where the slip condition was introduced, the problem we now have is

$$\frac{\partial u}{\partial x} + \frac{\partial v}{\partial y} = 0, \tag{218}$$

$$\rho\left(\frac{\partial \boldsymbol{u}}{\partial t} + \boldsymbol{u}\cdot\nabla\boldsymbol{u}\right) = -\nabla p + \mu\nabla^2\boldsymbol{u}, \tag{219}$$

subject to

$$\boldsymbol{u} - V_\omega \boldsymbol{t} = 2\hat{\beta}\boldsymbol{n}\cdot\boldsymbol{E}(\boldsymbol{u})\cdot(\boldsymbol{I} - \boldsymbol{n}\boldsymbol{n}) \qquad \text{on } h_\omega(x,y) = 0, \tag{220}$$

$$\boldsymbol{u} = 2\hat{\beta}\boldsymbol{n}\cdot\boldsymbol{E}(\boldsymbol{u})\cdot(\boldsymbol{I} - \boldsymbol{n}\boldsymbol{n}) \qquad \text{on } y = h_1(x), \tag{221}$$

$$\boldsymbol{u} \to \boldsymbol{0} \qquad \text{as } x \to \pm\infty,\ y \to \infty, \tag{222}$$

$$p \to 0 \qquad \text{as } x \to \pm\infty,\ y \to \infty, \tag{223}$$

where $\boldsymbol{t} = t_x\boldsymbol{e}_x + t_y\boldsymbol{e}_y$ is a unit tangent to $h_\omega(x,y) = 0$ with

$$t_x = \begin{cases} \frac{\sqrt{R^2-x^2}}{R} & \text{for } y > R + h_g, \\ -\frac{\sqrt{R^2-x^2}}{R} & \text{for } y \le R + h_g, \end{cases} \tag{224}$$

$$t_y = -\frac{x}{R}, \tag{225}$$

$\boldsymbol{n} = n_x\boldsymbol{e}_x + n_y\boldsymbol{e}_y$ denotes the inward pointing unit normal, given by

$$n_x = -\frac{x}{R}, \tag{226}$$

$$n_y = \begin{cases} -\frac{\sqrt{R^2-x^2}}{R} & \text{for } y > R + h_g, \\ \frac{\sqrt{R^2-x^2}}{R} & \text{for } y \le R + h_g, \end{cases} \tag{227}$$

on $h_\omega(x,y)=0$ and

$$n_x = 0 \qquad \text{for } x \geq 0, \tag{228}$$

$$n_y = 1 \qquad \text{for } x \geq 0, \tag{229}$$

$$n_x = -\frac{x}{R+h_g} \qquad \text{for } x \in (x_L, 0), \tag{230}$$

$$n_y = \frac{\sqrt{(R+h_g)^2 - x^2}}{R+h_g} \qquad \text{for } x \in (x_L, 0), \tag{231}$$

$$n_x = 0 \qquad \text{for } x \leq x_L, \tag{232}$$

$$n_y = 1 \qquad \text{for } x \leq x_L, \tag{233}$$

on $y = h_1(x)$, with

$$h_1(x) = \begin{cases} 0 & \text{for } x \geq 0, \\ R + h_g - \sqrt{(R+h_g)^2 - x^2} & \text{for } x \in (x_L, 0), \\ d_c & \text{for } x \leq x_L, \end{cases} \tag{234}$$

$$h_2(x) = R + h_g - \sqrt{R^2 - x^2}, \tag{235}$$

$$h_\omega(x,y) = x^2 + (y - R - h_g)^2 - R^2, \tag{236}$$

$$x_L = -(R+h_g)\sqrt{1 - \left(1 - \frac{d_c}{R+h_g}\right)^2}. \tag{237}$$

As the geometry of this problem is the same as in Section 4.3, the nondimensionalisation and consequent stretching of variables in the inner region is the

same. The nondimensional, stretched variables in the inner region are therefore given by

$$u = V_\omega \bar{u}^\star, \tag{238}$$

$$v = \sqrt{\varepsilon} V_\omega \bar{v}^\star, \tag{239}$$

$$x = \sqrt{\varepsilon} R \bar{x}^\star, \tag{240}$$

$$y = \varepsilon R \bar{y}^\star, \tag{241}$$

$$p = \frac{\mu V_\omega}{\varepsilon \sqrt{\varepsilon} R} \bar{p}^\star, \tag{242}$$

$$t = \frac{R}{V_\omega} \bar{t}. \tag{243}$$

As we did in Section 4.3, we will separate the stretched inner region into three domains, $\bar{\Omega}_i^\star, i = 1, 2, 3$, and denote variables which belong to $\bar{\Omega}_i^\star$ by subscript i, e.g. $\bar{u}_i^\star$. The domains $\bar{\Omega}_i^\star, i = 1, 2, 3$, are given by (170)-(172), respectively.

Compared to the no-slip case, we have an extra parameter $\hat{\beta}$ in the problem due to the slip condition. Substituting in the variables given by (238)-(243), we find that at leading order the slip condition (220) becomes

$$\bar{u}_i^\star + 1 = -\frac{\hat{\beta}}{\varepsilon R} \frac{\partial \bar{u}_i^\star}{\partial \bar{y}^\star} \qquad \text{on } \bar{y}^\star = \bar{h}_2^\star(\bar{x}^\star), \tag{244}$$

$$\bar{v}_i^\star + \bar{x}^\star = -\frac{\hat{\beta}}{\varepsilon R} \bar{x}^\star \frac{\partial \bar{u}_i^\star}{\partial \bar{y}^\star} \qquad \text{on } \bar{y}^\star = \bar{h}_2^\star(\bar{x}^\star), \tag{245}$$

for $i = 1, 2, 3$, and (221) becomes

$$\bar{u}_1^\star = \frac{\hat{\beta}}{\varepsilon R}\frac{\partial \bar{u}_1^\star}{\partial \bar{y}^\star} \qquad \text{on } \bar{y}^\star = \bar{h}_1^\star(\bar{x}^\star),\ \bar{x}^\star \geq 0, \tag{246}$$

$$\bar{v}_1^\star = 0 \qquad \text{on } \bar{y}^\star = \bar{h}_1^\star(\bar{x}^\star),\ \bar{x}^\star \geq 0, \tag{247}$$

$$\bar{u}_2^\star = \frac{\hat{\beta}}{\varepsilon R}\frac{\partial \bar{u}_2^\star}{\partial \bar{y}^\star} \qquad \text{on } \bar{y}^\star = \bar{h}_1^\star(\bar{x}^\star),\ \bar{x}^\star \in (\bar{x}_L^\star, 0), \tag{248}$$

$$\bar{v}_2^\star = \frac{\hat{\beta}}{\varepsilon R}\bar{x}^\star\frac{\partial \bar{u}_2^\star}{\partial \bar{y}^\star} \qquad \text{on } \bar{y}^\star = \bar{h}_1^\star(\bar{x}^\star),\ \bar{x}^\star \in (\bar{x}_L^\star, 0), \tag{249}$$

$$\bar{u}_3^\star = \frac{\hat{\beta}}{\varepsilon R}\frac{\partial \bar{u}_3^\star}{\partial \bar{y}^\star} \qquad \text{on } \bar{y}^\star = \bar{h}_1^\star(\bar{x}^\star),\ \bar{x}^\star \leq \bar{x}_L^\star, \tag{250}$$

$$\bar{v}_3^\star = 0 \qquad \text{on } \bar{y}^\star = \bar{h}_1^\star(\bar{x}^\star),\ \bar{x}^\star \leq \bar{x}_L^\star. \tag{251}$$

The expressions for $\bar{h}_1^\star$, $\bar{h}_2^\star$ and $\bar{x}_L^\star$ are as before, and are given by (167), (168) and (169), respectively.

In order to account for the effects of slip on the leading order flow, we will introduce the nondimensional, stretched slip length

$$\bar{\hat{\beta}}^\star = \frac{\hat{\beta}}{\varepsilon R}, \tag{252}$$

with assumption (116) that $\bar{\hat{\beta}}^\star = O(1)$.

4.6 LEADING ORDER ANALYTICAL SOLUTIONS WITH SLIP

The nondimensional equations governing the flow in the inner region are given by

$$\frac{\partial \bar{u}_i^\star}{\partial \bar{x}^\star} + \frac{\partial \bar{v}_i^\star}{\partial \bar{y}^\star} = 0, \tag{253}$$

$$\frac{\partial \bar{p}_i^\star}{\partial \bar{x}^\star} = \frac{\partial^2 \bar{u}_i^\star}{\partial \bar{y}^{\star 2}}, \tag{254}$$

$$\frac{\partial \bar{p}_i^\star}{\partial \bar{y}^\star} = 0, \tag{255}$$

for $(x, y) \in \bar{\Omega}_i^\star$, subject to the boundary conditions

$$\bar{u}_i^\star + 1 = -\bar{\beta}^\star \frac{\partial \bar{u}_i^\star}{\partial \bar{y}^\star} \qquad \text{on } \bar{y}^\star = \bar{h}_2^\star(\bar{x}^\star), \tag{256}$$

$$\bar{v}_i^\star + \bar{x}^\star = -\bar{\beta}^\star \bar{x}^\star \frac{\partial \bar{u}_i^\star}{\partial \bar{y}^\star} \qquad \text{on } \bar{y}^\star = \bar{h}_2^\star(\bar{x}^\star), \tag{257}$$

for $i = 1, 2, 3$, and

$$\bar{u}_1^\star = \bar{\beta}^\star \frac{\partial \bar{u}_1^\star}{\partial \bar{y}^\star} \qquad \text{on } \bar{y}^\star = \bar{h}_1^\star(\bar{x}^\star),\ \bar{x}^\star \geq 0, \tag{258}$$

$$\bar{v}_1^\star = 0 \qquad \text{on } \bar{y}^\star = \bar{h}_1^\star(\bar{x}^\star),\ \bar{x}^\star \geq 0, \tag{259}$$

$$\bar{u}_2^\star = \bar{\beta}^\star \frac{\partial \bar{u}_2^\star}{\partial \bar{y}^\star} \qquad \text{on } \bar{y}^\star = \bar{h}_1^\star(\bar{x}^\star),\ \bar{x}^\star \in (\bar{x}_L^\star, 0), \tag{260}$$

$$\bar{v}_2^\star = \bar{\beta}^\star \bar{x}^\star \frac{\partial \bar{u}_2^\star}{\partial \bar{y}^\star} \qquad \text{on } \bar{y}^\star = \bar{h}_1^\star(\bar{x}^\star),\ \bar{x}^\star \in (\bar{x}_L^\star, 0), \tag{261}$$

$$\bar{u}_3^\star = \bar{\beta}^\star \frac{\partial \bar{u}_3^\star}{\partial \bar{y}^\star} \qquad \text{on } \bar{y}^\star = \bar{h}_1^\star(\bar{x}^\star),\ \bar{x}^\star \leq \bar{x}_L^\star, \tag{262}$$

$$\bar{v}_3^\star = 0 \qquad \text{on } \bar{y}^\star = \bar{h}_1^\star(\bar{x}^\star),\ \bar{x}^\star \leq \bar{x}_L^\star, \tag{263}$$

with matching conditions

$$\lim_{\bar{x}^\star \to -\infty} \bar{p}_3^\star = 0, \tag{264}$$

$$\lim_{\bar{x}^\star \to \infty} \bar{p}_1^\star = 0, \tag{265}$$

and continuity conditions

$$\bar{p}_1^\star = \bar{p}_2^\star \qquad \text{at } \bar{x}^\star = 0, \tag{266}$$

$$\bar{p}_2^\star = \bar{p}_3^\star \qquad \text{at } \bar{x}^\star = \bar{x}_L^\star, \tag{267}$$

where

$$\bar{h}_1^\star\left(\bar{x}^\star\right) = \begin{cases} 0 & \text{for } \bar{x}^\star \geq 0, \\ \frac{\bar{x}^{\star 2}}{2} & \text{for } \bar{x}^\star \in \left(\bar{x}_L^\star, 0\right), \\ \delta & \text{for } \bar{x}^\star \leq \bar{x}_L^\star, \end{cases} \tag{268}$$

$$\bar{h}_2^\star\left(\bar{x}^\star\right) = \frac{1}{2}\left(\bar{x}^{\star 2} + 2\right), \tag{269}$$

$$\bar{x}_L^\star = -\sqrt{2\delta}. \tag{270}$$

Following the same procedure as in Section 4.4, we can derive the expressions for the flux in all three regions to be

$$\int_{\bar{h}_1^\star(\bar{x}^\star)}^{\bar{h}_2^\star(\bar{x}^\star)} \bar{u}_1^\star \mathrm{d}\bar{y}^\star = -\frac{\bar{x}^{\star 2} + 2}{4} - \frac{\left[\bar{x}^{\star 2} + 2\left(1 + 6\bar{\tilde{\beta}}^\star\right)\right]\left(\bar{x}^{\star 2} + 2\right)^2}{96}\frac{\mathrm{d}\bar{p}_1^\star}{\mathrm{d}\bar{x}^\star}, \tag{271}$$

$$\int_{\bar{h}_1^\star(\bar{x}^\star)}^{\bar{h}_2^\star(\bar{x}^\star)} \bar{u}_2^\star \mathrm{d}\bar{y}^\star = -\frac{1}{2} - \frac{1 + 6\bar{\tilde{\beta}}^\star}{12}\frac{\mathrm{d}\bar{p}_2^\star}{\mathrm{d}\bar{x}^\star}, \tag{272}$$

$$\begin{aligned} \int_{\bar{h}_1^\star(\bar{x}^\star)}^{\bar{h}_2^\star(\bar{x}^\star)} \bar{u}_3^\star \mathrm{d}\bar{y}^\star = &-\frac{\bar{x}^{\star 2} + 2\left(1 - \delta\right)}{4} \\ &- \frac{\left[\bar{x}^{\star 2} + 2\left(1 + 6\bar{\tilde{\beta}}^\star - \delta\right)\right]\left[\bar{x}^{\star 2} + 2\left(1 - \delta\right)\right]^2}{96}\frac{\mathrm{d}\bar{p}_3^\star}{\mathrm{d}\bar{x}^\star}, \end{aligned} \tag{273}$$

where we can again separate the flux in region $\bar{\Omega}_i^\star$ into two components, a flux component due to shear, $\bar{Q}_{s,i}^\star$, and a flux component due to pressure gradient, $\bar{Q}_{p,i}^\star$, i.e.

$$\int_{\bar{h}_1^\star(\bar{x}^\star)}^{\bar{h}_2^\star(\bar{x}^\star)} \bar{u}_i^\star \mathrm{d}\bar{y}^\star = \bar{Q}_{s,i}^\star + \bar{Q}_{p,i}^\star = \bar{Q}^\star, \tag{274}$$

with

$$\bar{Q}^{\star}_{s,1} = -\frac{\bar{x}^{\star 2}+2}{4}, \tag{275}$$

$$\bar{Q}^{\star}_{p,1} = -\frac{\left[\bar{x}^{\star 2}+2\left(1+6\bar{\beta}^{\star}\right)\right]\left(\bar{x}^{\star 2}+2\right)^{2}}{96}\frac{\mathrm{d}\bar{p}^{\star}_{1}}{\mathrm{d}\bar{x}^{\star}}, \tag{276}$$

$$\bar{Q}^{\star}_{s,2} = -\frac{1}{2}, \tag{277}$$

$$\bar{Q}^{\star}_{p,2} = -\frac{1+6\bar{\beta}^{\star}}{12}\frac{\mathrm{d}\bar{p}^{\star}_{2}}{\mathrm{d}\bar{x}^{\star}}, \tag{278}$$

$$\bar{Q}^{\star}_{s,3} = -\frac{\bar{x}^{\star 2}+2\left(1-\delta\right)}{4}, \tag{279}$$

$$\bar{Q}^{\star}_{p,3} = -\frac{\left[\bar{x}^{\star 2}+2\left(1+6\bar{\beta}^{\star}-\delta\right)\right]\left[\bar{x}^{\star 2}+2\left(1-\delta\right)\right]^{2}}{96}\frac{\mathrm{d}\bar{p}^{\star}_{3}}{\mathrm{d}\bar{x}^{\star}}. \tag{280}$$

Comparing expressions (271)-(273) to those with the no-slip boundary condition (178)-(180), we can see that slip manifests itself in the flux component due to the pressure gradient. Meanwhile, the shear component is given by the same expression as in the no-slip case.

For brevity, we will skip some details of the derivation for the pressure solution as it is similar to the no-slip case in Section 4.4. Briefly, when (253) is integrated with respect to $\bar{y}^{\star}$ in each domain and (271)-(273) are substituted in, we can observe that there are now five (compared to the previous three) different regimes for δ we must consider in order to integrate the pressure derivative. These are

$$0 < \delta < 1, \tag{281}$$

$$\delta = 1, \tag{282}$$

$$1 < \delta < 1+6\bar{\beta}^{\star}, \tag{283}$$

$$\delta = 1+6\bar{\beta}^{\star}, \tag{284}$$

$$\delta > 1+6\bar{\beta}^{\star}. \tag{285}$$

In each case, the expressions for the flux, $\bar{Q}^{\star}$, and the constants of integration, $\bar{C}^{\star}_{1}, \bar{C}^{\star}_{2}, \bar{C}^{\star}_{3}$, are far too arduous to both present and attempt to understand.

Hence, we will only show the expression for the pressure solution. However, we will present plots of the flux in each regime in order to understand how the parameters affect the flux through the grinding zone.

4.6.1 *Solution for* $0 < \delta < 1$

In this case, the expression for $\bar{p}^\star$ in each region is given by

$$\begin{aligned}
\bar{p}_1^\star = &- \Bigg\{ 2\left(\bar{Q}^\star - 3\bar{\hat{\beta}}^\star\right)\left(\bar{x}^{\star 2}+2\right)\tan^{-1}\left(\frac{\bar{x}^\star}{\sqrt{2\left(1+6\bar{\hat{\beta}}^\star\right)}}\right) \\
&+ \sqrt{2\left(1+\bar{\hat{\beta}}^\star\right)}\Bigg(\sqrt{2}\left(3\bar{\hat{\beta}}^\star\left(1+\bar{Q}^\star\right)-\bar{Q}^\star\right)\left(\bar{x}^{\star 2}+2\right)\tan^{-1}\left(\frac{\bar{x}^\star}{\sqrt{2}}\right) \\
&+ 6\bar{\hat{\beta}}^\star\bar{Q}^\star\bar{x}^\star\Bigg)\Bigg\} \Big/ 3\bar{\hat{\beta}}^{\star 2}\sqrt{2\left(1+6\bar{\hat{\beta}}^\star\right)}\left(\bar{x}^{\star 2}+2\right) \\
&+ \bar{C}_1^\star,
\end{aligned} \tag{286}$$

$$\bar{p}_2^\star = -\frac{6\left(1+2\bar{Q}^\star\right)\bar{x}^\star}{1+6\bar{\hat{\beta}}^\star} + \bar{C}_2^\star, \tag{287}$$

$$\begin{aligned}
\bar{p}_3^\star = &- 2\Bigg\{\sqrt{2\left(1-\delta\right)}\left(1-\delta\right)\left(\bar{Q}^\star - 3\bar{\hat{\beta}}^\star\right)\left(\bar{x}^{\star 2}+2\left[1-\delta\right]\right) \\
&\times \tan^{-1}\left(\frac{\bar{x}^\star}{\sqrt{2\left(1+6\hat{\beta}-\delta\right)}}\right) + \sqrt{2\left(1+6\hat{\beta}-\delta\right)}\Bigg(\\
&\left(\bar{x}^{\star 2}+2\left[1-\delta\right]\right)\left(\delta\left(\bar{Q}^\star - 3\bar{\hat{\beta}}^\star\right)+3\bar{\hat{\beta}}^\star\left(1+\bar{Q}^\star\right)-\bar{Q}^\star\right)\tan^{-1}\left(\frac{\bar{x}^\star}{\sqrt{2\left(1-\delta\right)}}\right) \\
&+ 3\bar{\hat{\beta}}^\star\bar{Q}^\star\sqrt{2\left(1-\delta\right)}\bar{x}^\star\Bigg)\Bigg\} \\
&\Big/ 3\bar{\hat{\beta}}^{\star 2}\left(1-\delta\right)\sqrt{2\left(1-\delta\right)}\sqrt{2\left(1+6\bar{\hat{\beta}}^\star-\delta\right)}\left(\bar{x}^{\star 2}+2\left[1-\delta\right]\right) \\
&+ \bar{C}_3^\star.
\end{aligned} \tag{288}$$

4.6.2 *Solution for* $\delta = 1$

In this case, $\bar{p}_1^\star, \bar{p}_2^\star$ are given by (286), (287), respectively, and

$$\bar{p}_3^\star = -\frac{\sqrt{3}\left(\bar{Q}^\star - 3\bar{\beta}\right)\bar{x}^{\star 3}\tan^{-1}\left(\frac{\bar{x}^\star}{2\sqrt{3\bar{\beta}^\star}}\right) + 6\bar{Q}^\star\sqrt{\bar{\beta}^\star}\bar{x}^{\star 2} - 6\sqrt{\bar{\beta}^{\star 3}}\left(3\bar{x}^{\star 2} + 4\bar{Q}^\star\right)}{9\sqrt{\bar{\beta}^{\star 5}}\bar{x}^{\star 3}} + \bar{C}_3^\star. \tag{289}$$

4.6.3 *Solution for* $1 < \delta < 1 + 6\bar{\beta}^\star$

For $1 < \delta < 1 + 6\bar{\beta}^\star$, we note that

$$\left|\frac{\bar{x}^\star}{\sqrt{2\left(\delta - 1\right)}}\right| > 1$$

for $\bar{x}^\star < \bar{x}_L^\star$. In this case, $\bar{p}_1^\star, \bar{p}_2^\star$ are given by (286), (287), respectively, and

$$\begin{aligned}\bar{p}_3^\star = &-2\Bigg\{\sqrt{2\left(\delta-1\right)}\left(\delta-1\right)\left(\bar{Q}^\star - 3\bar{\beta}^\star\right)\left(\bar{x}^{\star 2} - 2\left[\delta - 1\right]\right) \\ &\times \tan^{-1}\left(\frac{\bar{x}^\star}{\sqrt{2\left(1 + 6\bar{\beta}^\star - \delta\right)}}\right) + \sqrt{2\left(1 + 6\bar{\beta}^\star - \delta\right)}\Bigg(\\ &\left(\bar{x}^{\star 2} - 2\left[\delta - 1\right]\right)\left(\delta\left(\bar{Q}^\star - 3\bar{\beta}^\star\right) + 3\bar{\beta}^\star\left(1 + \bar{Q}^\star\right) - \bar{Q}^\star\right) \\ &\times \coth^{-1}\left(\frac{\bar{x}^\star}{\sqrt{2\left(\delta-1\right)}}\right) - 3\bar{\beta}^\star\bar{Q}^\star\sqrt{2\left(\delta-1\right)}\bar{x}^\star\Bigg)\Bigg\} \\ &\Big/ 3\bar{\beta}^{\star 2}\left(\delta-1\right)\sqrt{2\left(\delta-1\right)}\sqrt{2\left(1 + 6\bar{\beta}^\star - \delta\right)}\left(\bar{x}^{\star 2} - 2\left[\delta - 1\right]\right) \\ &+ \bar{C}_3^\star.\end{aligned} \tag{290}$$

4.6.4 *Solution for* $\delta = 1 + 6\bar{\beta}^\star$

For $\delta = 1 + 6\bar{\beta}^\star$, we note that

$$\left| \frac{\bar{x}^\star}{2\sqrt{3\bar{\beta}^\star}} \right| > 1$$

for $\bar{x}^\star < \bar{x}_L^\star$. In this case, $\bar{p}_1^\star, \bar{p}_2^\star$ are given by (286), (287), respectively, and

$$\begin{aligned} \bar{p}_3^\star = & \Bigg\{ 6\bar{Q}^\star \sqrt{\bar{\beta}^\star} \bar{x}^{\star 2} + 12\sqrt{\bar{\beta}^{\star 3}} \left(12\bar{\beta}^\star - \left[\bar{x}^{\star 2} + 4\bar{Q}^\star \right] \right) \\ & + \sqrt{3} \left(\bar{Q}^\star - 2\bar{\beta}^\star \right) \bar{x}^\star \left(\bar{x}^{\star 2} - 12\bar{\beta}^\star \right) \coth^{-1} \left(\frac{\bar{x}^\star}{2\sqrt{3\bar{\beta}^\star}} \right) \Bigg\} \\ & \Big/ 6\sqrt{\bar{\beta}^{\star 5}} \bar{x}^\star \left(12\bar{\beta}^\star - \bar{x}^{\star 2} \right) \\ & + \bar{C}_3^\star. \end{aligned} \tag{291}$$

4.6.5 *Solution for* $\delta > 1 + 6\bar{\beta}^\star$

For $\delta > 1 + 6\bar{\beta}^\star$, we note that

$$\left| \frac{\bar{x}^\star}{\sqrt{2\left(\delta - 1\right)}} \right| > 1,$$

$$\left| \frac{\bar{x}^\star}{\sqrt{2\left[\delta - \left(1 + \bar{\beta}^\star\right)\right]}} \right| > 1$$

for $\bar{x}^\star < \bar{x}_L^\star$. In this case, $\bar{p}_1^\star, \bar{p}_2^\star$ are given by (286), (287), respectively, and

$$\begin{aligned}\bar{p}_3^\star = 2\Bigg\{ & \sqrt{2\left(\delta-1\right)}\left(\delta-1\right)\left(\bar{Q}^\star - 3\bar{\bar{\beta}}^\star\right)\left[\bar{x}^{\star 2} - 2\left(\delta-1\right)\right] \\ & \times \coth^{-1}\left(\frac{\bar{x}^\star}{\sqrt{2\left[\delta-\left(1+\bar{\bar{\beta}}^\star\right)\right]}}\right) - \sqrt{2\left[\delta-\left(1+\bar{\bar{\beta}}^\star\right)\right]}\Bigg(\\ & \left[\bar{x}^{\star 2} - 2\left(\delta-1\right)\right]\left(\delta\left(\bar{Q}^\star - 3\bar{\bar{\beta}}^\star\right) + 3\bar{\bar{\beta}}^\star\left(1+\bar{Q}^\star\right) - \bar{Q}^\star\right) \\ & \times \coth^{-1}\left(\frac{\bar{x}^\star}{\sqrt{2\left(\delta-1\right)}}\right) - 3\bar{\bar{\beta}}^\star\bar{Q}^\star\sqrt{2\left(\delta-1\right)}\bar{x}^\star\Bigg)\Bigg\} \\ & \Bigg/ 3\bar{\bar{\beta}}^{\star 2}\left(\delta-1\right)\sqrt{2\left(\delta-1\right)}\sqrt{2\left[\delta-\left(1+\bar{\bar{\beta}}^\star\right)\right]}\left[\bar{x}^{\star 2} - 2\left(\delta-1\right)\right] \\ & + \bar{C}_3^\star.\end{aligned} \tag{292}$$

4.6.6 *Slip Solution Discussion*

Looking at the expressions for the pressure solution given by (286)-(292), we observe similarities with the pressure solution in the no-slip case given by (192)-(194), (198) and (203). Specifically, the solutions comprise of a mixture of rational polynomials with inverse trigonometric and inverse hyperbolic functions. The pressure in the grinding zone, $\bar{p}_2^\star$, is still given by a linear polynomial.

In figure 22, we plot the pressure solution across the inner region, $\bar{p}^\star$, for various values of δ and $\bar{\bar{\beta}}^\star$. For each value of δ shown, the solution converges to the no-slip solution, represented by the red dotted line, in the limit $\bar{\bar{\beta}}^\star \to 0$. In contrast, the graphs suggest that as $\bar{\bar{\beta}}^\star$ increases, the magnitude of the pressure solution decreases at every point in the inner region and eventually in the limit $\bar{\bar{\beta}}^\star \to \infty$, $\bar{p}^\star \to 0$. This can be verified by taking the limit as $\bar{\bar{\beta}}^\star \to \infty$ of $\bar{p}^\star$ in each of the five regimes (281)-(285), where we see that

$$\lim_{\bar{\bar{\beta}}^\star \to \infty} \bar{p}^\star = 0. \tag{293}$$

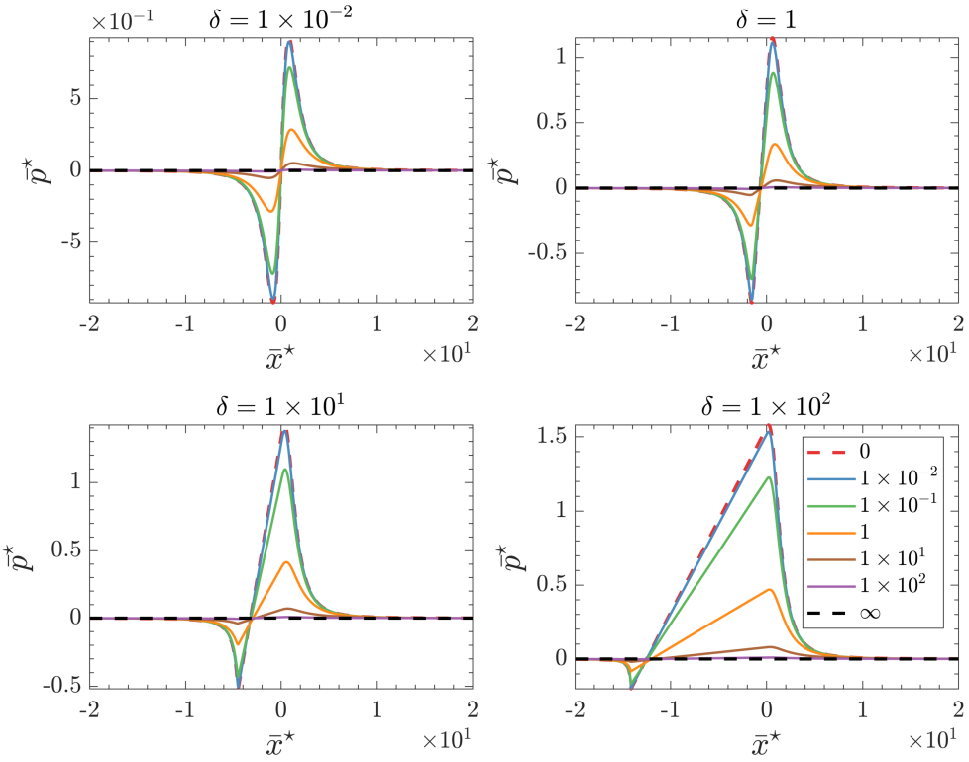

Figure 22: Plot of the pressure distribution, $\bar{p}^\star$, along the inner region for different values of δ, shown in the title. The legend corresponds to the value of $\bar{\beta}^\star$ in the slip regime.

In figure 23, we plot the derivative of the pressure solution, $\frac{\mathrm{d}\bar{p}^\star}{\mathrm{d}\bar{x}^\star}$, for various values of δ and $\bar{\beta}^\star$. We observe the same behaviour of the pressure derivative across all values of δ with regard to changing $\bar{\beta}^\star$. Namely, as $\bar{\beta}^\star$ increases, the magnitude of the pressure derivative decreases at every point. Similarly, we can show that in each regime

$$\lim_{\bar{\beta}^\star \to \infty} \frac{\mathrm{d}\bar{p}^\star}{\mathrm{d}\bar{x}^\star} = 0. \tag{294}$$

In figure 24, we plot the flux, $\bar{Q}^\star$, as a function of δ for various values of $\bar{\beta}^\star$. We immediately observe that for increasing $\bar{\beta}^\star$ there is an increase in $\bar{Q}^\star$,

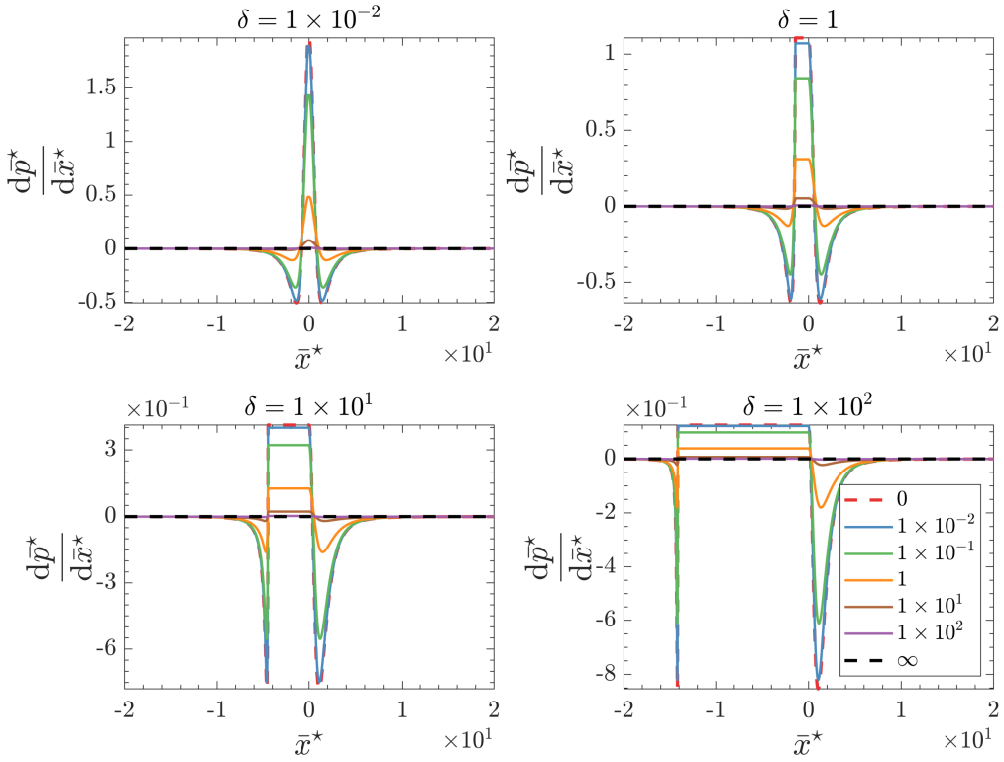

Figure 23: Plot of the pressure distribution, $\frac{d\bar{p}^\star}{d\bar{x}^\star}$, along the inner region for different values of δ, shown in the title. The legend corresponds to the value of $\bar{\beta}^\star$ in the slip regime.

despite figure 23 showing a decrease in the pressure derivative. Additionally, we can show that the maximum flux across all regimes is given by

$$\lim_{\substack{\delta \to 0 \\ \bar{\beta}^\star \to \infty}} \bar{Q}^\star = 1, \tag{295}$$

which occurs when there is full slip at both surfaces with a much smaller depth of cut in the workpiece relative to the separation distance between the grinding wheel and the workpiece.

In figure 25, we plot the fraction of the flux component due to pressure gradient, $\bar{Q}_p^\star$, and shear effects, $\bar{Q}_s^\star$. Focusing on the grinding zone domain, we see from the graphs that increasing $\bar{\beta}^\star$ leads to an increase in $\bar{Q}_{p,2}^\star$ relative to $\bar{Q}_{s,2}^\star$. This is surprising given the observations of figure 23. However, we recall from the fluxes given by (271)-(273) that in the slip regime there is a factor

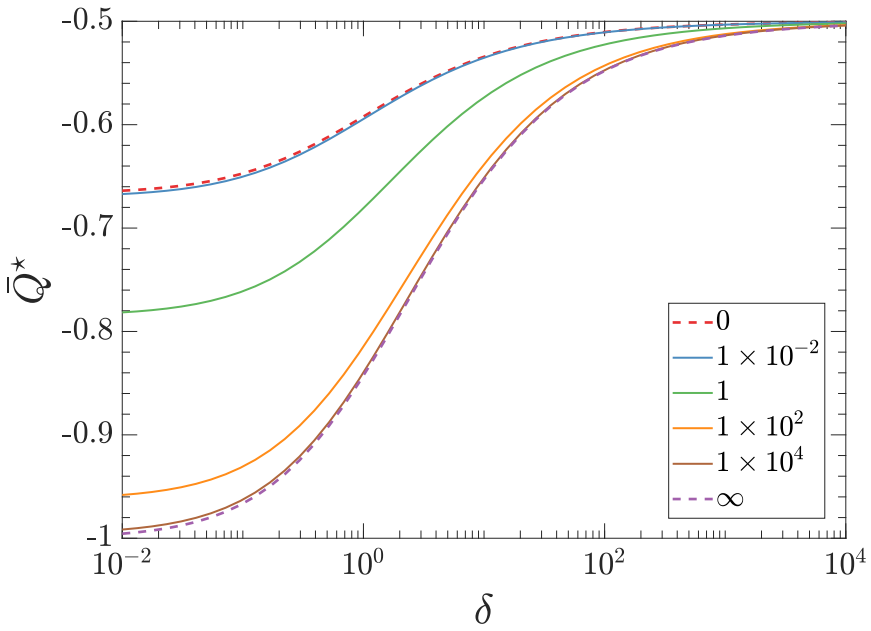

Figure 24: Plot of the flow rate, $\bar{Q}^\star$, as a function of δ. The legend corresponds to the value of $\bar{\bar{\beta}}^\star$ in the slip regime.

in the coefficient of the pressure derivative which involves $\bar{\bar{\beta}}^\star$. This tends to infinity as $\bar{\bar{\beta}}^\star \to \infty$, balancing the pressure derivative as it tends to 0.

We can calculate a simplified expression for $\frac{\bar{Q}^\star_{p,2}}{\bar{Q}^\star_{s,2}}$ as

$$\frac{\bar{Q}^\star_{p,2}}{\bar{Q}^\star_{s,2}} = -\left(1 + 2\bar{Q}^\star\right), \tag{296}$$

using (272) and (287). Expression (296) highlights the constant flux component fraction in the grinding zone, and using (188) we can calculate the fraction of the flux that is attributable to shear effects. In figure 26, we plot this as $\frac{\bar{Q}^\star_s}{\bar{Q}^\star}$ against $\bar{x}^\star$ in the grinding zone, i.e. $\bar{x}^\star \in (\bar{x}^\star_L, 0)$. In figure 27, we similarly plot the fraction of the flux that is attributable to the pressure gradient, $\frac{\bar{Q}^\star_p}{\bar{Q}^\star}$.

As we see from the plots, it is only in the small-δ, high-$\bar{\bar{\beta}}^\star$ regime where there is an equal contribution to the flux from both pressure gradient and shear effects. Outside of this regime, the flow is predominantly driven by the shearing of the

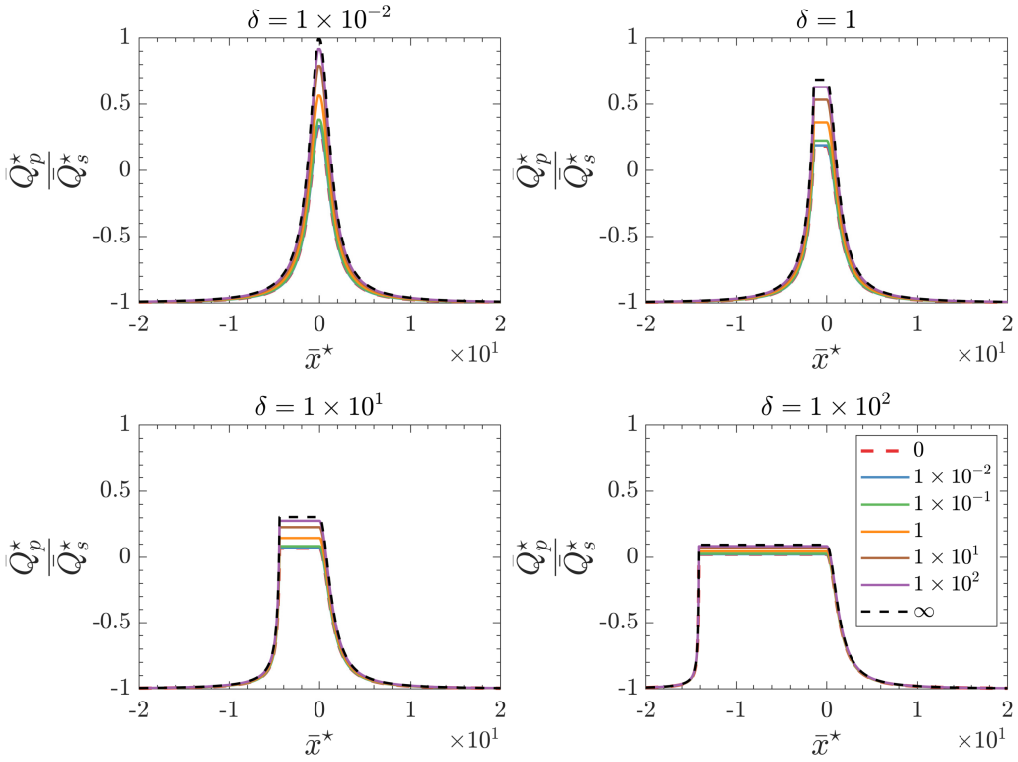

Figure 25: Plot of the flow rate fraction, $\frac{\bar{Q}_p^\star}{\bar{Q}_s^\star}$, along the inner region for different values of δ, shown in the title. The legend corresponds to the value of $\bar{\tilde{\beta}}^\star$ in the slip regime.

grinding wheel. To support this, let us consider our typical surface grinding regime with

$$\begin{aligned} \delta &= 2, \\ \bar{\tilde{\beta}}^\star &= 1 \times 10^{-3}, \end{aligned} \tag{297}$$

and creep-feed grinding regime with

$$\begin{aligned} \delta &= 4.8, \\ \bar{\tilde{\beta}}^\star &= 2 \times 10^{-5}, \end{aligned} \tag{298}$$

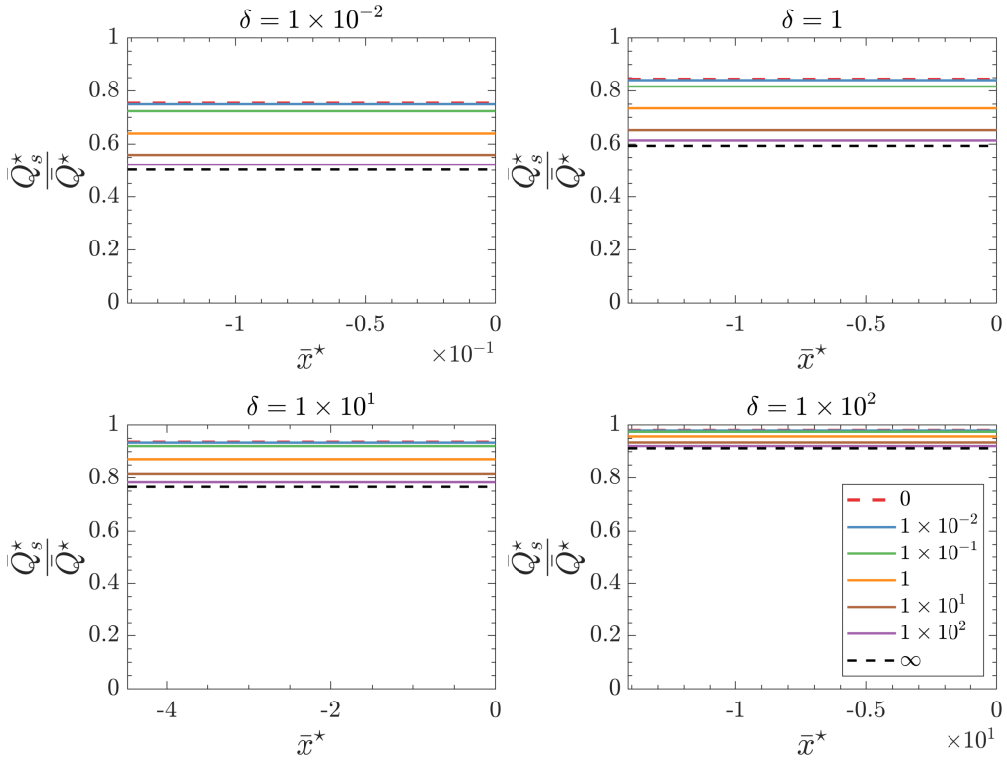

Figure 26: Plot of the fraction of flux attributable to shear effects, $\frac{\bar{Q}_s^\star}{\bar{Q}^\star}$, along the grinding zone for different values of δ, shown in the title. The legend corresponds to the value of $\bar{\beta}^\star$ in the slip regime.

where we have used the values presented in Section 4.1. As we did in Subsection 4.4.4, we can calculate that

$$\frac{\bar{Q}_{p,2}^\star}{\bar{Q}_{s,2}^\star} \approx 1.44 \times 10^{-1} \tag{299}$$

for the surface grinding regime characterised by (297), and

$$\frac{\bar{Q}_{p,2}^\star}{\bar{Q}_{s,2}^\star} \approx 1.04 \times 10^{-1} \tag{300}$$

for the creep-feed grinding regime characterised by (298). We can then calculate the percentages of the flux attributable to the pressure gradient and shear effects. In the surface grinding regime (297), the pressure gradient and shear effects contribute to 13% and 87% of the flux, respectively. In the creep-feed

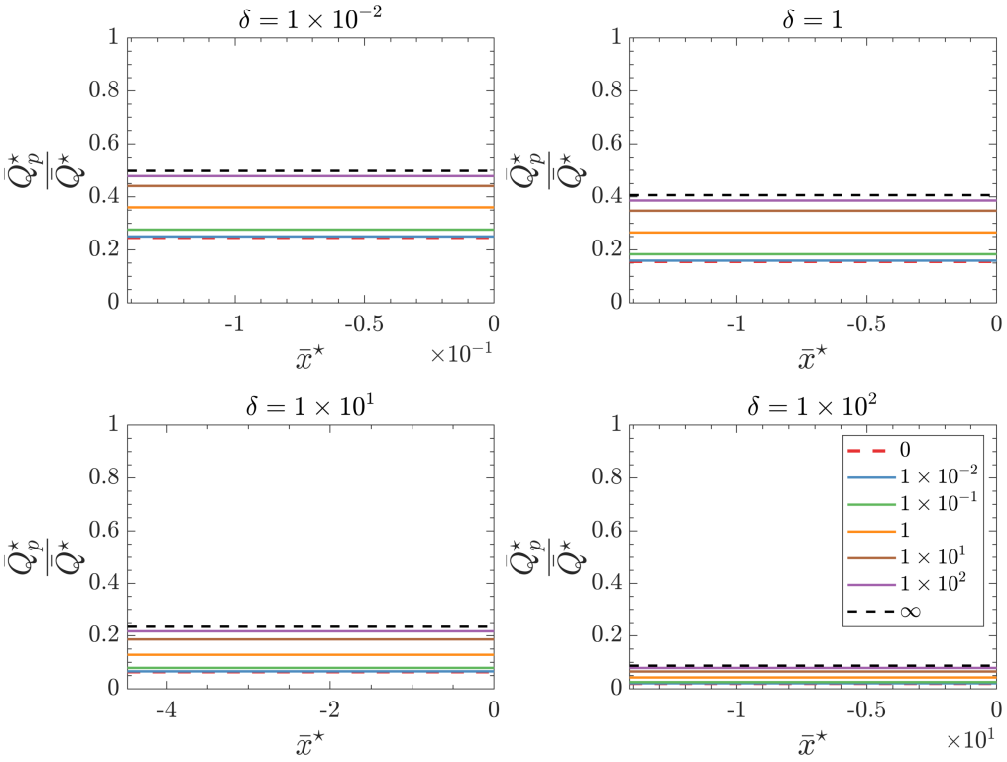

Figure 27: Plot of the fraction of flux attributable to the pressure gradient, $\frac{\bar{Q}_p^\star}{\bar{Q}^\star}$, along the grinding zone for different values of δ, shown in the title. The legend corresponds to the value of $\bar{\beta}^\star$ in the slip regime.

grinding regime (298), the pressure gradient and shear effects contribute to 9% and 91% of the flux, respectively.

4.7 CONCLUSION

In this chapter, we have studied the flow during grinding in a geometry where the depth of cut is modelled. We have seen that by following the same procedure as we did in Chapter 3, we can derive a solution for the flow in the grinding zone without needing to solve for the flow far from the grinding zone.

By considering typical values for surface and creep-feed grinding regimes, we saw that in both regimes $\delta = O(1)$, shown in (109) and (110), respectively. We were able to distinguish for both the no-slip and slip problems, three and five δ regimes, given by (189)-(191) and (281)-(285), respectively. In each case, we

were able to calculate the leading order analytical solution for the pressure near the grinding zone. This was done without the need of prescribing artificial or empirical boundary conditions, which is the current approach in the literature when applying the lubrication approximation to the flow in the grinding zone.

In the no-slip case, we observed that for a given δ, the pressure derivative along the grinding zone was constant. Consequently, the flux components due to shear effects and pressure gradient in the grinding zone, given by (184) and (185), respectively, were constant. We took typical values of δ in surface and creep-feed grinding regimes, specified by (109) and (110), respectively, and calculated the contribution of each flux component to the flux across the grinding zone. We found that in both regimes, the transport of the grinding fluid is primarily caused by the shearing of the grinding wheel, rather than the pressure gradient across the grinding zone. These values are shown in (216) and (217) for our surface and creep-feed grinding values, respectively.

In the slip case, we saw the same constant behaviour of the pressure derivative along the grinding zone as in the no-slip case, for a given δ and $\bar{\beta}^\star$. We also observed the dominance of shear effects on the transport of the grinding fluid for the typical surface and creep-feed grinding regimes we considered, with these regimes characterised by the parameters in (297) and (298).

We noticed that the predicted flux through the grinding zone increased with $\bar{\beta}^\star$. This suggests that grinding fluids which exhibit larger degrees of slip in the grinding zone are favourable from the perspective of maximising the advection of the grinding fluid through the grinding zone. There are many studies which support the mixing of additives such as nanoparticles in the grinding fluid to reduce the friction experienced by the abrasives and workpiece. See, for example, [26] showing that this results in reduced wear of the abrasives. However, there is no study to the author's knowledge which investigates how such additives affect the slip length of the grinding fluid at the surfaces, and the result this has on the flux through the grinding zone.

5

HOMOGENISATION OF THE GRINDING ZONE FLOW

5.1 INTRODUCTION

Frequently in lubrication processes, problems are encountered which involve a small, repeatable structure, on the microscale over a distinct, larger domain, the macroscale. Directly approaching these problems from the view of only the macroscale can result in an insufficient description of the problem: notably, intractable equations and highly oscillating coefficients cause issues, from loss of accuracy to costly numerics, which arise when attempting to find a solution.

Classically, these problems have been analysed using the concept of a representative volume element (RVE), where a small volume encompassing the periodic structure is defined and averaged over [69]. The result is a set of microscopic problems whose solution defines the so-called flow factors: these flow factors appear in the macroscale problem and it is through these variables that the (geometrically-simplified) macroscale problem is fed information from the (geometrically-complex) microscale. However, such approaches are heavily empirical by design.

Recently, the more rigorous approach of asymptotic homogenisation has been applied to these problems. The physical motivation of such studies has typically been in bearing applications, with two-scale asymptotic homogenisation previously being applied to study equations which arise in these lubrication problems; see, for example, [10], [11], [16] and [44].

The motivation for applying asymptotic homogenisation to the flow during grinding is the unsuitability of the lubrication approximation when applied to problems with steep gradients in the geometry, see, for example, [17] or [86]. Due to how grinding wheels are formed, the abrasives of the grinding wheel are expected to always have $O(1)$ slopes. This is far above the range where the lubrication approximation is generally valid.

In this chapter, we look to discover how the transport of grinding fluid through the grinding zone is affected by aspects of the abrasive profile. One aspect we will focus on is whether the angle that the abrasives are aligned on the grinding wheel has an effect on the direction of flow. Understanding this factor could drive cost-efficient optimisations in the manufacture of grinding wheels.

We will begin with a short introduction to the two-scale asymptotic homogenisation method and highlight some previous applications of this in the literature. We will then apply this technique to our problem of the grinding zone flow, considering exclusively the Trizact$^{\text{TM}}$ abrasive profile which we introduced in Section 2.4. For the grinding zone flow here, we return to the original mixture model given by (14)-(21).

As we will discover, by considering both the homogenisation and lubrication limits over the grinding zone in a cylindrical coordinate system, the derived equations deviate from the standard lubrication equations. This is due to extra, lower order curvature terms appearing from the continuity equation. After deriving the coupled local and global problems (for the microscopic abrasive length scale and macroscopic grinding zone length scale, respectively), we investigate numerical solutions to this system over different experimental parameters.

5.2 TWO-SCALE HOMOGENISATION

In nature, a wide variety of media display heterogeneities on a scale much smaller than the size of the medium itself. Certain applications require that

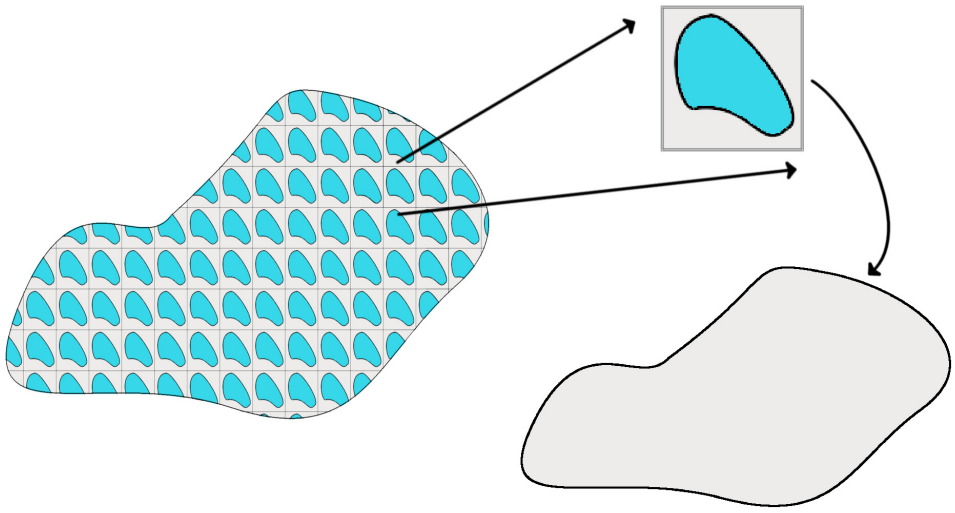

Figure 28: Illustration of the homogenisation procedure for a periodic medium. The problem is first considered over a periodic cell in the real domain, indicated by the two centre arrows. This microscopic system is then upscaled into some averaged domain of the original, where the periodicities have been replaced by some representative behaviour, indicated by the right arrow.

information about these small-scale heterogeneities be retained. For example, the cell make-up heterogeneities present in cancerous tumours are one of the difficulties faced in the treatment of these tumours; ignoring these heterogeneities can have catastrophic consequences on the health of a patient [61]. However, it is often the case that such detailed information of these heterogeneities is not necessary: rather, only the macroscopic manifestation of them is of interest. Homogenisation is the process of obtaining this macroscopic manifestation of the microscopic information.

Beginning at the (often periodic) microscale, a description of the problem there is sought. From here, the problem is built upon by using the solutions of the problem(s) on the microscale to derive the problem on the macroscale, the solution of which would give the average (homogenised) behaviour of the system, see figure 28. There are multiple possible methods to achieve this but given that we are dealing with a periodic geometry, we choose here to follow the two-scale asymptotic expansion method.

To consider the two-scale homogenisation method more meticulously, we start by introducing the general problem. Let Ω_ϵ be a domain representing some medium which admits a region comprised of periodic structures, with ϵ denoting the ratio of the period of these structures to the size of the medium. We wish to find u_ϵ in an appropriately defined function space such that

$$\mathcal{L}u_\epsilon = f \text{ in } \Omega_\epsilon, \tag{301}$$

where f is defined on Ω_ϵ and $\mathcal{L}$ is a differential operator.

For many physical problems, ϵ can be 1×10^{-3} or less. As briefly described in the introduction, this causes many problems to be intractable. However, we observe that for each distinct ϵ, we will have solution u_ϵ for our system. We expect that for ϵ sufficiently small, the sequence of these solutions converges to some u as $\epsilon \to 0$. Hence, our goal is to obtain this u without solving (301) for arbitrarily small ϵ. To this end, we wish to find an operator $\mathcal{H}$ such that this u satisfies

$$\mathcal{H}u = f \text{ in } \Omega, \tag{302}$$

where Ω is the domain Ω_ϵ with the periodic structures replaced by some representative smoothed region.

Generally in porous media flows, the system is described in three dimensional space by three Cartesian coordinates $\boldsymbol{x} = (x_1, x_2, x_3)$ with the periodic pores aligned with the coordinate system, $\boldsymbol{x}$. In the two-scale method, a new set of Cartesian coordinates $\boldsymbol{X} = (x_1, x_2, x_3)$ are introduced, with the condition of periodicity on $\boldsymbol{X}$ as $(0, \epsilon)^3$. These coordinates are referred to as the microscopic coordinates and one period in a microscopic coordinate corresponds to the wavelength of the periodic structure in that coordinate direction. It is then

supposed that u_ϵ is equal to some function u of the macroscopic coordinates and the scaled coordinates $\frac{\boldsymbol{X}}{\epsilon}$, i.e.

$$u_\epsilon(\boldsymbol{x}) = u\left(\boldsymbol{x}, \frac{\boldsymbol{X}}{\epsilon}\right). \tag{303}$$

The aim is to capture the behaviour of the system as $\epsilon \to 0$. The first step is replacing u in (301) with the asymptotic expansion

$$u_\epsilon = \sum_{i=0}^{\infty} \epsilon^i u_i\left(\boldsymbol{x}, \frac{\boldsymbol{X}}{\epsilon}\right). \tag{304}$$

Due to the change of variables introduced in (303), the chain rule must be used on differential operators. For example, in the case of the gradient operator acting on u_ϵ we have that

$$\nabla u_\epsilon = \sum_{i=0}^{\infty} \epsilon^i \nabla_{\boldsymbol{x}} u_i + \epsilon^{i-1} \nabla_{\boldsymbol{X}} u_i, \tag{305}$$

using (304), where the subscript denotes the gradient being taken with respect to that set of variables.

In contrast, for the flow during grinding the periodic coordinates are no longer given by a set of three periodic coordinates in three dimensional space. Instead, there are only 2 periodic coordinates, e.g. $\boldsymbol{X} = (x_1, x_2)$. There is a third microscopic coordinate, x_3, but this does not have the condition of periodicity due to the single layer of abrasives between the grinding wheel and the workpiece in the grinding zone. Instead of (303), we then assume

$$u_\epsilon(\boldsymbol{x}) = u\left(\hat{\boldsymbol{x}}, \frac{x_3}{\epsilon}, \frac{\boldsymbol{X}}{\epsilon}\right), \tag{306}$$

where $\hat{\boldsymbol{x}} = (x_1, x_2)$ and x_3 is scaled by ϵ with

$$\frac{x_3}{\epsilon} = O(1) \tag{307}$$

in the unit cell. Differential operators must also be expanded out in this case via the chain rule, similar to (305).

The next step is to consider the leading order terms in ϵ of (301). After defining and applying a suitable averaging operator over the periodicities, we arrive at the homogenised system (302), known as the global problem. Along with the global problem is a problem for the flow over an individual periodic cell, known as the local problem (or cell problem). The average of the local problem's solution is typically involved in the global problem, where the average ensures small-scale perturbations not seen on the global scale are smoothed out. Note that it is not necessarily the case that the global problem and local problem(s) can be posed independently; rather, it is the form of the original system which determines whether these will be independently closed systems or not. A widely known example of a global problem is Darcy's law in two dimensional porous media flow,

$$\boldsymbol{u} = -\boldsymbol{A} \cdot \nabla_{\boldsymbol{x}} p, \tag{308}$$

$$\nabla_{\boldsymbol{x}} \cdot \boldsymbol{u} = 0, \tag{309}$$

where $\boldsymbol{A}$ is the effective permeability tensor formed by averages over the unit cell, Y, of the local solutions to the local problems

$$\nabla_{\boldsymbol{X}} \gamma_i - \nabla^2_{\boldsymbol{X}} \boldsymbol{w}_i = \boldsymbol{e}_i, \tag{310}$$

$$\nabla_{\boldsymbol{X}} \cdot \boldsymbol{w}_i = 0, \tag{311}$$

for $i = 1, 2$, which is complemented by periodic boundary conditions on the sides of the unit cell.

Before proceeding, we make a few remarks on what we have studied in this chapter so far. It is neither true that there can only be two distinct scales, nor that the underlying physical problem needs to exhibit traces of periodicity: in the context of the finite element method, Allaire et al. [8] use a previously-known homogenisation result in order to separate an elliptic partial differential

equation with oscillating coefficients into a local (element) problem and a global problem defined over a coarse mesh. By solving each of the local problems, they show that the basis functions of the coarse mesh can be defined, using the local solutions, such that the size of the elements need not be necessarily smaller than the wavelength of oscillations in order to obtain suitable convergence of the global problem to the true solution. Further, it is not necessarily true that the solution to the homogenised system we arrive at after assuming the initial asymptotic expansion (304), and subsequent analysis, is the solution to (301) in the limit $\epsilon \to 0$ (should one exist at all). To do this for the first two terms of the expansion typically follows the energy method of Tartar [85], which we emphasise can also be used to derive the homogenised problem for non-periodic problems also. However, other methods exist in the context of periodic problems which can be used to derive and prove convergence results for the homogenised problem [7].

We remark that a similar problem has been studied in the literature before. Fabricius et al. [31] considered the two-scale homogenisation of single-phase Stokes flow in two dimensions where one boundary is given by an oscillating, $O(1)$ slope profile. The novelty of our work comes from our treatment of the multiphase equations and the application. We will see in Section 5.6 that while the form of the homogenised system is the same as found by Fabricius et al., the coordinate system we work in results in extra curvature correction-like terms due to the curvature of the grinding zone.

In the following section, we will elucidate the abstract explanation of the procedure by performing two-scale homogenisation on a periodic multiphase Stokes system.

5.3 PROBLEM INTRODUCTION

In Chapter 4, we saw that for the typical surface and creep-feed grinding regimes we considered there, the flow in the grinding zone was predominantly driven by the shearing of the grinding wheel. In this chapter, we will only consider the

flow domain to be the grinding zone. We denote the density, ρ, and dynamic viscosity, μ, of the grinding fluid and air phase by subscript l and g, respectively, in two-phase flows. We will consider a variety of different parameter values to reflect the vast parameter space that occurs in the flow during grinding. In particular, we will consider two variants of grinding fluid: a high viscosity lubricant and a low viscosity coolant. For the high viscosity lubricant, we consider rheological values around

$$\begin{aligned} \rho_l &= 9 \times 10^2 \text{ kg m}^{-3}, \\ \mu_l &= 1.53 \times 10^{-2} \text{ kg s m}^{-1}. \end{aligned} \tag{312}$$

For the low viscosity coolant, we consider rheological values around

$$\begin{aligned} \rho_l &= 8 \times 10^2 \text{ kg m}^{-3}, \\ \mu_l &= 2 \times 10^{-4} \text{ kg s m}^{-1}. \end{aligned} \tag{313}$$

For the air phase, we consider rheological values around

$$\rho_g = 1.13 \text{ kg m}^{-3}, \tag{314}$$

$$\mu_g = 1.92 \times 10^{-5} \text{ kg s m}^{-1}. \tag{315}$$

These values should be viewed as guidelines. Particularly, these fixed characteristic values can not reflect the reality of the flow which can have an extreme range of temperatures and rheological parameters for the fluids.

As in previous chapters, we denote the gap size between the grinding wheel and the workpiece as h_g, and we take this to be the size of an abrasive, i.e. the distance from base to peak. The radius of the grinding wheel is denoted by R. We will consider the three dimensional problem in this chapter, therefore we denote the width of the grinding wheel by h_w. We take the typical values

$$\begin{aligned} R &= 2 \times 10^{-1} \text{ m}, \\ h_w &= 2 \times 10^{-2} \text{ m}. \end{aligned} \tag{316}$$

The speed of the grinding wheel is denoted by V_ω. We introduce the microscopic Reynolds number Re_i associated with the flow over the microscale, i.e. the flow around an abrasive, as

$$\mathrm{Re}_i = \frac{\rho_l V_\omega h_g}{\mu_l}, \tag{317}$$

which is defined using the rheology of the grinding fluid. We note that

$$\mathrm{Re}_i = \varepsilon \mathrm{Re}, \tag{318}$$

where Re is defined by (48) and ε is defined by (50). Recalling assumption (53) that

$$\mathrm{Re} = O\left(\varepsilon^{-1}\right), \tag{319}$$

we have

$$\mathrm{Re}_i = O\left(1\right). \tag{320}$$

The abrasives we focus on in this chapter are Trizact$^{\mathrm{TM}}$ abrasives. We refer the reader back to Section 2.4 for more information on these abrasives. We denote the size of a Trizact$^{\mathrm{TM}}$ abrasive by d. In industry, the finest size used is 4×10^{-5} m and the coarsest size is 7.5×10^{-4} m. By definition of h_g and d,

$$h_g = \frac{d}{2}. \tag{321}$$

For a typical surface and creep-feed grinding regime, we have $d = 6 \times 10^{-5}$ m and $d = 4 \times 10^{-4}$ m, respectively. We take data from table 1 to calculate that in a: surface grinding regime

$$\varepsilon = 1.5 \times 10^{-4}, \tag{322}$$

$$\gamma = 1 \times 10^{-4}, \tag{323}$$

$$\delta = \frac{2}{3}, \tag{324}$$

where for a high viscosity lubricant and low viscosity coolant

$$\mathrm{Re}_i = 3.53 \times 10^{1}, \tag{325}$$

$$\mathrm{Re}_i = 2.4 \times 10^{3}, \tag{326}$$

respectively; creep-feed grinding regime

$$\varepsilon = 1 \times 10^{-3}, \tag{327}$$

$$\gamma = 1.2 \times 10^{-2}, \tag{328}$$

$$\delta = 1.2 \times 10^{1}, \tag{329}$$

where for a high viscosity lubricant and low viscosity coolant

$$\mathrm{Re}_i = 4.11 \times 10^{2}, \tag{330}$$

$$\mathrm{Re}_i = 2.8 \times 10^{4}, \tag{331}$$

respectively. We recall from (108) and (112) the definitions of γ and δ, respectively.

We see from (326) and (331) that assumption (320) is violated in certain grinding regimes. In fact, the flow around an individual abrasive is likely to be highly turbulent for low viscosity coolants. Despite this, we will continue under assumption (320) as there are still regimes, particularly with high viscosity lubricants in surface grinding, that this is true.

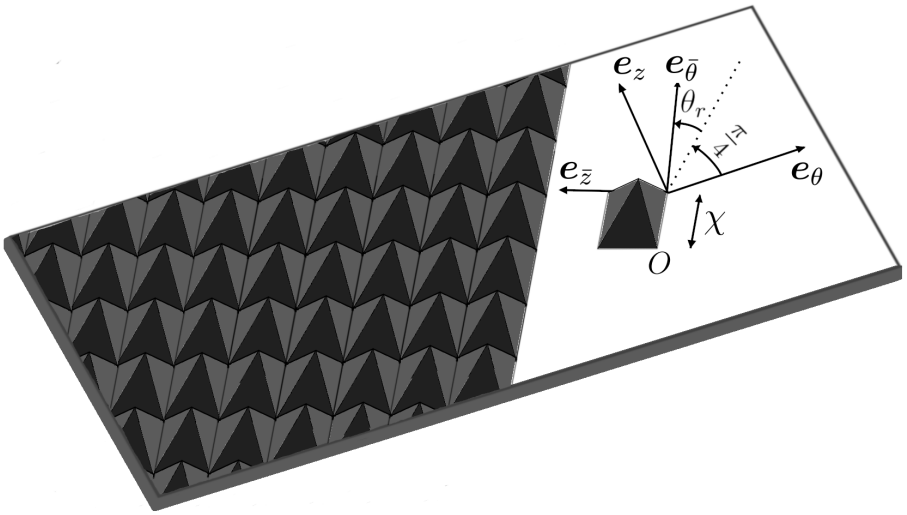

Figure 29: Illustration of the Trizact$^{\text{TM}}$ abrasive profile and microscopic coordinates. The abrasives are regular pyramids which protrude away from the substrate. Here, $\boldsymbol{e}_{\bar{\theta}}$ and $\boldsymbol{e}_{\bar{z}}$ are basis vectors that are parallel to the edges of the pyramid's base.

Looking at the values of δ in (324) and (329), we observe from figure 21 that they are both large enough that we are in the regime where the solutions under the lubrication approximation predict that the flow is dominantly driven by the shearing of the grinding wheel. Based on this, we will make the simplifying assumption in this chapter that the effect of the pressure difference across the grinding zone on the flow is negligible enough to consider homogeneous pressure at the entrance and exit of the grinding zone. That is, we assume there is no imposed pressure gradient due to a pressure difference at the ends of the grinding zone which drives the flow through it as in, for example, Poiseuille flow through a pipe. We assume the boundaries on the sides of the grinding zone are connected to the atmosphere and take homogeneous pressure there also.

In figure 29, we illustrate a segment of the Trizact$^{\text{TM}}$ abrasive profile on the surface of a grinding wheel. In the two-scale homogenisation method, we will take the microscale domain as the unit cell containing a single (scaled) Trizact$^{\text{TM}}$ abrasive.

We will begin by considering Stokes flow in the grinding zone. Although (326) and (331) suggest that inertial forces are far too dominating to approximate

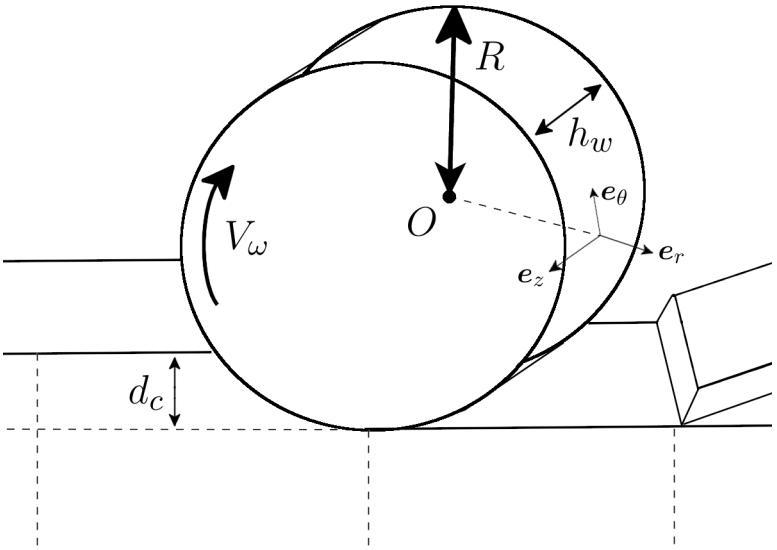

Figure 30: Illustration of the problem when viewed on the scale of the grinding wheel. The nozzle on the right hand side ejects grinding fluid into the grinding zone.

this flow with Stokes equations, it is an initial point for us to start and develop our method. Later in the chapter, we will build on the homogenisation of the Stokes flow to include inertial effects in the flow.

5.4 HOMOGENISATION OF A STOKES FLOW

We consider Stokes flow in the grinding zone. We specify points in the domain using a cylindrical coordinate system (r, θ, z). The origin is taken as the back, cross-sectional centre of the grinding wheel. The grinding wheel has radius R and width h_w. The flow domain in the grinding zone is represented as a thin gap with the workpiece taken as stationary with a depth of cut d_c and the grinding wheel's surface taken as rough and moving. We assume the rough surface is composed of identical, periodically positioned Trizact$^{\text{TM}}$ abrasives of size d which are inclined at an angle $\kappa = \frac{\pi}{4} + \theta_r$ to the boundary, $\theta_r \in \left[-\frac{\pi}{4}, \frac{\pi}{4}\right)$, with lateral length $\chi = \frac{d}{\sqrt{2}}$ and height $h_g = \frac{d}{2}$.

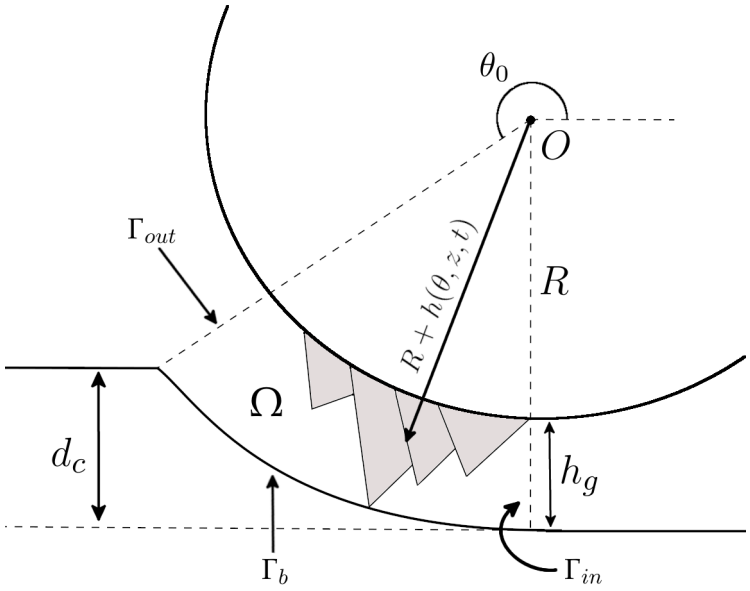

Figure 31: Illustration of a circular cross-section of the grinding zone in our homogenisation problem. Grinding fluid enters the domain through Γ_{in}. The shaded triangles on the grinding wheel represent abrasives.

The grinding wheel's surface is parameterised by $r = R + h(\theta, z, t)$ and the workpiece is located at $r = R + h_g$. The boundary profile $h(\theta, z, t)$ can be specified as the summation over the number of abrasives of equation (32) which gives the location of individual abrasives.

In this coordinate system, we assume the rough surface moves with velocity $\boldsymbol{V} = -V_\omega \boldsymbol{e}_\theta$, where $\boldsymbol{e}_r, \boldsymbol{e}_\theta, \boldsymbol{e}_z$ are the unit basis vectors of the cylindrical coordinate system. We denote the flow domain by Ω, the rough grinding wheel surface by Γ_ω, the workpiece surface by Γ_b, the entrance to the grinding zone

by Γ_{in}, the exit of the grinding zone by Γ_{out} and the remaining boundaries by Γ_s. We note that Ω and Γ_ω are time-dependent, and are given by

$$\Omega = \left\{(r,\theta,z) : r \in \left(R + h\left(\theta,z,t\right), R + h_g\right), \theta \in \left(\theta_0, \frac{3\pi}{2}\right), z \in (0,h_w)\right\}, \tag{332}$$

$$\Gamma_\omega = \left\{(r,\theta,z) : r = R + h\left(\theta,z,t\right), \theta \in \left(\theta_0, \frac{3\pi}{2}\right), z \in (0,h_w)\right\}, \tag{333}$$

$$\Gamma_b = \left\{(r,\theta,z) : r = R + h_g, \theta \in \left(\theta_0, \frac{3\pi}{2}\right), z \in (0,h_w)\right\}, \tag{334}$$

$$\Gamma_{in} = \left\{(r,\theta,z) : r \in \left(R + h\left(\theta,z,t\right), R + h_g\right), \theta = \frac{3\pi}{2}, z \in (0,h_w)\right\}, \tag{335}$$

$$\Gamma_{out} = \left\{(r,\theta,z) : r \in \left(R + h\left(\theta,z,t\right), R + h_g\right), \theta = \theta_0, z \in (0,h_w)\right\}, \tag{336}$$

$$\Gamma_s = \left\{(r,\theta,z) : r \in \left(R + h\left(\theta,z,t\right), R + h_g\right), \theta \in \left(\theta_0, \frac{3\pi}{2}\right), z \in \{0,h_w\}\right\}, \tag{337}$$

where

$$\theta_0 = \frac{3\pi}{2} - \cos^{-1}\left(\frac{R + h_g - d_c}{R + h_g}\right) \tag{338}$$

is calculated using trigonometric identities on the geometry.

The grinding zone is assumed to be occupied by two incompressible phases, air and grinding fluid, which are governed by a multiphase mixture model. The volume fraction of the grinding fluid is denoted by α_l and will be referred to simply as the volume fraction. The dynamic viscosity of the air and grinding fluid is denoted by μ_g and μ_l, respectively. We take pressure to be the atmospheric pressure on Γ_s. We assume that α_l is prescribed on Γ_{in} at points where there is flow into the domain, with $\alpha_l = \alpha_D\left(r,z,t\right)$. On other boundaries where there are regions of inflow, we prescribe $\alpha_l = 0$. We assume that initially at $t = 0$, there is no grinding fluid in the grinding zone. Sketches explaining the various quantities introduced here are shown in figures 30 and 31.

The governing equations for the flow in Ω are the multiphase mixture Stokes equations. These are given by (14)-(21) with inertial terms neglected, i.e.

$$-\nabla p + \nabla \cdot \left[\mu_m \left(\nabla \boldsymbol{u} + (\nabla \boldsymbol{u})^T\right)\right] = \mathbf{0}, \tag{339}$$

$$\nabla \cdot \boldsymbol{u} = 0, \tag{340}$$

$$\frac{\partial \alpha_l}{\partial t} + \nabla \cdot (\alpha_l \boldsymbol{u}) = 0, \tag{341}$$

where $\boldsymbol{u} = u_r \boldsymbol{e}_r + u_\theta \boldsymbol{e}_\theta + u_z \boldsymbol{e}_z$ denotes the mixture velocity, p denotes the mixture pressure, α_l denotes the volume fraction and $\mu_m = \alpha_l \mu_l + (1 - \alpha_l)\, \mu_g$ is the mixture viscosity. Body forces due to gravity are negligible at the scales investigated here. The mixture velocity and mixture pressure will be referred to as the velocity and pressure for the remainder of this chapter.

We have the initial condition

$$\alpha_l = 0 \qquad \text{on } \Omega \text{ at } t = 0. \tag{342}$$

The boundary conditions for equations (339)-(341) are

$$\boldsymbol{u} + V_\omega \boldsymbol{e}_\theta = 2\hat{\beta}\mu_m^\star \boldsymbol{n} \cdot \boldsymbol{E} \cdot (\boldsymbol{I} - \boldsymbol{n}\boldsymbol{n}) \qquad \text{on } \Gamma_\omega, \tag{343}$$

$$\boldsymbol{u} = 2\hat{\beta}\mu_m^\star \boldsymbol{n} \cdot \boldsymbol{E} \cdot (\boldsymbol{I} - \boldsymbol{n}\boldsymbol{n}) \qquad \text{on } \Gamma_b, \tag{344}$$

$$p = 0 \qquad \text{on } \Gamma_{in} \cup \Gamma_{out} \cup \Gamma_s, \tag{345}$$

$$\alpha_l = \alpha_D \qquad \text{on } \Gamma_{in} \text{ where } \boldsymbol{u} \cdot \boldsymbol{n} > 0, \tag{346}$$

$$\alpha_l = 0 \qquad \text{on } \Gamma_{out} \cup \Gamma_s \text{ where } \boldsymbol{u} \cdot \boldsymbol{n} > 0, \tag{347}$$

which are the slip conditions on the two surfaces, the domain boundary pressure condition and the inlet volume fraction conditions, respectively. Here, $\hat{\beta}$ is the slip length,

$$\mu_m^\star = \alpha_l + (1 - \alpha_l)\, \mu_{mix}, \tag{348}$$

$$\mu_{mix} = \frac{\mu_g}{\mu_l}, \tag{349}$$

$\boldsymbol{n}$ is the inward pointing unit normal to the boundary, $\boldsymbol{E}$ is the rate of strain tensor and $\boldsymbol{I}$ denotes the metric tensor. We refer the reader to Section 2.3 for further information on these multiphase slip conditions.

In the next section, we will see how the local problem and global (homogenised) problem can be posed from the system (339)-(347) by considering homogenisation over the abrasives on the rough surface.

5.5 LOCAL PROBLEM

We first begin by nondimensionalising the system given by (339)-(347). We assume that the gap between the surfaces, characterised by ε, is much less than unity. Values of ε are given in (322) and (327) for surface and creep-feed grinding regimes, showing that this assumption holds. We introduce the nondimensional radial distance

$$\bar{r} = \frac{r - R}{\varepsilon R}, \tag{350}$$

which shifts the radial coordinate to the surface of the grinding wheel and stretches the gap between the grinding wheel and the workpiece to $O(1)$ in $\bar{r}$. Regarding the z distance, typical values of R and h_w are given by (316) where we see that

$$\frac{h_w}{R} = 1 \times 10^{-1} \gg \varepsilon, \tag{351}$$

for the values of ε given in (322) and (327). Therefore, we choose to take the nondimensional z coordinate as

$$z = Rz^{\star}. \tag{352}$$

As the grinding wheel spins at speed V_ω, we take the characteristic value for the azimuthal velocity as V_ω, i.e.

$$u_\theta = V_\omega u_\theta^\star. \tag{353}$$

Previously for the problems studied in chapters 3 and 4, we scaled the velocity across the gap by $\sqrt{\varepsilon}$ (see, for example, (75)). However, in those cases we were dealing with two slowly varying boundaries. For the problem we are studying here, we have rapid moving, complex-shaped abrasives with $O(1)$ slope in each coordinate direction. For that reason, we take the characteristic value of V_ω for the velocity vector in the grinding zone, i.e.

$$\boldsymbol{u} = V_\omega \boldsymbol{u}^\star. \tag{354}$$

As we expect that the flow during grinding is shear dominated, we take the timescale as

$$t = \frac{R}{V_\omega} t^\star. \tag{355}$$

Due to the nondimensional values taken so far, we introduce

$$p = \frac{\mu_l V_\omega}{\varepsilon^2 R} p^\star, \tag{356}$$

$$\hat{\beta} = \varepsilon R \hat{\beta}^\star. \tag{357}$$

We denote the nondimensional gradient operator as

$$\nabla^\star q = \frac{\partial q}{\partial \bar{r}} \boldsymbol{e}_r + \frac{\varepsilon}{1+\varepsilon\bar{r}} \frac{\partial q}{\partial \theta} \boldsymbol{e}_\theta + \varepsilon \frac{\partial q}{\partial z^\star} \boldsymbol{e}_z, \tag{358}$$

the nondimensional divergence operator as

$$\nabla^\star \cdot \boldsymbol{q} = \frac{1}{1+\varepsilon\bar{r}} \frac{\partial}{\partial \bar{r}} \left[(1+\varepsilon\bar{r})\, q_r \right] + \frac{\varepsilon}{1+\varepsilon\bar{r}} \frac{\partial q_\theta}{\partial \theta} + \varepsilon \frac{\partial q_z}{\partial z^\star}, \tag{359}$$

the nondimensional vector gradient operator as

$$\begin{aligned}\nabla^\star \boldsymbol{q} = &\frac{\partial q_r}{\partial \bar{r}}\boldsymbol{e}_r\boldsymbol{e}_r + \frac{\partial q_\theta}{\partial \bar{r}}\boldsymbol{e}_r\boldsymbol{e}_\theta + \frac{\partial q_z}{\partial \bar{r}}\boldsymbol{e}_r\boldsymbol{e}_z \\ &+ \frac{\varepsilon}{1+\varepsilon\bar{r}}\left[\left(\frac{\partial q_r}{\partial \theta} - q_\theta\right)\boldsymbol{e}_\theta\boldsymbol{e}_r + \left(\frac{\partial q_\theta}{\partial \theta} + q_r\right)\boldsymbol{e}_\theta\boldsymbol{e}_\theta + \frac{\partial q_z}{\partial \theta}\boldsymbol{e}_\theta\boldsymbol{e}_z\right] \\ &+ \varepsilon\left(\frac{\partial q_r}{\partial z^\star}\boldsymbol{e}_z\boldsymbol{e}_r + \frac{\partial q_\theta}{\partial z^\star}\boldsymbol{e}_z\boldsymbol{e}_\theta + \frac{\partial q_z}{\partial z^\star}\boldsymbol{e}_z\boldsymbol{e}_z\right),\end{aligned} \tag{360}$$

and the nondimensional tensor divergence operator as

$$\begin{aligned}\nabla^\star \cdot \boldsymbol{T} = &\left(\frac{\partial T_{rr}}{\partial \bar{r}} + \frac{\varepsilon}{1+\varepsilon\bar{r}}\left[\frac{\partial T_{\theta r}}{\partial \theta} + (T_{rr} - T_{\theta\theta})\right] + \varepsilon\frac{\partial T_{zr}}{\partial z^\star}\right)\boldsymbol{e}_r \\ &+ \left(\frac{\partial T_{r\theta}}{\partial \bar{r}} + \frac{\varepsilon}{1+\varepsilon\bar{r}}\left[\frac{\partial T_{\theta\theta}}{\partial \theta} + (T_{r\theta} + T_{\theta r})\right] + \varepsilon\frac{\partial T_{z\theta}}{\partial z^\star}\right)\boldsymbol{e}_\theta \\ &+ \left(\frac{\partial T_{rz}}{\partial \bar{r}} + \frac{\varepsilon}{1+\varepsilon\bar{r}}\left(\frac{\partial T_{\theta z}}{\partial \theta} + T_{rz}\right) + \varepsilon\frac{\partial T_{zz}}{\partial z^\star}\right)\boldsymbol{e}_z,\end{aligned} \tag{361}$$

for a general scalar q, vector $\boldsymbol{q} = q_r\boldsymbol{e}_r + q_\theta\boldsymbol{e}_\theta + q_z\boldsymbol{e}_z$ and second order tensor $\boldsymbol{T} = T_{ij}\boldsymbol{e}_i\boldsymbol{e}_j$ where $i, j \in \{r, \theta, z\}$.

The problem that we will homogenise is the nondimensional form of (339)-(347), given by

$$-\nabla^\star p^\star + \varepsilon\nabla^\star \cdot \left[\mu_m^\star\left(\nabla^\star \boldsymbol{u}^\star + (\nabla^\star \boldsymbol{u}^\star)^T\right)\right] = \boldsymbol{0}, \tag{362}$$

$$\nabla^\star \cdot \boldsymbol{u}^\star = 0, \tag{363}$$

$$\varepsilon\frac{\partial \alpha_l}{\partial t^\star} + \nabla^\star \cdot (\alpha_l \boldsymbol{u}^\star) = 0 \tag{364}$$

on $\Omega^\star$, subject to the initial condition

$$\alpha_l = 0 \qquad \text{on } \Omega^\star \text{ at } t^\star = 0, \tag{365}$$

and boundary conditions

$$\boldsymbol{u}^\star + \boldsymbol{e}_\theta = 2\hat{\beta}^\star \mu_m^\star \boldsymbol{n} \cdot \boldsymbol{E}^\star \cdot (\boldsymbol{I} - \boldsymbol{n}\boldsymbol{n}) \qquad \text{on } \Gamma_\omega^\star, \tag{366}$$

$$\boldsymbol{u}^\star = 2\hat{\beta}^\star \mu_m^\star \boldsymbol{n} \cdot \boldsymbol{E}^\star \cdot (\boldsymbol{I} - \boldsymbol{n}\boldsymbol{n}) \qquad \text{on } \Gamma_b^\star, \tag{367}$$

$$p^\star = 0 \qquad \text{on } \Gamma_{in}^\star \cup \Gamma_{out}^\star \cup \Gamma_s^\star, \tag{368}$$

$$\alpha_l = \alpha_D \qquad \text{on } \Gamma_{in}^\star \text{ where } \boldsymbol{u}^\star \cdot \boldsymbol{n} > 0, \tag{369}$$

$$\alpha_l = 0 \qquad \text{on } \Gamma_{out}^\star \cup \Gamma_s^\star \text{ where } \boldsymbol{u}^\star \cdot \boldsymbol{n} > 0. \tag{370}$$

Here,

$$\Omega^\star = \left\{ (\bar{r}, \theta, z^\star) : \bar{r} \in \left(h^\star\left(\theta, z^\star, t^\star\right), 1\right), \theta \in \left(\theta_0, \frac{3\pi}{2}\right), z^\star \in (0, h_w^\star) \right\}, \tag{371}$$

$$\Gamma_\omega^\star = \left\{ (\bar{r}, \theta, z^\star) : \bar{r} = h^\star\left(\theta, z^\star, t^\star\right), \theta \in \left(\theta_0, \frac{3\pi}{2}\right), z^\star \in (0, h_w^\star) \right\}, \tag{372}$$

$$\Gamma_b^\star = \left\{ (\bar{r}, \theta, z^\star) : \bar{r} = 1, \theta \in \left(\theta_0, \frac{3\pi}{2}\right), z^\star \in (0, h_w^\star) \right\}, \tag{373}$$

$$\Gamma_{in}^\star = \left\{ (\bar{r}, \theta, z^\star) : \bar{r} \in \left(h^\star\left(\theta, z^\star, t^\star\right), 1\right), \theta = \frac{3\pi}{2}, z^\star \in (0, h_w^\star) \right\}, \tag{374}$$

$$\Gamma_{out}^\star = \left\{ (\bar{r}, \theta, z^\star) : \bar{r} \in \left(h^\star\left(\theta, z^\star, t^\star\right), 1\right), \theta = \theta_0, z^\star \in (0, h_w^\star) \right\}, \tag{375}$$

$$\Gamma_s^\star = \left\{ (\bar{r}, \theta, z^\star) : \bar{r} \in \left(h^\star\left(\theta, z^\star, t^\star\right), 1\right), \theta \in \left(\theta_0, \frac{3\pi}{2}\right), z^\star \in \{0, h_w^\star\} \right\}, \tag{376}$$

$$h^\star\left(\theta, z^\star, t^\star\right) = \frac{h\left(\theta, z^\star, t^\star\right)}{h_g}, \tag{377}$$

$$h_w^\star = \frac{h_w}{R}, \tag{378}$$

$$\boldsymbol{E}^\star = \frac{1}{2}\left(\nabla^\star \boldsymbol{u}^\star + \left(\nabla^\star \boldsymbol{u}^\star\right)^T\right). \tag{379}$$

From here on, we drop the superscript $\star$ denoting the dimensionless variables introduced here.

We now proceed with the two-scale homogenisation where we assume that each dimensionless variable depends not only on the cylindrical coordinates $(\bar{r}, \theta, z)$, but also on two geometrically periodic coordinates $(\bar{\theta}, \bar{z})$, where

$$\bar{\theta} = \frac{\tilde{\theta}}{\chi^\star} = \frac{\theta \cos\kappa + z \sin\kappa}{\chi^\star}, \tag{380}$$

$$\bar{z} = \frac{\tilde{z}}{\chi^\star} = \frac{-\theta \sin\kappa + z \cos\kappa}{\chi^\star}, \tag{381}$$

$$\chi^\star = \frac{d}{\sqrt{2}R} = \sqrt{2}\varepsilon, \tag{382}$$

with these coordinates belonging to the set specifying points over a periodic structure

$$Y = \left\{(\bar{r}, \bar{\theta}, \bar{z}) : \tilde{h} < \bar{r} < 1, 0 < \bar{\theta}, \bar{z} < 1\right\}, \tag{383}$$

$$Y_X = \left\{(\bar{\theta}, \bar{z}) : 0 < \bar{\theta}, \bar{z} < 1\right\}. \tag{384}$$

We denote the boundaries of Y by

$$\partial Y_{\tilde{h}} = \left\{(\bar{r}, \bar{\theta}, \bar{z}) : \bar{r} = \tilde{h}, 0 \leq \bar{\theta}, \bar{z} \leq 1\right\}, \tag{385}$$

$$\partial Y_1 = \left\{(\bar{r}, \bar{\theta}, \bar{z}) : \bar{r} = 1, 0 \leq \bar{\theta}, \bar{z} \leq 1\right\}, \tag{386}$$

$$\partial Y_p = \partial Y \setminus \left(\partial Y_{\tilde{h}} \cup \partial Y_1\right), \tag{387}$$

where we have

$$\partial Y = \partial Y_p \cup \partial Y_{\tilde{h}} \cup \partial Y_1. \tag{388}$$

We denote the set of macroscale coordinates as $\boldsymbol{x} = (\theta, z)$ and the set of microscale coordinates as $\boldsymbol{X} = (\bar{r}, \bar{\theta}, \bar{z})$. The reader is encouraged to review Appendix B regarding the asymptotic limit taken in the microscale coordinate system in the next section.

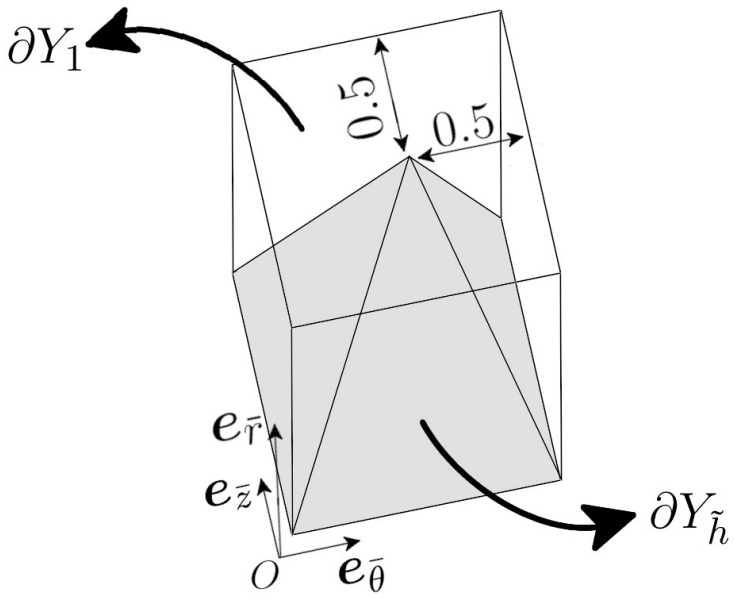

Figure 32: Illustration of an individual Trizact$^{\text{TM}}$ abrasive within the unit cell, with points here specified in the microscopic coordinates $(\bar{r}, \bar{\theta}, \bar{z})$. The abrasives are regular pyramids which protrude away from the substrate. Here, $\boldsymbol{e}_{\bar{r}}, \boldsymbol{e}_{\bar{\theta}}$ and $\boldsymbol{e}_{\bar{z}}$ are basis vectors that span the unit cell. The bottom and top boundaries are denoted by $\partial Y_{\tilde{h}}$ and ∂Y_1, respectively. The remaining boundary where periodic boundary conditions are enforced is denoted ∂Y_p.

In (383), the function $\tilde{h}$ is the equation of the abrasive's surface inside the unit cell. For the Trizact$^{\text{TM}}$ abrasive, this function can be found using equation (32). Specifically, in the unit cell we have

$$\tilde{h}\left(\bar{\theta}, \bar{z}\right) = 1 - \left(\left|\bar{\theta} - \bar{z}\right| + \left|\bar{z} + \bar{\theta} - 1\right| \right). \tag{389}$$

In figure 32, we illustrate the microscopic geometry, i.e. an individual Trizact$^{\text{TM}}$ abrasive.

We now assume our dimensionless variables spatially depend on both the cylindrical coordinates specifying points in the grinding zone and the unit-periodic coordinates, i.e.

$$\boldsymbol{u}\left(\bar{r},\theta,z,t\right)=\boldsymbol{u}_{\varepsilon}\left(\bar{r},\theta,z,\bar{\theta},\bar{z},t\right), \tag{390}$$

$$p\left(\bar{r},\theta,z,t\right)=p_{\varepsilon}\left(\bar{r},\theta,z,\bar{\theta},\bar{z},t\right), \tag{391}$$

$$\alpha_{l}\left(\bar{r},\theta,z,t\right)=\alpha_{l,\varepsilon}\left(\bar{r},\theta,z,\bar{\theta},\bar{z},t\right), \tag{392}$$

with the conditions of periodicity

$$q_{\varepsilon}\left(\bar{r},\theta,z,0,\bar{z},t\right)=q_{\varepsilon}\left(\bar{r},\theta,z,1,\bar{z},t\right), \tag{393}$$

$$q_{\varepsilon}\left(\bar{r},\theta,z,\bar{\theta},0,t\right)=q_{\varepsilon}\left(\bar{r},\theta,z,\bar{\theta},1,t\right), \tag{394}$$

for $q_{\varepsilon}=\boldsymbol{u}_{\varepsilon},p_{\varepsilon},\alpha_{l,\varepsilon}$.

We can now use the chain rule with differential operators acting on (390)-(392) to express them in terms of each coordinate system separately. As an example, we consider the pressure derivative

$$\frac{\partial p\left(\bar{r},\theta,z,t\right)}{\partial\theta}=\frac{\partial p_{\varepsilon}\left(\bar{r},\theta,z,\bar{\theta},\bar{z},t\right)}{\partial\theta}. \tag{395}$$

We know that $\bar{\theta}$ and $\bar{z}$ depend on θ by (380) and (381) with

$$\frac{\partial\bar{\theta}}{\partial\theta}=\frac{\cos\kappa}{\sqrt{2}\varepsilon}, \tag{396}$$

$$\frac{\partial\bar{z}}{\partial\theta}=-\frac{\sin\kappa}{\sqrt{2}\varepsilon}. \tag{397}$$

The application of the chain rule to (395) gives that

$$\frac{\partial p\left(\bar{r},\theta,z,t\right)}{\partial\theta}=\frac{\partial p_{\varepsilon}}{\partial\theta}+\frac{\cos\kappa}{\sqrt{2}\varepsilon}\frac{\partial p_{\varepsilon}}{\partial\bar{\theta}}-\frac{\sin\kappa}{\sqrt{2}\varepsilon}\frac{\partial p_{\varepsilon}}{\partial\bar{z}}. \tag{398}$$

Letting q and $\boldsymbol{q}$ denote a general scalar and vector function, respectively, we apply the chain rule (398) to other derivatives to find that the differential operators (358) and (359) can be expressed as

$$\begin{aligned}\nabla q = &\frac{\partial q_\varepsilon}{\partial \bar{r}}\hat{\boldsymbol{e}}_r + \frac{1}{\sqrt{2}\,(1+\varepsilon\bar{r})}\left(\frac{\partial q_\varepsilon}{\partial \bar{\theta}}\cos\kappa - \frac{\partial q_\varepsilon}{\partial \bar{z}}\sin\kappa\right)\hat{\boldsymbol{e}}_\theta \\ &+ \frac{1}{\sqrt{2}}\left(\frac{\partial q_\varepsilon}{\partial \bar{\theta}}\sin\kappa + \frac{\partial q_\varepsilon}{\partial \bar{z}}\cos\kappa\right)\hat{\boldsymbol{e}}_z \\ &+ \varepsilon\left(\frac{1}{1+\varepsilon\bar{r}}\frac{\partial q_\varepsilon}{\partial \theta}\hat{\boldsymbol{e}}_\theta + \frac{\partial q_\varepsilon}{\partial z}\hat{\boldsymbol{e}}_z\right) \\ = &\nabla_{\boldsymbol{X}} q_\varepsilon + \varepsilon\nabla_{\boldsymbol{x}} q_\varepsilon,\end{aligned} \tag{399}$$

$$\begin{aligned}\nabla\cdot\boldsymbol{q} = &\frac{1}{1+\varepsilon\bar{r}}\frac{\partial}{\partial \bar{r}}\left[(1+\varepsilon\bar{r})\,q_{r,\varepsilon}\right] + \frac{1}{\sqrt{2}\,(1+\varepsilon\bar{r})}\left(\frac{\partial q_{\theta,\varepsilon}}{\partial \bar{\theta}}\cos\kappa - \frac{\partial q_{\theta,\varepsilon}}{\partial \bar{z}}\sin\kappa\right) \\ &+ \frac{1}{\sqrt{2}}\left(\frac{\partial q_{z,\varepsilon}}{\partial \bar{\theta}}\sin\kappa + \frac{\partial q_{z,\varepsilon}}{\partial \bar{z}}\cos\kappa\right) + \varepsilon\left(\frac{1}{1+\varepsilon\bar{r}}\frac{\partial q_{\theta,\varepsilon}}{\partial \theta} + \frac{\partial q_{z,\varepsilon}}{\partial z}\right) \\ = &\nabla_{\boldsymbol{X}}\cdot\boldsymbol{q}_\varepsilon + \varepsilon\nabla_{\boldsymbol{x}}\cdot\boldsymbol{q}_\varepsilon.\end{aligned} \tag{400}$$

Note that as the system (362)-(370) has been presented following the notation in previous chapters, the subscript ε has now been used to indicate the homogenised solution, in contrast with its use in (301). However, this does not affect our derivation and we now drop the subscript ε for convenience.

Substituting (399) and (400) into equations (362)-(364) and rearranging (recalling that we dropped the superscript $\star$ which indicated a nondimensional quantity), we arrive at

$$\begin{aligned}&-\frac{1}{\varepsilon}\nabla_{\boldsymbol{X}} p - \nabla_{\boldsymbol{x}} p \\ &+ \left(\nabla_{\boldsymbol{X}}\cdot + \varepsilon\nabla_{\boldsymbol{x}}\cdot\right)\left\{\mu_m\left[\left(\nabla_{\boldsymbol{X}} + \varepsilon\nabla_{\boldsymbol{x}}\right)\boldsymbol{u} + \left[\left(\nabla_{\boldsymbol{X}} + \varepsilon\nabla_{\boldsymbol{x}}\right)\boldsymbol{u}\right]^T\right]\right\} = \boldsymbol{0},\end{aligned} \tag{401}$$

$$\nabla_{\boldsymbol{X}}\cdot\boldsymbol{u} + \varepsilon\nabla_{\boldsymbol{x}}\cdot\boldsymbol{u} = 0, \tag{402}$$

$$\varepsilon\frac{\partial \alpha_l}{\partial t} + \nabla_{\boldsymbol{X}}\cdot(\alpha_l\boldsymbol{u}) + \varepsilon\nabla_{\boldsymbol{x}}\cdot(\alpha_l\boldsymbol{u}) = 0. \tag{403}$$

Let us consider the asymptotic expansions

$$\boldsymbol{u} = \sum_{i=0}^{\infty} \varepsilon^i \boldsymbol{u}_i, \tag{404}$$

$$p = \sum_{i=0}^{\infty} \varepsilon^i p_i, \tag{405}$$

$$\alpha_l = \sum_{i=0}^{\infty} \varepsilon^i \alpha_{i,l}, \tag{406}$$

for the unknown variables in the flow domain, where we also expand the mixture viscosity in powers of ε as

$$\mu_m = \sum_{i=0}^{\infty} \varepsilon^i \mu_{i,m} \tag{407}$$

with

$$\mu_{0,m} = \alpha_{0,l} + (1 - \alpha_{0,l})\, \mu_{mix}, \tag{408}$$

$$\mu_{i,m} = \alpha_{i,l}\, (1 - \mu_{mix}) \qquad\qquad i \geq 1. \tag{409}$$

The differential operators defined in (399) and (400) involve powers of ε. As we will only need to consider the leading order operators, for the remainder of this chapter we will denote $\nabla_{\boldsymbol{X}}$ and $\nabla_{\boldsymbol{x}}$ by the forms given in (399) and (400) with $\varepsilon = 0$.

Substituting (404)-(407) into equations (401)-(403), we can collect terms in various orders of ε in order to find the leading order flow behaviour at the microscale. To this end, we consider $O(\varepsilon^{-1})$ terms in (401) to see that the leading order pressure field behaves as

$$p_0 = p_0(\theta, z, t). \tag{410}$$

Meanwhile, equating $O(1)$ terms in (401), we have the following equation involving macroscale and microscale derivatives,

$$-\nabla_{\boldsymbol{x}} p_0 - \nabla_{\boldsymbol{X}} p_1 + \nabla_{\boldsymbol{X}} \cdot \left[\mu_{0,m} \left(\nabla_{\boldsymbol{X}} \boldsymbol{u}_0 + (\nabla_{\boldsymbol{X}} \boldsymbol{u}_0)^T\right)\right] = \boldsymbol{0}. \tag{411}$$

However, regarding the continuity equation (402) and advection equation (403), more care is necessary due to the curvature correction term $(1+\varepsilon\bar{r})^{-1}$. Under the lubrication approximation from earlier chapters, this term would not affect the flow as only leading order, $O(1)$ terms need to be considered. That is contrary to here as we must look below leading order to derive the global problem. As this term deviates from unity below leading order, we must deal with this in our equations.

Thus, we multiply both (402) and (403) through by $1+\varepsilon\bar{r}$ so that at $O(1)$, we simply have

$$\nabla_{\boldsymbol{X}} \cdot \boldsymbol{u}_0 = 0, \tag{412}$$

$$\nabla_{\boldsymbol{X}} \cdot (\alpha_{0,l}\boldsymbol{u}_0) = 0, \tag{413}$$

respectively, while at $O(\varepsilon)$ we instead get

$$\nabla_{\boldsymbol{x}} \cdot \boldsymbol{u}_0 + \nabla_{\boldsymbol{X}} \cdot \boldsymbol{u}_1 = -\left[\frac{\partial}{\partial \bar{r}}(\bar{r}u_{r,0}) + \frac{\bar{r}}{\sqrt{2}}\left(\frac{\partial u_{z,0}}{\partial \bar{\theta}}\sin\kappa + \frac{\partial u_{z,0}}{\partial \bar{z}}\cos\kappa\right)\right], \tag{414}$$

$$\begin{aligned}&\frac{\partial \alpha_{0,l}}{\partial t} + \nabla_{\boldsymbol{x}} \cdot (\alpha_{0,l}\boldsymbol{u}_0) + \nabla_{\boldsymbol{X}} \cdot (\alpha_{0,l}\boldsymbol{u}_1 + \alpha_{1,l}\boldsymbol{u}_0)\\ &= -\left[\frac{\partial}{\partial \bar{r}}(\bar{r}\alpha_{0,l}u_{r,0}) + \frac{\bar{r}}{\sqrt{2}}\left(\frac{\partial}{\partial \bar{\theta}}(\alpha_{0,l}u_{z,0})\sin\kappa + \frac{\partial}{\partial \bar{z}}(\alpha_{0,l}u_{z,0})\cos\kappa\right)\right],\end{aligned} \tag{415}$$

respectively.

From (366) and (367), at $O(1)$ we have the leading order boundary conditions

$$\boldsymbol{u}_0 + \boldsymbol{e}_\theta = 2\hat{\beta}\mu_{0,m}\boldsymbol{n} \cdot \boldsymbol{E}_{\boldsymbol{X}} \cdot (\boldsymbol{I} - \boldsymbol{nn}) \qquad \text{on } \bar{r} = \tilde{h}, \tag{416}$$

$$\boldsymbol{u}_0 = 2\hat{\beta}\mu_{0,m}\boldsymbol{n} \cdot \boldsymbol{E}_{\boldsymbol{X}} \cdot (\boldsymbol{I} - \boldsymbol{nn}) \qquad \text{on } \bar{r} = 1, \tag{417}$$

where

$$\boldsymbol{E}_{\boldsymbol{X}} = \frac{1}{2}\left(\nabla_{\boldsymbol{X}}\boldsymbol{u}_0 + (\nabla_{\boldsymbol{X}}\boldsymbol{u}_0)^T\right). \tag{418}$$

From the periodic conditions (393) and (394), at $O(1)$ we have

$$\boldsymbol{u}_0(\bar{r},\theta,z,0,\bar{z},t) = \boldsymbol{u}_0(\bar{r},\theta,z,1,\bar{z},t), \tag{419}$$

$$\boldsymbol{u}_0(\bar{r},\theta,z,\bar{\theta},0,t) = \boldsymbol{u}_0(\bar{r},\theta,z,\bar{\theta},1,t), \tag{420}$$

and at $O(\varepsilon)$ we have

$$p_1(\bar{r},\theta,z,0,\bar{z},t) = p_1(\bar{r},\theta,z,1,\bar{z},t), \tag{421}$$

$$p_1(\bar{r},\theta,z,\bar{\theta},0,t) = p_1(\bar{r},\theta,z,\bar{\theta},1,t). \tag{422}$$

We now look to simplify the problem by reducing the number of independent spatial variables in the global problem down to two. To this end, we note that by using (412), a solution to (413) is where the volume fraction is constant over each individual abrasive, i.e.

$$\alpha_l \equiv \alpha_l(\theta,z,t). \tag{423}$$

The physical interpretation of (423) is that diffusion of the mixture concentration happens over a much smaller timescale than the timescale associated with the advection across the abrasives: therefore, the amount of grinding fluid is the same at each point around the abrasive.

For the remainder of this chapter, we will look for solutions of the form (423). Consequently, equation (415) no longer needs to be considered in the microscopic system. However, we will return to analyse this equation once we upscale and obtain the macroscale, homogenised system.

After assuming (423) on α_l, (411) can be rewritten as

$$-\nabla_{\boldsymbol{x}} p_0 - \nabla_{\boldsymbol{X}} p_1 + \mu_{0,m} \nabla_{\boldsymbol{X}} \cdot \left[\left(\nabla_{\boldsymbol{X}} \boldsymbol{u}_0 + (\nabla_{\boldsymbol{X}} \boldsymbol{u}_0)^T \right) \right] = \boldsymbol{0}, \tag{424}$$

which is a linear partial differential equation with respect to the microscopic coordinates, with a forcing term dependent on the macroscopic coordinates.

Currently, $\boldsymbol{u}_0$ and p_1 depend on both microscopic and macroscopic coordinates. We seek a solution to the problem given by equations (412) and (424) subject to the conditions (416), (417), (419)-(422), of the form

$$\boldsymbol{u_0} = \boldsymbol{w}_0 + \boldsymbol{w}_1 \frac{\partial p_0}{\partial \theta} + \boldsymbol{w}_2 \frac{\partial p_0}{\partial z}, \tag{425}$$

$$p_1 = \gamma_0 + \gamma_1 \frac{\partial p_0}{\partial \theta} + \gamma_2 \frac{\partial p_0}{\partial z}, \tag{426}$$

where $\boldsymbol{w}_i\left(\bar{r}, \bar{\theta}, \bar{z}\right)$ and $\gamma_i\left(\bar{r}, \bar{\theta}, \bar{z}\right)$ for $i = 0, 1, 2$ are local solutions which satisfy the periodicity of the geometry. We will refer to $\boldsymbol{w}_i$ and γ_i as a microscopic velocity and microscopic pressure, respectively, for $i = 0, 1, 2$. Expressions (425) and (426) separate the variables $\boldsymbol{u}_0$ and p_1 into terms which depend solely on either the microscopic or macroscopic coordinates.

Substituting (425) and (426) into (424) and (412) leaves us with the local equations

$$-\nabla_{\boldsymbol{X}} \gamma_i + \mu_{0,m} \nabla_{\boldsymbol{X}} \cdot \left(\nabla_{\boldsymbol{X}} \boldsymbol{w}_i + \left(\nabla_{\boldsymbol{X}} \boldsymbol{w}_i\right)^T\right) = \boldsymbol{f}_i, \tag{427}$$

$$\nabla_{\boldsymbol{X}} \cdot \boldsymbol{w}_i = 0, \tag{428}$$

respectively, for $i = 0, 1, 2$, with

$$\boldsymbol{f}_0 = \boldsymbol{0}, \tag{429}$$

$$\boldsymbol{f}_1 = \boldsymbol{e}_\theta, \tag{430}$$

$$\boldsymbol{f}_2 = \boldsymbol{e}_z. \tag{431}$$

By substituting (425) and (426) into (393) and (394), we get the periodic boundary conditions on the local solutions

$$\boldsymbol{w}_i\left(\bar{r}, 0, \bar{z}\right) = \boldsymbol{w}_i\left(\bar{r}, 1, \bar{z}\right), \tag{432}$$

$$\gamma_i\left(\bar{r}, 0, \bar{z}\right) = \gamma_i\left(\bar{r}, 1, \bar{z}\right), \tag{433}$$

$$\boldsymbol{w}_i\left(\bar{r}, \bar{\theta}, 0\right) = \boldsymbol{w}_i\left(\bar{r}, \bar{\theta}, 1\right), \tag{434}$$

$$\gamma_i\left(\bar{r}, \bar{\theta}, 0\right) = \gamma_i\left(\bar{r}, \bar{\theta}, 1\right). \tag{435}$$

Similarly, substitution of (425) and (426) into (416) and (417) gives the local slip boundary conditions with no penetration

$$\boldsymbol{w}_i + \mathbf{1}_{\{i=0\}}\boldsymbol{e}_\theta = 2\hat{\beta}\mu_{0,m}\boldsymbol{n}\cdot\boldsymbol{E}_i\cdot(\boldsymbol{I}-\boldsymbol{nn}) \quad \text{on } \bar{r}=\tilde{h}, \tag{436}$$

$$\boldsymbol{w}_i = 2\hat{\beta}\mu_{0,m}\boldsymbol{n}\cdot\boldsymbol{E}_i\cdot(\boldsymbol{I}-\boldsymbol{nn}) \quad \text{on } \bar{r}=1, \tag{437}$$

for $i = 0, 1, 2$, with $\boldsymbol{E}_i = \frac{1}{2}\left(\nabla_{\boldsymbol{X}}\boldsymbol{w}_i + (\nabla_{\boldsymbol{X}}\boldsymbol{w}_i)^T\right)$ and $\mathbf{1}_{\{i=0\}}$ the characteristic function which takes the value 1 when $i = 0$ and 0 when $i = 1, 2$.

The motivation of separating $\boldsymbol{u}_0$ and p_0 via (425) and (426), respectively, both follow from the linearity of the local system given by (412), (416), (417), (419)-(422) and (424). There are three components due to the microscopic three dimensional coordinate system we use. These components can be interpreted as the separation of the flow into the three intrinsic elements that drive it. These are shear due to the movement of the grinding wheel, given by $\boldsymbol{w}_0, \gamma_0$, and the macroscopic pressure gradient across the grinding zone, given by $\boldsymbol{w}_i, \gamma_i, i = 1, 2$.

We know from the superposition principle that the sum of any two solutions is also a solution. Therefore, if $\boldsymbol{w}_i, \gamma_i$ satisfy the local equation (427) for $i = 0, 1, 2$, then the sum

$$\boldsymbol{w}_0 + \boldsymbol{w}_1\frac{\partial p_0}{\partial\theta} + \boldsymbol{w}_2\frac{\partial p_0}{\partial z} \tag{438}$$

$$\gamma_0 + \gamma_1\frac{\partial p_0}{\partial\theta} + \gamma_2\frac{\partial p_0}{\partial z} \tag{439}$$

must satisfy (424) as this can be found from the summation of the local equations given by (427) (with the appropriate multiplication of a macroscopic pressure derivative for $i = 1, 2$). The same argument holds for the remaining equations and boundary conditions in the system due to linearity. As the solution sums (438) and (439) are $\boldsymbol{u}_0$ and p_1, respectively, we therefore have that $\boldsymbol{u}_0$ and p_1 given by (425) and (426), respectively, are solutions to the local system given by (412), (416), (417), (419)-(422) and (424).

5.6 GLOBAL PROBLEM

The local problem (427), (428), (432)-(437) is not currently a closed system as it involves $\alpha_{0,l}$, a function dependent on macroscale coordinates. Due to this, we require knowledge of $\alpha_{0,l}$ on the macroscale domain. Hence, we look to upscale the problem onto the macroscale and derive a governing equation for $\alpha_{0,l}$. This is the process for deriving a global problem. To do so, we define the two averaging operators

$$\langle q \rangle^{\tilde{h}} = \int_{\tilde{h}}^{1} q \mathrm{d}\bar{r}, \tag{440}$$

$$\langle q \rangle^{Y_X} = \int_0^1 \int_0^1 q \mathrm{d}\bar{\theta} \mathrm{d}\bar{z}, \tag{441}$$

for some general quantity q, where Y_X is given by (384) and $\tilde{h}$ is given by (389).

Recalling (410) and (423), p_0 and $\alpha_{0,l}$ depend only on macroscale coordinates. However, $\boldsymbol{u}_0$ depends on both microscale and macroscale coordinates. We use the averaging operators (440) and (441) on (425) to define the leading order macroscopic velocity, $\boldsymbol{U}_0(\theta, z, t)$, via

$$\begin{aligned} \boldsymbol{U}_0(\theta, z, t) &= \int_Y \boldsymbol{u}_0(\bar{r}, \theta, z, \bar{\theta}, \bar{z}, t) \, \mathrm{d}Y \\ &= \left\langle \langle \boldsymbol{u}_0 \rangle^{\tilde{h}} \right\rangle^{Y_X} \\ &= \left\langle \langle \boldsymbol{w}_0 \rangle^{\tilde{h}} \right\rangle^{Y_X} + \left\langle \langle \boldsymbol{w}_1 \rangle^{\tilde{h}} \right\rangle^{Y_X} \frac{\partial p_0}{\partial \theta} + \left\langle \langle \boldsymbol{w}_2 \rangle^{\tilde{h}} \right\rangle^{Y_X} \frac{\partial p_0}{\partial z}. \end{aligned} \tag{442}$$

Recalling that $\boldsymbol{n}$ denotes the inward pointing unit normal, we observe that

$$\left\langle \langle \nabla_{\boldsymbol{X}} \cdot \boldsymbol{u}_1 \rangle^{\tilde{h}} \right\rangle^{Y_X} = -\int_{\partial Y} \boldsymbol{u}_1 \cdot \boldsymbol{n} \mathrm{d}\Gamma \tag{443}$$

by application of the divergence theorem. Using (388), we then have that

$$\int_{\partial Y} \boldsymbol{u}_1 \cdot \boldsymbol{n} \mathrm{d}\Gamma = \int_{\partial Y_{\tilde{h}}} \boldsymbol{u}_1 \cdot \boldsymbol{n} \mathrm{d}\Gamma + \int_{\partial Y_1} \boldsymbol{u}_1 \cdot \boldsymbol{n} \mathrm{d}\Gamma + \int_{\partial Y_p} \boldsymbol{u}_1 \cdot \boldsymbol{n} \mathrm{d}\Gamma. \tag{444}$$

By the periodicity conditions (393) and (394) at $O(\varepsilon)$,

$$\int_{\partial Y_p} \boldsymbol{u}_1 \cdot \boldsymbol{n} \mathrm{d}\Gamma = 0. \tag{445}$$

Taking the normal projection of the slip boundary conditions (366) and (367), we see that at all orders of the asymptotic expansion for $\boldsymbol{u}$, we have impermeability. In particular,

$$\int_{\partial Y_{\tilde{h}}} \boldsymbol{u}_1 \cdot \boldsymbol{n} \mathrm{d}\Gamma = \int_{\partial Y_1} \boldsymbol{u}_1 \cdot \boldsymbol{n} \mathrm{d}\Gamma = 0, \tag{446}$$

hence

$$\left\langle \langle \nabla_{\boldsymbol{X}} \cdot \boldsymbol{u}_1 \rangle^{\tilde{h}} \right\rangle^{Y_X} = 0. \tag{447}$$

Applying the averaging operators $\left\langle \langle \cdot \rangle^{\tilde{h}} \right\rangle^{Y_X}$ to equation (414), we get

$$\begin{aligned} &\nabla_{\boldsymbol{x}} \cdot \left\langle \langle \boldsymbol{u}_0 \rangle^{\tilde{h}} \right\rangle^{Y_X} \\ &= -\left(\left\langle \left\langle \frac{\partial}{\partial \bar{r}} \left(\bar{r} u_{r,0} \right) \right\rangle^{\tilde{h}} \right\rangle^{Y_X} + \left\langle \left\langle \frac{\bar{r}}{\sqrt{2}} \left(\frac{\partial u_{z,0}}{\partial \bar{\theta}} \sin \kappa + \frac{\partial u_{z,0}}{\partial \bar{z}} \cos \kappa \right) \right\rangle^{\tilde{h}} \right\rangle^{Y_X} \right), \end{aligned} \tag{448}$$

where we have used the definition of $\boldsymbol{U}_0$ from (442), (447) and that $\tilde{h}$ is independent of the macroscale coordinates.

Using (425), we can apply the averaging operators to express equation (448) in the form of

$$\nabla_{\boldsymbol{x}} \cdot (\boldsymbol{A} \cdot \nabla_{\boldsymbol{x}} p_0 + \boldsymbol{c}) + \boldsymbol{b} \cdot \nabla_{\boldsymbol{x}} p_0 + s_1 = 0, \tag{449}$$

where:

$$\boldsymbol{A} = \begin{pmatrix} \left\langle \left\langle w_{\theta,1} \right\rangle^{\tilde{h}} \right\rangle^{Y_X} & \left\langle \left\langle w_{\theta,2} \right\rangle^{\tilde{h}} \right\rangle^{Y_X} \\ \left\langle \langle w_{z,1} \rangle^{\tilde{h}} \right\rangle^{Y_X} & \left\langle \langle w_{z,2} \rangle^{\tilde{h}} \right\rangle^{Y_X} \end{pmatrix}; \tag{450}$$

$$\boldsymbol{b} = \begin{pmatrix} \left\langle \left\langle \frac{\partial}{\partial \bar{r}} \left(\bar{r} w_{r,1} \right) \right\rangle^{\tilde{h}} \right\rangle^{Y_X} + \frac{1}{\sqrt{2}} \left(\left\langle \left\langle \bar{r} \frac{\partial w_{z,1}}{\partial \bar{\theta}} \right\rangle^{\tilde{h}} \right\rangle^{Y_X} \sin\kappa + \left\langle \left\langle \bar{r} \frac{\partial w_{z,1}}{\partial \bar{z}} \right\rangle^{\tilde{h}} \right\rangle^{Y_X} \cos\kappa \right) \\ \left\langle \left\langle \frac{\partial}{\partial \bar{r}} \left(\bar{r} w_{r,2} \right) \right\rangle^{\tilde{h}} \right\rangle^{Y_X} + \frac{1}{\sqrt{2}} \left(\left\langle \left\langle \bar{r} \frac{\partial w_{z,2}}{\partial \bar{\theta}} \right\rangle^{\tilde{h}} \right\rangle^{Y_X} \sin\kappa + \left\langle \left\langle \bar{r} \frac{\partial w_{z,2}}{\partial \bar{z}} \right\rangle^{\tilde{h}} \right\rangle^{Y_X} \cos\kappa \right) \end{pmatrix}; \tag{451}$$

$$\boldsymbol{c} = \begin{pmatrix} \left\langle \left\langle w_{\theta,0} \right\rangle^{\tilde{h}} \right\rangle^{Y_X} \\ \left\langle \langle w_{z,0} \rangle^{\tilde{h}} \right\rangle^{Y_X} \end{pmatrix}; \tag{452}$$

$$s_1 = \left\langle \left\langle \frac{\partial}{\partial \bar{r}} \left(\bar{r} w_{r,0} \right) \right\rangle^{\tilde{h}} \right\rangle^{Y_X} \tag{453}$$

$$+ \frac{1}{\sqrt{2}} \left(\left\langle \left\langle \bar{r} \frac{\partial w_{z,0}}{\partial \bar{\theta}} \right\rangle^{\tilde{h}} \right\rangle^{Y_X} \sin\kappa + \left\langle \left\langle \bar{r} \frac{\partial w_{z,0}}{\partial \bar{z}} \right\rangle^{\tilde{h}} \right\rangle^{Y_X} \cos\kappa \right). \tag{454}$$

Focusing on the advection equation (415), we again apply the averaging operators $\left\langle \langle \cdot \rangle^{\tilde{h}} \right\rangle^{Y_X}$ to the equation while noting that

$$\left\langle \langle 1 \rangle^{\tilde{h}} \right\rangle^{Y_X} = 1 - \left\langle \tilde{h} \right\rangle^{Y_X} \tag{455}$$

is constant, and use the divergence theorem and periodicity to obtain

$$\begin{aligned}
&\frac{\partial \alpha_{0,l}}{\partial t} + \nabla_{\boldsymbol{x}} \cdot \left(\frac{\left\langle \langle \boldsymbol{u}_0 \rangle^{\tilde{h}} \right\rangle^{Y_X}}{1 - \left\langle \tilde{h} \right\rangle^{Y_X}} \alpha_{0,l} \right) \\
&= - \frac{\alpha_{0,l}}{1 - \left\langle \tilde{h} \right\rangle^{Y_X}} \left(\left\langle \left\langle \frac{\partial}{\partial \bar{r}} \left(\bar{r} u_{r,0} \right) \right\rangle^{\tilde{h}} \right\rangle^{Y_X} + \right. \\
&\qquad \left. \left\langle \left\langle \frac{\bar{r}}{\sqrt{2}} \left(\frac{\partial u_{z,0}}{\partial \bar{\theta}} \sin\kappa + \frac{\partial u_{z,0}}{\partial \bar{z}} \cos\kappa \right) \right\rangle^{\tilde{h}} \right\rangle^{Y_X} \right).
\end{aligned} \tag{456}$$

This can be represented in the form

$$\frac{\partial \alpha_{0,l}}{\partial t} + \nabla_{\boldsymbol{x}} \cdot (\boldsymbol{k} \alpha_{0,l}) = s_2, \tag{457}$$

where

$$\boldsymbol{k} = \frac{\boldsymbol{U}_0}{1 - \left\langle \tilde{h} \right\rangle^{Y_X}}, \tag{458}$$

$$\begin{aligned}
s_2 = &- \frac{\alpha_{0,l}}{1 - \left\langle \tilde{h} \right\rangle^{Y_X}} \left\{ \left\langle \left\langle \frac{\partial}{\partial \bar{r}} \left(\bar{r} w_{r,0} \right) \right\rangle^{\tilde{h}} \right\rangle^{Y_X} \right. \\
&+ \frac{1}{\sqrt{2}} \left(\left\langle \left\langle \bar{r} \frac{\partial w_{z,0}}{\partial \bar{\theta}} \right\rangle^{\tilde{h}} \right\rangle^{Y_X} \sin\kappa + \left\langle \left\langle \bar{r} \frac{\partial w_{z,0}}{\partial \bar{z}} \right\rangle^{\tilde{h}} \right\rangle^{Y_X} \cos\kappa \right) \\
&\qquad + \left[\left\langle \left\langle \frac{\partial}{\partial \bar{r}} \left(\bar{r} w_{r,1} \right) \right\rangle^{\tilde{h}} \right\rangle^{Y_X} \right. \\
&+ \frac{1}{\sqrt{2}} \left(\left\langle \left\langle \bar{r} \frac{\partial w_{z,1}}{\partial \bar{\theta}} \right\rangle^{\tilde{h}} \right\rangle^{Y_X} \sin\kappa + \left\langle \left\langle \bar{r} \frac{\partial w_{z,1}}{\partial \bar{z}} \right\rangle^{\tilde{h}} \right\rangle^{Y_X} \cos\kappa \right) \left. \right] \frac{\partial p_0}{\partial \theta} \\
&\qquad + \left[\left\langle \left\langle \frac{\partial}{\partial \bar{r}} \left(\bar{r} w_{r,2} \right) \right\rangle^{\tilde{h}} \right\rangle^{Y_X} \right. \\
&+ \left. \left. \frac{1}{\sqrt{2}} \left(\left\langle \left\langle \bar{r} \frac{\partial w_{z,2}}{\partial \bar{\theta}} \right\rangle^{\tilde{h}} \right\rangle^{Y_X} \sin\kappa + \left\langle \left\langle \bar{r} \frac{\partial w_{z,2}}{\partial \bar{z}} \right\rangle^{\tilde{h}} \right\rangle^{Y_X} \cos\kappa \right) \right] \frac{\partial p_0}{\partial z} \right\}.
\end{aligned} \tag{459}$$

As the initial and boundary conditions given by (365), (368)-(370) are independent of microscale coordinates, the initial and boundary conditions for the leading order macroscale variables are readily obtained.

Thus, the global homogenised problem which governs the leading order macroscopic variables, $\boldsymbol{U}_0, p_0$ and $\alpha_{0,l}$, is given by

$$\nabla_{\boldsymbol{x}} \cdot (\boldsymbol{A} \cdot \nabla_{\boldsymbol{x}} p_0 + \boldsymbol{c}) + \boldsymbol{b} \cdot \nabla_{\boldsymbol{x}} p_0 + s_1 = 0, \tag{460}$$

$$\frac{\partial \alpha_{0,l}}{\partial t} + \nabla_{\boldsymbol{x}} \cdot (\boldsymbol{k} \alpha_{0,l}) = s_2, \tag{461}$$

$$\boldsymbol{U}_0 = \left\langle \langle \boldsymbol{w}_0 \rangle^{\tilde{\hbar}} \right\rangle^{Y_X} + \left\langle \langle \boldsymbol{w}_1 \rangle^{\tilde{\hbar}} \right\rangle^{Y_X} \frac{\partial p_0}{\partial \theta} + \left\langle \langle \boldsymbol{w}_2 \rangle^{\tilde{\hbar}} \right\rangle^{Y_X} \frac{\partial p_0}{\partial z}, \tag{462}$$

on $\hat{\Omega}$, subject to

$$\alpha_{0,l} = 0 \qquad \text{on } \hat{\Omega} \text{ at } t = 0, \tag{463}$$

$$p_0 = 0 \qquad \text{on } \hat{\Gamma}_{in} \cup \hat{\Gamma}_{out} \cup \hat{\Gamma}_s, \tag{464}$$

$$\alpha_{0,l} = \alpha_D \qquad \text{on } \hat{\Gamma}_{in} \text{ where } \boldsymbol{U}_0 \cdot \boldsymbol{n} > 0, \tag{465}$$

$$\alpha_{0,l} = 0 \qquad \text{on } \hat{\Gamma}_{out} \cup \hat{\Gamma}_s \text{ where } \boldsymbol{U}_0 \cdot \boldsymbol{n} > 0, \tag{466}$$

where

$$\hat{\Omega} = \left\{ (\theta, z) : \theta \in \left(\theta_0, \frac{3\pi}{2} \right), z \in (0, h_w) \right\}, \tag{467}$$

$$\hat{\Gamma}_{in} = \left\{ (\theta, z) : \theta = \frac{3\pi}{2}, z \in (0, h_w) \right\}, \tag{468}$$

$$\hat{\Gamma}_{out} = \left\{ (\theta, z) : \theta = \theta_0, z \in (0, h_w) \right\}, \tag{469}$$

$$\hat{\Gamma}_s = \left\{ (\theta, z) : \theta \in \left(\theta_0, \frac{3\pi}{2} \right), z \in \{0, h_w\} \right\}, \tag{470}$$

$\boldsymbol{A}, \boldsymbol{c}, \boldsymbol{b}, s_1$ are given by (450)-(454), respectively, $\boldsymbol{k}$ is given by (458) and s_2 is given by (459).

5.7 HOMOGENISED SYSTEM DISCUSSION

The full homogenisation problem consists of the local problem (427), (428), (432)-(437) which governs the microscopic variables $\boldsymbol{w}_i, \gamma_i, i = 0, 1, 2$, and global problem (460)-(466) which governs the macroscopic variables $\boldsymbol{U}_0, p_0, \alpha_{0,l}$.

To compare both the local problem's governing equations (427) and (428) and global problem's governing equations (460)-(462) with other work, let us consider the single-phase case where $\alpha_{0,l} = 1$. Substituting (425) into (448), we observe that equation (461) is automatically satisfied.

The governing equation (460) has similarities to both the Reynolds equation (98) derived in Chapter 3 and Darcy's law given by (308) and (309). Here, $\boldsymbol{A}$ behaves as an effective permeability tensor which appears due to flow in the gaps between the abrasives and workpiece. The vector $\boldsymbol{c}$ appears due to flow induced from the shearing of the wheel. While an equivalent shear term appears in equation (98), flow in porous media does not typically involve microscopic surfaces moving relative to each other. Therefore, an equivalent term does not appear in (308) and (309). The vector $\boldsymbol{b}$ and scalar s_1 arise due to the $O(\varepsilon)$ curvature correction-like terms which appear in (448). These curvature terms were not reported by the work of Fabricius et al. [31]. This is due to their consideration of the problem under a Cartesian coordinate system with no curvature present, unlike the channel in the grinding zone where the effect of curvature appears below leading order. Similarly, equation (98) was derived by only considering leading order terms in a Cartesian coordinate system, so equivalent terms do not appear there either.

The form of the local equations (427) and (428) is in agreement with the form found by Fabricius et al. [31], but in contrast to the form derived by Kane et al. [44]. The reason for this is due to the latter considering homogenisation of the Reynolds equation, therefore the channel height is implicitly assumed to be small compared to the length scale characterising the microscale periodicities. Consequently, the lubrication approximation is assumed to also hold on the microscale, resulting in the microscale system being a two dimensional problem.

We denote the curvature terms appearing in the right-hand side of equation (448) by

$$I = -\left\langle \left\langle \frac{\partial}{\partial \bar{r}} \left(\bar{r} u_{r,0} \right) + \frac{\bar{r}}{\sqrt{2}} \left(\frac{\partial u_{z,0}}{\partial \bar{\theta}} \sin \kappa + \frac{\partial u_{z,0}}{\partial \bar{z}} \cos \kappa \right) \right\rangle^{\tilde{h}} \right\rangle^{Y_X}. \tag{471}$$

To gain a deeper understanding of how I varies with different parameters, we express I as

$$I = -\int_0^1 \int_0^1 \int_{\tilde{h}}^1 \nabla_{\boldsymbol{X}} \cdot \left[\bar{r} \left(u_{r,0} \boldsymbol{e}_r + u_{z,0} \boldsymbol{e}_z \right) \right] \mathrm{d}\bar{r} \mathrm{d}\bar{\theta} \mathrm{d}\bar{z}. \tag{472}$$

Here, we have used the definition of $\nabla_{\boldsymbol{X}} \cdot$ acting on a vector with zero θ component.

Applying the divergence theorem on the volume integral in (472), it can be written as the surface integral

$$I = \int_{\partial Y} \bar{r} \left(u_{r,0} \boldsymbol{e}_r + u_{z,0} \boldsymbol{e}_z \right) \cdot \boldsymbol{n} \mathrm{d}\Gamma, \tag{473}$$

with $\boldsymbol{n}$ the inward pointing unit normal.

Using the impermeability conditions from (436) and (437), i.e.

$$\left(\boldsymbol{u}_0 + \boldsymbol{e}_\theta \right) \cdot \boldsymbol{n} = 0 \text{ on } \bar{r} = \tilde{h}, \tag{474}$$

$$\boldsymbol{u}_0 \cdot \boldsymbol{n} = 0 \text{ on } \bar{r} = 1, \tag{475}$$

where $\boldsymbol{e}_\theta$ is the unit basis vector in the θ direction, along with the periodicity of the unit cell, this surface integral can be restated as

$$\begin{aligned} I &= -\int_{\partial Y_{\tilde{h}}} \tilde{h} \left(u_{\theta,0} + 1 \right) \boldsymbol{e}_\theta \cdot \boldsymbol{n} \mathrm{d}\Gamma \\ &= \int_{\partial Y_{\tilde{h}}} \frac{\left(u_{\theta,0} \right)_{\bar{r}=\tilde{h}} + 1}{2\sqrt{1 + \left(\frac{\partial \tilde{h}}{\partial \bar{\theta}} \right)^2 + \left(\frac{\partial \tilde{h}}{\partial \bar{z}} \right)^2}} \left(\frac{\partial \tilde{h}^2}{\partial \bar{\theta}} \cos \kappa - \frac{\partial \tilde{h}^2}{\partial \bar{z}} \sin \kappa \right) \mathrm{d}\Gamma. \end{aligned} \tag{476}$$

Here, we have used that $\bar{r} = \tilde{h}$ on $\partial Y_{\tilde{h}}$,

$$q\frac{\partial q}{\partial x} = \frac{1}{2}\frac{\partial q^2}{\partial x}, \tag{477}$$

for general function $q \equiv q(x)$ and variable x,

$$\left(u_{r,0}\boldsymbol{e}_r + u_{z,0}\boldsymbol{e}_z\right)\cdot\boldsymbol{n} = -\left(u_\theta + 1\right)\cdot\boldsymbol{n} \tag{478}$$

from (474) and

$$\boldsymbol{e}_\theta\cdot\boldsymbol{n} = \frac{1}{\sqrt{1+\left(\frac{\partial\tilde{h}}{\partial\bar{\theta}}\right)^2+\left(\frac{\partial\tilde{h}}{\partial\bar{z}}\right)^2}}\left(\frac{\partial\tilde{h}}{\partial\bar{z}}\sin\kappa - \frac{\partial\tilde{h}}{\partial\bar{\theta}}\cos\kappa\right) \tag{479}$$

using identities in Appendix B.

Hence, we observe from (476) that when no-slip holds on the rough surface (i.e. when $\left(u_{\theta,0}\right)_{\bar{r}=\tilde{h}} = -1$), $I = 0$. However, when the velocity profile is not constant, in particular when the slip boundary condition is considered, it is not clear how this term should behave.

5.8 HOMOGENISED SYSTEM NUMERICAL SCHEME

5.8.1 *Local Problem Scheme*

For the local problem, we look to solve the system (427) and (428), subject to periodic boundary conditions (432)-(435) and slip boundary conditions (436), (437) using the finite element method (FEM). Specifically, we spatially discretise the system with the continuous Galerkin (CG) FEM. To this end, we define various objects we will use in finding the solution. Let $H^1_{per}(Y)$ and $L^2_{per}(Y)$ be the solution spaces such that

$$H^1_{per}(Y) = \left\{f \in H^1(Y) : f(\bar{r},\bar{\theta},\bar{z}) \text{ is periodic in } \bar{\theta},\bar{z} \text{ on } Y\right\}, \tag{480}$$

$$L^2_{per}(Y) = \left\{f \in L^2(Y) : f(\bar{r},\bar{\theta},\bar{z}) \text{ is periodic in } \bar{\theta},\bar{z} \text{ on } Y\right\}, \tag{481}$$

where H^1 and L^2 are Sobolev and Lebesgue spaces as defined in most textbooks on functional analysis. See, for example, [21].

To formulate the discrete problem, we first define the mesh $\mathcal{T}$ which partitions the domain Y into tetrahedra elements, denoted by κ. The CG FEM then restricts the spaces (480) and (481) to finite dimensional polynomial subspaces over $\mathcal{T}$. The finite element spaces we consider are

$$\boldsymbol{V}_{h,2,per} = \left\{ \boldsymbol{w} \in \left[H^1_{per}(Y) \right]^3 : \boldsymbol{w}|_\kappa \in \left[\mathbb{P}_2(\kappa) \right]^3 \ \forall \kappa \in \mathcal{T} \right\}, \tag{482}$$

$$Q_{h,1,per} = \left\{ q \in L^2_{per}(Y) : q|_\kappa \in \mathbb{P}_1(\kappa) \ \forall \kappa \in \mathcal{T} \right\}, \tag{483}$$

where $\mathbb{P}_k(\kappa)$ is the set of continuous polynomials of degree at most k on the element $\kappa \in \mathcal{T}$. The spaces (482) and (483) satisfy the inf-sup condition [19] on the saddle-point structure [18] that arises from the discretisation of the Stokes equations [22]. The inf-sup condition must be satisfied to ensure the scheme is stable.

We also define $\boldsymbol{n}, \boldsymbol{t}_1, \boldsymbol{t}_2$ to be the inward pointing unit normal and two unit tangent vectors, respectively, to ∂Y which form an orthogonal system of vectors. Additionally, we denote $\boldsymbol{E_X}$ as the local rate of strain tensor.

With these definitions, we state our discrete formulation: find $\boldsymbol{w}_{i,h} \in \boldsymbol{V}_{h,2,per}$, $\gamma_{i,h} \in Q_{h,1,per}$ such that

$$A^s_{i,h}(\boldsymbol{w}_{i,h}, \boldsymbol{v}_{i,h}; \alpha_{0,l}) + B^s_h(\boldsymbol{v}_{i,h}, \gamma_{i,h}) = l^s_i(\boldsymbol{v}_{i,h}), \tag{484}$$

$$B^s_h(\boldsymbol{w}_{i,h}, q_{i,h}) = 0, \tag{485}$$

for all $\boldsymbol{v}_{i,h} \in \boldsymbol{V}_{h,2,per}$, $q_{i,h} \in Q_{h,1,per}$, where $\alpha_{0,l} \in L^\infty(Y)$ (informally, this is the requirement that $\alpha_{0,l}$ is bounded on Y; see [21] for a precise definition of this space).

In (484) and (485), for $i = 0, 1, 2$, the form: A_h^s is given by

$$\begin{aligned} A_h^s\left(\boldsymbol{w}_{i,h}, \boldsymbol{v}_{i,h}; \alpha_{0,l}\right) = &- \int_Y 2\mu_{0,m} \boldsymbol{E}_{\boldsymbol{X}}\left(\boldsymbol{w}_{i,h}\right) : \boldsymbol{E}_{\boldsymbol{X}}\left(\boldsymbol{v}_{i,h}\right) \mathrm{d}Y \\ &- \int_{\partial Y_{\tilde{h}} \cup \partial Y_1} \frac{1}{\zeta}\left(\boldsymbol{w}_{i,h} \cdot \boldsymbol{n}\right) \boldsymbol{n} \cdot \boldsymbol{v}_{i,h} \mathrm{d}\Gamma \\ &- \int_{\partial Y_{\tilde{h}} \cup \partial Y_1} \frac{1}{\hat{\beta}} \sum_{j=1}^{2}\left(\boldsymbol{w}_{i,h} \cdot \boldsymbol{t}_j\right) \boldsymbol{t}_j \cdot \boldsymbol{v}_{i,h} \mathrm{d}\Gamma; \end{aligned} \tag{486}$$

B_h^s is given by

$$B_h^s\left(\boldsymbol{v}_{i,h}, \gamma_{i,h}\right) = \int_Y \gamma_{i,h} \nabla \cdot \boldsymbol{v}_{i,h} \mathrm{d}Y; \tag{487}$$

l_i^s is given by

$$\begin{aligned} l_i^s\left(\boldsymbol{v}_{i,h}\right) = &\int_Y \boldsymbol{f}_i \cdot \boldsymbol{v}_{i,h} \mathrm{d}Y \\ &+ \int_{\partial Y_{\tilde{h}}} \frac{1}{\hat{\beta}} \mathbf{1}_{\{i=0\}} \sum_{j=1}^{2}\left(\boldsymbol{e}_\theta \cdot \boldsymbol{t}_j\right) \boldsymbol{t}_j \cdot \boldsymbol{v}_{i,h} \mathrm{d}\Gamma. \end{aligned} \tag{488}$$

In (488), $\boldsymbol{f}_i$ is given by

$$\boldsymbol{f}_0 = \mathbf{0}, \tag{489}$$

$$\boldsymbol{f}_1 = \boldsymbol{e}_\theta, \tag{490}$$

$$\boldsymbol{f}_2 = \boldsymbol{e}_z, \tag{491}$$

for $i = 0, 1, 2$, respectively.

To weakly enforce the slip conditions (436) and (437), we look to split the surface stress tensor term as

$$\boldsymbol{n} \cdot \boldsymbol{P}_i = \boldsymbol{n} \cdot \boldsymbol{P}_i \cdot (\boldsymbol{I} - \boldsymbol{n}\boldsymbol{n}) + \left(\boldsymbol{n} \cdot \boldsymbol{P}_i \cdot \boldsymbol{n}\right) \boldsymbol{n}. \tag{492}$$

and then substitute in the velocity differences for the surface tangential stress component. However, with no condition on the surface normal stress component, this results in an ill-posed problem. We alleviate this issue by weakly enforce the impermeability condition with a regularisation method, following

John [41]. We note that Nitsche's method (see, for example, [32] and [67]) and Lagrange multipliers (see, for example, [87] and [88]) are other possible methods to avoid this ill-posedness. Each method can be seen to act similarly on the normal stress component, thus the regularisation method is chosen for its simple implementation and physical explanation.

To this end, we consider the general boundary condition describing a linear dependency between velocity difference at a surface and the stress exerted by the fluid there. Specifically, this is

$$\boldsymbol{w}_i - \boldsymbol{V} = 2\hat{\beta}\mu_{0,m}\boldsymbol{n}\cdot\boldsymbol{E}_{\boldsymbol{X}}\left(\boldsymbol{w}_i\right)\cdot\left(\boldsymbol{I}-\boldsymbol{n}\boldsymbol{n}\right)+\zeta\left(\boldsymbol{n}\cdot\boldsymbol{P}_i\cdot\boldsymbol{n}\right)\boldsymbol{n}. \tag{493}$$

Physically, the normal projection of (493) gives the resistance condition

$$\left(\boldsymbol{w}_i-\boldsymbol{V}\right)\cdot\boldsymbol{n}=\zeta\boldsymbol{n}\cdot\boldsymbol{P}_i\cdot\boldsymbol{n}. \tag{494}$$

Equation (494) states that the penetration of fluid through a surface is resisted by the normal stress at the surface with a resistance coefficient denoted by ζ. We see that when $\zeta\to\infty$ in (494), there is free penetration of fluid through the surface. Conversely, when $\zeta\to 0$ there is no penetration of fluid through the surface, yielding the familiar impermeability with slip condition. Indeed, John used $\zeta = 1\times 10^{-12}$ to weakly enforce impermeability in this way.

Thus, to derive the discrete form A_h^s given by (486), the first term uses that the contraction of a symmetric and antisymmetric tensor is 0. The second and third terms arise from the splitting given by (492) and the general boundary condition (493) with the regularisation constant ζ which weakly enforces impermeability. Taking the projection of (493) with $\boldsymbol{n},\boldsymbol{t}_1,\boldsymbol{t}_2$ then substituting in for each orthogonal velocity difference projection yields these terms. Typically, we took $\zeta\approx 1\times 10^{-8}$ as the matrix problem became ill-conditioned for smaller values.

Finally, for the purposes of clarity when interpreting local solutions, the shear velocity $\boldsymbol{w}_0$ will be translated such that the pyramid is considered at rest and

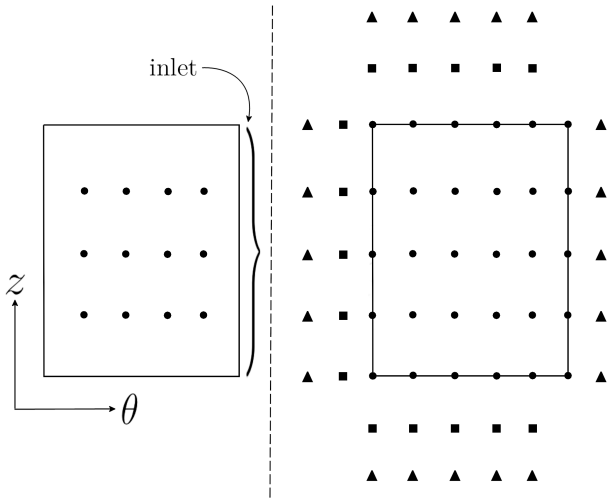

Figure 33: Illustration of the solution and ghost grid points necessary for us to solve equation (460) (left) and the advection equation (461) (right). Circles show solution grid points of the discretised domain while squares and triangles represent ghost points originating from the numerical schemes used: squares show ghost points required for both the central difference and KT schemes whilst triangles show ghost points needed only for the KT scheme.

the workpiece is moving. To this end, we solve for the vector components $w_{\bar{r},0}, \tilde{w}_{\bar{\theta},0}$ and $\tilde{w}_{\bar{z},0}$ such that

$$\begin{aligned} \boldsymbol{w}_0 &= w_{\bar{r},0}\hat{\boldsymbol{e}}_{\bar{r}} + w_{\bar{\theta},0}\hat{\boldsymbol{e}}_{\bar{\theta}} + w_{\bar{z},0}\hat{\boldsymbol{e}}_{\bar{z}} \\ &= w_{\bar{r},0}\hat{\boldsymbol{e}}_{\bar{r}} + \left(\tilde{w}_{\bar{\theta},0} - \cos\kappa\right)\hat{\boldsymbol{e}}_{\bar{\theta}} + \left(\tilde{w}_{\bar{z},0} + \sin\kappa\right)\hat{\boldsymbol{e}}_{\bar{z}}, \end{aligned} \tag{495}$$

where $\hat{\boldsymbol{e}}_{\bar{r}}, \hat{\boldsymbol{e}}_{\bar{\theta}}, \hat{\boldsymbol{e}}_{\bar{z}}$ are the leading order unit basis vectors for the microscopic coordinate system. For expressions of the local basis vectors in terms of the macroscopic basis vectors and expressions for the normal and tangent vectors we use in the scheme presented here, see Appendix B.

5.8.2 *Global Problem Numerical Scheme*

Here we detail our numerical scheme for solving the global problem (460)-(466). Regarding the spatial discretisation, we use a standard central difference finite difference method [56] for equation (460) and the Kurganov-Tadmor (KT)

scheme [50] for the discretisation of the advection equation (461). For the temporal discretisation, a total variation diminishing Runge-Kutta (RK) 2^{nd} order scheme is used, specifically the modified Euler method [81]. We can exploit the appearance of a time derivative in only one of the equations in order to solve the system in a segregated manner. That is, each equation is solved alone for the solution of one numerical variable using recent approximations to the remaining variable. This method will be explained in greater depth below. The problem domain, including the boundaries, is discretised by N equally spaced grid points over the θ axis and M equally spaced grid points over the z axis.

At every grid point lying on the domain boundary in the discretised domain, we assign a value of $p_0 = 0$ to satisfy boundary condition (464). The volume fraction boundary conditions require more care. The characteristic structure of the advection equation (461) requires that a Dirichlet boundary condition for $\alpha_{0,l}$ is provided at every point of the boundary where $\boldsymbol{U}_0 \cdot \boldsymbol{n} > 0$, where $\boldsymbol{n}$ is the inward pointing unit normal to the boundary. Thus, during the numerical scheme we must check at every grid point on the boundaries whether $\boldsymbol{U}_0$ is directed into the domain. As we are using an explicit scheme, it is possible for us to calculate $\boldsymbol{U}_0 \cdot \boldsymbol{n}$ using previous solutions. At grid points on the z boundaries where an influx is predicted, we assign the value $\alpha_{0,l} = 0$ to represent the surrounding air entering the grinding zone. Otherwise, the volume fraction at those grid points is found from the numerical solution using the KT scheme.

The spatial discretisations we use for the global problem require grid points which exist outside the physical domain. Therefore, we require a consistent method to manage how we treat these grid points. In the scheme introduced here, quantities at ghost points, for example, pressure, are assigned the value of the quantity at the nearest grid point located on the physical boundary. Thus, the pressure at, for example, the ghost point situated at grid point $(k, M+1)$, for some $1 \leq k \leq N$, will be 0. The value of $\alpha_{0,l}$ at this ghost point will take the value of $\alpha_{0,l}$ at the grid point (k, M). This is dependent on the sign of $\boldsymbol{U}_0$ at that point and will be either 0 or found via the KT scheme. The use of ghost points in this way allows us to avoid needing to switch our numerical scheme to

a lower order, one-sided derivative approximation at the boundaries. Also, it prescribes the value of p_0 that we would physically expect for any point located outside the grinding zone. Other possible methods are described in [55].

Pressure Equation

For the central difference discretisation of equation (460), the spatial derivatives are approximated with 2^{nd} order accuracy [55]. The approximations to the partial derivatives are given by

$$\frac{\partial q}{\partial \theta} \approx \frac{q_{i+1,j} - q_{i-1,j}}{2\Delta\theta}, \tag{496}$$

$$\frac{\partial q}{\partial z} \approx \frac{q_{i,j+1} - q_{i,j-1}}{2\Delta z}, \tag{497}$$

$$\frac{\partial^2 q}{\partial \theta^2} \approx \frac{q_{i+1,j} - 2q_{i,j} + q_{i-1,j}}{(\Delta\theta)^2}, \tag{498}$$

$$\frac{\partial^2 q}{\partial z^2} \approx \frac{q_{i,j+1} - 2q_{i,j} + q_{i,j-1}}{(\Delta z)^2}. \tag{499}$$

Here, q could be the mixture viscosity or pressure, $\Delta\theta, \Delta z$ are the grid spacings in the θ, z coordinates and subscript i, j denotes the numerical value of a quantity at the grid point $\theta = i\Delta\theta, z = j\Delta z$, respectively. In the discretisation of the domain, the standard ordering for the grid points was used, that is, ordering began at the bottom left grid point and incremented by one per grid point in the positive θ direction, before reaching the end of the row and incrementing the order by one at the next row's left-most grid point and continuing the process as for the previous row.

Upon substituting the approximations (496)-(499) into (460), we arrive at a linear system of equations of the form

$$\boldsymbol{M}\boldsymbol{z} = \boldsymbol{y}, \tag{500}$$

where $\boldsymbol{M}$ is an $(N-2)(M-2) \times (N-2)(M-2)$ sparse matrix of coefficients, $\boldsymbol{z}$ is an $(N-2)(M-2)$ row matrix of the pressure solution at each grid point

and $\boldsymbol{y}$ is an $(N-2)(M-2)$ row matrix of the source term at each grid point. The reduction of grid points is due to the Dirichlet boundary condition for p_0.

To calculate the solution to this matrix problem and obtain the pressure distribution, we use a direct solver. To this end, the sparse system (500) was solved for the pressure distribution, represented by $\boldsymbol{z}$, by LU decomposition using the C++ library Eigen [35]. Eigen is natively written and optimised for C++, implementing features such as vectorisation and cache blocking to increase the floating point operations per second, while being simple to incorporate in a program.

With the numerical solution for p_0, we are able to use this in the advection equation in order to calculate the volume fraction distribution, $\alpha_{0,l}$.

Advection Equation

To numerically approximate a solution for the advection equation (461), the semi-discrete KT scheme is used to spatially discretise the divergence of the flux and a RK 2^{nd} order scheme is used for the temporal discretisation. A constant step size is used throughout the scheme for each of the spatial coordinates, with the same grid points used for the KT scheme as were used in the central difference discretised pressure PDE (with the addition of new ghost points). Figure 33 displays an illustration of the (spatially discretised) numerical grid used to solve the equations with these two schemes.

The KT scheme assumes that at some initial time t_0, a piecewise continuous linear polynomial based upon the initial data at the specified grid points is fitted, and the cell averages of this known. The fundamental idea begins from Godunov's seminal work where an evolving discontinuity at a cell boundary can be considered as a local Riemann problem, with Riemann fans (waves of rarefaction) joining the initial discontinuities in the data [34]. The KT scheme proceeds by temporally integrating the (averaged) conservation law along a time step and then spatially integrating the known solution at t_0 over a cell at the regions occupied by the Riemann fans and the remaining cell separately. Using quadrature methods to approximate these integrals allows for the cell

averages solution at the next time step to be constructed using a piecewise linear representation to combine the solutions in the separate cell regions.

The KT scheme is spatially 2^{nd} order accurate which offers no discernible advantage over other schemes such as, for example, the relaxation scheme [40] and Nessyahu-Tadmor (NT) scheme [65]. However, its advantage comes from two main parts: the lack of explicit dependence of numerical viscosity on the time step, which makes the KT scheme more appropriate for convection-type problems than the NT scheme which has a $\frac{1}{\Delta t}$ dependence and, thus, encounters problems over small-time steps; ease of implementation, for example the relaxation scheme requires the addition of a source term involving a small, user-defined relaxation parameter. The KT scheme also has a 3^{rd} order accurate extension, which uses higher order polynomials to interpolate between the solutions in the separate cell regions [49].

We note that we have source terms appearing in the advection equation (461). As source terms were not included in the original KT scheme derivation, they must be included as an extension to the original scheme. Here, the source terms are spatially discretised following a method used for a similar scheme in [64]. Doing so, it can be found that source terms are included in the semi-discrete KT scheme through the terms' evaluation at the current grid point.

Implementation

We will write the spatially discretised pressure equation (460) and advection equation (461) in the form

$$0 = G\left(p_0, \alpha_{0,l}\right), \tag{501}$$

$$\frac{\mathrm{d}\alpha_{0,l}}{\mathrm{d}t} = F\left(p_0, \alpha_{0,l}\right), \tag{502}$$

which we can represent as the system

$$\frac{\mathrm{d}}{\mathrm{d}t}\begin{pmatrix} 0 \\ \alpha_{0,l} \end{pmatrix} = \begin{pmatrix} G\left(p_0, \alpha_{0,l}\right) \\ F\left(p_0, \alpha_{0,l}\right) \end{pmatrix}, \tag{503}$$

where G and F represent terms spatial discretisation of (460) and (461), respectively, through central differences and the KT scheme. Both arguments p_0 and $\alpha_{0,l}$ have a dependency on t. In the following exposition, we will suppose the time step is the same $\Delta t > 0$ throughout the numerical solution. This allows the notation of superscript (k) to denote a quantity at time $t = k\Delta t$ (after temporal discretisation).

To solve the system in a segregated manner, we begin at $t_0 = 0$ and specify the initial $\alpha_{0,l}^{(0)}$ profile as the zero profile via the initial condition (463). The value of $\alpha_{0,l}$ at the inlet grid points given by the time-dependent boundary condition (465). Next, we denote $\tilde{t}_0 = t_0 + \frac{\Delta t}{2}$ and time step to $t_1 = t_0 + \Delta t$.

Now, with the aforementioned RK discretisation, we perform the predictor step (the backward Euler method) for the intermediate solution, denoted by $\tilde{\cdot}$, of $\alpha_{0,l}$ to arrive at the system

$$\begin{pmatrix} 0 \\ \widetilde{\alpha_{0,l}^{(t_1)}} \end{pmatrix} = \begin{pmatrix} G\left(p_0^{(t_0)}, \alpha_{0,l}^{(t_0)}\right) \\ \alpha_{0,l}^{(t_0)} + \Delta t \left[F\left(p_0^{(t_0)}, \alpha_{0,l}^{(t_0)}\right)\right] \end{pmatrix}. \tag{504}$$

These equations can be solved sequentially due to the quasistatic nature of the pressure equation and the explicit time stepping. In detail, since we know $\alpha_{0,l}^{(t_0)}$, we can rearrange the linear equation

$$G\left(p_0^{(t_0)}, \alpha_{0,l}^{(t_0)}\right) = 0, \tag{505}$$

into a matrix equation of the form (500). This can then be solved to find the value of $p_0^{(t_0)}$ after the local solutions have been computed at all grid points using $\alpha_{0,l}^{(t_0)}$. With this, we can calculate

$$\widetilde{\alpha_{0,l}^{(t_1)}} = \alpha_{0,l}^{(t_0)} + \Delta t \left[F\left(p_0^{(t_0)}, \alpha_{0,l}^{(t_0)}\right)\right] \tag{506}$$

in a straightforward manner. The corrector step then uses the computed solution $\widetilde{\alpha_{0,l}^{(t_1)}}$ to calculate an improved solution at t_1. Specifically, we have the system

$$\begin{pmatrix} 0 \\ \alpha_{0,l}^{(t_1)} \end{pmatrix} = \begin{pmatrix} G\left(p_0^{(\tilde{t}_0)}, \widetilde{\alpha_{0,l}^{(t_1)}}\right) \\ \frac{1}{2}\alpha_{0,l}^{(t_0)} + \frac{1}{2}\widetilde{\alpha_{0,l}^{(t_1)}} + \frac{\Delta t}{2}\left[F\left(p_0^{(\tilde{t}_0)}, \widetilde{\alpha_{0,l}^{(t_1)}}\right)\right] \end{pmatrix}. \tag{507}$$

The method for solving the system (507) is identical to (504): as we know $\widetilde{\alpha_{0,l}^{(t_1)}}$, we can solve the corresponding local problem at all grid points so that we can solve

$$G\left(p_0^{(\tilde{t}_0)}, \widetilde{\alpha_{0,l}^{(t_1)}}\right) = 0 \tag{508}$$

for $p_0^{(\tilde{t}_0)}$. This lets us calculate

$$\alpha_{0,l}^{(t_1)} = \frac{1}{2}\alpha_{0,l}^{(t_0)} + \frac{1}{2}\widetilde{\alpha_{0,l}^{(t_1)}} + \frac{\Delta t}{2}\left[F\left(p_0^{(\tilde{t}_0)}, \widetilde{\alpha_{0,l}^{(t_1)}}\right)\right] \tag{509}$$

at all grid points.

We remark that the region of the boundaries on $z = 0, h_w$ where fluid enters the grinding zone are unknown a-priori, so it must be determined using (462). To determine where these regions occur so that boundary conditions (465) and (466) can be applied, the local solutions must be calculated at all boundary grid points.

Once the predictor step is complete, $p_0^{(t_1)}$ is found by calculating the local solutions using $\alpha_{0,l}^{(t_1)}$ and the RK scheme is repeated. The l^2 norm of the relative approximation difference for the two recently found $\alpha_{0,l}^{(t_1)}$ is then calculated, and this process is repeated until the error is below a tolerance. That is, iterations

are performed until two subsequent solutions at t_1 are found, $\alpha^{(t_1)}_{0,l,current}$ and $\alpha^{(t_1)}_{0,l,previous}$, such that

$$tol > \frac{||\alpha^{(t_1)}_{0,l,current} - \alpha^{(t_1)}_{0,l,previous}||_{l^2}}{||\alpha^{(t_1)}_{0,l,current}||_{l^2}} = \sqrt{\frac{\sum_j \left(\alpha^{(t_1)}_{0,l,j,current} - \alpha^{(t_1)}_{0,l,j,previous}\right)^2}{\sum_j \left(\alpha^{(t_1)}_{0,l,j,current}\right)^2}}, \tag{510}$$

where subscript j denotes the value at grid point j of the corresponding approximation. Relative convergence is usually achieved after the first two predictor steps are undertaken.

The procedure following the specification of the initial $\alpha_{0,l}$ distribution above can be repeated until the desired final time is reached.

5.8.3 *Local to Global Coupling*

The main complexity of the homogenised system lies in the two-way coupling of the governing equations: coefficients in the global problem depend on the averaged local solutions, which themselves depend on $\alpha_{0,l}$. Consequently, how this coupling is handled will be a major part of the numerical scheme.

In the local problem, we observe that each local problem is distinguished by three factors: the geometry, the slip length, $\hat{\beta}$, and the volume fraction, $\alpha_{0,l}$. Thus, if the physical system is specified, the only parameterisation of each (independent) local problem is through $\alpha_{0,l}$. In addition to this, the coupling of the two systems is manifested in the global problem only through the microscopic velocity averages appearing as coefficients. Acknowledging these two features, the numerical procedure begins with the initialisation of all physical parameters in the problem, e.g the radius of the wheel, velocity of the wheel, slip length. The local problem is then solved for a range of values of $\alpha_{0,l}$ between $[0, 1]$, with a greater density of sampling points in regions where the microscopic velocity solutions experience relatively large changes.

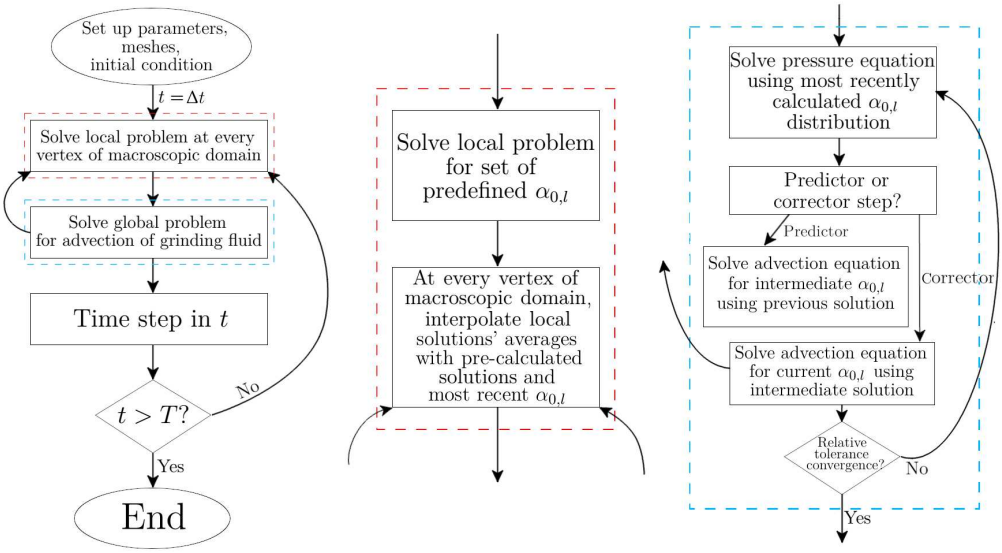

Figure 34: Flow chart graphically demonstrating the numerical procedure for finding solutions to the homogenised system.

The intention of pre-calculating local solutions is that we will be able to avoid the extremely computationally expensive procedure of iterating solutions back and forth at every grid point in the global domain. Instead, we can determine the global problem's coefficients (which consist of averages of the microscopic velocity components) for a specified $\alpha_{0,l}$ by interpolation of the pre-calculated averages of the microscopic velocity components. Such a method would not be suitable in situations where the local flow was highly chaotic or displayed a large degree of sensitivity to perturbations in $\alpha_{0,l}$, for example, if the local flow exhibited effects such as the Rayleigh-Taylor instability or was dominated by turbulent effects (see [27] for further details on the Rayleigh-Taylor instability or more examples of unstable flows). However, for the current Stokes flow we consider, these inertial phenomena are not present in the flow and pre-calculating the local solutions is appropriate[1].

Concentrating on the global problem, the solution of a local problem is required at every grid point in order to determine the system. By interpolating the value of the average of the local solution, based on the numerical approxi-

1 In fact, for the inertial problems that are considered later on in this thesis, the local flow showed no extreme sensitivity to perturbations in $\alpha_{0,l}$ there either.

```
space_element_velocity = df.VectorElement("Lagrange", mesh.ufl_cell(), 2)
space_element_pressure = df.FiniteElement("Lagrange", mesh.ufl_cell(), 1)
mixed_element = df.MixedElement([space_element_velocity,
    space_element_pressure])
mixed_space = df.FunctionSpace(mesh, mixed_element, constrained_domain =
    boundary.mesh_periodic_boundaries())
F1 = df.inner(ns_f.stress(tru1, trp1, alpha_val, mix_visc), \
        ns_f.strainRate(tev1))*dx + teq1*ns_f.divergence(tru1)*dx \
\
+ df.inner(f1, tev1)*dx

a1 = df.lhs(F1)
L1 = df.rhs(F1)
df.solve(a1 == L1, sol1, bcs1)
```

Figure 35: Short Python code showing the polynomial space setup and weak formulation definition for Stokes flow. The ns_f module contains user-defined differential operators which act on the microscopic coordinate system, X.

mation of $\alpha_{0,l}$ from the initial condition or found with the KT and RK schemes, the coefficients can be specified and the global problem can be solved. Figure 34 presents a condensed illustration of the numerical scheme outlined here.

5.8.4 *Finite Element Method Solver*

To solve the discretised system arising from (484) and (485), we use the FEM package FEniCS [13]. Once FEniCS has been given a mesh, we are able to setup pre-built polynomial spaces over the mesh simply by calling a function in the FEniCS library, dolfin. The weak formulation must then be implemented. Although standard differential operators are built into FEniCS, our local problem involves scaled differential operators which must be implemented ourselves. A short representative snippet of our FEniCS code that sets up and solves the discrete Stokes problem is shown in figure 35. The ns_f module contains the differential operators acting on X.

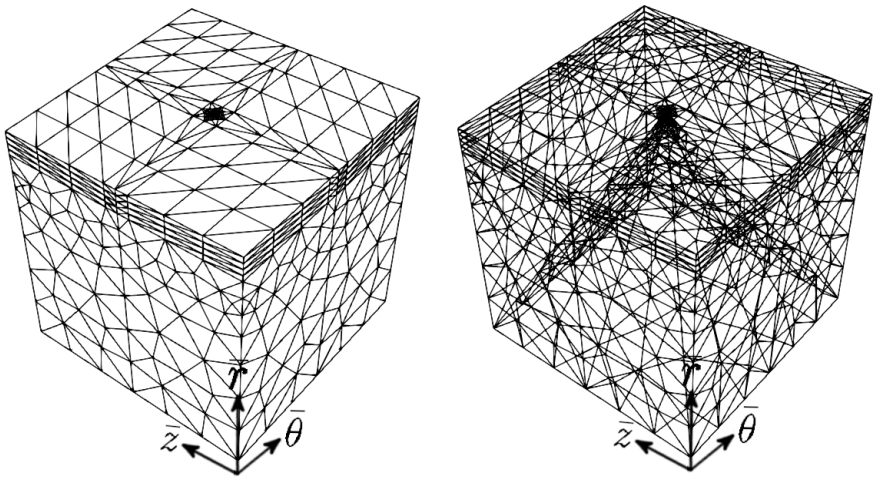

Figure 36: Two views of the surface mesh for a mesh used in simulations of the local problem. The four-fold rotational symmetry is clearly exhibited on the surfaces.

5.8.5 *Local Geometry Meshing*

Focusing on the geometry, the meshes that were generated generally had rotational symmetry of order four as well as two planes of reflection symmetry and were formed of three distinct parts: a structured boundary layer mesh, a dense unstructured mesh surrounding the contact point and a relatively coarse unstructured mesh further from the top surface (remembering that the problem was posed such that the workpiece is stationary). The sub-slip length size of the elements in the dense meshed region around the contact point ensures that any flow features due to the slip condition are fully resolved there. Figure 36 provides two views of the surface mesh for a mesh used in simulations of the local problem. As a reference, this mesh with Taylor-hood elements resulted in 1.1787×10^5 degrees of freedom to solve for.

The surface integral over $\partial Y_{\tilde{h}}$ is separated over the four individual faces and each are evaluated with Gaussian quadrature using sampling points in the faces' interior [73]. Doing so avoids the evaluation of the unit normal at points where it can not be uniquely defined. All geometries and meshes were created using the open-source software Gmsh [33].

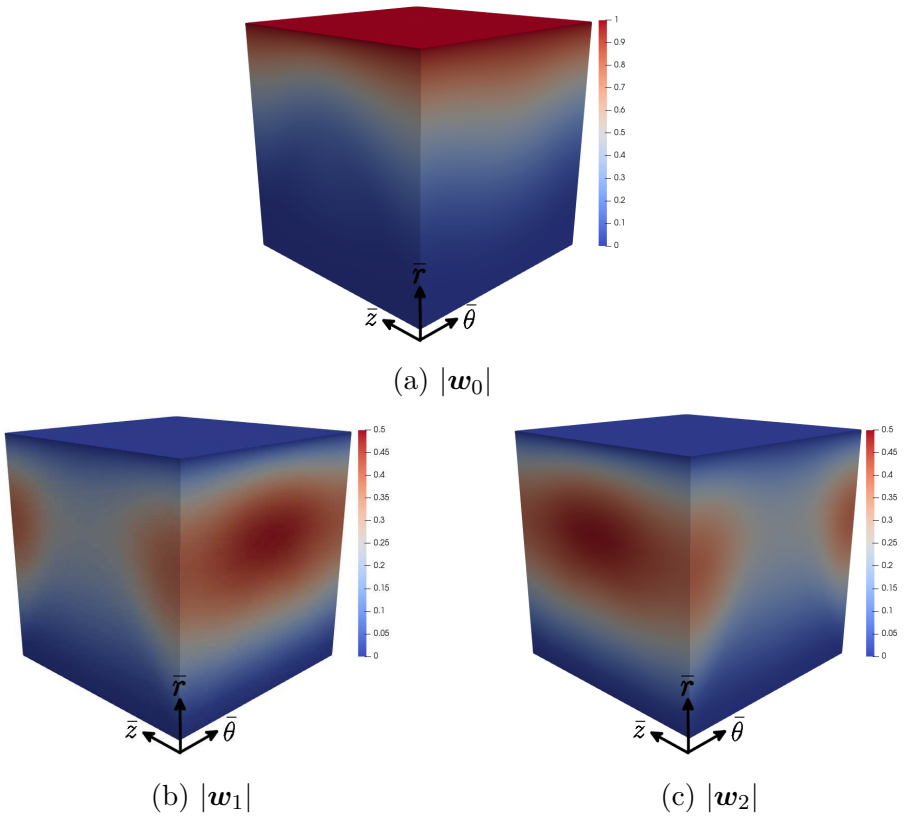

(a) $|\boldsymbol{w}_0|$

(b) $|\boldsymbol{w}_1|$

(c) $|\boldsymbol{w}_2|$

Figure 37: Visualisations of the magnitudes of the microscopic velocity solutions $\boldsymbol{w}_0, \boldsymbol{w}_1$ and $\boldsymbol{w}_2$ at the surface of the local problem's domain.

5.9 SOLUTIONS

In this section, we will analyse both local and global solutions across the parameter space. For the purposes of comprehension of the local solutions, we present figure 37 which shows the microscopic velocity solutions' magnitudes at the boundary of the local problem's domain. We emphasise the similarity of $|\boldsymbol{w}_1|$ and $|\boldsymbol{w}_2|$: due to linearity of the governing equations and symmetry in the geometry, $\boldsymbol{w}_1$ and $\boldsymbol{w}_2$ are rotations of each other.

5.9.1 *Effect of Gap Size*

In order to investigate the effect of the space between the abrasives and the grinding wheel, we begin by looking at results of the local and global problem

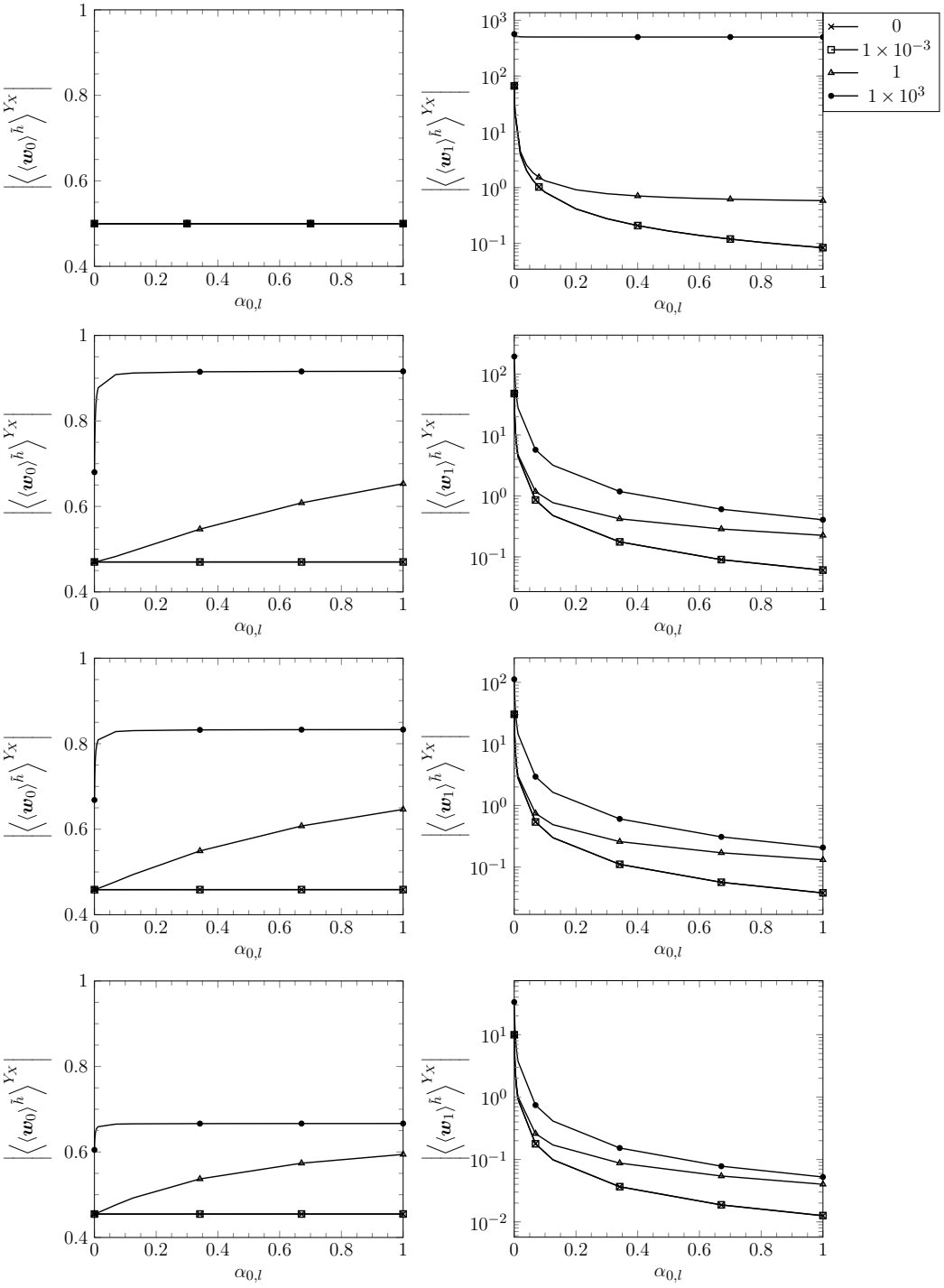

Figure 38: Graphs showing how the magnitudes of the microscopic velocity averages are affected by the choice of slip length, $\hat{\beta}$, as shown in the legend. Here, $\mu_{mix} = \dfrac{1.92 \times 10^{-5}}{1.53 \times 10^{-2}} = 1.25 \times 10^{-3}$ and $h_p = 0, 2.5 \times 10^{-1}, 5 \times 10^{-1}$ and 1 for the first, second, third and four row graphs, respectively.

when the abrasives, i.e. the local geometry, approach contact. To study this, we denote, in the unit cube, the apex point of the pyramid geometry by $0 \leq h_p \leq 1$. As h_p decreases, the slant of the pyramid inside the unit cube will decrease. We recall from (32) that the scale factor, h_p, reduced the peak of the pyramids. Using (389), we can give a formula for the abrasive's boundary location in the unit cell as

$$\tilde{h}\left(\bar{\theta}, \bar{z}\right) = h_p \left[1 - \left(\left|\bar{\theta} - \bar{z}\right| + \left|\bar{z} + \bar{\theta} - 1\right|\right)\right]. \tag{511}$$

Figure 38 presents results for the magnitudes of the microscopic velocity averages at $h_p = 0, 2.5 \times 10^{-1}, 5 \times 10^{-1}$ and 1, in that respective row order. Only results for $\left\langle \langle \boldsymbol{w}_0 \rangle^{\tilde{h}} \right\rangle^{Y_X}$ and $\left\langle \langle \boldsymbol{w}_1 \rangle^{\tilde{h}} \right\rangle^{Y_X}$ are presented since $\boldsymbol{w}_1$ and $\boldsymbol{w}_2$ are equivalent by linearity of the Stokes equations. We remark that the geometry of $h_p = 0$ is simply the unit cube. This causes remarkably different behaviours in the solution as $h_p \to 0$ in comparison to $h_p = 0$.

Focusing on $h_p = 0$, there appears to be considerable flow across the cube's axes at low $\alpha_{0,l}$, and this flow is more pronounced for larger slip lengths. However, it must be remembered throughout the analyses of these solutions that the influence of $\left\langle \langle \boldsymbol{w}_1 \rangle^{\tilde{h}} \right\rangle^{Y_X}$ and $\left\langle \langle \boldsymbol{w}_2 \rangle^{\tilde{h}} \right\rangle^{Y_X}$ on the macroscopic velocity, $\boldsymbol{U}_0$ given by (442), is through a multiplicative relationship with their respective pressure gradient. As such, it is not possible to comment on the effect of $\boldsymbol{w}_1$ and $\boldsymbol{w}_2$ on the global transport of $\alpha_{0,l}$ without knowledge of the pressure gradients, which we must solve the global problem to find.

Once the local geometry involves a protrusion on the moving surface[2], the local flow behaves very differently. Looking at the second row of figure 38, we see that the value of the slip length can have a large effect on $\left\langle \langle \boldsymbol{w}_0 \rangle^{\tilde{h}} \right\rangle^{Y_X}$, and therefore on the transport of the grinding fluid through $\boldsymbol{U}_0$. At small slip lengths, however, $\left\langle \langle \boldsymbol{w}_0 \rangle^{\tilde{h}} \right\rangle^{Y_X}$ appears to deviate relatively negligibly from the no-slip solution in comparison to larger slip lengths. Interestingly, larger slip lengths seem to induce greater local flow. We will comment on this aspect of

2 In the physical problem

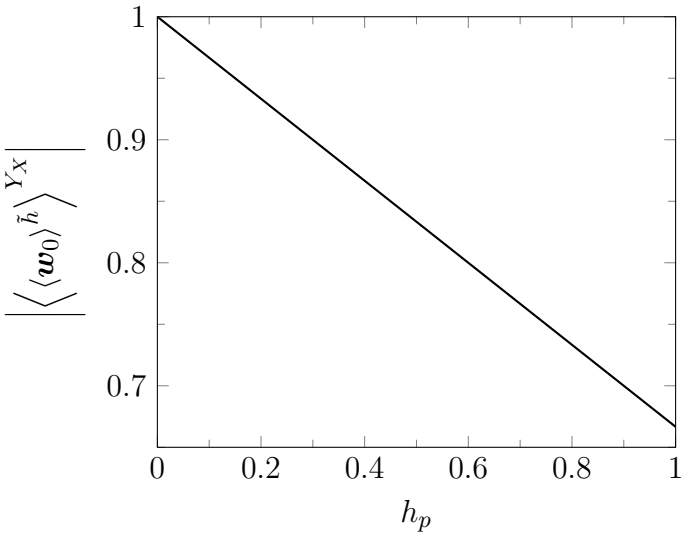

Figure 39: Plot of the magnitude of the average microscopic velocity due to shear, $\left|\left\langle \langle \boldsymbol{w}_0 \rangle^{\tilde{h}} \right\rangle^{Y_X}\right|$, for different pyramid heights, h_p, at $\alpha_{0,l} = 6 \times 10^{-1}$. The slip length is taken to be large, i.e. $\hat{\beta} = 1 \times 10^6$, to mimic the behaviour of the solution in the full slip limit, $\hat{\beta} \to \infty$.

the flow shortly. As before, the magnitudes of $\left\langle \langle \boldsymbol{w}_1 \rangle^{\tilde{h}} \right\rangle^{Y_X}$ and $\left\langle \langle \boldsymbol{w}_2 \rangle^{\tilde{h}} \right\rangle^{Y_X}$ are much larger (by three orders of magnitude) than the magnitude of $\left\langle \langle \boldsymbol{w}_0 \rangle^{\tilde{h}} \right\rangle^{Y_X}$ at low $\alpha_{0,l}$.

These behaviours observed in the local solutions at $h_p = 2.5 \times 10^{-1}$ are also seen when $h_p = 5 \times 10^{-1}$ and 1, i.e. at contact. In fact, recalling that the flux in the advection equation (461) is multiplied by a factor of $\left(1 - \left\langle \tilde{h} \right\rangle^{Y_X}\right)^{-1}$, it can be noticed that as the gradient of the pyramid becomes steeper, there is a larger flux of $\alpha_{0,l}$ along the grinding zone due to the shearing of the grinding wheel. This is a behaviour that could not be reliably predicted under the lubrication approximation due to the inherent low-slope assumption on the boundary profile.

In figure 39, the magnitude of the average of the microscopic velocity due to shear, $\left|\langle \boldsymbol{w}_0 \rangle^{Y_X}\right|$, is presented for $h_p \in (0, 1]$. The slip length has been taken as $\hat{\beta} = 1 \times 10^6$ in order to infer information of the local flow for $\hat{\beta} \to \infty$. As we can see, there appears to be a linear decrease in $\left|\langle \boldsymbol{w}_0 \rangle^{Y_X}\right|$ with increasing h_p. In fact, if the presented values are multiplied by $\left(1 - \left\langle \tilde{h} \right\rangle^{Y_X}\right)^{-1}$, as it

appears in the flux of equation (461), the speed that $\alpha_{0,l}$ is advected through the grinding zone is 1. In contrast, looking back to the first row of figure 38, the slip length does not appear to influence $\left|\langle \boldsymbol{w}_0 \rangle^{Y_X}\right|$. This aspect of the local flow is surprising, though it can be explained. A change in the slip length for the channel geometry must still conserve the mass flux, but the velocity profile will change. As a protrusion appears, we expect the same behaviours to occur. However, as a consequence of the no-penetration and full-slip conditions, flow is induced around the pyramid by the inability of fluid to penetrate the pyramid walls. Due to full-slip, the flow profile is constant through the domain. This is unseen in the channel geometry due to the planar boundaries.

The case where $h_p = 0$ corresponds to the smooth boundary profile that we considered in Chapter 4. Looking at the first row of figure 38, $\left|\langle \boldsymbol{w}_0 \rangle^{Y_X}\right| = 5 \times 10^{-1}$ for all sampled $\alpha_{0,l}$ and $\hat{\beta}$. Comparing $\left|\langle \boldsymbol{w}_0 \rangle^{Y_X}\right|$ to the flux that was predicted under the lubrication approximation, $\bar{Q}^\star$, in figure 24, we observe that the homogenisation results suggest that under the homogenisation limit we are in the $\delta \to \infty$ limit. We recall that

$$\delta = \frac{d_c}{h_g} = 2\frac{d_c}{d} \tag{512}$$

denotes the ratio between the depth of cut, d_c, and the representative distance between the grinding wheel and workpiece, h_g. In the $\delta \to \infty$ limit, the results for the shear and pressure gradient-induced flux components from figure 26 and 27, respectively, suggested that the transport of the grinding fluid was solely driven by the shearing of the grinding wheel. Meanwhile, the transport of the grinding fluid due to the pressure gradient was negligible. This was true for all values of the slip length, $\hat{\beta}$. We emphasise that as we have prescribed $\alpha_{0,l}$ in the local problem here, we have not yet considered the global problem. Hence, we have not used the assumption of negligible pressure difference across the grinding zone, i.e. boundary condition (464), supporting the claim that this flow is shear-dominated.

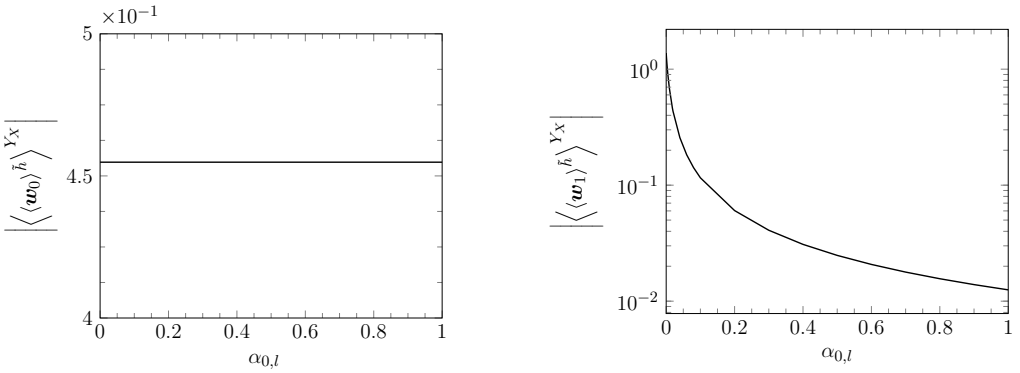

Figure 40: Graphs plotting magnitudes of the microscopic velocity averages against volume fraction.

5.9.2 *Velocity Components*

To evaluate how the microscopic velocities $\boldsymbol{w}_1$ and $\boldsymbol{w}_2$ influence the transport of the grinding fluid in the grinding zone, we must solve the global problem for the pressure distribution. Both local and global problems will now be solved and the behaviour of the three constituent terms of the macroscopic velocity, $\boldsymbol{U}_0$, will be probed.

In figure 40, we present results for the magnitudes of the microscopic velocity averages for different $\alpha_{0,l}$ with the parameters taken as

$$\begin{aligned} \theta_0 &= 4.59, \\ h_w &= 6.67 \times 10^{-2}, \\ \varepsilon &= 6.67 \times 10^{-4}, \\ \delta &= 1.2 \times 10^{1}, \\ \mu_{mix} &= 9.09 \times 10^{-3}, \\ \theta_r &= \frac{\pi}{16}, \\ \hat{\beta} &= 1 \times 10^{-6}. \end{aligned} \tag{513}$$

These are parameter values for a creep-feed grinding regime with a low viscosity grinding fluid. The results are similar to those seen previously in figure 38 for small $\hat{\beta}$.

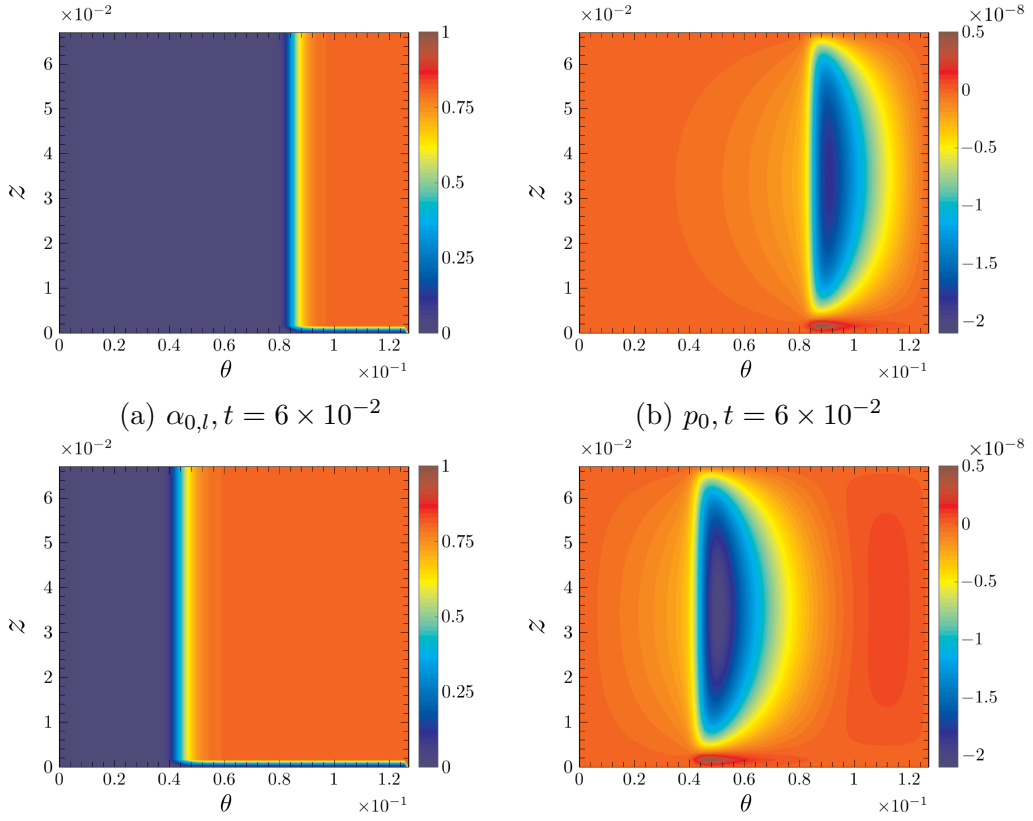

(a) $\alpha_{0,l}, t = 6 \times 10^{-2}$ (b) $p_0, t = 6 \times 10^{-2}$

(c) $\alpha_{0,l}, t = 1.2 \times 10^{-1}$ (d) $p_0, t = 1.2 \times 10^{-1}$

Figure 41: Graphs showing the volume fraction, $\alpha_{0,l}$, and pressure, p_0, at $t = 6 \times 10^{-2}$, given in (a) and (b), respectively, and at $t = 1.2 \times 10^{-1}$, given in (c) and (d), respectively. Here we have translated the θ coordinate by $-\left(\frac{3\pi}{2} - \theta_0\right)$ with $\theta_0 \approx 4.59$.

In figure 41, the global solutions of the volume fraction, $\alpha_{0,l}$, and pressure distribution, p_0, are presented at $t = 6 \times 10^{-2}$ and 1.2×10^{-1}, subject to $\alpha_D = 8 \times 10^{-1}$. We remark on the absence of grinding fluid along one side of the grinding zone. This is a facet of the flow which could have substantial consequences on the efficiency of the grinding process. We will return to this in greater detail later on.

We see that for these parameter values, p_0 is considerably different to the pressures seen in solutions under the lubrication approximation, e.g. those in figure 17. While previously there was a constant pressure gradient across the grinding zone, that is missing here. It is likely that due to our assumption of the high shear limit with zero pressure gradient across the grinding zone, in the homogenisation limit the small scale pressures generated around the abrasives

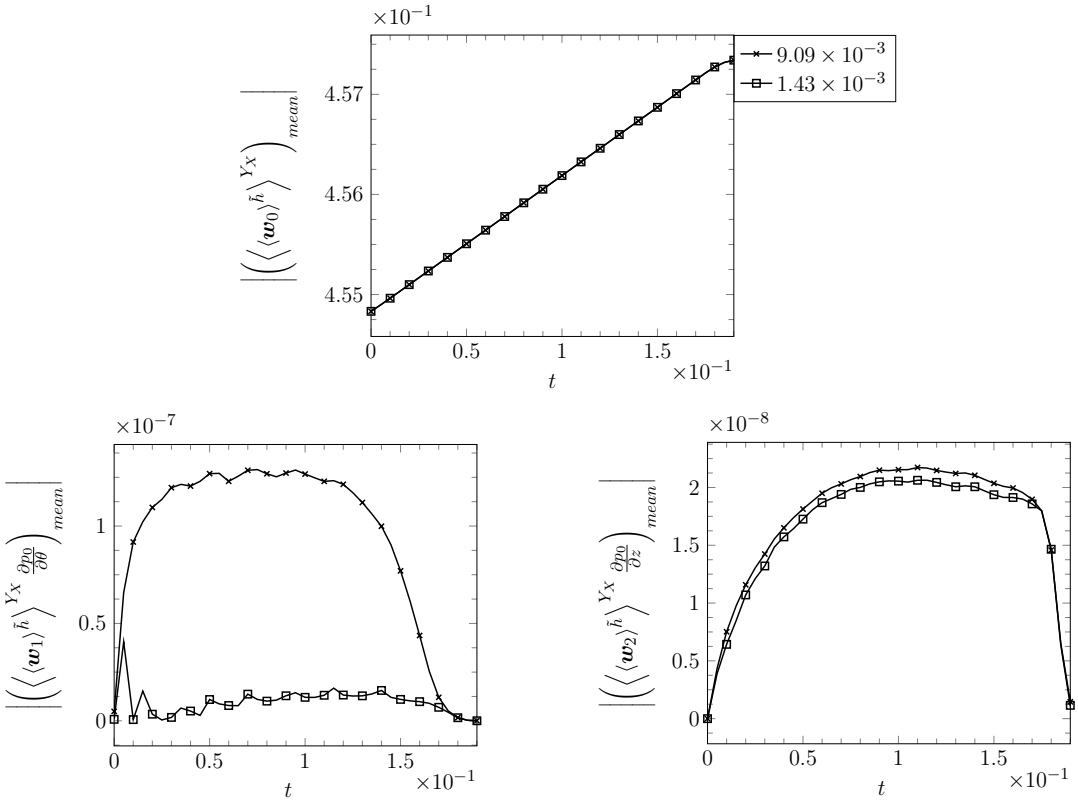

Figure 42: Graphs showing magnitudes of the means for the terms comprising the macroscopic velocity, $\boldsymbol{U}_0$, against time as the grinding fluid is transported further into the grinding zone in a creep-feed grinding regime. The plots for two different viscosity fractions are presented, with these values indicated in the legend.

are smoothed out. Hence, the values we have for the pressure are at the order of magnitude of numerical error.

Despite these negligible pressure values, it is worthwhile to look at how the magnitude of each term comprising the macroscopic velocity, $\boldsymbol{U}_0$, varies during the flow. To this end, figure 42 presents the values for the magnitude of the mean of these terms for the low viscosity grinding fluid with parameters specified by (513), and a higher viscosity grinding fluid with $\mu_{mix} = 1.43 \times 10^{-3}$. The mean is taken over the macroscopic flow domain, $\hat{\Omega}$. We see from the graphs that the small pressure across the domain results in $\left\langle \langle \boldsymbol{w}_1 \rangle^{\tilde{h}} \right\rangle^{Y_X} \frac{\partial p_0}{\partial \theta}$ and $\left\langle \langle \boldsymbol{w}_2 \rangle^{\tilde{h}} \right\rangle^{Y_X} \frac{\partial p_0}{\partial z}$ having much smaller contributions to $\boldsymbol{U}_0$ than $\left\langle \langle \boldsymbol{w}_0 \rangle^{\tilde{h}} \right\rangle^{Y_X}$. Overall, $\left(\left\langle \langle \boldsymbol{w}_1 \rangle^{\tilde{h}} \right\rangle^{Y_X} \frac{\partial p_0}{\partial \theta}\right)_{mean}$ and $\left(\left\langle \langle \boldsymbol{w}_2 \rangle^{\tilde{h}} \right\rangle^{Y_X} \frac{\partial p_0}{\partial z}\right)_{mean}$ are also on the scale of numerical error.

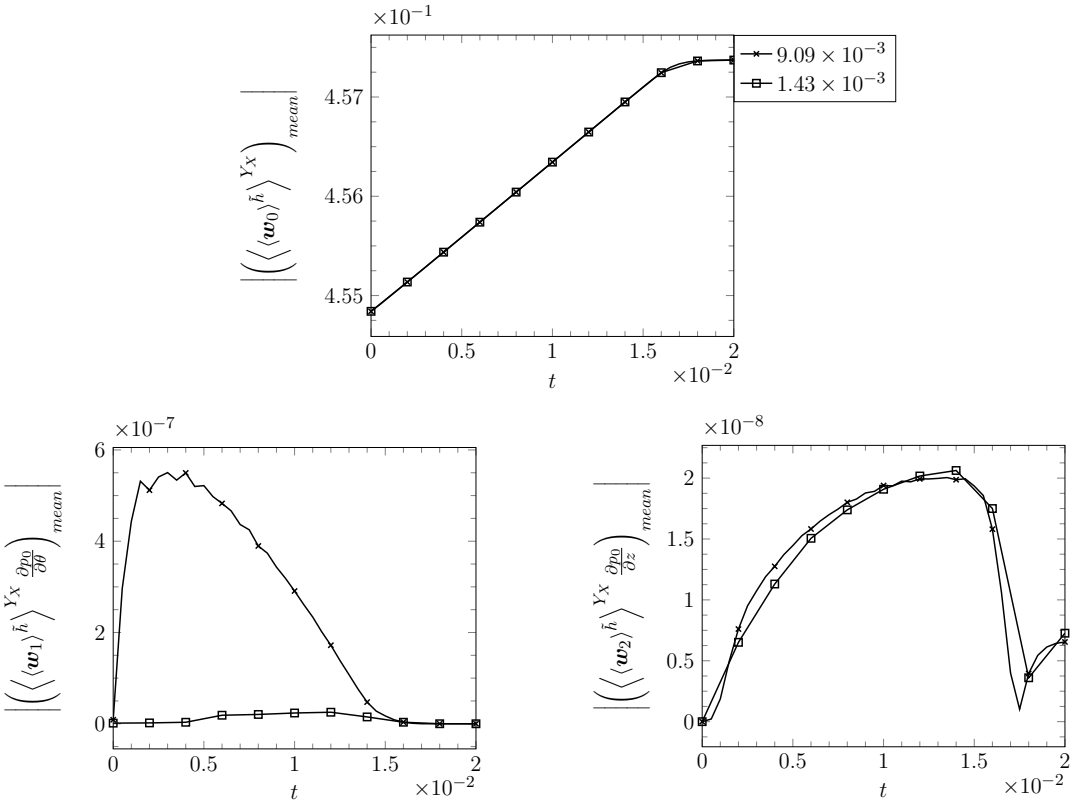

Figure 43: Graphs showing values of the macroscopic velocity's constituent terms as the grinding fluid is transported further into the grinding zone in a surface grinding regime.

These results suggest that pressure fluctuations across abrasives are not large enough to affect the pressure across the grinding zone, with any pressure fluctuations averaged out by homogenisation. The results for both grinding fluids indicate that negligible pressure change across the grinding zone is observed regardless of the particular grinding fluid used.

In figure 43, we plot the magnitudes of the means for each term comprising the macroscopic velocity, $\boldsymbol{U}_0$, with the parameters

$$\begin{aligned} \varepsilon &= 8.33 \times 10^{-5}, \\ \delta &= 8 \times 10^{-1}, \\ \theta_r &= \frac{\pi}{16}, \\ \hat{\beta} &= 8 \times 10^{-4}. \end{aligned} \tag{514}$$

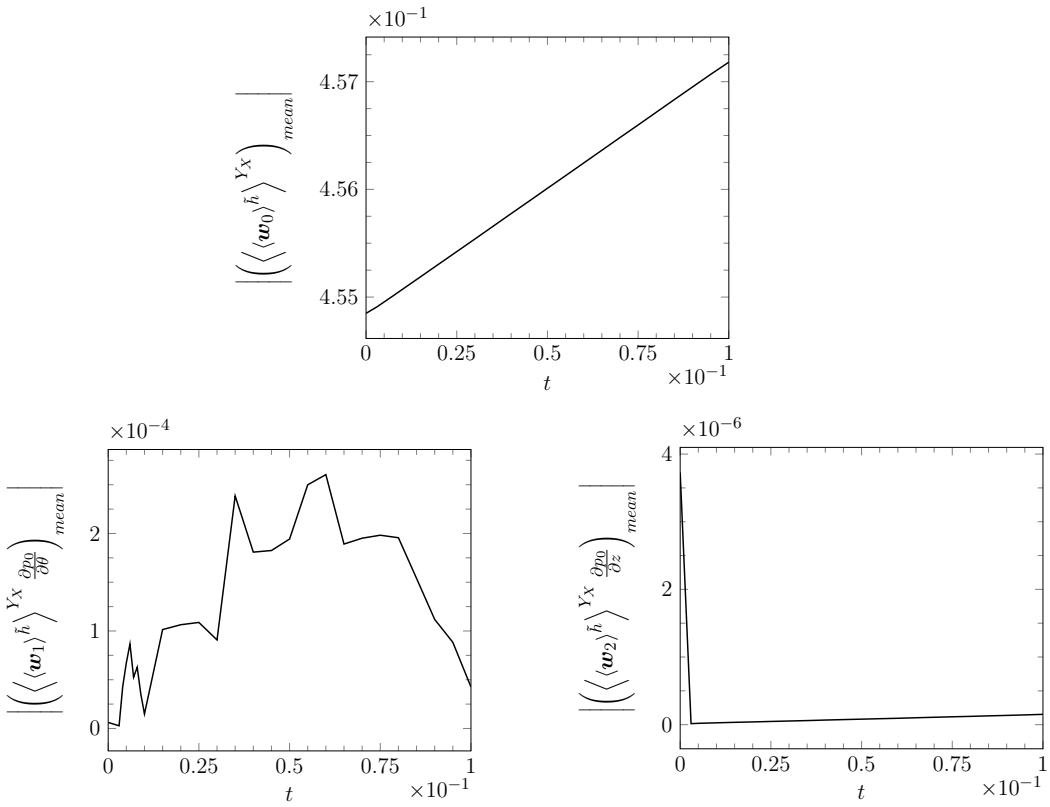

Figure 44: Graphs showing values of the macroscopic velocity's constituent terms as the grinding fluid is transported further into the grinding zone.

The solutions for two sets of viscosity fractions are plotted: one with $\mu_{mix} = 9.09 \times 10^{-3}$; the other with $\mu_{mix} = 1.43 \times 10^{-3}$. These are parameter values one would expect from a surface grinding regime with a low viscosity grinding fluid and high viscosity grinding fluid, respectively. It is evident that the same behaviour of $\left\langle \langle \boldsymbol{w}_1 \rangle^{\tilde{h}} \right\rangle^{Y_X} \frac{\partial p_0}{\partial \theta}$ and $\left\langle \langle \boldsymbol{w}_2 \rangle^{\tilde{h}} \right\rangle^{Y_X} \frac{\partial p_0}{\partial z}$ is observed in this grinding regime also. This supports the claim that we are in the high shear regime where transport across the grinding zone is primarily due to the shear-induced microscopic velocity, $\boldsymbol{w}_0$, which dominates over the negligible flow due to the macroscopic pressure gradient across the grinding zone.

Figure 44 extends the parameter values away from these two specific grinding regimes and plots the magnitude of the means for each term comprising $\boldsymbol{U}_0$. We take the parameters

$$\begin{aligned} \varepsilon &= 6.67 \times 10^{-4}, \\ \delta &= 4, \\ \mu_{mix} &= 1.25 \times 10^{-3}, \\ \theta_r &= 0, \\ \hat{\beta} &= 1.3 \times 10^{-2}. \end{aligned} \tag{515}$$

The graphs support the view that the shear-dominated aspect of the flow is characteristic of the grinding process, not of particular grinding flow regimes.

Before proceeding, we remark that in our problem formulation from Section 5.4, we assumed homogeneous pressure boundary conditions on the grinding zone boundaries. The justification was that in Chapter 4 we observed that shear effects were primarily driving the flow. A next key step of the work on the Stokes flow homogenisation is to consider the full problem without assuming homogeneous pressure boundary conditions. To this end, a first order approximation could use pressure values from empirical measurements or those from a suitable model, for example, pressure values from Chapter 4. A more rigorous approach would require the treatment of the flow outside the grinding zone. One option is to consider artificial boundaries around the grinding zone. Outside of the grinding zone, the Navier-Stokes equations would hold, with a rough boundary that represents the grinding wheel's surface. Within the grinding zone, the homogenisation approach from this chapter would be followed. At the artificial boundaries, continuity of flow variables would couple the systems.

This inclusion of nonhomogeneous boundary conditions in the Stokes flow homogenisation model will be left for future work. In the next section, we look to extend the analysis we have done here to a realistic flow regime: in particular, when inertial effects are considered in the flow. So far in this thesis, we have neglected inertial effects inside the grinding zone. However, in reality

the Reynolds number is too large to neglect such terms in the homogenised regime, and we go into the next section with a view to include such effects in the local flow problem. To this end, we will build on everything we have learned so far of the flow inside the grinding zone with the goal of capturing a more accurate understanding of the transport there.

5.10 INERTIAL EFFECTS

5.10.1 *Introduction*

In the previous section, we considered the flow with viscosity effects dominating over inertial effects; specifically, we analysed a Stokes flow regime. In reality, the local Reynolds number, Re_i, over a single abrasive can have a typical value of 10^3, as we saw in (326). Thus, it cannot be expected that the Stokes approximation will provide an accurate description of the flow. In order to attempt to fully understand the transport of grinding fluid in the grinding zone, we must consider nonlinear effects in the flow. We recall assumption (53) which states that the (global) Reynolds number, Re, satisfies

$$\mathrm{Re} = O\left(\varepsilon^{-1}\right), \tag{516}$$

therefore

$$\mathrm{Re}_i = \varepsilon \mathrm{Re} = O\left(1\right). \tag{517}$$

To include inertial effects, our problem formulation is as before, with the governing system given by (340)-(347) and the equation governing conservation of momentum

$$\rho_m \left(\frac{\partial \boldsymbol{u}}{\partial t} + \boldsymbol{u} \cdot \nabla \boldsymbol{u} \right) = -\nabla p + \nabla \cdot \left[\mu_m \left(\nabla \boldsymbol{u} + (\nabla \boldsymbol{u})^T \right) \right]. \tag{518}$$

We denote the density of air by ρ_g and the density of the grinding fluid by ρ_l with

$$\rho_{mix} = \frac{\rho_g}{\rho_l}. \tag{519}$$

The multiphase turbulent tensor term arising from the volume averaging has been omitted in equation (518). This is not without consequence for capturing the interaction dynamics between the two phases, and turbulent aspects of the flow are lost. However, it is not expected that the ambient air will greatly influence the broad transport of grinding fluid once it has reached the grinding zone in this strongly shear-induced flow. Further, the choice of the most appropriate turbulence model for such complex geometries would not be trivial: to include a turbulence model which has not been calibrated or shown to apply in flows similar to our local flow risks the loss or inaccurate predictions of important flow details.

5.10.2 *Homogenisation*

Although the equations we are now considering have a similar form to those in the Stokes regime, the nonlinearity of the inertial term in (518) introduces considerable complications to the homogenisation procedure. Due to this nonlinearity, the derivation of local and global problems is considerably more difficult than the Stokes equations. By taking the characteristic pressure as before, i.e. (356), we find that we can no longer separate the governing Navier-Stokes equations into appropriate local and global problems following the substitution of the macroscopic variables for microscopic variables with a macroscopic pressure gradient factor, i.e. (425) and (426).

In the related field of pressure gradient-driven flow in porous media, previous research has been conducted into extensions of (425) and (426) when inertial effects are present in the flow. We refer the interested reader to: [63] for the proof that inertial terms do not affect the form of the local problem, Darcy's

law, when $\mathrm{Re}_i = O(\varepsilon^n)$ for $n > -1$ as $\varepsilon \to 0$; [83] for an empirical extension of Darcy's law when $\varepsilon^{\frac{1}{2}} \ll \mathrm{Re}_i \ll 1$, as $\varepsilon \to 0$, and references herein for an overview of extensions in other regimes.

Other approaches have been followed in porous media flows which allow for local and global problems of the Navier-Stokes equations to be derived in a few specific geometries, for example, a domain covered by cells that have a suitably small circular hole in the centre [6]. Unfortunately, a general result has not yet been discovered for either porous media flows or shear-driven flows.

In spite of these difficulties, we are able to find a way forward by seeking shear-dominated solutions. As we previously saw in the local equation (427), the system of equations involves macroscopic pressure gradients which act as forcing terms, influencing the flow to move from regions of high pressure to areas of low pressure. This term would be expected to appear, and be the dominant transport mechanism, in flows which are not induced by the shearing of boundaries: blood flow through thin blood vessels [77] and flow through fractured medium [89] are just two examples of these pressure-driven flows. However, for the high-speed flow during grinding, the flow is primarily driven by the dragging of fluid against the spinning wheel due to the force exerted from wall shear stresses. As such, we postulate that the flow induced by macroscopic pressure gradients is a small perturbation relative to the flow that is induced from the shearing of the grinding wheel. Indeed, recalling, for example, figures 27 and 42, the influence of the macroscopic pressure gradients on the flow appear to be small.

Based on this recent discussion, let us adjust the characteristic pressure scale to instead be

$$P = \frac{\mu_l V_\omega}{h_g}. \tag{520}$$

As we will see, this causes the macroscopic pressure gradient term to no longer be in the leading order microscopic equations. This will allow us to derive

suitable local and global problems which are able to capture high Reynolds number inertial effects.

In contrast to the characteristic pressure taken in the Stokes regime, given by (356), this pressure scale is small. Aside from the choice of pressure scale (520), the nondimensionalisation procedure remains identical to the homogenisation of the Stokes regime. The nondimensional variables are given by (350), (352), (354), (355) and (357). The local unit cell domain, Y, and global domain, $\hat{\Omega}$, are given by (383) and (467), respectively. The asymptotic expansions we take for $\boldsymbol{u}, p, \alpha_l$ are given by (404)-(406), respectively. To avoid repetition, we will omit details and simply state the equations that we obtain. Notably, we assume (423) again, i.e. the volume fraction is independent of the microscale.

5.10.3 *Local Problem*

We denote the leading order mixture density by

$$\rho_{0,m} = \alpha_{0,l} + (1 - \alpha_{0,l})\, \rho_{mix}. \tag{521}$$

At $O(1)$: (518) is

$$\mathrm{Re}_i \rho_{0,m} \boldsymbol{u}_0 \cdot \nabla_{\boldsymbol{X}} \boldsymbol{u}_0 = -\nabla_{\boldsymbol{X}} p_0 + \mu_{0,m} \nabla_{\boldsymbol{X}} \cdot \left(\nabla_{\boldsymbol{X}} \boldsymbol{u}_0 + (\nabla_{\boldsymbol{X}} \boldsymbol{u}_0)^T \right); \tag{522}$$

(340) is

$$\nabla_{\boldsymbol{X}} \cdot \boldsymbol{u}_0 = 0; \tag{523}$$

(341) is

$$\nabla_{\boldsymbol{X}} \cdot (\alpha_{0,l} \boldsymbol{u}_0) = 0. \tag{524}$$

At $O(\varepsilon)$, (341) is

$$\begin{aligned}&\frac{\partial \alpha_{0,l}}{\partial t} + \nabla_{\boldsymbol{x}} \cdot (\alpha_{0,l}\boldsymbol{u}_0) + \nabla_{\boldsymbol{X}} \cdot (\alpha_{0,l}\boldsymbol{u}_1 + \alpha_{1,l}\boldsymbol{u}_0) \\ &= -\left[\frac{\partial}{\partial \bar{r}}(\bar{r}\alpha_{0,l}u_{r,0}) + \frac{\bar{r}}{\sqrt{2}}\left(\frac{\partial}{\partial \bar{\theta}}(\alpha_{0,l}u_{z,0})\sin\kappa + \frac{\partial}{\partial \bar{z}}(\alpha_{0,l}u_{z,0})\cos\kappa\right)\right].\end{aligned} \tag{525}$$

At $O(1)$, we find that the slip boundaries conditions (343) and (344) give

$$\boldsymbol{u}_0 + \hat{\boldsymbol{e}}_\theta = 2\hat{\beta}\mu_{0,m}\boldsymbol{n} \cdot \boldsymbol{E}_0 \cdot (\boldsymbol{I} - \boldsymbol{nn}) \qquad \text{on } \bar{r} = \tilde{h}, \tag{526}$$

$$\boldsymbol{u}_0 = 2\hat{\beta}\mu_{0,m}\boldsymbol{n} \cdot \boldsymbol{E}_0 \cdot (\boldsymbol{I} - \boldsymbol{nn}) \qquad \text{on } \bar{r} = 1, \tag{527}$$

where $\boldsymbol{E}_0 = \frac{1}{2}\left(\nabla_{\boldsymbol{X}}\boldsymbol{u}_0 + (\nabla_{\boldsymbol{X}}\boldsymbol{u}_0)^T\right)$.

As the only macroscopic influence on the local flow in equations (522) and (523) comes from the parameter $\alpha_{0,l}$ which alters the (unit cell-constant) density and viscosity, we can express the microscopic velocity as

$$\boldsymbol{u}_0 \equiv \boldsymbol{u}_0(\boldsymbol{X}; \alpha_{0,l}). \tag{528}$$

Writing the velocity as (528) highlights the shear-dominated aspect of the flow and the absence of macroscopic pressure gradients driving the flow, when compared to the velocity in Stokes regime (425). We emphasise that $\boldsymbol{u}_0$ is still a function of macroscopic variables through the macroscopically varying $\mu_{0,m}$ in equation (522).

Our local problem is therefore to solve

$$\mathrm{Re}_i \rho_{0,m}\boldsymbol{u}_0 \cdot \nabla_{\boldsymbol{X}}\boldsymbol{u}_0 = -\nabla_{\boldsymbol{X}}p_0 + \mu_{0,m}\nabla_{\boldsymbol{X}} \cdot \left(\nabla_{\boldsymbol{X}}\boldsymbol{u}_0 + (\nabla_{\boldsymbol{X}}\boldsymbol{u}_0)^T\right), \tag{529}$$

$$\nabla_{\boldsymbol{X}} \cdot \boldsymbol{u}_0 = 0, \tag{530}$$

in the unit cell Y subject to the periodicity conditions

$$\boldsymbol{u}_0\left(\bar{r},\theta,z,0,\bar{z},t\right)=\boldsymbol{u}_0\left(\bar{r},\theta,z,1,\bar{z},t\right), \tag{531}$$

$$p_0\left(\bar{r},\theta,z,0,\bar{z},t\right)=p_0\left(\bar{r},\theta,z,1,\bar{z},t\right), \tag{532}$$

$$\boldsymbol{u}_0\left(\bar{r},\theta,z,\bar{\theta},0,t\right)=\boldsymbol{u}_0\left(\bar{r},\theta,z,\bar{\theta},1,t\right), \tag{533}$$

$$p_0\left(\bar{r},\theta,z,\bar{\theta},0,t\right)=p_0\left(\bar{r},\theta,z,\bar{\theta},1,t\right), \tag{534}$$

and the slip boundary conditions

$$\boldsymbol{u}_0+\hat{\boldsymbol{e}}_\theta=2\hat{\beta}\mu_{0,m}\boldsymbol{n}\cdot\boldsymbol{E}_0\cdot\left(\boldsymbol{I}-\boldsymbol{n}\boldsymbol{n}\right)\quad\text{on }\bar{r}=\tilde{h}, \tag{535}$$

$$\boldsymbol{u}_0=2\hat{\beta}\mu_{0,m}\boldsymbol{n}\cdot\boldsymbol{E}_0\cdot\left(\boldsymbol{I}-\boldsymbol{n}\boldsymbol{n}\right)\quad\text{on }\bar{r}=1. \tag{536}$$

5.10.4 *Global Problem*

The domain and boundaries of the global problem are given by

$$\hat{\Omega}=\left\{(\theta,z):\theta\in\left(\theta_0,h_w\right),z\in\left(0,h_w\right)\right\}, \tag{537}$$

$$\hat{\Gamma}_{in}=\left\{(\theta,z):\theta=\frac{3\pi}{2},z\in\left(0,h_w\right)\right\}, \tag{538}$$

$$\hat{\Gamma}_{out}=\left\{(\theta,z):\theta=\theta_0,z\in\left(0,h_w\right)\right\}, \tag{539}$$

$$\hat{\Gamma}_s=\left\{(\theta,z):\theta\in\left(\theta_0,\frac{3\pi}{2}\right),z\in\left\{0,h_w\right\}\right\}, \tag{540}$$

respectively.

Similarly to (442), using (528) we obtain the leading order macroscopic velocity, $\boldsymbol{U}_0\left(\theta,z,t\right)$, as

$$\boldsymbol{U}_0=\left\langle\langle\boldsymbol{u}_0\rangle^{\tilde{h}}\right\rangle^{Y_X}. \tag{541}$$

The leading order macroscopic pressure, $P_0(\theta, z, t)$, is now found from the average

$$P_0 = \left\langle \langle p_0 \rangle^{\tilde{h}} \right\rangle^{Y_X}. \tag{542}$$

By averaging boundary condition (345) over Y, we get that at leading order,

$$P_0 = 0 \quad \text{on } \hat{\Gamma}_{in} \cup \hat{\Gamma}_{out} \cup \hat{\Gamma}_s. \tag{543}$$

To obtain the global problem, we average equation (525) over Y. Following the derivation in Section 5.6, we find that we have the same form of equation (456). Namely, on $\hat{\Omega}$ we have

$$\begin{aligned} &\frac{\partial \alpha_{0,l}}{\partial t} + \nabla_{\boldsymbol{x}} \cdot \left(\frac{\boldsymbol{U}_0}{1 - \left\langle \tilde{h} \right\rangle^{Y_X}} \alpha_{0,l} \right) \\ &= -\frac{\alpha_{0,l}}{1 - \left\langle \tilde{h} \right\rangle^{Y_X}} \left(\left\langle \left\langle \frac{\partial}{\partial \bar{r}} \left(\bar{r} u_{r,0} \right) \right\rangle^{\tilde{h}} \right\rangle^{Y_X} + \right. \\ &\qquad \left. \left\langle \left\langle \frac{\bar{r}}{\sqrt{2}} \left(\frac{\partial u_{z,0}}{\partial \bar{\theta}} \sin\kappa + \frac{\partial u_{z,0}}{\partial \bar{z}} \cos\kappa \right) \right\rangle^{\tilde{h}} \right\rangle^{Y_X} \right), \end{aligned} \tag{544}$$

subject to

$$\alpha_{0,l} = 0 \qquad \text{on } \hat{\Omega} \text{ at } t = 0, \tag{545}$$

$$\alpha_{0,l} = \alpha_D \qquad \text{on } \hat{\Gamma}_{in} \text{ where } \boldsymbol{U}_0 \cdot \boldsymbol{n} > 0, \tag{546}$$

$$\alpha_{0,l} = 0 \qquad \text{on } \hat{\Gamma}_{out} \cup \hat{\Gamma}_s \text{ where } \boldsymbol{U}_0 \cdot \boldsymbol{n} > 0. \tag{547}$$

Thus, we have obtained a closed system of equations. The local problem we solve for the microscopic variables $\boldsymbol{u}_0$ and p_0 is (529) and (530) subject to the periodicity conditions (531)-(534) and slip boundary conditions (535) and (536). The global problem we solve for the macroscopic variables $\boldsymbol{U}_0$, P_0 and $\alpha_{0,l}$ is (541), (542) and (544), respectively, subject to (543), (545)-(547). The

time-dependent global solution will give us the (shear-dominated) transport behaviour of the grinding fluid.

We remark that the absence of macroscopic pressure gradients mean that boundary conditions on the macroscopic pressure are no longer needed. Hence, condition (543) is not a boundary condition in the global problem, unlike the equivalent boundary condition (464) in the Stokes regime. However, condition still manifests in the homogenised system. To see this, we note that due to the boundary conditions of the local problem, the local solution of p_0 on a unit cell is defined up to an arbitrary constant. In order to fix the pressure value, we could additionally impose that the mean value of the pressure is a constant, for example, 0 via

$$\int_Y p_0 \mathrm{d}Y = 0. \tag{548}$$

Condition (548) can instead be written as

$$\left\langle \langle p_0 \rangle^{\tilde{h}} \right\rangle^{Y_X} = 0, \tag{549}$$

which is the same condition as (543). Therefore, boundary condition (464) appears in the inertial homogenised problem by specifying the arbitrary constant of the local pressure in unit cells located at the boundary of the macroscopic domain.

Furthermore, condition (548) on the local problem is a means to satisfy the assumption of negligible pressure gradient across the domain in the inertial regime. By fixing the mean pressure value of every unit cell as 0 via the local problem, we satisfy both (543) and the implicit assumption that $\nabla_{\boldsymbol{x}} P_0 = 0$. For the problems considered in this thesis, it is not necessary to impose (548) on the local problem in the inertial regime due to the macroscopic pressure not appearing in the global problem outside of (542). Hence, as this will not affect our analysis, all pressures on local problems will be solved up to an arbitrary constant. In future work, it may be necessary to impose (548) on the local problem depending on the form of the global problem.

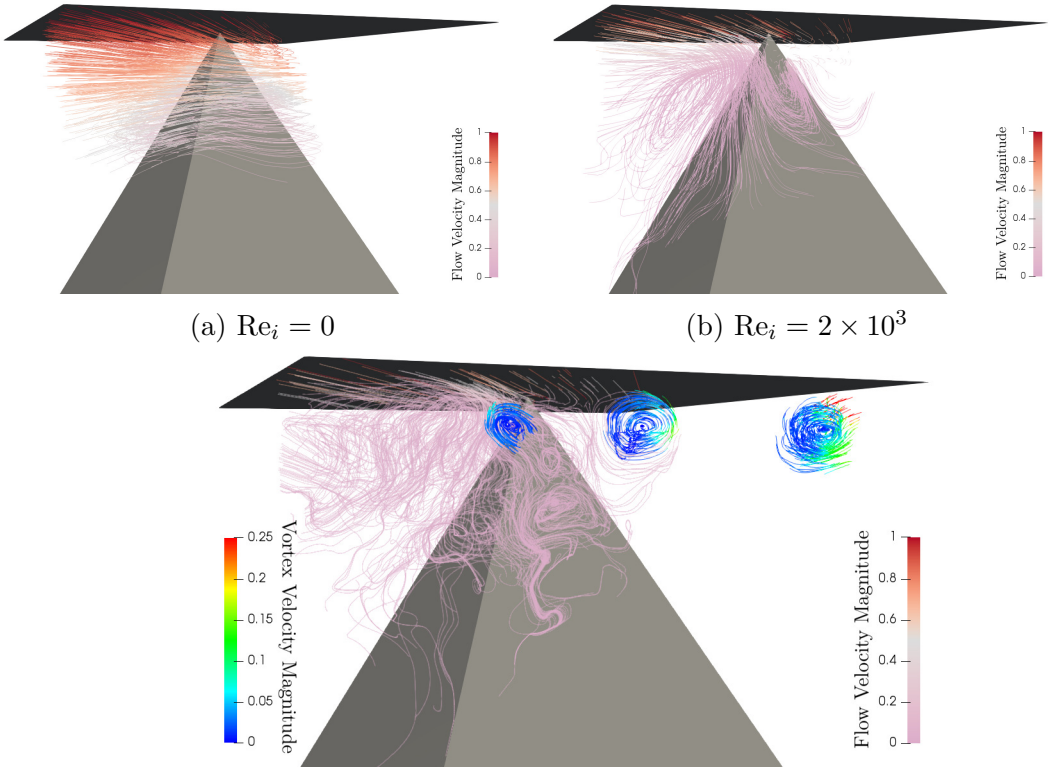

(a) $\mathrm{Re}_i = 0$ (b) $\mathrm{Re}_i = 2 \times 10^3$

(c) $\mathrm{Re}_i = 3.1 \times 10^4$

Figure 45: Streamline visualisations for local inertial solutions of $\boldsymbol{w}_0$ at increasing microscopic Reynolds number, Re_i, as given in the relevant captions. The appearance of vortices in the flow at non-zero Reynolds number is highlighted in (c).

5.11 INERTIAL LOCAL PROBLEM NUMERICAL SCHEME

The discrete formulation of the local problem follows similarly to the Stokes problem in Subsection 5.8.1. However, the weak formulation is now nonlinear in $\boldsymbol{u}_0$. The discrete formulation of the inertial local system (529)-(536) is now: find $\boldsymbol{u}_{0,h} \in \boldsymbol{V}_{h,2,per}$, $p_{0,h} \in Q_{h,1,per}$ such that

$$C_h^{ns}\left(\boldsymbol{u}_{0,h}, \boldsymbol{v}_h; \alpha_{0,l}\right) - A_h^s\left(\boldsymbol{u}_{0,h}, \boldsymbol{v}_h; \alpha_{0,l}\right) - B_h^s\left(\boldsymbol{v}_h, p_{0,h}\right) = -l_0^s\left(\boldsymbol{v}_h\right), \tag{550}$$

$$B_h^s\left(\boldsymbol{u}_{0.h}, q_h\right) = 0, \tag{551}$$

for all $\boldsymbol{v}_h \in \boldsymbol{V}_{h,2,per}$, $q_h \in Q_{h,1,per}$, where $\alpha_{0,l} \in L^\infty\left(\Omega\right)$ and the spaces $\boldsymbol{V}_{h,2,per}$ and $Q_{h,1,per}$ are given by (482) and (483), respectively.

In (550) and (551), the forms $A_h^s, B_h^s, l_{0,h}^s$ are given by (486)-(488), respectively, and C_h^{ns} is given by

$$C_h^{ns}\left(\boldsymbol{u}_{0,h}, \boldsymbol{v}_h; \alpha_{0,l}\right) = \int_Y \mathrm{Re}_i \rho_{0,m} \boldsymbol{u}_{0,h} \cdot \nabla_{\boldsymbol{X}} \boldsymbol{u}_{0,h} \cdot \boldsymbol{v}_h \mathrm{d}Y, \tag{552}$$

with $\rho_{0,m} = \alpha_{0,l} + (1 - \alpha_{0,l})\, \rho_{mix}$.

As with (484), the impermeability condition is enforced by regularisation with the resistance condition via (493). The velocity we solve for is taken in a frame of reference where the pyramid is stationary, as in (495).

Due to the nonlinearity of C_h^{ns} in $\boldsymbol{u}_{0,h}$, the numerical scheme is not identical to that for the local Stokes problem. The problem is linearised through Newton's method and the resulting linear system is directly solved via LU decomposition. We perform continuation of the solution on Re_i by making incremental increases in Re_i to alleviate issues related to divergence of Newton's method at high Re_i. This is done by using the solution for the previous increment of Re_i as the initial guess for Newton's method at the current Re_i. The initial guess for the first Re_i uses the solution to the linear Stokes problem which does not require Newton's method to solve.

Regarding the computational domain, similar meshes to figure 36 are used. However, in the meshes for the nonlinear problem we ensure that the distribution of degrees of freedom is concentrated closer to the moving wall. We do this to capture small scale boundary layer and inertial effects associated with non-zero Reynolds numbers. Between 1.8×10^5 and 1.9×10^5 degrees of freedom were solved for on the meshes we used.

For the solution to the global problem given by the advection equation (544), the scheme is presented in Subsection 5.8.2. It is no longer required to solve an equation for the pressure distribution.

5.12 INERTIAL SOLUTIONS

In order to gain a basic understanding of the local flow solutions at higher microscopic Reynolds numbers, Re_i, figure 45 presents the streamlines of the velocity solution at various Re_i. As we expect, the Stokes solution where $\mathrm{Re}_i = 0$ behaves as a slow, viscous fluid flow around the pyramid. However, the flow becomes increasingly complex as Re_i increases. While large regions of circulation can be spotted in (b), the streamlines in (c) show considerably irregular behaviour. In addition, small scale trailing vortices are seen to be generated at higher Re_i. Although these small scale flow structures would not be seen on the macroscopic scale, the flow on the macroscopic scale is driven by averages of the local flow. Hence, possible consequences such as flow stagnation or unexpected changes in the direction of the flow may be experienced on the macroscopic scale.

Thus, from figure 45 it is realised that there are highly complex flow patterns which arise for non-zero Re_i. As the flow around each abrasive will occur at a non-zero Re_i, it is important to understand what factors, and how much they, affect the flow behaviour. Hence, the aim of this section will be to find out how the flow, and therefore the transport of grinding fluid, is affected by changes in the parameter space.

5.12.1 *Curvature Correction Terms*

To begin with, we return to expression (471) in order to find out how these curvature terms affect the global transport. In order to examine the behaviour of I in a slip regime, we consider different geometries of skew pyramids, as shown in figure 46. This study is motivated by the appearance of partial derivatives of $\tilde{h}$ in the surface integral (476), noting that the surface integral of the partial derivative terms alone would be 0 for a symmetrical geometry. Alongside this, motivated by the velocity difference term in (476), we will look at the effect of

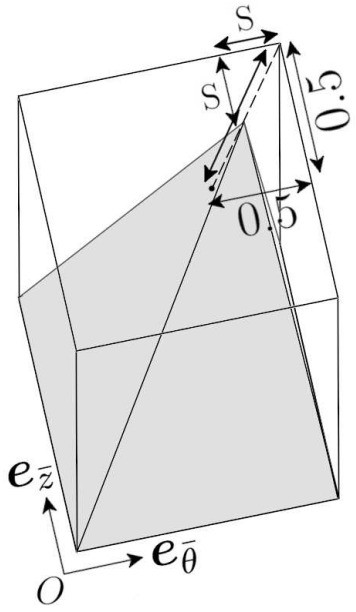

Figure 46: Illustration of the unit cell of a skew pyramid. The skew factor, calculated as $5 \times 10^{-1} - S$, is a measure of the deformity from a regular pyramid along the diagonal dashed line.

changing the slip length. The intent of studying both of these is to understand which of the terms in (476) primarily affects the magnitude of the curvature terms: is it the symmetry of the local geometry (i.e. the partial derivatives of $\tilde{h}$) or the velocity difference due to slip? We choose to present values of these terms from solutions in the Navier-Stokes regime as greater insight can be found.

We define the skew factor as $5 \times 10^{-1} - S, 0 \leq S \leq 5 \times 10^{-1}$. The skew factor is a measure of the deformity that the skew pyramids exhibit towards the corner with microscopic coordinates at $\bar{r} = 1, \bar{\theta} = 1, \bar{z} = 1$, compared to a regular pyramid with tip at $\bar{r} = 1, \bar{\theta} = 5 \times 10^{-1}, \bar{z} = 5 \times 10^{-1}$. For the purposes of investigation of these local terms, we consider only liquid, i.e. $\alpha_{0,l} = 1$.

Graphs of the values of the curvature terms comprising I are plotted against the local Reynolds number, Re_i, in figures 47 and 48 for various slip lengths

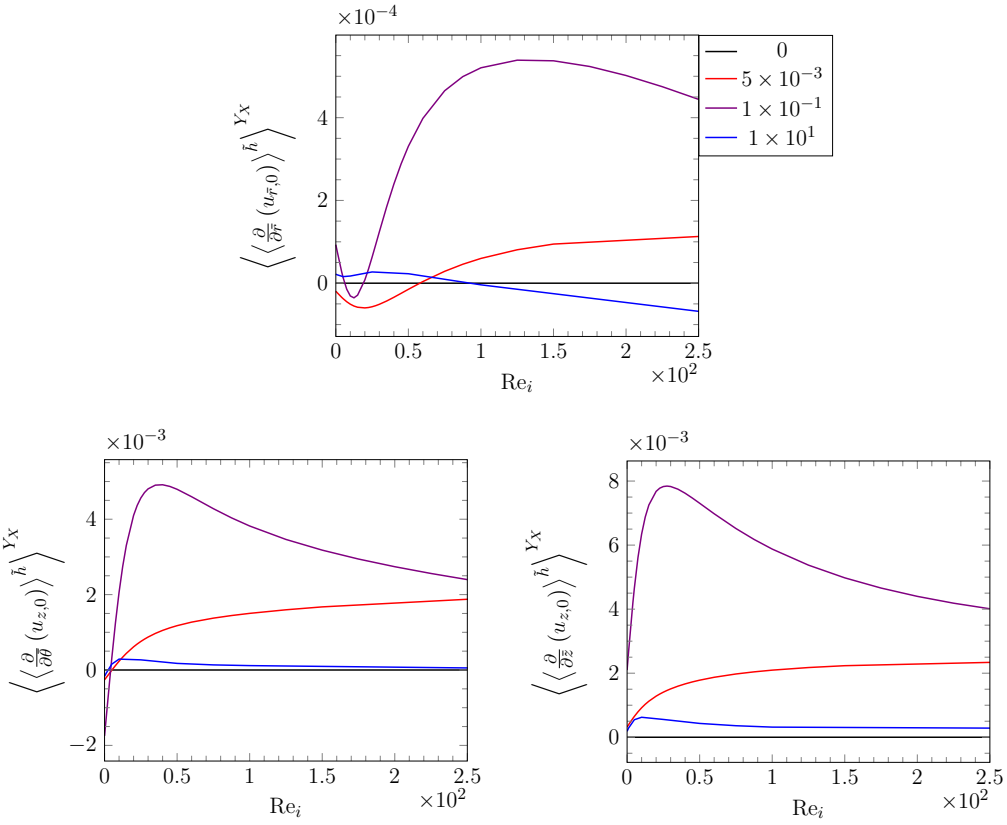

Figure 47: Graphs showing how the curvature terms in the inertial regime are affected by the slip length, $\hat{\beta}$, with these values shown in the legend. Here, $\mu_{mix} = \dfrac{1.92 \times 10^{-5}}{1.53 \times 10^{-2}} \approx 1.25 \times 10^{-3}$ and $\theta_r = \frac{\pi}{16}$.

and skew factors, respectively. For the results we present here, we take the parameters

$$\begin{aligned} \alpha_{0,l} &= 1, \\ \rho_{mix} &= 1.41 \times 10^{-3}, \\ \mu_{mix} &= 9.6 \times 10^{-2}, \\ \theta_r &= \frac{\pi}{16}. \end{aligned} \tag{553}$$

In figure 47, the solutions are presented with $S = 0$, i.e. symmetry of the geometry. We immediately make the observation that the no-slip solution has zero values for the curvature source terms, as we noted from (476). For non-zero slip lengths, the terms take non-zero values, with the largest terms typically coming from the solutions with $\hat{\beta} = 1 \times 10^{-1}$. Despite this variance in magnitude of

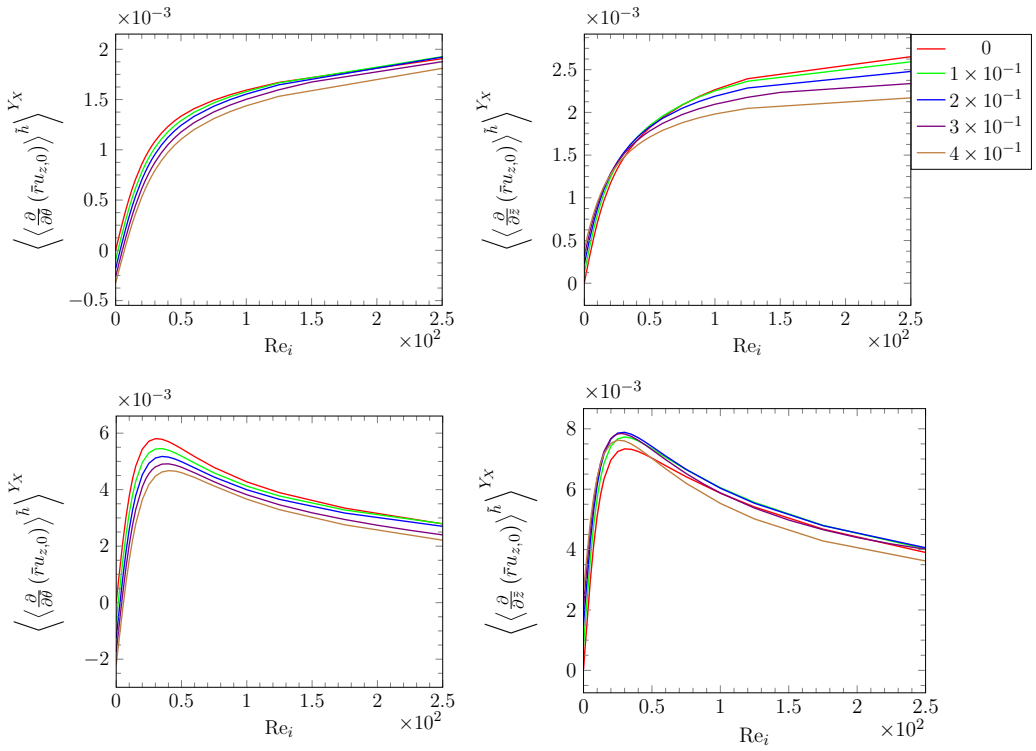

Figure 48: Graphs showing some values of the extra curvature terms seen in the global problem. The first row is solutions for $\hat{\beta} = 5 \times 10^{-3}$ and the second row $\hat{\beta} = 1 \times 10^{-1}$. The line colours represent different slant values, with the legend in the top right specifying the colour-to-slant correspondence.

the terms, the plots for each $\hat{\beta}$ show the same behaviour across Re_i. The terms appear to become non-zero as the flow regime transitions from no-slip to slip, and then tend back towards 0 in the large-slip regime.

Figure 48 presents values of the two curvature terms $\left\langle \left\langle \frac{\partial}{\partial \theta} (\bar{r} u_{z,0}) \right\rangle^{\tilde{h}} \right\rangle^{Y_X}$ and $\left\langle \left\langle \frac{\partial}{\partial \bar{z}} (\bar{r} u_{z,0}) \right\rangle^{\tilde{h}} \right\rangle^{Y_X}$ for various values of S, shown in the legend. The results in the first and second row are plotted for slip length $\hat{\beta} = 5 \times 10^{-3}$ and $\hat{\beta} = 1 \times 10^{-1}$, respectively.

Comparing the results with the two slip lengths, different behaviours of the terms are seen for increasing Re_i. In particular, the terms appear to increase for larger Re_i with the smaller slip length while the opposite situation occurs for the larger slip length. Comparing the results for different values of S, we see similarity between the behaviour of the curvature terms. For increasing

Re_i, the terms are of the same magnitude and have the same shape. Thus, the asymmetry of the local geometry appears to have a much smaller effect on the curvature terms in comparison to the effect of the slip length on these terms.

As a final remark, we see from figures 47 and 48 that the largest magnitude a curvature term takes (in the presented solutions) is roughly

$$\left| \left\langle \left\langle \frac{\partial \left(\bar{r} u_{z,0} \right)}{\partial \bar{z}} \right\rangle^{\tilde{h}} \right\rangle^{Y_X} \right| \approx 8 \times 10^{-3}. \tag{554}$$

Hence, we can conclude that, although small, these source terms have a non-negligible effect in a slip regime and their role in influencing the transport of the grinding fluid can not be neglected in equation (544).

5.12.2 *Effect of Reynolds Number*

Intuitively, we understand that an increase in the microscopic Reynolds number, Re_i, should result in faster transport through the grinding zone. However, given the observation of vortices appearing in the local flow from figure 45, it is worthwhile to quantitatively examine how the local flow responds to an increase in Re_i. Furthermore, the onset of turbulence is a valuable aspect of the flow to understand with the potential impact it can have on the transport of the grinding fluid. To this end, we begin this subsection by stating the parameters that we take for the problem and then proceed by presenting results for different Re_i.

For the results we present here, we take the parameters

$$\begin{aligned} \rho_{mix} &= 1.41 \times 10^{-3}, \\ \mu_{mix} &= 9.6 \times 10^{-2}, \\ \theta_r &= \frac{3\pi}{16}, \\ \hat{\beta} &= 2 \times 10^{-4}. \end{aligned} \tag{555}$$

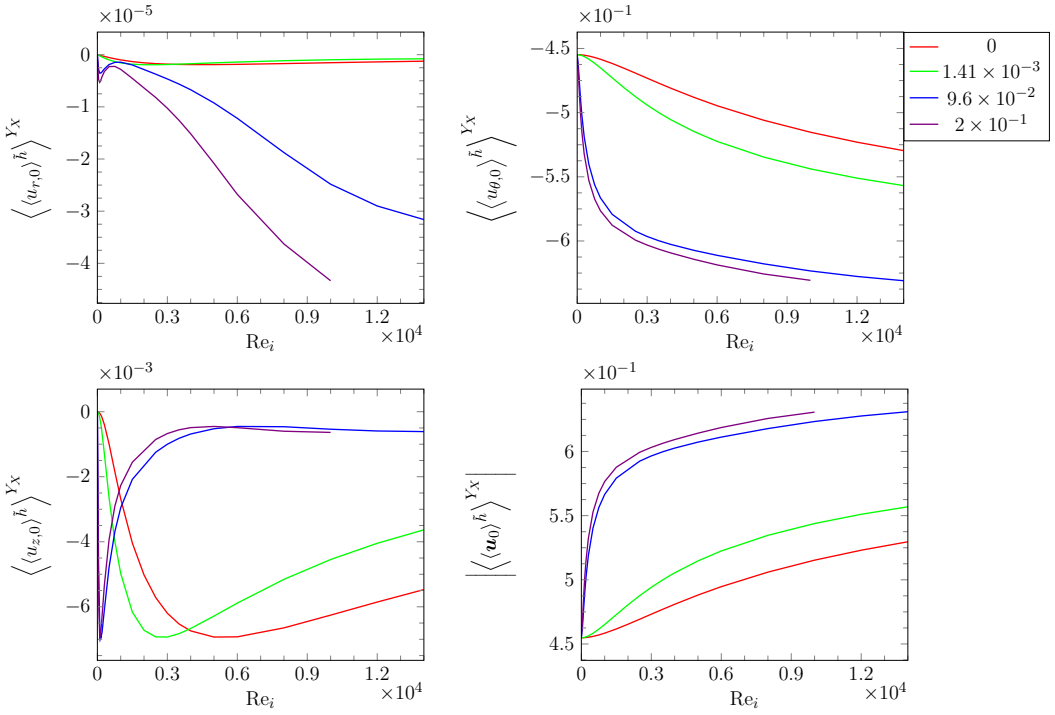

Figure 49: Graphs showing how the constituent components of $\boldsymbol{U}_0$ change with Re_i at different values of $\alpha_{0,l}$, as shown in the legend. These values of $\alpha_{0,l}$ are given in the legend, where $\frac{1.13}{8\times10^2} \approx 1.41 \times 10^{-3}$ is the density fraction, ρ_{mix}, and $\frac{1.92\times10^{-5}}{2\times10^{-4}} \approx 9.6 \times 10^{-2}$ is the viscosity fraction, μ_{mix}.

As we will only be interested in the local solutions across various Re_i in this subsection, we will leave the remaining parameters unstated here. We recall that the coefficient of the inertial terms is not Re_i as in incompressible single phase flows, but $\mathrm{Re}_i\rho_{0,m}$.

Figure 49 presents the averages of the microscopic velocity components and magnitude of the microscopic velocity average, $\left|\left\langle \langle \boldsymbol{u}_0 \rangle^{\tilde{h}} \right\rangle^{Y_X}\right|$, for varying Re_i at different volume fractions. The behaviour of the θ and z components appears to be consistent across volume fractions. As one would expect, $\left\langle \langle u_{\theta,0} \rangle^{\tilde{h}} \right\rangle^{Y_X}$ increases in magnitude as Re_i increases. However, $\left\langle \langle u_{z,0} \rangle^{\tilde{h}} \right\rangle^{Y_X}$ appears to have a sharp decrease for non-zero Re_i. This is partially because $\left\langle \langle u_{z,0} \rangle^{\tilde{h}} \right\rangle^{Y_X} = 0$ in the Stokes regime due to the linearity of the equations. As Re_i increases, $\left\langle \langle u_{z,0} \rangle^{\tilde{h}} \right\rangle^{Y_X}$ appears to tend back to 0, though at faster rates the larger that $\alpha_{0,l}$ is. The radial component, $\left\langle \langle u_{r,0} \rangle^{\tilde{h}} \right\rangle^{Y_X}$, seems to have different behaviours

across the various $\alpha_{0,l}$. For $\alpha_{0,l} = 0, 1.41 \times 10^{-3}$, we observe that $\left\langle \langle u_{z,0} \rangle^{\tilde{h}} \right\rangle^{Y_X}$ experiences a small increase in magnitude at $\mathrm{Re}_i \approx 1 \times 10^3$ and then decays back to 0. In contrast, $\left\langle \langle u_{z,0} \rangle^{\tilde{h}} \right\rangle^{Y_X}$ at the two largest presented values of $\alpha_{0,l}$ appears to continue increasing in magnitude as Re_i increases. This unpredictable behaviour is not unexpected. As we saw in figure 45, the nonlinear nature of the local flow gives rise to complex flow structures which complicates the study of the flow behaviour.

We observe from the plots in figure 49 that the speed at which the grinding fluid is advected through the grinding zone, $\left| \left\langle \langle \boldsymbol{u}_0 \rangle^{\tilde{h}} \right\rangle^{Y_X} \right|$, appears to be dominated by the contribution from $\left\langle \left\langle u_{\theta,0} \right\rangle^{\tilde{h}} \right\rangle^{Y_X}$. That is, the grinding fluid travels azimuthally through the grinding zone faster than it is transported radially and axially. However, recalling equation (544), $\left\langle \langle u_{z,0} \rangle^{\tilde{h}} \right\rangle^{Y_X}$ is important for understanding the transport of the grinding fluid. This is due to the role of this component in determining the flux of fluid through the sides of the grinding zone. Indeed, the graphs show that $\left\langle \langle u_{z,0} \rangle^{\tilde{h}} \right\rangle^{Y_X}$ maintains the same sign for the specified parameter values and sampled values of Re_i and $\alpha_{0,l}$. This has potential for impact in industry as the capability of a-priori determining that one side of the grinding zone will leak grinding fluid allows for measures to be taken to reduce this effect. By ensuring that a guard is set up along the side that is predicted to leak fluid, grinding fluid can be forced to stay in the grinding zone and splashing of potentially hazardous grinding fluid can be prevented from reaching the machine operator, to name two possible benefits. Later on, we will investigate the factors behind the sign of $\left\langle \langle u_{z,0} \rangle^{\tilde{h}} \right\rangle^{Y_X}$.

Let us comment on the plots corresponding to $\alpha_{0,l} = 2 \times 10^{-1}$ in figure 49. The final Re_i that results are shown for is $\mathrm{Re}_i = 1 \times 10^4$, due to the flow becoming unsteady beyond this Re_i and our scheme with Newton's method being unable to find further solutions. Given the size of Re_i and, recalling figure 45, the appearance of small vortices in the flow field, it is likely that this unsteadiness coincides with the onset of turbulent flow.

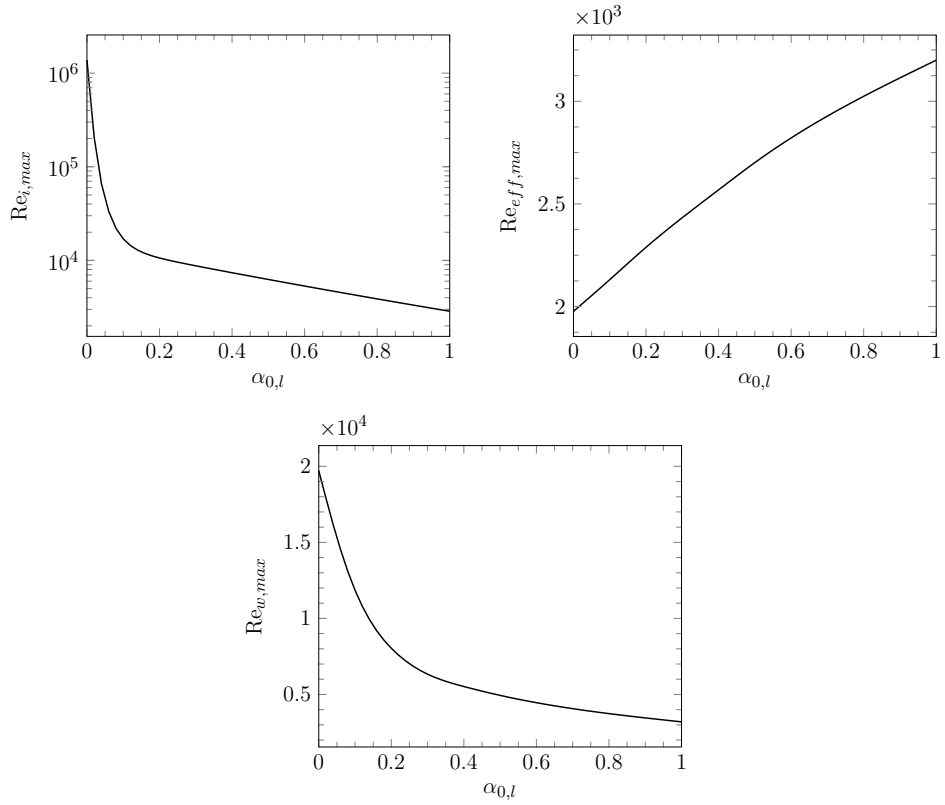

Figure 50: Plots showing the maximum microscopic Reynolds number, $\mathrm{Re}_{i,max}$, before further solutions can not be found, as well as corresponding plots for the effective maximum microscopic Reynolds number, $\mathrm{Re}_{eff,max} = \mathrm{Re}_{i,max}\rho_{0,m}$, and the weighted maximum microscopic Reynolds number, $\mathrm{Re}_{w,max} = \frac{\mathrm{Re}_{i,max}\rho_{0,m}}{\mu_m}$.

In fact, we can find such a maximum microscopic Reynolds number, $\mathrm{Re}_{i,max}$, at every $\alpha_{0,l}$ we solve the local problem for. We define the effective maximum microscopic Reynolds number by

$$\mathrm{Re}_{eff,max} = \mathrm{Re}_{i,max}\rho_{0,m} \tag{556}$$

and weighted maximum microscopic Reynolds number by

$$\mathrm{Re}_{w,max} = \frac{\mathrm{Re}_{i,max}\rho_{0,m}}{\mu_{0,m}}. \tag{557}$$

We present graphs of $\mathrm{Re}_{i,max}, \mathrm{Re}_{eff,max}$ and $\mathrm{Re}_{w,max}$ against $\alpha_{0,l}$ in figure 50.

Focusing on the graph of $\mathrm{Re}_{i,max}$, we observe that Re_i can take extremely large values before the flow becomes unsteady, especially at small $\alpha_{0,l}$. This

is not surprising, given that $\rho_{mix} \approx 1.41 \times 10^{-3}$ and Re_i is defined from the grinding fluid's rheological parameters. Looking at the graph of $\mathrm{Re}_{eff,max}$, the coefficient of the inertial terms in the local problem, we see that this increases with increasing $\alpha_{0,l}$. This is expected as the grinding fluid has a higher viscosity than the ambient air, thus the coefficient of the viscous terms increases with increasing $\alpha_{0,l}$. Unexpectedly, there appears to be an almost linear relationship between $\mathrm{Re}_{eff,max}$ and $\alpha_{0,l}$ in the local cell.

These observations motivate us to look at the graph of $\mathrm{Re}_{w,max}$ for greater insight. While it follows the same qualitative behaviour of $\mathrm{Re}_{i,max}$ for increasing $\alpha_{0,l}$, the values of $\mathrm{Re}_{w,max}$ are typical of the Reynolds number observed at the onset of turbulence in single-phase, wall-bounded flows. This supports our recent hypothesis that the unsteadiness coincides with the onset of turbulence in the flow. It can therefore be argued that the graphs suggest there is an earlier onset of turbulence in the local flow as the concentration of grinding fluid increases.

Turbulence in the grinding zone has the potential to have a devastating impact on the effectiveness of application of the grinding fluid. If adverse pressure gradients develop inside the grinding zone, or in extreme cases flow separation, then the transport of the grinding fluid could be severely affected. Poor cooling and lack of lubrication due to stagnated and starved regions of the grinding zone are two direct consequences of the onset of turbulence.

Thus, figure 50 suggests that deeper understanding here is necessary when optimising the application of the grinding fluid. Intuitively, a larger concentration of grinding fluid in the grinding zone would be expected to lead to greater cooling and lubrication. However, these results suggest that larger concentrations of grinding fluid could prompt the occurrence of turbulent structures, e.g. vortices. These may obstruct the flow and hinder the transport of grinding fluid through the grinding zone, thereby eventually leading to a decline in the grinding fluid present across the grinding zone. Therefore, larger concentrations of grinding fluid may be unfavourable for the effectiveness of the grinding fluid.

Additionally, flooding of the grinding zone is sometimes done in grinding. This is where the grinding zone is submerged in a layer of grinding fluid prior to the start of the grinding operation and a large quantity of grinding fluid is delivered throughout the process to surround the grinding zone with grinding fluid. The results indicate that this could cause unsteady (and turbulent) effects to be present from the start, and inhibit the transport of grinding fluid when compared to the non-flood scenario. Indeed, flooding is a contentious method in grinding, with published arguments existing which opposite its use; see, for example, comments in [4] and [79]. In particular, in the latter reference, the metalworking company Master Chemical Corporation comment that, "'Fluid application is not just a matter of bathing the area in fluid and assuming it will be in the right place' ... A lot of people will flood the grinding area, but this is actually not beneficial". Previous studies have only focused on the inability of flooding to penetrate through the air boundary layer into the grinding zone, and no studies exist on possible detrimental effects of large concentrations of grinding fluid inside the grinding zone, primarily due to the difficulty of measuring such effects. However, these results suggest another possible reason for inefficient flow with flooding which support the argument against it, though more work here is necessary to better understand this.

5.12.3 *Effect of Abrasive Orientation*

Previously in the Stokes regime, the angle of orientation of the Trizact$^{\text{TM}}$ abrasives was not explicitly investigated. This was due to the linearity of the Stokes regime failing to accurately capture the flow behaviour of the grinding fluid around these abrasives. However, now that the nonlinear inertial effects are included in the local flow, we are able to gain valuable insight in this area.

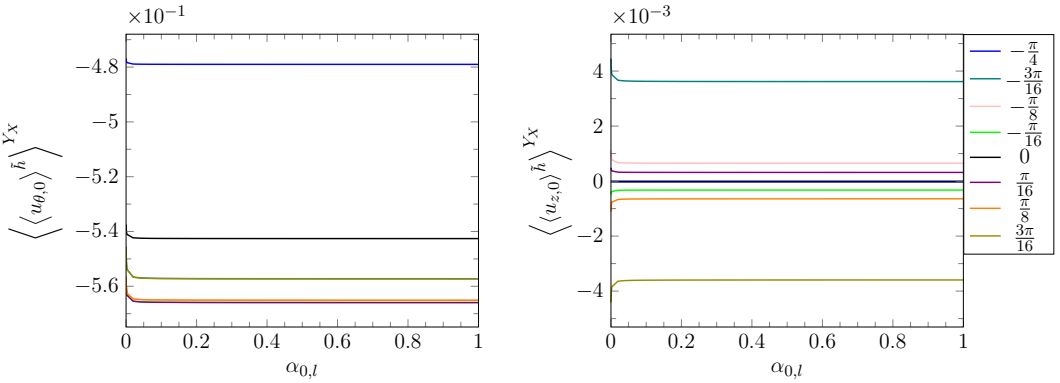

Figure 51: Graphs showing the averages of two microscopic velocity components for different abrasive angles of orientation, θ_r, in a creep-feed grinding regime. The line colours which correspond to the angles are specified in the legend.

Figure 51 presents the results for the microscopic velocity components in a creep-feed grinding regime with parameters taken as

$$\begin{aligned} \mathrm{Re}_i &= 4.12 \times 10^{2}, \\ h_w &= 6.67 \times 10^{-2}, \\ \varepsilon &= 6.67 \times 10^{-4}, \\ \delta &= 1.2 \times 10^{1}, \\ \rho_{mix} &= 1.05 \times 10^{-3}, \\ \mu_{mix} &= 1.43 \times 10^{-3}, \\ \hat{\beta} &= 1 \times 10^{-4}. \end{aligned} \tag{558}$$

Results are presented for various angles of orientation, θ_r, shown in the legend.

Even from a brief look, it is evident that the angle of orientation influences the local flow velocity and, by extension, the transport of grinding fluid through the grinding zone. Focusing on the solutions for $\left\langle \left\langle u_{\theta,0} \right\rangle^{\tilde{h}} \right\rangle^{Y_X}$, a clear minimum in the magnitude exists when $\theta_r = -\frac{\pi}{4}$. For the presented values of θ_r between $-\frac{\pi}{4}$ and 0, $\left\langle \left\langle u_{\theta,0} \right\rangle^{\tilde{h}} \right\rangle^{Y_X}$ lies near the global maximum, while $\theta = 0$ corresponds to a slight decrease in the magnitude. As θ_r increases, $\left\langle \left\langle u_{\theta,0} \right\rangle^{\tilde{h}} \right\rangle^{Y_X}$ again increases

towards the maximum, correlating with an increase in the transport speed of the grinding fluid through the grinding zone.

Turning our attention to $\left\langle \langle u_{z,0} \rangle^{\tilde{h}} \right\rangle^{Y_X}$, antisymmetry about $\theta_r = 0$ is observed. That is, for each value of θ_r that $\left\langle \langle u_{z,0} \rangle^{\tilde{h}} \right\rangle^{Y_X}$ has been plotted for, e.g. $\theta_r = \theta_t$, the solution of $\left\langle \langle u_{z,0} \rangle^{\tilde{h}} \right\rangle^{Y_X}$ for $\theta_r = -\theta_t$ is equal in magnitude but with opposite sign. We emphasise our point in the previous subsection: $\left\langle \langle u_{z,0} \rangle^{\tilde{h}} \right\rangle^{Y_X}$ is a valuable quantity to understand due to its role in determining the direction of the flow through the sides of the grinding wheel. These results indicate that the orientation of the abrasives determines which side of the grinding zone that grinding fluid is ejected from and atmospheric air is sucked in through. This is due to the observed link between θ_r and the sign of $\left\langle \langle u_{z,0} \rangle^{\tilde{h}} \right\rangle^{Y_X}$. With the reverse orientation, these sides are switched.

Despite the observed antisymmetry of $\left\langle \langle u_{z,0} \rangle^{\tilde{h}} \right\rangle^{Y_X}$ about $\theta_r = 0$, the behaviour is not straightforward. Due to symmetry of the geometry, we expect, and indeed observe, that $\left\langle \langle u_{z,0} \rangle^{\tilde{h}} \right\rangle^{Y_X} = 0$ when $\theta_r = 0, -\frac{\pi}{4}$. An increase to $\theta_r = \frac{\pi}{16}$ causes $\left\langle \langle u_{z,0} \rangle^{\tilde{h}} \right\rangle^{Y_X}$ to increase and become positive for all $\alpha_{0,l}$. This indicates that atmospheric air surrounding the grinding wheel is sucked in through the side of the grinding wheel at $z = 0$, and grinding fluid inside the grinding zone is ejected out of the side of the grinding wheel at $z = h_w$. However, the situation reverses as the angle of orientation increases further to $\theta_r = \frac{\pi}{8}, \frac{3\pi}{16}$. By periodicity of the solution in θ_r, we then know that $\left\langle \langle u_{z,0} \rangle^{\tilde{h}} \right\rangle^{Y_X}$ rapidly decreases to 0 when $\theta_r = \frac{\pi}{4}$.

We remark that the jump in the graph of the solution seen for small $\alpha_{0,l}$ is due to the coefficient of the advection term, $\rho_{0,m}\mathrm{Re}_i$, undergoing rapid change. When $\alpha_{0,l} = 0$, we have

$$\mathrm{Re}_i \rho_{0,m} = \mathrm{Re}_i \rho_{mix} \approx 4.3 \times 10^{-1}, \tag{559}$$

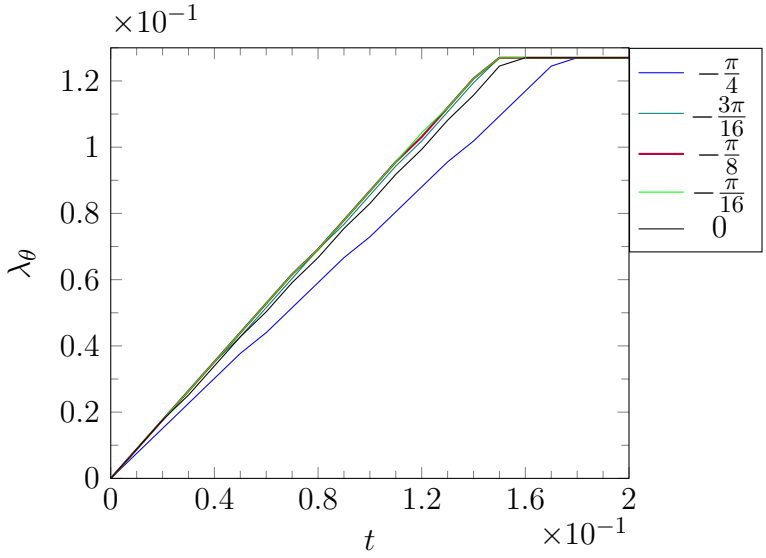

Figure 52: Plots of the azimuthal distance that the grinding fluid has travelled through the grinding zone, denoted by λ_θ, at various times for different angles of orientation of the abrasives. The lines corresponding to angles $-\frac{\pi}{8}$ and $-\frac{\pi}{16}$ have a large overlap.

using values from (558). Since $\rho_{mix} \approx 1 \times 10^{-3}$ is small, then as $\alpha_{0,l}$ increases past ρ_{mix} the coefficient $\rho_{0,m}\mathrm{Re}_i \approx \alpha_{0,l}\mathrm{Re}_i$. For example, when $\alpha_{0,l} = 1 \times 10^{-1}$ we have that

$$\mathrm{Re}_i\rho_{0,m} \approx 4.2 \times 10^1, \tag{560}$$

which is 1×10^2 times larger than the value in (559) for $\alpha_{0,l} = 0$. The almost-constant profile for $\alpha_{0,l}$ beyond the small near-zero region is due to the flow regime no longer experiencing a rapid transition from a viscous dominated flow regime to an inertia dominated flow regime.

In figure 52, we plot the azimuthal distance that grinding fluid has travelled over time for different angles of orientation when $\alpha_D = 8 \times 10^{-1}$. As the solution for $\left\langle \left\langle u_{\theta,0} \right\rangle^{\tilde{h}} \right\rangle^{Y_X}$ is symmetric about $\theta_r = 0$ and the solution for $\left\langle \langle u_{z,0} \rangle^{\tilde{h}} \right\rangle^{Y_X}$ is two orders of magnitude smaller than $\left\langle \left\langle u_{\theta,0} \right\rangle^{\tilde{h}} \right\rangle^{Y_X}$, as seen in figure 51, the azimuthal distance for the remaining angles are very close to the corresponding angle symmetric about 0. As such, these angles are not presented.

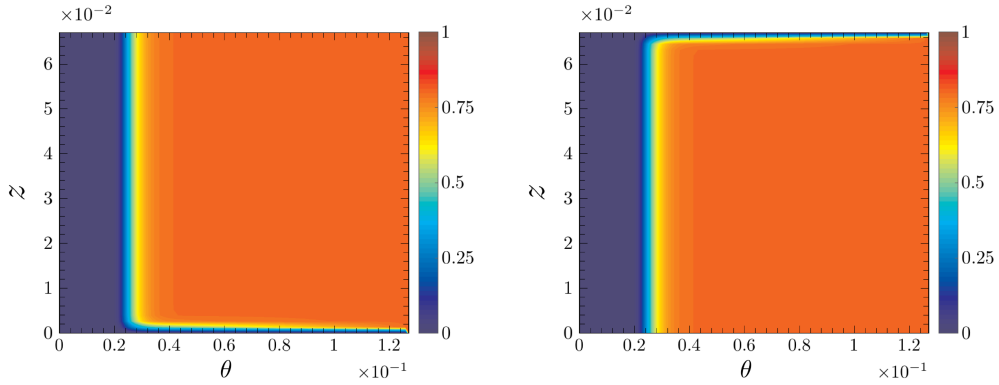

(a) $\theta_r = -\frac{3\pi}{16}$ (b) $\theta_r = \frac{3\pi}{16}$

Figure 53: Plots showing the volume fraction, $\alpha_{0,l}$, at $t = 1.2 \times 10^{-1}$ in a creep-feed grinding regime for angles $\theta_r = -\frac{3\pi}{16}$ and $\theta_r = \frac{3\pi}{16}$ as shown in (a) and (b), respectively. The absence of grinding fluid along the sides of the wheel can be seen to change depending on the angle. Here we have translated θ by $-\left(\frac{3\pi}{2} - \theta_0\right)$, where $\theta_0 \approx 4.59$.

An obvious increase in the speed that the grinding fluid front gets transported through the grinding zone is seen. The angles $\theta_r = -\frac{3\pi}{16}, -\frac{\pi}{8}, -\frac{\pi}{16}$ appear to reach the end of the grinding zone at similar times, approximately $t = 1.5 \times 10^{-1}$. However, for $\theta = 0$ and $\theta = -\frac{\pi}{4}$, the grinding fluid takes approximately 7% and 20% longer to reach the end of the grinding zone, respectively. Despite these time differences appearing small, the realistic physics of the grinding fluid flow are unforgiving and over small timescales, effects such as fluid boiling can result in irreversible damage to the workpiece. As such, it is important that any such optimisations as this are considered during the design of grinding wheels.

Figure 53 shows the solution of (544) for the volume fraction distribution at $t = 1.2 \times 10^{-1}$ with the nondimensional numbers and parameters given by (558). Two different angles of orientation are presented as indicated in the subcaption. The absence of grinding fluid along the sides of the wheel follows the predicted behaviour based on figure 51. For $\theta_r = -\frac{3\pi}{16}$, $\left\langle \langle u_{z,0} \rangle^{\tilde{h}} \right\rangle^{Y_X}$ is positive for all $\alpha_{0,l}$ and grinding fluid is ejected from $z = h_w$ whilst fluid from the atmosphere enters side of the grinding zone at $z = 0$. For $\theta_r = \frac{3\pi}{16}$, the situation reversed which is not surprising given that the solution of $\left\langle \langle u_{z,0} \rangle^{\tilde{h}} \right\rangle^{Y_X}$ is negative for all $\alpha_{0,l}$. These results support the idea that the angle of orientation for the abrasives is a main factor that determines how fluid behaves at the sides of the

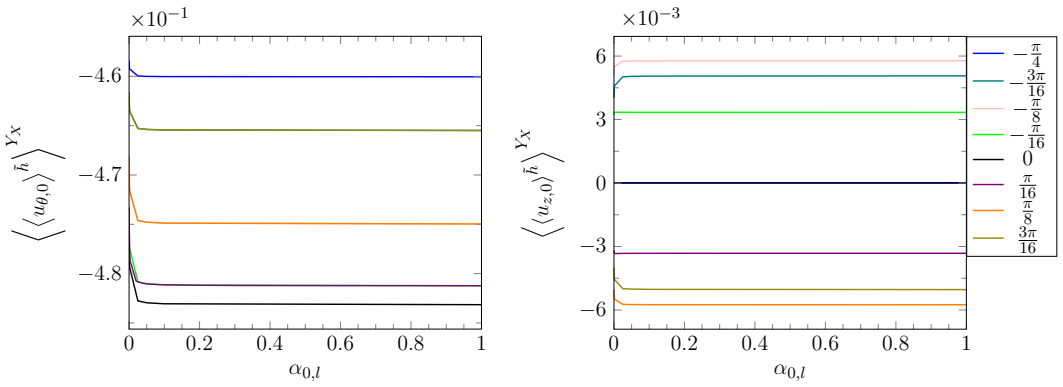

Figure 54: Graphs showing the averages of two microscopic velocity components for different abrasive angles of orientation, θ_r, in a surface grinding regime. The line colours which correspond to the angles are specified in the legend.

grinding zone. Consequently, the angle of orientation affects how the sides of the grinding wheel can experience the effects of a poorly lubricated and cooled cutting region, including increased wear of the abrasives and wheel damage due to insufficient flushing of the chips by the grinding fluid.

Figure 54 presents the results for the microscopic velocity components of a surface grinding regime with parameters taken to as

$$\begin{aligned} \mathrm{Re}_i &= 2.94 \times 10^{1}, \\ h_w &= 5 \times 10^{-2}, \\ \varepsilon &= 8.33 \times 10^{-5}, \\ \delta &= 8 \times 10^{-1}, \\ \rho_{mix} &= 1.05 \times 10^{-3}, \\ \mu_{mix} &= 1.43 \times 10^{-3}, \\ \hat{\beta} &= 8 \times 10^{-4}. \end{aligned} \tag{561}$$

Results are presented for various angles of orientation, θ_r, shown in the legend.

Looking at the plots of $\left\langle \left\langle u_{\theta,0} \right\rangle^{\tilde{h}} \right\rangle^{Y_X}$, similarities in the general behaviour of the solutions to the creep-feed grinding regime can be seen. One similarity is that $\theta_r = -\frac{\pi}{4}$ corresponds to the lowest speed through the grinding zone.

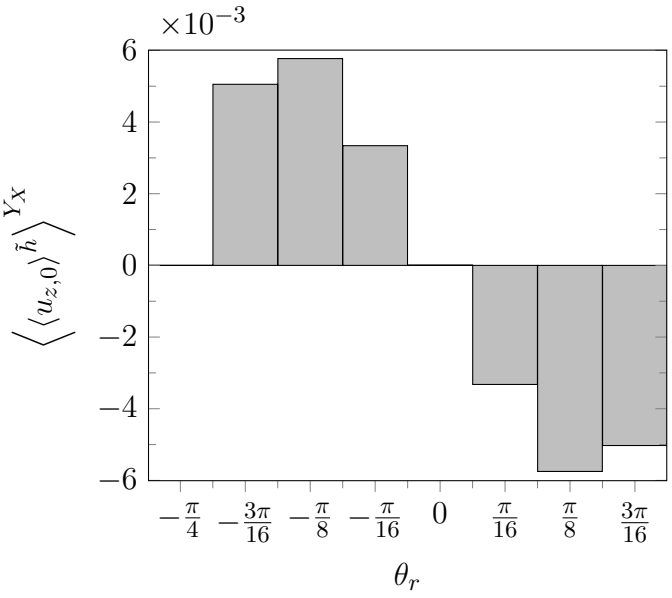

Figure 55: Bar chart showing the value of $\left\langle \langle u_{z,0} \rangle^{\tilde{h}} \right\rangle^{Y_X}$ for different angles of orientation of the abrasives, θ_r, with $\alpha_{0,l} = 1 \times 10^{-1}$.

Interestingly, the fastest transport through the grinding zone now occurs when $\theta_r = 0$, which was not the previously observed behaviour.

For the plots of $\left\langle \langle u_{z,0} \rangle^{\tilde{h}} \right\rangle^{Y_X}$, the solutions maintain the symmetry about $\theta_r = 0$ that was seen previously. However, a noticeable difference is seen regarding the sign of $\left\langle \langle u_{z,0} \rangle^{\tilde{h}} \right\rangle^{Y_X}$. Specifically, unlike before, $\left\langle \langle u_{z,0} \rangle^{\tilde{h}} \right\rangle^{Y_X}$ has the same sign for every θ_r that is positive and every θ_r that is negative. In figure 55, we show this more clearly by plotting the same results for $\left\langle \langle u_{z,0} \rangle^{\tilde{h}} \right\rangle^{Y_X}$ against θ_r with $\alpha_{0,l} = 1 \times 10^{-1}$.

Evidently, the angle of orientation is not the only factor which determines the behaviour of $\left\langle \left\langle u_{\theta,0} \right\rangle^{\tilde{h}} \right\rangle^{Y_X}$, $\left\langle \langle u_{z,0} \rangle^{\tilde{h}} \right\rangle^{Y_X}$ and, consequently, the transport of the grinding fluid. As such, different grinding regimes are predicted to show different behaviours of the transport even for the same abrasive profiles.

5.13 CONCLUSION

In this section, we began by developing the homogenisation process for a problem involving periodic coefficients. We then used this homogenisation tool to

develop governing equations for the flow in the grinding zone when the abrasives profile on the belt is periodic. Initially, we derived local equations which governed the periodic flow over a single abrasive. We then upscaled these to derive global equations which governed the transport of the grinding fluid through the grinding zone.

From investigating solutions of both the local and global problems, it was found that the local flow over the abrasives generates a negligible fluid pressure in the grinding zone. As we already assumed we were in the regime of negligible enforced pressure gradient across the grinding zone, based on the results of Chapter 4, we rescaled the characteristic pressure and found that this allowed us to neglect the pressures inside the grinding zone. In addition, it was found that with this characteristic pressure, we could find governing equations for the shear-dominated, local flow around the abrasives which include inertial effects. This was a considerable leap from the Stokes regime that we dealt with at the start of the chapter, given that inertial effects are expected to be present and have a strong influence in the flow around the abrasives.

With governing equations which included inertial effects in the flow, we were able to infer flow behaviour from the solutions of the flow in certain grinding regimes. A key finding here was the presence of a terminal microscopic Reynolds number which depended on the concentration of grinding fluid. Above this microscopic Reynolds number, the flow was anticipated to become fully turbulent. From the viewpoint of ensuring the maximum quantity of grinding fluid is efficiently transported throughout the grinding zone, this is a very undesirable property of the flow which could have negative consequences in the effectiveness of the application of grinding fluid.

Another key understanding came from investigating the effect of changing the angle of orientation of the pyramid abrasives. Notably, we found different behaviours in the transport of the grinding fluid depending on the grinding regime we considered. However, the essential knowledge was consistent in both regimes. Namely, that the angle of orientation can have a considerable effect on

how fast the grinding fluid is transported through the grinding zone, and the angle affects how the grinding fluid behaves at the sides of the grinding zone.

6

CONCLUSION

6.1 THESIS SUMMARY

The aim of this thesis was a greater understanding of the flow during grinding. Practically, experimental measuring constraints reduce the applicability of experimentally understanding the flow inside the grinding zone. Thus, we used multiphase and multiscale modelling techniques to derive novel governing systems of equations for the flow inside the grinding zone to better understand how the grinding fluid was transported here. Chapter 1 began with the introduction of the problem and the motivation for studying this.

Next, Chapter 2 set up the fundamentals for our study. Here we introduced the Trizact$^{\text{TM}}$ abrasives which became a vital part of the thesis later on. Chapter 3 was a succinct introduction to the method of matched asymptotic expansions which formed the basis of the multiscale methods in this thesis. Notably here, it was first seen that under an assumption on the distance between the grinding wheel and the workpiece, the investigation of the flow inside the grinding region does not require the solution far from the grinding zone. It was seen that this was due to the pressures far from the grinding zone acting as smaller order perturbations to the pressure inside the grinding zone. However, as a consequence of the thin grinding region, we discovered that only a very small amount of grinding fluid actually makes it into the grinding zone. With $\varepsilon \ll 1$ characterising the gap between the workpiece and the grinding wheel, the flux through the grinding zone is of $O(\varepsilon)$.

In Chapter 4, the tools that were developed in the aforementioned chapters were used to derive systems of equations which govern the flow inside and outside the grinding zone. In both of these chapters, certain assumptions were taken for the flow of the grinding fluid during grinding. In this chapter, it was supposed that the typical lubrication approximation constraints were applicable for the flow inside the grinding zone. Specifically, these were the lack of inertial effects of the flow and the small-slope assumption on the surfaces. We set up the domain to include a depth of cut and we were able to calculate the analytical solution for the pressure across the grinding zone. The parameter

$$\delta = \frac{d_c}{h_g} \tag{562}$$

first appeared in this chapter, quantifying the scale separation between the depth of cut, d_c, and the separation distance between the grinding wheel and the workpiece, h_g. We explored aspects of the analytical solution, discovering that the flux in the grinding zone is primarily driven by the shearing of the grinding wheel. However, the limitations of the lubrication approximation motivated the need for governing equations which more accurately captured aspects of the flow.

An improvement in the method proposed in Chapter 4 over the current models in the literature is that the grinding flow problem is fully closed. This reduces the necessity for difficult-to-measure data that a lot of models depend on. For example, the flow rate. As we saw in this chapter, the flux through the grinding zone is extremely small and in these quantities, the measurement error is too large to accurately measure.

We also considered the case where slip is present at the surfaces. We observed that the flux through the grinding zone increased with the slip length, $\hat{\beta}$. This result suggests that using additives which reduce the viscosity and friction at surfaces could lead to improvements in the transport of grinding fluid through the grinding zone. We remark that such additives have become popular in

recent years, however the focus has primarily been on the effect these additives have on reducing the wear of the grinding wheel.

In the $O(1)$ regime for δ, we observed that the flux through the grinding zone depends on the value of δ. With larger values of δ we saw a decrease in the flux through the grinding zone. This is another result with implications in industry. While a larger depth of cut is often ideal due to the improved speed of the job, these results suggest that it could hinder the amount of grinding fluid reaching the grinding zone.

Due to the limitations of the lubrication approximation for boundaries with $O(1)$ slopes, we used two-scale homogenisation in Chapter 5 with the assumption of a periodic abrasive profile on the wheel to derive systems of equations governing the local flow around each abrasive and the global flow throughout the grinding zone. Motivated by the findings of Chapter 4, we made the assumption that we were working in the high shear limit, where pressure gradients were negligible. By homogenising over the Stokes equations, it was found that the local flow behaved just like a Stokes flow while the global flow reduced to a Reynolds-like equation with species transport, though with the addition of extra curvature source terms. However, by considering the Stokes regime, important aspects of the flow were neglected which have a vital role on how the grinding fluid is transported; in particular, inertial effects.

Based on the observed negligible pressure effects on the transport of grinding fluid, the problem was scaled to look for shear-dominated solutions. It was found that in this case, we were able to derive equations governing the local flow which included inertial effect by using the two-scale homogenisation method. In addition, the global problem was reduced to a single transport equation for the concentration of grinding fluid. A surprising result is that in both the local and global problems, fewer differential equations need to be solved than in the Stokes regime.

Most importantly, in this section fundamental understanding in mechanisms which influence how the grinding fluid is transported through the grinding zone was gained. Information was presented which supported the existence of tur-

bulence occurring in the flow in the grinding zone. The potentially devastating effect of this on the effectiveness of the application of grinding fluid was described, with a remark that a strategy sometimes used by grinding operators may, based on the information presented, actually have a negative influence on the transport of grinding fluid through the grinding zone; namely, flooding the grinding zone prior to beginning and during the grinding process. This supports an existing argument amongst some people with grinding expertise against the use of flooding.

In addition, it was seen how the design of the grinding wheel's abrasive profile can affect properties of the flow. In particular, it was seen that the angle of orientation of the abrasives can have an appreciable influence on the speed at which the grinding fluid is advected through the grinding zone. As well as this, the dependency of the fluid's behaviour at the sides of the grinding zone on the angle was observed, with the angle of orientation determining which side was starved of grinding fluid. The benefits of such knowledge to the designer of grinding wheels and the operator of the grinding process are great. Understanding this mechanism allows the designer to transfer information such as this to the grinding operator, who in turn can take measures to ensure the grinding zone does not become starved of grinding fluid. An example of this could be the application of grinding fluid to the side predicted to suck in fluid from the atmosphere. In this way, the risks associated with poor application of grinding fluid can be mitigated, such as increased rate of wear of the wheel or thermal damage to the workpiece.

To conclude, three questions were asked in Section 1.3. Concerning the first question on the appropriateness of multiscale methods, it has been shown that multiscale methods can be used on the flow during grinding to derive coupled as well as reduced order models. Compared with the original, full-scale model, these models allow for a deep probing of factors which influence the flow. We have also observed improvements with the lubrication model compared to those in the literature, notably around the lack of dependence on empirical to calculate the solution. Concerning the second question on using these models to

enhance knowledge, we have gained deep insight into factors that influence the transport of grinding fluid through the grinding zone. An example of this is the study in the onset of turbulence which supports pre-existing arguments against flooding. Additionally, understanding how the ratio between the depth of cut and the separation distance between the grinding wheel and the workpiece influences the flux through the grinding zone is a key piece of knowledge for improving the application of grinding fluids.

Finally, concerning the question of optimisation. One key finding of this thesis was identifying that the arrangement of the abrasives can influence where the grinding fluid leaks out of the grinding zone. This is the first work identifying this to the author's knowledge. However, future collaborative work is necessary for a deeper understanding of the relation between the angle of orientation of abrasives to side of the grinding zone that grinding fluid leaks out of. This is one possible path for optimisation of grinding fluid application from this thesis which is realisable in industry.

6.2 FUTURE WORK

Although not treated in this thesis, the motivation for applying grinding fluid is to reduce the heat generated during the cutting of workpieces. Hence, to comprehensively model the grinding flow, the most important extension of this work is to adapt the multiphase model in this thesis to include an energy equation, particularly to facilitate the inclusion of heat. The multiscale methods in this thesis would then be applied to this new system to derive a coupled, multiphase, multiscale system of equations for the flow in and around the grinding zone. One possible method to treat the heat equation in the lubrication or homogenised framework would be through Dirichlet boundary conditions in the grinding zone using experimental data from the literature. There is a variety of such data which has been collected using thermocouples near the surface of the workpiece. Extending the model to involve heat transfer and phase change is the key extension behind gaining important insight into the flow during grind-

ing. An open question in the field is the occurrence of film boiling in the grinding zone. Due to the difficulties associated with measuring in the grinding zone, it is currently a hypothesis that this phenomena exists. If this were to be theoretically predicted, it would have large implications on the application of grinding fluid.

In Chapter 4, we only studied the two dimensional case. A valuable extension here would be the investigation of the three dimensional case. One important question is how the side boundaries of the grinding zone influence the flux and pressure gradient across it.

The problem that was considered in this thesis was an idealised one, where cutting was described by point contacts of the abrasives and the workpiece. While the flow domains in this situation and in reality with small depth of cut might not vary considerably, this will not be true in large depth of cut scenarios, i.e. creep-feed grinding regimes with high rates of material removal. In such cases, taking the geometry with the abrasive having an area of contact, to model the embedded abrasive in the workpiece, is one potential direction for this. Extending the work done in the homogenisation chapter to incorporate this geometry is trivial as it is simply a change in the unit cell geometry. However, this was not explored in this thesis, though it would be interesting to see how the grinding zone transport is affected by this, and whether more realistic local geometries (for example, trenches trailing the abrasive due to the cutting) are worth further exploring.

A

NONDIMENSIONAL NUMBERS ESTIMATION

Table 2 shows typical values of some dimensionless numbers of interest for the small range of grinding fluids that they can be calculated for. Below,

$$\mathrm{Re} = \frac{\rho V L}{\mu}, \tag{563}$$

$$\mathrm{Ca} = \frac{\mu V}{\sigma}, \tag{564}$$

$$\mathrm{We} = \frac{\rho V^2 L}{\sigma}, \tag{565}$$

$$\mathrm{Fr} = \frac{V}{\sqrt{gL}}, \tag{566}$$

where Re is the Reynolds number, Ca is the capillary number, We is the Weber number, Fr is the Froude number, ρ is the density of the fluid, μ is the viscosity of the fluid, σ is the surface tension of the air-fluid interface, V is the characteristic velocity and L is the characteristic length scale.

$V = 2.5 \times 10^1$ m s^{-1} $L = 2 \times 10^{-1}$ m	Re	Ca	We	Fr
Air at 25°C	3.22×10^5	N/A	N/A	2.52×10^1
Water at 25°C [45]	5.60×10^6	3.10×10^{-1}	1.73×10^6	2.52×10^1
Mineral Oil (20°C to 40°C) [59]	1.11×10^5 to 2.50×10^6	1.45 to 3.26×10^1	3.62×10^6	2.52×10^1

Table 2: Values of dimensionless numbers of interest for some grinding fluids.

B

MICROSCOPIC COORDINATE SYSTEM

We introduce the ordered coordinates of a cylindrical coordinate system as $\bar{\boldsymbol{x}} = (r, \theta, z)$, with the position vector $\boldsymbol{r}$ given by

$$\boldsymbol{r} = r\cos\theta\hat{\boldsymbol{e}}_x + r\sin\theta\hat{\boldsymbol{e}}_y + z\hat{\boldsymbol{e}}_z, \tag{567}$$

where $\hat{\boldsymbol{e}}_x, \hat{\boldsymbol{e}}_y, \hat{\boldsymbol{e}}_z$ are the Cartesian unit basis vectors. Defining the (covariant) basis vectors of a coordinate system by

$$\boldsymbol{e}_i = \frac{\partial \boldsymbol{r}}{\partial y^i}, \tag{568}$$

where y^i are the coordinates of the coordinate system, then we can write the cylindrical basis vectors in terms of the Cartesian basis vectors as

$$\boldsymbol{e}_r = \cos\theta\hat{\boldsymbol{e}}_x + \sin\theta\hat{\boldsymbol{e}}_y, \tag{569}$$

$$\boldsymbol{e}_\theta = -r\sin\theta\hat{\boldsymbol{e}}_x + r\cos\theta\hat{\boldsymbol{e}}_y, \tag{570}$$

$$\boldsymbol{e}_z = \boldsymbol{e}_z. \tag{571}$$

In view of the work in this thesis, let us nondimensionalise the z coordinate with some characteristic value R and make the substitution

$$r = R + h_g\bar{r} = R\left(1 + \varepsilon\bar{r}\right), \tag{572}$$

with h_g some small positive small number such that $\varepsilon = \frac{h_g}{R} \ll 1$ and $\bar{r} \in [0, 1]$. The nondimensional form of the position vector (567) will then be given by the expression

$$\boldsymbol{r} = (1 + \varepsilon\bar{r}) \cos\theta \hat{\boldsymbol{e}}_x + (1 + \varepsilon\bar{r}) \sin\theta \hat{\boldsymbol{e}}_y + z\hat{\boldsymbol{e}}_z, \tag{573}$$

where we have dropped any asterisk superscripts in $\boldsymbol{r}$ and z to denote nondimensionalised quantities for convenience. This coordinate system will be referred to as the macroscopic coordinate system.

Following this, we introduce the microscopic coordinate system defined by the (ordered) dimensionless coordinates $\boldsymbol{X} = (\bar{r}, \bar{\theta}, \bar{z})$, where $\bar{r}$ is given by (572) and

$$\bar{\theta} = \frac{\tilde{\theta}}{\chi^\star} = \frac{\theta\cos\kappa + z\sin\kappa}{\chi^\star}, \tag{574}$$

$$\bar{z} = \frac{\tilde{z}}{\chi^\star} = \frac{-\theta\sin\kappa + z\cos\kappa}{\chi^\star}, \tag{575}$$

$$\chi^\star = \frac{d}{R\sqrt{2}} = \sqrt{2}\varepsilon, \tag{576}$$

with $\kappa \in \left(\frac{\pi}{8}, \frac{3\pi}{8}\right]$ and $d = 2h_g$. We take the position vector $\bar{\boldsymbol{r}}$ of this coordinate system as

$$\boldsymbol{r} = \bar{r}\hat{\boldsymbol{e}}_{\bar{r}} + \bar{\theta}\hat{\boldsymbol{e}}_{\bar{\theta}} + \bar{z}\hat{\boldsymbol{e}}_{\bar{z}}, \tag{577}$$

where the microscopic basis vectors in (577) are given by

$$\boldsymbol{e}_{\bar{r}} = \frac{\partial\boldsymbol{r}}{\partial\bar{r}} = \varepsilon\left(\cos\theta\hat{\boldsymbol{e}}_x + \sin\theta\hat{\boldsymbol{e}}_y\right), \tag{578}$$

$$\boldsymbol{e}_{\bar{\theta}} = \frac{\partial\boldsymbol{r}}{\partial\bar{\theta}} = \chi^\star\left[(1 + \varepsilon\bar{r})\cos\kappa\left(-\sin\theta\hat{\boldsymbol{e}}_x + \cos\theta\hat{\boldsymbol{e}}_y\right) + \sin\kappa\hat{\boldsymbol{e}}_z\right], \tag{579}$$

$$\boldsymbol{e}_{\bar{z}} = \frac{\partial\boldsymbol{r}}{\partial\bar{z}} = \chi^\star\left[(1 + \varepsilon\bar{r})\sin\kappa\left(\sin\theta\hat{\boldsymbol{e}}_x - \cos\theta\hat{\boldsymbol{e}}_y\right) + \cos\kappa\hat{\boldsymbol{e}}_z\right], \tag{580}$$

using that θ and z in terms of $\bar{\theta}$ and $\bar{z}$, found through the inversion of the transformation matrix for (574) and (575), are

$$\theta = \chi^{\star}\left(\bar{\theta}\cos\kappa - \bar{z}\sin\kappa\right), \tag{581}$$

$$z = \chi^{\star}\left(\bar{\theta}\sin\kappa + \bar{z}\cos\kappa\right). \tag{582}$$

We observe that we can write the microscopic basis vectors (578)-(580) in terms of the macroscopic unit basis vectors as

$$\boldsymbol{e}_{\bar{r}} = \varepsilon\hat{\boldsymbol{e}}_r, \tag{583}$$

$$\boldsymbol{e}_{\bar{\theta}} = \chi^{\star}\left[(1+\varepsilon\bar{r})\cos\kappa\hat{\boldsymbol{e}}_{\theta} + \sin\kappa\hat{\boldsymbol{e}}_z\right], \tag{584}$$

$$\boldsymbol{e}_{\bar{z}} = \chi^{\star}\left(-(1+\varepsilon\bar{r})\sin\kappa\hat{\boldsymbol{e}}_{\theta} + \cos\kappa\hat{\boldsymbol{e}}_z\right), \tag{585}$$

and vice versa

$$\hat{\boldsymbol{e}}_r = \frac{1}{\varepsilon}\boldsymbol{e}_{\bar{r}}, \tag{586}$$

$$\hat{\boldsymbol{e}}_{\theta} = \frac{1}{\chi^{\star}(1+\varepsilon\bar{r})}\left(\cos\kappa\boldsymbol{e}_{\bar{\theta}} - \sin\kappa\boldsymbol{e}_{\bar{z}}\right), \tag{587}$$

$$\hat{\boldsymbol{e}}_z = \frac{1}{\chi^{\star}}\left(\sin\kappa\boldsymbol{e}_{\bar{\theta}} + \cos\kappa\boldsymbol{e}_{\bar{z}}\right). \tag{588}$$

Denoting the metric tensor by $\boldsymbol{I} = g^{ij}\boldsymbol{e}_i\boldsymbol{e}_j$, with component g^{ij} such that

$$g_{ij}g^{ij} = \delta^i_j = \begin{cases} 1, & \text{if } i = j, \\ 0, & \text{if } i \neq j, \end{cases} \tag{589}$$

where $g_{ij} = \boldsymbol{e}_i \cdot \boldsymbol{e}_j$, we find the non-zero covariant components of $\boldsymbol{I}$ to be

$$g_{\bar{r}\bar{r}} = \varepsilon^2, \tag{590}$$

$$g_{\bar{\theta}\bar{\theta}} = \chi^{\star^2}\left(\cos^2\kappa\left(1+\varepsilon\bar{r}\right)^2 + \sin^2\kappa\right), \tag{591}$$

$$g_{\bar{z}\bar{z}} = \chi^{\star^2}\left(\sin^2\kappa\left(1+\varepsilon\bar{r}\right)^2 + \cos^2\kappa\right), \tag{592}$$

$$g_{\bar{\theta}\bar{z}} = g_{\bar{z}\bar{\theta}} = \chi^{\star^2}\cos\kappa\sin\kappa\left(1-\left(1+\varepsilon\bar{r}\right)^2\right), \tag{593}$$

and the non-zero contravariant components of $\boldsymbol{I}$ to be

$$g^{\bar{r}\bar{r}} = \frac{1}{\varepsilon^2}, \tag{594}$$

$$g^{\bar{\theta}\bar{\theta}} = \frac{\left(1+\varepsilon\bar{r}\right)^2 - \varepsilon\bar{r}\left(2+\varepsilon\bar{r}\right)\cos^2\kappa}{\chi^{\star 2}\left(1+\varepsilon\bar{r}\right)^2}, \tag{595}$$

$$g^{\bar{z}\bar{z}} = \frac{1+\varepsilon\bar{r}\cos^2\kappa\left(2+\varepsilon\bar{r}\right)}{\chi^{\star 2}\left(1+\varepsilon\bar{r}\right)^2}, \tag{596}$$

$$g^{\bar{\theta}\bar{z}} = g^{\bar{z}\bar{\theta}} = \frac{\varepsilon\bar{r}\left(2+\varepsilon\bar{r}\right)\sin\kappa\cos\kappa}{\chi^{\star 2}\left(1+\varepsilon\bar{r}\right)^2}. \tag{597}$$

As can be seen by the non-diagonal components of the metric tensor, the microscopic coordinate system is not orthogonal. Therefore, we must calculate the Christoffel symbols before taking derivatives in this coordinate system. Using the expression for the Christoffel symbols of the second kind as

$$\Gamma^i_{jk} = \frac{g^{is}}{2}\left(\frac{\partial g_{js}}{\partial X^k} + \frac{\partial g_{ks}}{\partial X^j} - \frac{\partial g_{jk}}{\partial X^s}\right), \tag{598}$$

the non-zero components are

$$\Gamma^{\bar{\theta}}_{\bar{\theta}\bar{r}} = \frac{\varepsilon\cos^2\kappa}{1+\varepsilon\bar{r}}, \tag{599}$$

$$\Gamma^{\bar{z}}_{\bar{\theta}\bar{r}} = -\frac{\varepsilon\cos\kappa\sin\kappa}{1+\varepsilon\bar{r}}, \tag{600}$$

$$\Gamma^{\bar{\theta}}_{\bar{z}\bar{r}} = -\frac{\varepsilon\cos\kappa\sin\kappa}{1+\varepsilon\bar{r}}, \tag{601}$$

$$\Gamma^{\bar{z}}_{\bar{z}\bar{r}} = -\frac{\varepsilon\sin^2\kappa}{1+\varepsilon\bar{r}}, \tag{602}$$

$$\Gamma^{\bar{r}}_{\bar{\theta}\bar{\theta}} = -\chi^{\star 2}\frac{\cos^2\kappa\left(1+\varepsilon\bar{r}\right)}{\varepsilon}, \tag{603}$$

$$\Gamma^{\bar{r}}_{\bar{z}\bar{\theta}} = \chi^{\star 2}\frac{\cos\kappa\sin\kappa\left(1+\varepsilon\bar{r}\right)}{\varepsilon}, \tag{604}$$

$$\Gamma^{\bar{r}}_{\bar{z}\bar{z}} = -\chi^{\star 2}\frac{\sin^2\kappa\left(1+\varepsilon\bar{r}\right)}{\varepsilon}, \tag{605}$$

noting the symmetry in the covariant indices.

The divergence of a vector is defined as

$$\nabla\cdot\boldsymbol{q} = \frac{\partial q^i}{\partial X^i} + q^s\Gamma^i_{is}, \tag{606}$$

which we can now straightforwardly find to be

$$\nabla \cdot \boldsymbol{q} = \frac{1}{(1+\varepsilon\bar{r})}\frac{\partial\left(1+\varepsilon\bar{r}\right)q^{\bar{r}}}{\partial\bar{r}} + \frac{\partial q^{\bar{\theta}}}{\partial\bar{\theta}} + \frac{\partial q^{\bar{z}}}{\partial\bar{z}}. \tag{607}$$

Let us define the physical components as the components of a tensor object with respect to a normalised basis, i.e. for some general vector $\boldsymbol{q}$,

$$\begin{aligned}\boldsymbol{q} &= q^{\bar{r}}\boldsymbol{e}_{\bar{r}} + q^{\bar{\theta}}\boldsymbol{e}_{\bar{\theta}} + q^{\bar{z}}\boldsymbol{e}_{\bar{z}} \\ &= q^{\bar{r}}\sqrt{g_{\bar{r}\bar{r}}}\frac{\boldsymbol{e}_{\bar{r}}}{\sqrt{g_{\bar{r}\bar{r}}}} + q^{\bar{\theta}}\sqrt{g_{\bar{\theta}\bar{\theta}}}\frac{\boldsymbol{e}_{\bar{\theta}}}{\sqrt{g_{\bar{\theta}\bar{\theta}}}} + q^{\bar{z}}\sqrt{g_{\bar{z}\bar{z}}}\frac{\boldsymbol{e}_{\bar{z}}}{\sqrt{g_{\bar{z}\bar{z}}}} = \bar{q}^{\bar{r}}\hat{\boldsymbol{e}}_{\bar{r}} + \bar{q}^{\bar{\theta}}\hat{\boldsymbol{e}}_{\bar{\theta}} + \bar{q}^{\bar{z}}\hat{\boldsymbol{e}}_{\bar{z}},\end{aligned} \tag{608}$$

where the overline on components indicate a physical component. Now, we can use (583)-(585) to express the components of $\boldsymbol{q}$ in the two different coordinate systems in terms of each other:

$$\bar{q}^{r} = \bar{q}^{\bar{r}}; \tag{609}$$

$$\bar{q}^{\theta} = \frac{\left(1+\varepsilon\bar{r}\right)\cos\kappa}{\sqrt{\left(1+\varepsilon\bar{r}\right)^{2}\cos^{2}\kappa+\sin^{2}\kappa}}\bar{q}^{\bar{\theta}} - \frac{\left(1+\varepsilon\bar{r}\right)\sin\kappa}{\sqrt{\left(1+\varepsilon\bar{r}\right)^{2}\sin^{2}\kappa+\cos^{2}\kappa}}\bar{q}^{\bar{z}}; \tag{610}$$

$$\bar{q}^{z} = \frac{\sin\kappa}{\sqrt{\left(1+\varepsilon\bar{r}\right)^{2}\cos^{2}\kappa+\sin^{2}\kappa}}\bar{q}^{\bar{\theta}} + \frac{\cos\kappa}{\sqrt{\left(1+\varepsilon\bar{r}\right)^{2}\sin^{2}\kappa+\cos^{2}\kappa}}\bar{q}^{\bar{z}}. \tag{611}$$

As we see, the divergence of a vector in physical components is $O\left(\varepsilon^{-1}\right)$ so we define a (normalised) microscopic divergence as

$$\nabla_{\boldsymbol{X}} \cdot \boldsymbol{q} = \varepsilon\nabla \cdot \boldsymbol{q}, \tag{612}$$

with this microscopic divergence representing an $O\left(1\right)$ operator.

Taking leading order as $\varepsilon \to 0$, we observe the microscopic coordinate system's objects simplify considerably due to the non-diagonal components of the metric tensor being of a smaller order than the diagonal components. That is to say, the microscopic coordinate system at leading order is orthogonal. Further,

in this orthogonal system, we note that the Lamé coefficients are independent of $\bar{r}$:

$$|\boldsymbol{e}_{\bar{r}}| = \varepsilon; \tag{613}$$

$$|\boldsymbol{e}_{\bar{\theta}}| = \chi^{\star}; \tag{614}$$

$$|\boldsymbol{e}_{\bar{z}}| = \chi^{\star}. \tag{615}$$

Consequently, at leading order we have that the microscopic divergence of a vector expressed in physical components of the global coordinate system is

$$\nabla_{\boldsymbol{X}} \cdot \boldsymbol{q} = \frac{\partial \bar{q}^{\bar{r}}}{\partial \bar{r}} + \frac{1}{\sqrt{2}} \left(\frac{\partial \bar{q}^{\bar{\theta}}}{\partial \bar{\theta}} \cos\kappa - \frac{\partial \bar{q}^{\bar{\theta}}}{\partial \bar{z}} \sin\kappa + \frac{\partial \bar{q}^{\bar{z}}}{\partial \bar{\theta}} \sin\kappa + \frac{\partial \bar{q}^{\bar{z}}}{\partial \bar{z}} \cos\kappa \right). \tag{616}$$

Following the same procedure, at leading order as $\varepsilon \to 0$ it can be shown that the (normalised) microscopic gradient of a scalar q is

$$\begin{aligned} \nabla_{\boldsymbol{X}} q = \frac{\partial q_{\varepsilon}}{\partial \bar{r}} \hat{\boldsymbol{e}}_r + \frac{1}{\sqrt{2}} \left(\frac{\partial q_{\varepsilon}}{\partial \bar{\theta}} \cos\kappa - \frac{\partial q_{\varepsilon}}{\partial \bar{z}} \sin\kappa \right) \hat{\boldsymbol{e}}_{\theta} \\ + \frac{1}{\sqrt{2}} \left(\frac{\partial q_{\varepsilon}}{\partial \bar{\theta}} \sin\kappa + \frac{\partial q_{\varepsilon}}{\partial \bar{z}} \cos\kappa \right) \hat{\boldsymbol{e}}_z. \end{aligned} \tag{617}$$

In addition, if we suppose an arbitrary surface is given by $\bar{r} = f \equiv f(\bar{\theta}, \bar{z}, t)$, where t denotes the temporal coordinate, we can find two unit tangents, denoted by $\hat{\boldsymbol{t}}_{\bar{\theta}}$ and $\hat{\boldsymbol{t}}_{\bar{z}}$, and the inward pointing unit normal, denoted by $\hat{\boldsymbol{n}}$, to the surface at leading order. Specifically, these are given by

$$\hat{\boldsymbol{t}}_{\bar{\theta}} = \frac{1}{\sqrt{1 + \left(\frac{\partial f}{\partial \bar{\theta}}\right)^2}} \left(\frac{\partial f}{\partial \bar{\theta}} \hat{\boldsymbol{e}}_{\bar{r}} + \hat{\boldsymbol{e}}_{\bar{\theta}} \right), \tag{618}$$

$$\hat{\boldsymbol{t}}_{\bar{z}} = \frac{1}{\sqrt{1 + \left(\frac{\partial f}{\partial \bar{z}}\right)^2}} \left(\frac{\partial f}{\partial \bar{z}} \hat{\boldsymbol{e}}_{\bar{r}} + \hat{\boldsymbol{e}}_{\bar{z}} \right), \tag{619}$$

$$\hat{\boldsymbol{n}} = \frac{1}{\sqrt{1 + \left(\frac{\partial f}{\partial \bar{\theta}}\right)^2 + \left(\frac{\partial f}{\partial \bar{z}}\right)^2}} \left(\hat{\boldsymbol{e}}_{\bar{r}} - \frac{\partial f}{\partial \bar{\theta}} \hat{\boldsymbol{e}}_{\bar{\theta}} - \frac{\partial f}{\partial \bar{z}} \hat{\boldsymbol{e}}_{\bar{z}} \right). \tag{620}$$

BIBLIOGRAPHY

[1] Training & Testing Services, https://www.trainingandtestingservices.co.uk/, Accessed: 2019-09-09.

[2] *Ansys® fluent, release 18.0*. http://www.ansys.com/products/fluids/ansys-fluent. Accessed: 2017-05-20.

[3] *Openfoam*. http://www.openfoam.org. Accessed: 2017-05-20.

[4] *Understanding grinding fluid*. https://www.canadianmetalworking.com/canadianindustrialmachinery/article/metalworking/understanding-grinding-fluid. Accessed: 2019-07-01.

[5] S. Alenius and J. Johansson, *Air flows and particle distribution around a rotating grinding wheel*, Aerosol Sci. Tech., 25 (1996), pp. 121–133.

[6] G. Allaire, *Homogenization of the navier-stokes equations in open sets perforated with tiny holes i. abstract framework, a volume distribution of holes*, Arch. Rational Mech. Anal., 113 (1991), pp. 209–259.

[7] ——, *Homogenization and two-scale convergence*, SIAM J. Math. Anal., 23 (1992), pp. 1482–1518.

[8] G. Allaire and R. Brizzi, *A multiscale finite element method for numerical homogenization*, Multiscale Model. Sim., 4 (2005), pp. 790–812.

[9] S. R. Allmaras, F. T. Johnson, and P. R. Spalart, *Modifications and clarifications for the implementation of the spalart-allmaras turbulence model*, ICCFD7, (2012).

[10] A. Almqvist, *Homogenization of the reynolds equation governing hydrodynamic flow in a rotating device*, J. Tribol., 133 (2011), pp. 021705–021705–8.

[11] A. Almqvist and J. Dasht, *The homogenization process of the reynolds equation describing compressible liquid flow*, Tribol. Int., 39 (2006), pp. 994–1002.

[12] A. Almqvist, J. Fabricius, and P. Wall, *Homogenization of the unstationary incompressible reynolds equation*, Tribol. Int., 40 (2007), pp. 1344–1350.

[13] M. S. Alnaes, J. Blechta, J. Hake, A. Johansson, B. Kehlet, A. Logg, C. Richardson, J. Ring, M. E. Rognes, and G. N. Wells, *The fenics project version 1.5*, Arch. Numer. Softw., 3 (2015), pp. 9–23.

[14] E. B. Arkilic, M. A. Schmidt, and K. S. Breuer, *Gaseous slip flow in long microchannels*, Phys. Fluids, 6 (1997), pp. 167–178.

[15] G. K. Batchelor, *An Introduction to Fluid Dynamics*, Cambridge University Press, Cambridge, 1967.

[16] G. Bayada and M. Chambat, *Homogenization of the stokes system in a thin film flow with rapidly varying thickness*, Math. Model. Numer. Anal., 23 (1989), pp. 205–234.

[17] E. S. Benilov and V. N. Lapin, *An example where lubrication theory comes short: Hydraulic jumps in a flow down an inclined plate*, J. Fluid Mech., 764 (2014), pp. 277–295.

[18] M. Benzi, G. H. Golub, and J. Liesen, *Numerical solution of saddle point problems*, Acta Numer., 14 (2005), pp. 1–137.

[19] D. Boffi, F. Brezzi, and M. Fortin, *Mixed Finite Element Methods and Applications*, vol. 44 of Springer Series in Computational Mathematics, Springer-Verlag, Berlin Heidelberg, 2013.

[20] C. E. Brennen, *Fundamentals of Multiphase Flow*, Cambridge University Press, Cambridge, 2005.

[21] H. Brezis, *Functional Analysis, Sobolev Spaces and Partial Differential Equations*, Universitext, Springer-Verlag, New York, 2011.

[22] F. Brezzi and M. Fortin, *Mixed and Hybrid Finite Element Methods*, vol. 7 of Springer Series in Computational Mathematics, Springer-Verlag, New York, 1991.

[23] A. L. Carrano and J. B. Taylor, *Geometric modeling of engineered abrasive processes*, J. Manuf. Process, 7 (2005), pp. 17–27.

[24] C. C. Chang, S. H. Wang, and A. Z. Szeri, *On the mechanism of fluid transport across the grinding zone*, J. Manuf. Sci. Eng., 118 (1996), pp. 332–338.

[25] P. de Gennes, *Wetting: Statics and dynamics*, Rev. Mod. Phys., 57 (1985), pp. 827–863.

[26] Z. Dongkun, L. Changhe, J. Dongzhou, Z. Yanbin, and Z. Xiaowei, *Specific grinding energy and surface roughness of nanoparticle jet minimum quantity lubrication in grinding*, Chinese J. Aeronaut., 28 (2014), pp. 570–581.

[27] P. G. Drazin and W. H. Reid, *Hydrodynamic Stability*, Cambridge Mathematical Library, Cambridge University Press, 2 ed., 2004.

[28] S. Ebbrell, N. H. Woolley, Y. D. Tridimas, D. R. Allanson, and W. B. Rowe, *The effects of cutting fluid appliction method on the grinding process*, Int. J. Mach. Tools Manuf., 40 (2000), pp. 209–223.

[29] F. Engineer, C. Guo, and S. Malkin, *Experimental measurement of fluid flow through the grinding zone*, J. Eng. Ind., 114 (1992), pp. 61–66.

[30] C. J. Evans and J. B. Bryan, *"structured", "textured" or "engineered" surfaces*, CIRP Ann., 48 (1999), pp. 541 – 556.

[31] J. Fabricius, Y. O. Koroleva, A. Tsandzana, and P. Wall, *Asymptotic behaviour of stokes flow in a thin domain with a moving rough boundary*, P. Roy. Soc. A.-Math. Phy., 470 (2014).

[32] J. Freund and R. Stenberg, *On weakly imposed boundary conditions for second order problems*, Proc. Int. Conf. Finite Elem. Fluids - New Trend Appl., Venezia (1995), pp. 15–21.

[33] C. Geuzaine and J.-F. Remacle, *Gmsh: a three-dimensional finite element mesh generator with built-in pre- and post-processing facilities*, Int. J. Numer. Meth. Eng., 79 (2009), pp. 1309–1331.

[34] S. K. Godunov, *A difference method for numerical calculation of discontinuous solutions of the equations of hydrodynamics*, Mat. Sb., 47 (1959), pp. 271–306.

[35] G. Guennebaud, B. Jacob, et al., *Eigen v3*. http://eigen.tuxfamily.org, 2010.

[36] P. Hryniewicz, A. Z. Szeri, and S. Jahanmir, *Application of lubrication theory to fluid flow in grinding: Part i - flow between smooth surfaces*, J. Tribol., 123 (2000), pp. 94–100.

[37] ——, *Application of lubrication theory to fluid flow in grinding: Part ii - influence of wheel and workpiece roughness*, J. Tribol., 123 (2000), pp. 101–107.

[38] W. Hu, B. Lin, and M. Morgan, *Investigation of the grinding wheel air boundary layer flow*, Adv. Mater. Res., 76-78 (2009), pp. 113–118.

[39] M. Ishii and T. Hibiki, *Thermo-Fluid Dynamics of Two-Phase Flow*, Springer-Verlag, New York, 2 ed., 2011.

[40] S. Jin and Z. Xin, *The relaxation schemes for systems of conservation laws in arbitrary space dimensions*, Commun. Pure Appl. Math., 48 (1995), pp. 235–276.

[41] V. John, *Slip with friction and penetration with resistance boundary conditions for the navier–stokes equations—numerical tests and aspects of the implementation*, J. Comput. Appl. Math., 147 (2002), pp. 287 – 300.

[42] R. S. Johnson, *A Modern Introduction to the Mathematical Theory of Water Waves*, Cambridge University Press, Cambridge, 1997.

[43] P. Jost, *Lubrication (Tribology) - Eduction and Research, A Report on the Present Position and Industry Needs*, Department of Education and Science, London, 1966.

[44] M. Kane and B. Bou-Said, *Comparison of homogenization and direct techniques for the treatment of roughness in incompressible lubrication*, J. Tribol., 126 (2004), pp. 733–737.

[45] J. Kestin, M. Sokolov, and W. A. Wakeham, *Viscosity of liquid water in the range* $-8°C$ *to* $150°C$, J. Phys. Chem., 7 (1978), pp. 941–948.

[46] J. Kettle, T. Lamminmäki, and P. Gane, *Improving grinding fluid delivery using pneumatic barrier and compound nozzle*, Prod. Eng. Res. Dev., 8 (2014), pp. 187–193.

[47] F. Klocke and G. Eisenblätter, *Dry cutting*, CIRP Ann.-Manuf. Technol., 46 (1997), pp. 519–526.

[48] A. N. Kolmogorov, *The local structure of turbulence in incompressible viscous fluid for very large reynolds numbers*, Proc. USSR Acad. Sci., 30 (1941), pp. 299–303.

[49] A. Kurganov and D. Levy, *A third-order semidiscrete central scheme for conservation laws and convection-diffusion equations*, SIAM J. Sci. Comput., 22 (2000), pp. 1461–1488.

[50] A. Kurganov and E. Tadmor, *New high-resolution central schemes for nonlinear conservation laws and convection-diffusion equations*, J. Comput. Phys., 160 (2000), pp. 241–282.

[51] E. Lauga and M. P. Brenner, *Hydrodynamic model of steady movement of a solid/liquid/fluid contact line*, J. Colloid Interface Sci., 35 (1971), pp. 85–101.

[52] ——, *Dynamic mechanisms for apparent slip on hydrophobic surfaces*, Phys. Rev. E, 70 (2004), p. 026311.

[53] B. Launder and B. Sharma, *Application of the energy-dissipation model of turbulence to the calculation of flow near a spinning disc*, Lett. Heat Mass Tran., 1 (1974), pp. 131 – 137.

[54] L. G. Leal, *Advanced Transport Phenomena: Fluid Mechanics and Convective Transport Processes*, Cambridge Series in Chemical Engineering, Cambridge University Press, 2007.

[55] R. LeVeque, *Finite Volume Methods for Hyperbolic Equations*, Cambridge University Press, Cambridge, 2002.

[56] ——, *Finite Difference Methods for Ordinary and Partial Differential Equations: Steady-State and Time-Dependent Problems*, SIAM, Philadelphia, 2007.

[57] D. Li, D. Jing, Y. Pan, B. Bhushan, and X. Zhao, *Study of the relationship between boundary slip and nanobubbles on a smooth hydrophobic surface*, Langmuir, 32 (2016), pp. 11287–11294.

[58] S. Malkin and C. Guo, *Thermal analysis of grinding*, CIRP Ann.-Manuf. Technol., 56 (2007), pp. 760–782.

[59] I. D. Marinescu, M. P. Hitchiner, E. Uhlmann, W. B. Rowe, and I. Inasaki, *Handbook of Machining with Grinding Wheels*, CRC Press, Florida, 2 ed., 2016.

[60] I. D. Marinescu, W. B. Rowe, B. Dimitrov, and H. Ohmori, *Tribology of Abrasive Machining Processes*, Elsevier, Amsterdam, 2 ed., 2013.

[61] A. Marusyk and K. Polyak, *Tumor heterogeneity: causes and consequences*, Biochim. Biophys., 1805 (2009), pp. 105–117.

[62] S. D. Mihić, S. Cioc, I. D. Marinescu, and M. C. Weismiller, *Detailed study of fluid flow and heat transfer in the abrasive grinding contact using computational fluid dynamics methods*, J. Manuf. Sci. Eng., 135 (2013), pp. 041002–1–041002–13.

[63] A. Mikelić, *Homogenization of nonstationary navier-stokes equations in a domain with a grained boundary*, Ann. Mat. Pura Appl., 158 (1991), pp. 167–179.

[64] R. Naidoo and S. Baboolal, *Application of the kurganov–levy semi-discrete numerical scheme to hyperbolic problems with nonlinear source terms*, Future Gener. Comput. Syst., 20 (2004), pp. 465–473.

[65] H. Nessyahu and E. Tadmor, *Non-oscillatory central differencing for hyperbolic conservation laws*, J. Comput. Phys., 87 (1990), pp. 408–463.

[66] X. B. Nie, S. Y. Chen, W. N. E, and M. O. Robbins, *A continuum and molecular dynamics hybrid method for micro- and nano-fluid flow*, J. Fluid Mech., 500 (2004), pp. 55–64.

[67] J. Nitsche, *Über ein variationsprinzip zur lösung von dirichlet-problemen bei verwendung von teilräumen, die keinen randbedingungen unterworfen sind*, Abh. Math. Semin. Univ. Hambg., 36 (1971), pp. 9–15.

[68] T. S. O'Donovan, D. B. Murray, and A. A. Torrance, *Jet heat transfer in the vicinity of a rotating grinding wheel*, J. Mech. Eng. Sci., 220 (2007), pp. 837–845.

[69] N. Patir and H. S. Cheng, *An average flow model for determining effects of three-dimensional roughness on partial hydrodynamic lubrication*, J. Lubr. Technol., 100 (1978), pp. 12–17.

[70] G. Pavliotis and A. Stuart, *Multiscale Methods: Averaging and Homogenization*, Springer, New York, 2008.

[71] S. B. Pope, *Turbulent Flows*, Cambridge University Press, Cambridge, 2000.

[72] L. Prandtl, *Z. angew*, Math. Mech., 5 (1925), pp. 136–139.

[73] A. Quarteroni, R. Sacco, and F. Saleri, *Numerical Mathematics*, Texts in Applied Mathematics, Springer-Verlag, Berlin, Heidelberg, 2 ed., 2007.

[74] O. Reynolds, *On the theory of lubrication and its application to mr. beauchamp tower's experiments, including an experimental determination of the viscosity of olive oil*, Philos. Trans. R. Soc., 177 (1886), pp. 157–235.

[75] L. F. Richardson, *Weather Prediction by Numerical Process*, Cambridge University Press, Cambridge, 1922.

[76] J. P. Rothstein, *Slip on superhydrophobic surfaces*, Annu. Rev. Fluid Mech., 42 (2010), pp. 89–109.

[77] D. A. Rubenstein, W. Yin, and M. D. Frame, *Chapter 6 - microvascular beds*, in Biofluid Mechanics (Second Edition), Biomedical Engineering, Academic Press, Boston, second edition ed., 2015, pp. 227 – 266.

[78] M. R. Schumack, J. Chung, W. W. Schultz, and E. Kannatey-Asibu Jr., *Analysis of fluid flow under a grinding wheel*, J. Eng. Ind., 113 (1991), pp. 190–197.

[79] S. Shaji and V. Radhakrishnan, *An investigation on surface grinding using graphite as lubricant*, International Journal of Machine Tools and Manufacture, 42 (2002), pp. 733 – 740.

[80] B.-J. Shi and T.-Y. Y., *Simplified model of reynolds equation with linearized flow rate for ultra-thin gas film lubrication in hard disk drives*, Microsyst. Technol., 16 (2010), pp. 1727–1734.

[81] C.-W. Shu and S. Osher, *Efficient implementation of essentially non-oscillatory shock-capturing schemes*, J. Comput. Phys., 77 (1988), pp. 439–471.

[82] M. L. Shur, M. K. Strelets, A. K. Travin, and P. R. Spalart, *Turbulence modeling in rotating and curved channels: Assessing the spalart-shur correction*, AIAA J., 38 (2000), pp. 784–792.

[83] E. Skjetne and J. Auriault, *New insights on steady, non-linear flow in porous media*, Eur. J. Mech. B Fluids, 18 (1999), p. 131–145.

[84] P. R. Spalart and S. R. Allmaras, *A one-equation turbulence model for aerodynamic flows*, Rech. Aerosp., (1994), pp. 5–21.

[85] L. Tartar, *The General Theory of Homogenization*, vol. 7 of Lecture Notes of the Unione Matematica Italiana, Springer-Verlag, Berlin, 2010.

[86] B. Tavakol, G. Froehlicher, D. P. Holmes, and H. A. Stone, *Extended lubrication theory: improved estimates of flow in channels with variable geometry*, Proc. R. Soc. A, 473 (2017), p. 20170234.

[87] J. M. Urquiza, A. Garon, and M. I. Farinas, *Weak imposition of the slip boundary condition on curved boundaries for stokes flow*, J. Comput. Phys., 256 (2014), pp. 748 – 767.

[88] R. Verfürth, *Finite element approximation of steady navier-stokes equations with mixed boundary conditions*, ESAIM-Math. Model. Numer. Anal., 19 (1985), pp. 461–475.

[89] J. Warren and P. Root, *The behavior of naturally fractured reservoirs*, Soc. Pet. Eng. J., 3 (1963), p. 245–255.

[90] S. J. Weinstein and K. J. Ruschak, *Coating flows*, Annu. Rev. Fluid Mech., 36 (2004), pp. 29–53.

[91] D. C. Wilcox, *Reassessment of the scale-determining equation for advanced turbulence models*, AIAA J., 26 (1988), pp. 1299–1310.

[92] ——, *Turbulence Modeling for CFD, 3rd ed.*, DCW Industries, California, 2006.

[93] H. Wu, *Investigation of Fluid Flow in Grinding using LDA Techniques and CFD Simulation*, PhD thesis, Liverpool John Moores University, 2009.

[94] M. W. Zeemansky and R. H. Dittman, *Heat and Thermodynamics*, McGraw-Hill, 7 ed., 1997.